Design and Application of Dendrimer-like Molecules:
I. for Diffusion in Membranes
II. as Oligomer Complexing Agents

By

Cuihua Liu

Graduate Program in Chemistry

Submitted in partial fulfilment
of the requirements for the degree of
Doctor of Philosophy

Faculty of Graduate Studies
The University of Western Ontario
London, Ontario
May 1999

National Library
of Canada

Bibliothèque nationale
du Canada

Acquisitions and
Bibliographic Services

Acquisitions et
services bibliographiques

395 Wellington Street
Ottawa ON K1A 0N4
Canada

395, rue Wellington
Ottawa ON K1A 0N4
Canada

The author has granted a non-exclusive licence allowing the National Library of Canada to reproduce, loan, distribute or sell copies of this thesis in microform, paper or electronic formats.

The author retains ownership of the copyright in this thesis. Neither the thesis nor substantial extracts from it may be printed or otherwise reproduced without the author's permission.

L'auteur a accordé une licence non exclusive permettant à la Bibliothèque nationale du Canada de reproduire, prêter, distribuer ou vendre des copies de cette thèse sous la forme de microfiche/film, de reproduction sur papier ou sur format électronique.

L'auteur conserve la propriété du droit d'auteur qui protège cette thèse. Ni la thèse ni des extraits substantiels de celle-ci ne doivent être imprimés ou autrement reproduits sans son autorisation.

0-612-42541-X

Canada

ABSTRACT

The overall goal of this thesis is to establish a relationship between dendritic molecules and their dynamic properties in solutions and model membranes. Particularly, we have probed the effect of size and shape of molecules on their lateral diffusion in model membranes; also we have obtained the aggregation of defined size of proteins using two sets of dendritic chelating agents.

A series of fluorescent nitrobenzoxadiazole-labelled macrocyclic polyamide amphiphiles have been incorporated into model membranes. Their lateral diffusion coefficients determined by fluorescence photobleaching recovery, exhibit different size dependence. The diffusion of molecules with surface areas smaller than 1 nm^2 can be described by a modified free area theory, while that of molecules with surface areas greater than 1 nm^2 can be interpreted with a hydrodynamic Evans-Sackmann model adapted by Tamm. These results lead to a "triple layer" view of the bilayer membrane.

Two sets of dendritic chelating agents are designed and synthesized through sequential and convergent synthetic strategies. The dendritic chelating agents possess shorter and longer pendants with multiple terminal nitrilotriacetic acid groups. In total thirteen intermediates and seven final products are obtained and their structures are characterized. Temperature dependent ^{1}H-NMR experiments suggest the structure of cyclic polyamide ring is planar due to the restricted rotation of amide bonds. The size and the shape of molecules can be defined by the number of nitrogen atoms in the ring of macrocycle.

His-tagged *E. coli* thioredoxin is chosen as a model protein to test the ability of these chelating agents to complex proteins. We demonstrate with native polyacrylamide gel electrophoresis that stoichiometric His-tagged thioredoxin complexes can be formed using the two sets of dendritic chelating agents. By labeling His-tagged thioredoxin with fluorescent Rhodamine Red™-X (RRX) probe, the oligomers of His-tagged thioredoxin molecules can be subsequently detected by confocal laser scanning microscopy and analyzed by image correlation spectroscopy. This technique is applied to analyze the stoichiometry of each protein aggregate quantitatively. Decreasing values of cluster density (CD) and an increasing values of the degree of aggregation confirm that the aggregation of protein can be controlled specifically and selectively in solutions and on the glass surfaces.

This work demonstrates the power of combining novel synthetic strategies with modern biophysical techniques. The results presented in this thesis will provide the background for application of the new compounds to study protein aggregation in cell membranes.

Key Words: Dendritic Complexing agents, His-tagged Thioredoxin, Diffusion, Aggregation

ACKNOWLEDGMENTS

The first and the most, I would like to express my sincere gratitude to my supervisor, Dr. Nils O. Petersen. Thank you for your guidance and encouragement over the course of my entire graduate studies. He has always been patient in assisting me and allowing me to build my own confidence during difficult times. I have been deeply impressed by his incredible scientific abilities. I truly respect his wonderful ideas in solving many problems. Especially, I appreciate his understanding and sending me to my home country (China) several times during the past two years. Without his support and enthusiasm, I would not be here to finish my degree and this thesis would not be possible.

Secondly, I am very grateful to our collaborators: Dr. Robert H. E. Hudson, Dr. Eric Ball. Thanks Robert for your help and creative discussions for my synthesis and Eric for your providing generous protein and great suggestions. Without both of them, my work would not be done as scheduled. Thank Dr. David Cramb and Becky for your time and effort, although our FCS experiments are not attributed to this thesis. Many thanks go to Dr. Peter Norton and Dr. Ron Martin for their examinations of my work. I also would like to thank Drs. Hunter, Baines and Cory for allowing me to join their group meetings to learn more within the organic chemistry field.

Thirdly, I owe many thanks to the members of NOP's group both past and present: Claire, John, Clarence, Glenn, Mamta, Niki, Nora, Kathy, all summer and 490 students for their friendship and various help. It was these people who made my stay more enjoyable.

Fourthly, I would like to extend my thanks to other people who have also helped me get through my study from various aspects: Ms Gaye Hongisto from Graduate Studies, Ms Sandy Dengler and Jane Plus from International Student Office, Dr. Leaist from the Chemistry Department and to many friends who are not mentioned here.

Finally, my deepest gratitude is extended to my family: both my parents and my parents-in-law, particularly to my husband and daughter. This work could not have been completed without their love, support, patience, understanding and the sacrifices that I have asked them to make. They have always been there with me, no matter where I go. Because of their sacrifices over the past four years, this thesis is dedicated to my husband Tianjie Wu and my dearest daughter Pianpian, whom I love the most in my entire life.

TABLE OF CONTENTS

Chapter 3 Synthesis of Dendritic Chelating Agents Containing Multiple Terminal Nitrilotriacetic Acid (NTA) Groups

Chapter 4 Formation of His-tagged *Escherichia Coli* Thioredoxin Aggregates in Solution

Chapter 5 Confirmation of His-tagged thioredoxin Aggregation by Image Correlation Spectroscopy

Chapter 6 Conclusions

LIST OF EQUATIONS

LIST OF FIGURES

LIST OF SCHEMES

LIST OF TABLES

NUMERICAL LIST OF COMPOUNDS

1	1-(nitrobenzoxadiazoyl)-4-lauroyl-1,4-diazacyclohexane
2	1-(nitrobenzoxadiazoyl)-4,7-dilauroyl-1,4,7-triazacyclononane
3	1-(nitrobenzoxadiazoyl)-4,7,10-trilauroyl-1,4,7,10-tetraazacyclododecane
4	1-(nitrobenzoxadiazoyl)-4,7,10,13-tetralauroyl-1,4,7,10,13-pentaazacyclopentadecane
5	1-(nitrobenzoxadiazoyl)-4,7,10,13,16-pentalauroyl-1,4,7,10,13,16-hexaaza-cyclooctadecane
6a	1,4-Bis[4'-N,N-di(carboxymethyl)amino-4'-carboxylbutanoyl)]diazacyclohexane
6b	1,4,7-Tris[4'-N,N-di(carboxymethyl)amino-4'-carboxybutanoyl]triazacyclononane
6c	1,4,7,10-Tetrakis[4'-N,N-di(carboxymethyl)amino-4'-carboxybutanoyl]-tetraazacyclododecane
6d	1,4,7,10,13-Pentakis[4'-N,N-di(carboxymethyl)amino-4'-carboxybutanoyl]-pentaazacyclopentadecane
6e	1,4,7,10,13,16-Hexakis[4'-N,N-di(carboxymethyl)amino-4'-carboxybutanoyl]-hexaazacyclooctadecane
7a	Piperazine, or 1,4-diazacyclohexane
7b	1,4,7-Triazacyclononane
7c	Cyclen or 1,4,7,10-tetraazacyclododecane
7d	1,4,7,10,13-Pentaazacyclopentadecane
7e	1,4,7,10,13-Hexaazacycloocadecane or hexacyclen
8a	1,4-Bis[4'-(N-benzyloxycarbonyl)amino-4'-benzyloxycarbonylbutanoyl]diazacyclohexane
8b	1,4,7-Tris[4'-N-benzyloxycarbonylamino-4'-benzyloxycarbonylbutanoyl]-triazacyclononane
8c	1,4,7,10-Tetrakis[4'-(N-benzyloxycarbonyl)amino-4'-benzyloxycarbonylbutanoyl]-tetraazacyclododecane
8d	1,4,7,10,13-Pentakis[4'-(N-benzyloxycarbonyl)amino-4'-benzyloxycarbonylbutanoyl]- pentaazacyclopentadecane
8e	1,4,7,10,13,16-Hexakis[4'-(N-benzyloxycarbonyl)amino-4'-benzyloxycarbonyl butanoyl]hexaazacycloocadecane
9a	1,4-Bis(4'-amino-4'-carboxybutanoyl)diazacyclohexane
9b	1,4,7-Tris(4'-amino-4'-carboxybutanoyl)triazacyclononane
9c	1,4,7,10-Tetrakis(4'-amino-4'-carboxybutanoyl)tetraazacyclododecane
9d	1,4,7,10,13-Pentakis(4'-amino-4'-carboxybutanoyl)pentaazacyclopentadecane
9e	1,4,7,10,13,16-Hexakis(4'-amino-4'-carboxybutanoyl)hexaazacycloocadecane
10e	1,4,7,10,13,16-Hexakis(4'-amino-4'-methyloxycarbonylbutanoyl-hexaazacycloocadecane
11e	1,4,7,10,13,16-Hexakis[4'-N,N-(dimethyloxylcarbobylmethyl)amino-4'-(methyloxylcarbonylbutanoyl)]hexaazacycloocadecane
12a	1,4-Bis[5'-N,N-di(carboxymethyl)amino-5'-carboxypentylamino-3-oxo-

LIST OF SYMBOLS AND ABBREVIATIONS

a^*	The critical free area
a_0	The van der Waals area per lipid molecule
a	Free area
b_1	The viscous coefficient of friction for the diffusant with the substrate
b_2	The viscous coefficient of the drag between the two monolayers.
b_3	The viscous coefficient of friction for the diffusant with water
δ	Chemical shift in ppm units
D	Lateral diffusion coefficient
g(0,0)	Zero lag amplitude of the autocorrelation function
g_0	Offset of the correlation function from zero due to finite image size
h	The height of a diffusing particle, or the thickness of bilayer in Saffmann-Delbrück model
J	Coupling constant in Hz
k	Boltzmann's constant
L	ligand
N_{max}	Maxium number of molecules on a surface area of $3.14 \times 10^8 \ \mu m^2$
N_c	Total number of molecules per cluster
$\bar{N}_m$	Total number of proteins, monomers
$\bar{N}_p$	Average number of particles, particles can be its monomers, or protein aggregates
<i>	Average pixel intensity
η_M	Viscosity of membrane
η_w	Viscosity of water
ε	Dimensionless radius of a particle
ω	e^{-2} radius of the laser beam
ζ	Numerical factor that accounts for the overlap of free area
P	Protein monomers, which is His-tagged thioredoxin in our case
R	Hydrodynamic radius of particles
R_f	Relative migration distance of protein in polyacrylamide gel
T	Temperature in Kelvin or Celsius
Z	Benzyloxycarbonyl
Bis	N,N-Methylene-bis-acrylamide
Boc	$tert$-butyloxycarbonyl
t-Bu	$tert$-butyl
CD	Cluster density
$CDCl_3$	Deuterium chloroform
^{13}C-NMR	Carbon-13 nuclear magnetic resonance
DA	Degree of aggregation
DCC	N,N'-Dicyclohexylcarbodiimide
DMF	Dimethylformamide
DMPC	Dimyristoylphosphatidylcholine

DMSO	Dimethyl sulfoxide
DSS	2,2-Dimethyl-2-silapentane-5-sulfate
EDTA	Ethylene diamine tetraacetic acid
FAB	Fast atom bombardment
FCS	Fluorescence correlation spectroscopy
FITC	Fluorescein isothiocyanate
FPR	Fluorescence photobleaching recovery
FTIR	Fluorier transform infrared spectroscopy
^{1}H-NMR	Proton-1 nuclear magnetic resonance
His-tagged	Six histidine residues attached to C-terminal or N-terminal of protein
HRMS	High-resolution mass spectra
ICS	Image correlation spectroscopy
IDA	Iminodiacetic acid
MeOH	Methanol
Me	Methyl
MS	Mass spectra
MW	Molecular weight
m/z	Mass per charge
$N_2L[NBD]$	1-(nitrobenzoxadiazoyl)-4-lauroyl-1,4-diazacyclohexane
$N_3L_2[NBD]$	1-(nitrobenzoxadiazoyl)-4,7-dilauroyl-1,4,7-triazacyclononane
$N_4L_3[NBD]$	1-(nitrobenzoxadiazoyl)-4,7,10-trilauroyl-1,4,7,10-tetraazacyclododecane
$N_5L_4[NBD]$	1-(nitrobenzoxadiazoyl)-4,7,10,13-tetralauroyl-1,4,7,10,13-pentaazacyclopentadecane
$N_6L_5[NBD]$	1-(nitrobenzoxadiazoyl)-4,7,10,13,16-pentalauroyl-1,4,7,10,13,16-hexaaza-cyclooctadecane
NBD	7-Nitro-2,1,3-benzoxadiazol-4-yl
NBD-PE	Nitrobenzodiazoyl-egg-phosphatidylcholine
Ni-NTA	Nickel complexed by NTA
$N_2[NTA-Ni]_2$	Mixture of chelating agent **6a** and $NiCl_2$ (1/3)
$N_3[NTA-Ni]_3$	Mixture of chelating agent **6b** and $NiCl_2$ (1/4.5)
$N_4[NTA-Ni]_4$	Mixture of chelating agent **6c** and $NiCl_2$ (1/6)
$N_5[NTA-Ni]_5$	Mixture of chelating agent **6d** and $NiCl_2$ (1/7)
$N_6[NTA-Ni]_6$	Mixture of chelating agent **6e** and $NiCl_2$ (1/7.5)
$N_2[NTA-Ni]_2P_2$	Dimeric **6a**-Ni-His-tagged thioredoxin complex
$N_3[NTA-Ni]_3P_3$	Trimeric **6b**-Ni-His-tagged thioredoxin complex
$N_4[NTA-Ni]_4P_4$	Tetrimeric **6c**-Ni-His-tagged thioredoxin complex
$N_5[NTA-Ni]_5P_5$	Pentameric **6d**-Ni-His-tagged thioredoxin complex
$N_6[NTA-Ni]_6P_6$	Hexameric **6e**-Ni-His-tagged thioredoxin complex
$N_2.[NTA-Ni]_2.$	Mixture of chelating agent **12a** and $NiCl_2$ (1/3)
$N_3.[NTA-Ni]_3.$	Mixture of chelating agent **12b** and $NiCl_2$ (1/6)
$N_2.[NTA-Ni]_2P_2$	Dimeric **12a**-Ni-His-tagged thioredoxin complex
$N_3.[NTA-Ni]_3P_3$	Trimeric **12b**-Ni-His-tagged thioredoxin complex
NMR	Nuclear magnetic resonance

NTA	Nitrilotriacetic acid
RRX	Rhodamine Red™-X; succinimidyl ester of Lissamine Rhodamine B
SD	Surface density in number of molecules per μm^2
SEM	Standard error of the mean
TBTU	2-(1H-benzotriazol-1-yl)1,1,3,3-tetramethyluronium tetrafluoroborate
TFA	Trifluoroacetic acid
TFP-OH	Tetrafluorophenol
TLC	Thin-layer chromatography
TMED	*N,N,N',N'*-tetramethylethylenediamine
TMS	Tetramethylsilane
Tris	Tris-hydroxymethylaminomethane
Trx-S$_2$	Oxidized *E. coli* thioredoxin
Trx-(SH)$_2$	Reduced *E. coli* thioredoxin
UV	Ultraviolet-visible spectroscopy
Z-Glu-OBzl	*N*-α-benzyloxycarbonyl-L-glutamic acid α-benzyl ester

CHAPTER 1 INTRODUCTION

1.1 Biological membranes

Membranes define the outer boundary of a living cell. They participate in many essential cell activities, including barrier functions, transmembrane signalling, forming a locus for metabolic reactions, energy transduction, cell compartmentalization, and intercellular recognition. The membrane allows nutrients to enter but prevents the entry of noxious substances. Transmembrane signalling is a substantial and ubiquitous function initiated by molecules, such as hormones, neurotransmitters, and growth factors. Membranes provide a two-dimensional stable surface which allows enzymatic machinery to operate in a more organized assembly line fashion, since the enzymatic reaction rates are enhanced by clustering the enzymes into a multisubunit complex and/or by restricting their location to two dimensions instead of three. The two-dimensional bilayer membranes form a sealed structure, which allows light or chemical energy to be converted into other forms. In eukaryotes, membranes segregate a compartmentalized cytoplasm in order to increase the efficiency of cell function or to compartmentalize the cell into distinct membrane-bound organelles. Membrane-to-membrane interactions allow cells to recognize one another and to coordinate their activities.

Because of the many membrane functions, the structure of cytoplasmic membrane has been the focus of interest in cell biology. Considerable efforts have been spent over the years in trying to characterize molecular structures of the individual membrane components and their intermolecular interactions in an attempt to relate the structure of membranes to their function. One of the most successful models of membrane structure was introduced by Singer and Nicolson in 1972 (1, 2). The basis of the cell membrane model is a bilayer of lipid molecules where proteins are either embedded as integral proteins, or surface-adsorbed as peripheral proteins (1). Integral proteins span the membrane; peripheral proteins are bound noncovalently to the membrane but do not cross it. The fluid model regarded the membranes as two-dimensional solutions of oriented lipids and globular proteins where the lipids in the bilayer function mainly as a solvent for membrane proteins as shown in Figure 1.1.
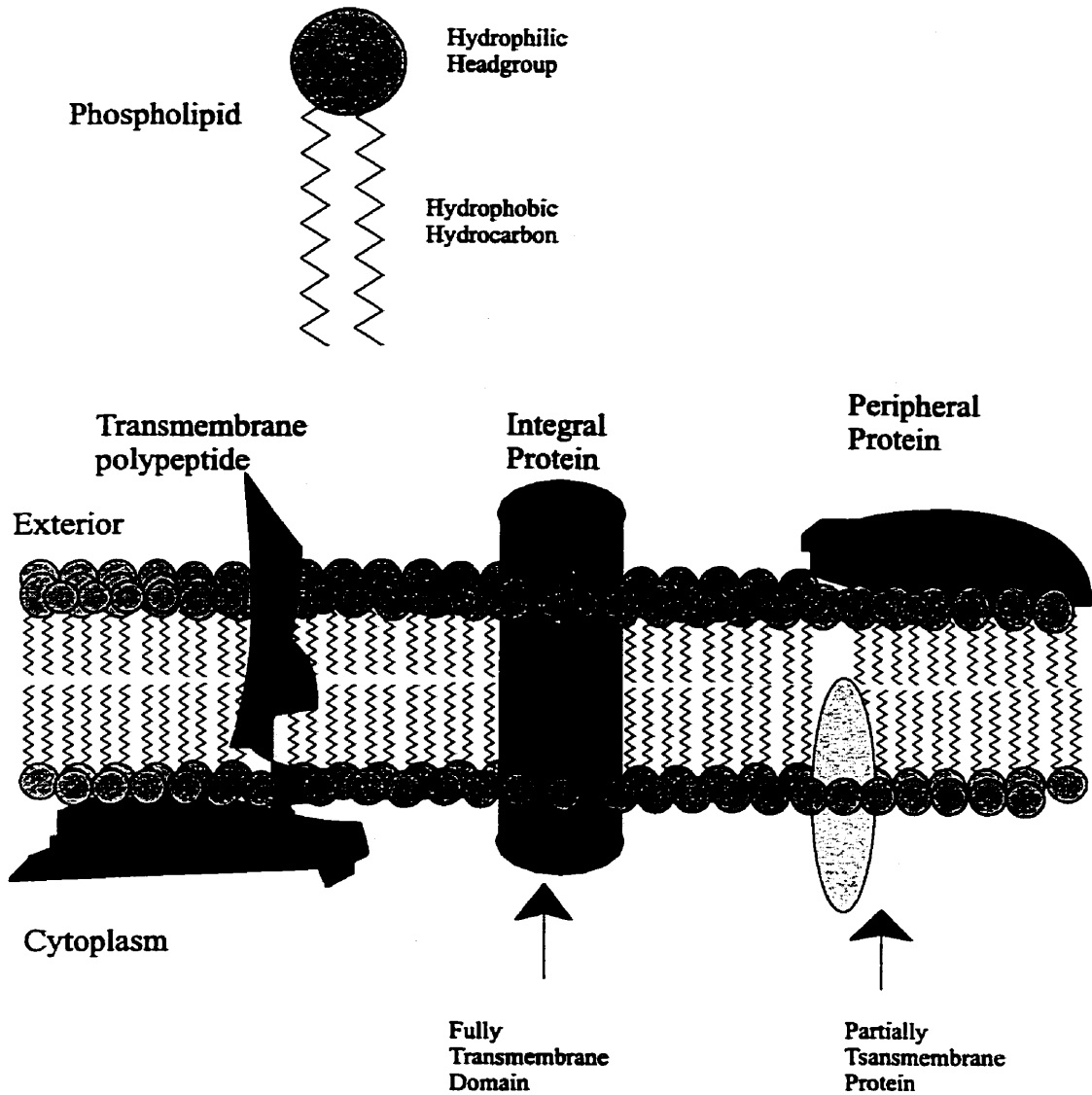
Figure 1.1. The Singer-Nicolson fluid mosaic model
of cell membranes. In this model, lipids are long,
amphiphilic molecules, and spontaneously self-organize
in aqueous media. Their hydrophilic head-groups are
exposed to water and their hydrophobic "tails" are hidden.

According to this model, the lipids and proteins are free to diffuse in the plane of the bilayer and, as a consequence, are randomly distributed in the cell membrane. The biological membranes can be characterized as a complex assembly by the coexistence of major membrane components such as lipids, proteins, and polysaccharides. This assembling process can be simply described by the term "fluidity".

Recent work suggests that membrane organization is much more complicated. The biological membrane is now seen to have some components with highly restricted lateral mobility yet having great rotational freedom (3, 4, 5, 6, 7). For example, in functionally polarized cells (spermatozoa, eggs, epithelia, etc.), the membrane lipids and proteins are organized into domains whose protein and lipid composition differ from the bulk of the membrane (5, 6, 8). This type of microcompartmentalization can be observed on other cell types as well, and the size of these domains is on a micrometer scale (9, 10, 11). Therefore, some modifications in the current fluid mosaic model are needed to account for other structural elements and the apparent membrane heterogeneity (11, 12, 13).

In the original fluid mosaic model, one of the most important structural elements, the cytoskeleton, is not considered. There is an increasing interest in understanding how the cytoskeleton can immobilize proteins directly or indirectly and how it can hinder movement by formation of putative corrals near the membrane surface (12, 14). Single particle tracking measurements have confirmed that movement of proteins is controlled largely by interactions with cytoskeleton within submicron domains (15). The proteins occasionally move between these domains but at a much slower rate (16). Other membrane associated structures, such as coated pits (17), caveolae (18), and detergent-insoluble domains (19), have also been identified.

Although the model of the structure of cell membranes has been modified to induce other components associated with the lipids, the research interest in artificial bilayer membranes has not diminished. They still provide useful model systems for the study of the physico-chemical properties of biological membranes. In model membranes, the properties of membrane as a whole and the interactions between its components are generally quite simple and more easily understood. The model membranes also have the advantage that their

complexity is, in principle, largely under the control of the investigator. It has been observed that protein diffusion within the membrane domains in cell membranes is rapid and comparable to that measured in model membranes. Studies on the diffusion of membrane components in model membranes, therefore, provide a baseline for comparison of studies on the diffusion of cell membrane components in the absence of other interactions.

1.2 Lateral diffusion in biological membranes

Now we attempt to focus on the "fluidity" of biological membranes. The term "membrane fluidity" is usually attributed mostly or solely to the dynamic features of lipid constituents and it is often called "lipid fluidity" (4). Membrane fluidity is governed by a complex pattern of the component mobilities. These mainly include three types of motions of individual lipid molecules: lateral, rotational, and transverse diffusion (6). These types of motions and their corresponding correlation times are depicted in Figure 1.2. The chemical structure of a lipid molecule, such as the nature of the polar head or the length of the hydrocarbon tails, highly influences its dynamic behaviour (20, 21, 22). The hydrophobic tails are composed of saturated or unsaturated fattic acyl chains. The polar head of the lipid may interact with the aqueous medium and with ions, or glycolipids may form a network of hydrogen bonds at the membrane interface.

The basic structure of a membrane as a two-dimensional bilayer was described prior to the fluid mosaic model, but the new feature includes movement of lipids and integral proteins in the plane of lipid bilayer. Lateral diffusion refers to this two-dimensional translocation of the molecules in the plane of the membrane. The characteristic time for moving a molecular dimension is a nanosecond or less. Rotational diffusion allows movement around the long axis of the molecules to the membrane but is restricted to the plane of biological membranes. The correlation time, or the time to rotate a radium is on the 1- to 100-ns time scale (21, 23). The third type of molecular motion is the redistribution of lipid molecules between the two leaflets of the bilayer. This out of plane rotation is termed as "flip-flop" motion. The characteristic time for this type of motion in lipid bilayers is on the order of hours to days. The fluidity of membrane is generally reflected in two major
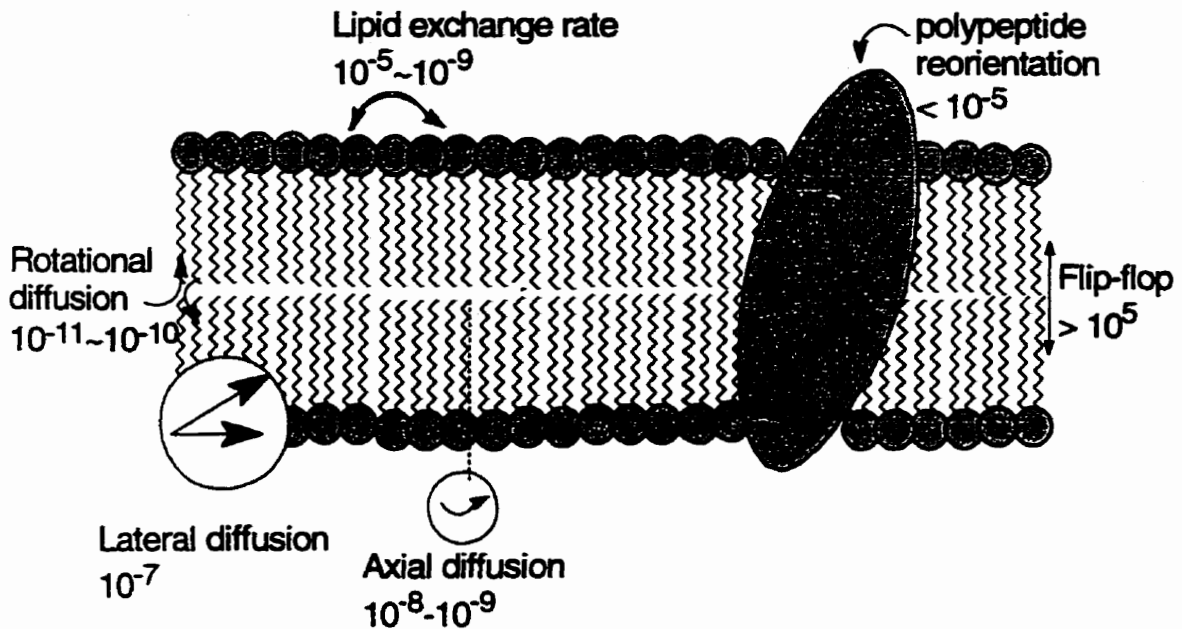
Figure 1.2: Schematic representation of different mobilities of biological membrane components. These include six types of motions of individual lipid molecules: lateral diffusion, rotational diffusion, axial diffusion, lipid exchange, polypeptide reorientation, and transverse (flip-flop) diffusion. However only lateral diffusion, rotational diffusion and flip-flop diffusion are considered for the mobilities of membranes. The correlation times of various dynamic motions are given in seconds. This figure is not drawn in scale. (Adapted from Smith, R. L. and Olefield, E. *Science*, **1984**, 225, 280.)

components: lateral and rotational diffusions. While they must be dependent on similar properties in the membrane such as density and viscosity, to date there is no reliable means of calculating one from the other.

For biological membranes, lateral diffusion is by far the most studied, in part because the measurement is easier to perform. Our interest is restricted to the lateral diffusion although a complete understanding should include both rotational and lateral diffusion. The lateral diffusion of membrane components is believed to be important in a variety of physiological processes in cells (22, 23). For example, the lateral diffusion may control the rate of association of mobile receptors on cell membranes. This may influence the effect of insulin, epidermal growth factor, or nerve growth factor, since they bind their receptors in the first step of signal transduction (24). Lateral diffusion in adhesion was important for the adherence of vesicles to cells (25) and cells to supported lipid bilayers (26). Lateral diffusion increases bond formation and allows adhesion molecules to accumulate at the contact region (27). Diffusion-coupled reactions are also essential, e.g. electron transfer in mitochondria (28) and chloroplast (29) requires diffusion of mobile redox carriers.

1. 3 Aggregation of membrane proteins

While the lateral diffusion is essential to many functions of biological membranes, the aggregation of proteins is significant as well. The coordination of cell growth, differentiation, and other activities in a multicellular organism are precisely controlled by a plethora of growth factors or cytokines that achieve their effects on the cell by binding to specific cell-surface receptors (30). The majority of these numerous receptors for growth factors and cytokines are mainly integral-membrane proteins that contain an extracellular ligand-binding domain, a transmembrane domain with one or more α-helix structures, and a cytoplasmic-effector domain (30, 31). Aggregation of macromolecules within the plasma membrane is believed to play a fundamental role in the regulation of various cellular activities, including the immune response and signal transduction (32, 33). There are two models (34) for signal transduction (Figure 1.3): allosteric receptor-ligand complex activation (Figure 1.3A) and receptor oligomerization (Figure 1.3B). These models are
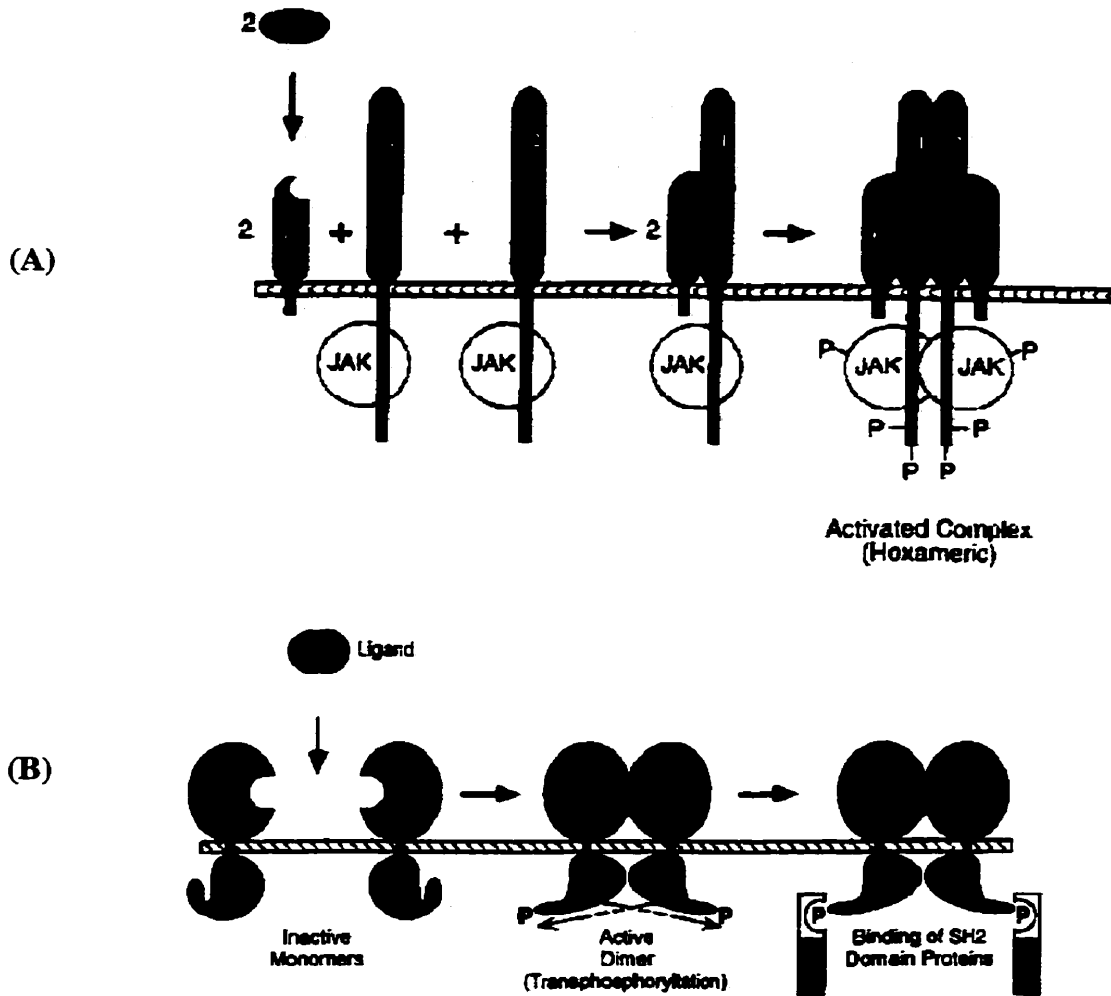
Figure 1.3: (A) Schematic representation of the assembly of an activated ligand/receptor complex. In this case, it is proposed that the cytokine first forms a 1:1 complex with a receptor α-chain. Two such 1:1 complexes then bind to two receptors β to form the tetrameric complex shown. In the complex depicted here, two dimers are brought into close proximity and may autophosphorylate in *trans*, resulting in their activation. (B) Schematic representation of signal activation by ligand-induced dimerization. Prior to ligand binding, the receptor exists in the cell membrane as an inactive monomer. Binding of bivalent ligand stabilizes a dimeric form of the receptor that is active. In the active complex, tyrosine autophosphorylation occurs, in an intermolecular reaction (within or between dimers), leading to activation of the receptor' kinase activity. The binding site represents the downstream signal transduction. (Adapted from Lemmon, M.A. and Schiessinger, J. Transmembrane signaling by receptor oligomerization. *Methods in Molecular Biology, Vol. 84: Transmembrane Signaling Protocols*. Edited by: Bar-Sagi, D., Humana Press Inc., Totowa, NJ. **1998**, 49-71.

widely accepted and invoked to explain molecular mechanism of activation and signalling for many cell surface receptors, including the receptor tyrosine kinases (25, 34, 35). The general oligomerization model (36) holds that inactive receptor monomers are in equilibrium with active receptor dimers such that, in the absence of ligand, the equilibrium greatly favours the monomeric form. Upon ligand binding, the equilibrium is shifted in favour of the activated dimer (which may be a homo- or heterodimer), with resultant biological effects. For example, histamine release by mast cells is triggered by aggregation of FcεRI receptors for IgE (37). It has been recognized that the signalling ligand binds to the extracellular domain of dispersed monomeric receptors in the plasma membrane, inducing the receptor subunits to dimerize. This dimerization event is hypothesized to be integral to activation of the receptor and subsequent transduction of signal inside the cell. It has taken a long time to find experimental evidence to support signal transduction models in bilayer membranes. For example, several research groups have provided experimental data that signal is transduced via conformational changes after binding of the ligand to preaggregated receptors (38, 39, 40). The significance of receptor aggregation is schematically drawn in Figure 1.3.

One special interest is in simultaneous binding of a single multivalent-ligand. This binding entity to two or more receptor molecules is responsible for cytokine-induced receptor oligomerization. The ligand entity may be a bivalent monomer as in the case of human-growth hormone (hGH) receptor (41, 42), or a bivalent dimer as in the case of interferon-γ (IFN-γ) (43), or a multivalent oligomer of higher order as seen with the tumour necrosis factor (TNF) trimer (44). Considering the perceived ubiquity of macromolecular oligomerization as a biological control mechanism and the unresolved questions of mechanistic role in signal transduction, it is of interest to design a system that can selectively and specifically control the molecular aggregation on a membrane surface. It would be then necessary to perform experiments that can directly assess the aggregation state of macromolecules in solution or model membrane system. The overall objective of this thesis work was: (1) to develop a series of dendritic molecules with multiple binding sites to cause specific aggregation, and (2) to test the abilities of these molecules to form specific states of aggregation in solution and on surfaces.

1.4 Research proposal

First, we probe the effect of size and shape of molecules on their lateral diffusion in model biological membranes. Macrocyclic polyamide amphiphiles were synthesized and labelled with a fluorescent dye (NBD) by Alison Paprica during her Ph.D. in our group. The amphiphiles were designed to adopt defined size and shape in the membrane monolayer. They were made to span the size region of interest, from the lipid-scale to membrane protein-scale area (surface area is from 0.3 nm^2 to 3 nm^2). The objective of studying diffusion of these molecules in model membranes was to address a key question raised by Vaz and his coworkers in 1985: Where is the transition in diffusion from free area type diffusion to hydrodynamic like diffusion? Paprica's preliminary finding in 1994 showed that the lateral diffusion of these NBD-labelled macrocyclic polyamides was indeed dependent on their size. Chapter 2 describes a detailed study of this size dependence as a function of temperature. The fluorescent amphiphiles were incorporated into DMPC model membranes, and studied by standard fluorescence photobleaching recovery techniques. The measured diffusion coefficients were compared to predictions from theoretical models, with conclusion that free area theories work well for molecules smaller than 1 nm^2, while hydrodynamic theories are better for molecules larger than 1 nm^2. The results are compared to previous work and a general "triple layer" view of membrane is proposed to account for apparently contradictory behaviour. It is hoped that these properties apply to microdomains in cell membranes, since the diffusive behaviour of molecules in model membrane is comparable to those within the microdomains.

Second, we synthesize molecules needed to study aggregation of proteins in model membranes. The objective is to selectively and specifically control the shape and size of protein aggregates. In solution, we aim to control the state of association and develop methods for selective intermolecular associations. For example, assembly of complexes of proteins which may collectively enhance reaction by improved proximity. In model membranes, we hope to establish specific sizes of protein or peptide clusters to determine the effect of protein sizes on the dynamics (diffusion) of membranes. In cell surface

membranes, we wish to induce signal processing as a model for signal activation of cell surface receptors.

The design and successful preparation of two sets of multivalent dendritic chelating agents are described in Chapter 3. Nitrilotriacetic acid (NTA) was selected as a target chelating agent. Previously NTA has been employed as a chelator to purify proteins by immobilized metal affinity chromatography (IMAC). In modern protein chemistry, NTA is a widely used ligand because it binds strongly to oligomeric histidine residues on proteins of interest. We used NTA as a pendant terminal group and attached two or more to a rigid central ring structure. As a result, specific chelating agents possessing two, three, four, five, or six NTA groups were obtained. In principle, changing the length of the dendritic arms may control the tightness of protein clusters formed by these ligands.

Third, we test if the chelating agents can form specific oligomers of proteins in solution. For this purpose, we use a protein which was expressed as a fusion protein with an oligo-histidine tag by Dr. Ball in the Department of Biochemistry, at the University of Western Ontario. He kindly provided His-tagged *Escherichia coli* thioredoxin for this project. *E. coli* thioredoxin is a small, heat-stable protein with well known structure. Since it is easy to label with a fluorescent probe, *E. coli* thioredoxin is an excellent model protein for the study of protein aggregation by other techniques also. Chapter 4 describes how specific protein complexes (dimers, trimers, tetramers, pentamers, and hexamers) of His-tagged thioredoxin can be formed and observed using nondenaturing (native) polyacrylamide gel electrophoresis (Native PAGE).

Fourth, we demonstrate that the aggregates formed in solution can be observed on a surface. The objective is on the one hand to demonstrate that complexes could be detected on a membrane, and on the other hand that the technique of Image Correlation Spectroscopy is able to discriminate the sizes of the aggregates formed. His-tagged thioredoxin was fluorescently labelled with Rhodamine Red™-X (RRX). Specific complexes of the fluorescent His-tagged thioredoxin were made using the NTA-reagents described in Chapter 3. These samples of dimers, trimers, tetramers, pentamers, and hexamers were prepared using the same procedure as those used in the native PAGE studies. The solutions were dried onto

the surface of glass coverslips and subsequently observed by laser scanning confocal microscopy (LSCM). Confocal images were collected and analysed by image correlation spectroscopy (ICS) to characterize the density of clusters and the degree of aggregation for each sample. The results are described in Chapter 5 and confirm the conclusions from Chapter 4 that the reagents are able to create specific complexes. They also show that in principle, these reagents can be used in membrane studies.

1.5 References

1.   Singer, S.J. and Nicolson, G., The fluid mosaic model of the structure of cell membranes, *Science*, **1972**, 175, 720-729.

2.   Singer, S.J., The molecular organization of membranes. *Ann. Rev. Biochem.* **1974**, 43, 805-833.

3.   Alberts, B., Bray, D., Lewis, J., Roberts, K., and Watson, J.D., Molecular biology of the cell, Garland, London, **1983**, 255.

4.   Shinitzky, M., Membrane fluidity and cellular functions, in *Physiology of Membrane Fluidity*, Shinitzky, M., Ed., CRC Press, Boca Raton, FL, **1984**, Chap. 1.

5.   Edidin, M., Tissue artichiteture and lateral diffusion, *Comments Mol. Cell Biophys.*, **1984**, 2, 285

6.   Damjanovich, S., SzöllÖsi, J., Trón, L. and Edidin, M. "Mobility and proximity in biological membranes". CRC Press, Boca Raton, Florida, **1994**.

7.   Abney, J.R. and Scalettar, B.A. Fluctuations and membrane heterogeneity. *Biophys. Chem.* **1995**, 57, 27-36.

8.   Edidin, M. Lipid microdomains in cell surface membranes. *Curr. Opin. Struct. Biol.* **1997**, 7, 528-532.

9.   Edidin, M. and Stroynowski, I., Differences between the lateral organization of conventional and inositol phospholipid-anchored membrane proteins. A further definition of micrometer scale membrane domains, *J. Cell Biol.* **1991**, 112, 1143-1150.

10.   Simons, K. and Ikonen, E. Functional rafts in cell membranes. *Nature* **1997**, 387,

569-572.

11. Jacobson, K., Sheets, E.D., and Simson, R. Revisiting the fluid mosaic model of membranes. *Science (Washington, D.C.)* **1995**, 268, 1441-1442.

12. Morrow, J.S., Rimm, D.L., Kennedy, S.P., Cianci, C.D., Sinard, J.H., and Weed, S.A. Of membrane stability and mosaics: the spectrin cytoskeleton. In *"Handbook of Physiology. Section 14: Cell Physiology"* . Hoffman, J.F. and Jamieson, J.D., Eds. **1997**, pp. 485-540. Oxford University Press, New York.

13. Devaux, P.F. Protein involvement in transmembrane lipid asymmetry. *Annu. Rev. Biophys. Biomol. Struct.* **1992**, 21, 417-439.

14. Janmey, P. Cell membranes and the cytoskeleton. In " *Structure and Dynamics of Membranes. Generic and Specific Interactions."* Lipowsky, R. and Sackmann, E., Eds. **1995**, Vol. 1B, pp. 805-849. Elsevier, Amsterdam.

15. Kusumi, A. and Sako, Y. Cell surface organization by the membrane skeleton. *Curr. Opin. Cell Biol.* **1996**, 8, 566-574.

16. Kusumi, A., Sako, Y., Fujiwara, T. and Tomishige, M. Application of laser tweezers to studies of the fences and tethers of the membrane skeleton that regulate the movements of plasma membrane proteins. *Methods Cell Biol.* **1998**, 55, 173-194.

17. Schmidt, S.L. Clathrin-coated vesicle formation and protein sorting: an integrated process. *Annu. Rev. Biochem.* **1997**, 66, 511-548.

18. Parton, R.G. Caveolae and caveolins. *Curr. Opin. Cell Biol.* **1996**, 8, 542-548.

19. Brown, D.A., and London, E. Structure of detergent-resistant membrane domains: does phase separation occur in biological membranes? *Biochem. Biophys. Res. Commun.* **1997**, 240, 1-7.

20. Israelachivili, J.N., Marcelja, S., and Horn, R.G., Physical principles of membrane organization, *Q. Rev. Biophys.*, **1980**, 13, 121-200.

21. Axelrod, D. Lateral motion of membrane proteins and biological function, *J. Membr. Biol.*, **1983**, 75, 1-10.

22. McCloskey, M., and Poo, M.-M, Protein diffusion in cell membranes: some biological implications. *Int. Rev. Cytol.* **1984**, 87, 19-81.

23. Jacobson, K., Lateral diffusion in membranes, *Cell Motibility*, **1983**, 3, 367-373.

24. Schlessinger, J., Cellular signaling by receptor tyrosine kinases, Harvey Lect., **1993-94**, 89, 105-123.

25. Heldin, C.H., Dimerization of cell surface receptors in signal transduction. *Cell*, **1995**, 80, 213-223.

26. McCloskey, M.A. and Poo, M.-m, Contact-induced redistribution of specific membrane components: local accumulation and development of adhesion. *J. Cell Biol.*, **1986**, 102, 2185-2196.

27. Dustin, M.L., Ferguson, L.M., Chan, P.-Y., Springer, T.A., and Golan, D.E. Visualization of CD2 interaction with LFA-3 and determination of the two-dimensional dissociation constant for adhesion receptors in a contact area. *J. Cell Biol.* **1996**, 132, 465-474.

28. Chazotte, B. and Hackenbrock, C.R. Lateral diffusion as a rate-limiting step in ubiquinone-mediated mitochondrial electron transport. *J. Biol. Chem.* **1989**, 264, 4978-4985.

29. Lavergne, J., and Joliot, P. Restricted diffusion in photosynthetic membranes. *Trends Biochem. Sci.* **1991**, 16, 129-134.

30. Kishimoto, T., Taga, T., and Akira, S. Cytokine signal transduction. *Cell*, **1994**, 76, 252-262.

31. Ihle, J.N. Cytokine receptor signaling. *Nature*, **1995**, 377, 591-594.

32. Metzger, H. Transmembrane signaling: the joy of aggregation. *J. Immunol.* **1992**, 149, 1477-1487.

33. Ullrich, A., and Schlessinger, J. Signal transduction by receptors with tyrosine kinase activity. *Cell*, **1990**, 61, 203-212.

34. Lemmon, M.A. and Schlessinger, J. Transmembrane signaling by receptor oligomerization. In Transmembrane signaling protocols. *Methods in Molecular Biology*, Edited by Bar-Sagi D. Human Press Inc., Totowa, NJ. **1998**, Vol. 84, pp49-71.

35. Lemmon, M.A., and Schlessinger, J. Regulation of singal transduction and signal

diversity by receptor oligomerization. *Trends Biol. Sci.*, **1994**, 19, 459-463.

36.   Heldin, C.-H. Dimerization of cell surface receptors in signal transduction, *Cell*, **1995**, 80, 213-223.

37.   Holowka, D., and Baird, B. Antigen-mediated IgE receptor aggregation and signaling: a window on cell surface structure and dynamics. *Annu. Rev. Biophys. Biomol. Struct.* **1996**, 25, 79-112.

38.   Gadella, T.W.Jr., and Jovin, T.M. Oligomerization of epidermal growth factor receptors on A431 cells studied by time-resolved fluorescence imaging microscopy. A sterochemical model for tyrosine kinase receptor activation. *J. Cell Biol.* **1995**, 129, 1543-1558.

39.   Sánchez-Mejorada, G. And Rosales, C. Signal transduction by immunoglobulin Fc receptors. *J. Leukocyte Biol.* **1998**, 63, 521-533.

40.   Lynch, R.G. The biology and pathology of lymphocyte Fc receptors. *Americian Journal of Pathology*, **1998**, 152, 631-639.

41.   Sprang, S.R. Bazan, J.F. Cytokine structural taxonomy and mechanisms of receptor engagement. *Curr. Opin. Struct. Biol.* **1993**, 3, 815-827.

42.   Bazan, J.F. Haemopoietic receptors and helical cytokines. *Immunol. Today*, **1990**, 11, 350-354.

43.   Walter, M.R., Windsor, W.T., Nagabhushan, T.L., Lundell, D.J., Lunn, C.A., Zauodny, P.J., and Narula, S.K. Crystal structure of a complex between interferon-γ and its soluble high-affinity receptor. *Nature*, **1995**, 376, 230-235.

44.   Baker, S.J. and Reddy, E.P. Transducer of life and death: TNF receptor superfamily and associated proteins. *Oncogene*, **1996**, 12, 1-9.

CHAPTER 2 SIZE EFFECT OF MACROCYCLIC POLYAMIDES ON THEIR RATE OF DIFFUSION IN MODEL MEMBRANES

2.1 Introduction

The lateral transport of membrane components in the plane of the lipid bilayer is of intrinsic physicochemical interest (1, 2) and of biological and biochemical interest because many membrane-linked, multimolecular biochemical reactions may be diffusion controlled (3, 4). However, an important consequence of the two-dimensional fluid nature of lipid membranes is the unusual size dependence of the lateral diffusion coefficient on the particle radius (5). It has been shown experimentally that the lateral diffusion coefficient (D) for lipids in the fluid phase of artificial bilayers is 1-10 $\mu m^2/s$. For lipids in cell membranes, the D value is lower, in the range of 0.05-2 $\mu m^2/s$, depending on the size of molecules, and the presence of restrictive membrane components (6). Why is the diffusion coefficient of membrane components in the cell membrane one or two orders of magnitude lower than the diffusion in an artificial bilayer? To answer this question, extensive investigations have been focussed on the lateral diffusion of membrane components in both model membranes and plasma membranes. Here, we want to draw attention to the unusual effect of size and shape on diffusion of molecules in model membranes. The approach in this chapter is to measure the lateral diffusion coefficients of a series of fluorescent molecules with similar structure and properties by fluorescence photobleaching recovery (FPR) technique. FPR has played a remarkable role in the study of the structures and interactions of membranes.

2.1.1 Theoretical models of diffusion in membranes

There are several theoretical studies on the size dependence of the diffusion coefficients in both two and three dimensional systems which are based on quite different models (7, 8, 9, 10, 11, 12). Several factors affect the lateral diffusion coefficient: the viscosities of membranes and surrounding water, the size and shape of diffusant, obstructions, hydrodynamic interactions, binding to immobile species, and association among

mobile species.

The rate of lateral diffusion of molecules which are comparable in size to phospholipids can be described by a free area theory (7, 13) as shown in Equation 2.1.

Equation 2.1 $D = D' \exp[-\zeta a^* / a_f(T)]$

Where D is the predicted lateral diffusion coefficient, D' is a pre-exponential factor, which may be thought of as the diffusion coefficient in the limit of infinitely large free area, ζ is numerical constant which corrects for the overlap of free areas, a* is the closed packed area of the diffusing molecule, in this case, phospholipid, and $a_f(T)$ is the mean free area per phospholipid molecule at a given temperature. This latter parameter is a measure of the two-dimensional density of the bilayer. This model is an adaptation of free volume theory (13), which states that the rate of diffusion of a solute is governed by vacancies created by the diffusion of solvent molecules. According to the free area theory, the diffusants which have areas smaller, or equal to those of phospholipids will diffuse at the rate of the lipid itself (14). Once the size of the diffusant exceeds the size of the phospholipids, there is a rapid exponential decrease in the rate of lateral diffusion (2). The prediction of the free area model is diagrammatically illustrated in Figure 2.1.

This analysis of lateral diffusion is too simplified since only phospholipids and diffusants were considered. Nevertheless, there is experimental evidence in support of Equation 2.1 in simple systems. Specifically, a linear relationship between $a_f(T)^{-1}$ and log D has been noted for several phospholipids at various temperatures (15,16). The free area theory takes into account the discreteness of the lipid bilayer and is thus best suited to describe lipid diffusion.

For molecules which are considered large relative to the size of the solvent, continuum hydrodynamic theories for diffusion are considered more appropriate (2, 9, 11, 17, 18). In these theories, the lipid bilayer is represented as a two-dimensional continuum with no structure. The bilayer is treated as a viscous fluid sheet with a thickness h and a

(a)

(b)

(c)
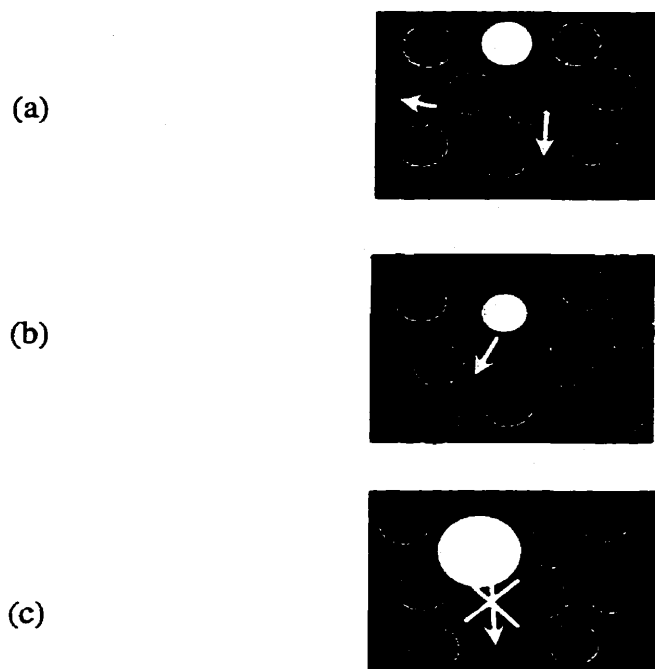
Figure 2.1: Schematic representation of free area theory. (a) Random lateral diffusion of phospholipid molecules by thermal fluctuation. (b) Molecules (white solid dot) with surface area equal to or smaller than that of the phospholipids fill in vacant spaces via lateral diffusion. The diffusion coefficient of molecules is equivalent to that of lipids. (c) Molecules (white solid dot) which have surface areas greater than lipids may be too large to diffuse into spaces created by the lateral diffusion of lipids.

a viscosity η, bounded on both sides by three-dimensional fluids of much smaller viscosities η_M (viscosity of the membrane) and η_w (viscosity of bathing phase, usually water). The diffusing molecule is approximated as a cylinder of height h (to match the bilayer thickness) and radius R. Its diffusion coefficient is given by the Einstein relation (19), $D = kT/f$, and the problem is now to calculate the friction coefficient, f, from hydrodynamic theories. Saffman and Delbrück (9) originally solved the problem for the case where $\eta_M = \eta$, with the result given in Equation 2.2.

Equation 2.2 $\quad f = 4\pi\eta_M h(\ln \dfrac{\eta_M h}{\eta_w R} - \chi)^{-1}$

Where, η_w is the viscosity of medium (water), η_M is the viscosity of the membrane, and h is the membrane thickness. The constant χ is Euler's constant and R stands for the radius of the particle. The system can be characterized by the dimensionless parameter $\varepsilon' = (R/h)[(\eta_w + \eta_M)/\eta_M]$ (17). The solution given by Saffman-Delbrück is an approximation which is valid only for $\varepsilon' \leq 0.1$, that is, when $\eta_w \ll \eta_M$. This is appropriate for model membranes bound by water or dilute salt solutions but may not be valid for systems where the surrounding solutions are highly viscous. When $\varepsilon' \leq 1.0$, a better approximation is given by Hughes as:

Equation 2.3 $\qquad f = 4\pi\eta_M h \, [\ln \dfrac{2}{\varepsilon'} - \chi + \dfrac{4}{\varepsilon'} - \dfrac{(\varepsilon')^2}{2}\ln\dfrac{2}{\varepsilon'}]^{-1}$

Wiegel (20) treated the case of a porous cylinder diffusing within the two-dimensional viscous sheet. This type of particle could correspond to a large, integral protein complex in biological membranes, and the friction factor is then as expressed in Equation 2.4

Equation 2.4 $\qquad f = 4\pi\eta_M h(\ln \dfrac{\eta_M h}{\eta_w R} - \chi + \dfrac{2}{\sigma^2} + \dfrac{Q_0(\sigma)}{\sigma Q_1(\sigma)})^{-1}$

Where Q_0 and Q_1 are modified Bessel functions of the first kind, and $\sigma = R/h_0^{1/2}$, h_0 being the

thickness by which the membrane fluid penetrates the porous cylinder.

Evans and Sackmann (11) considered the effect of weak dynamic coupling of a membrane to an adjacent solid support. This would apply for example to bilayers or monolayers adsorbed to a solid planar surface. They obtained the expression indicated in Equation 2.5, where the diffusing cylinder experiences a different viscous drag at the two ends.

Equation 2.5
$$f = 4\pi\eta_M h \left[\frac{\varepsilon^2}{4} + \frac{\varepsilon K_1}{K_0}\right]^{-1}$$

Where K_0 and K_1 are modified Bessel functions of the second kind, and the dimensionless parameter $\varepsilon = (R/h)(b_s h/\eta_M)^{1/2}$, b_s is a new coefficient of friction between the membrane and the support. If a thin layer of fluid of thickness $\delta \ll \eta_M h/\eta_w$ is inserted between the support and the membrane, $b_s = \eta_w/\delta$. If $\delta \approx \eta_M h/2\eta_w$, then ε becomes identical to ε'.

From the above equations, it is obvious that the diffusion coefficient is dependent on radius of the diffusant (R), as well as the viscosity of the media. However, the dependence on R is relatively weak and much less than the linear dependence predicted in three-dimensional solvents.

2.1.2 Key question

Many researchers have investigated the diffusive behaviour of phospholipids as well as that of large integral membrane proteins whose radii in the plane of the membrane are 1.0 nm or greater (14, 21, 22, 23, 24, 25, 26). The experimental work supports the theoretical argument that it is reasonable to divide diffusive behaviour in lipid bilayers into two regimes as originally proposed by Nir and Stein (27) based on whether the molecular size of the diffusant is comparable to or much larger than that of the solvent, i.e., the lipids of the bilayer. For molecules comparable in size to the host phospholipid, with surface area about 0.65 nm^2, a free area model based on free volume models in three dimensional fluids (8, 12, 13, 17) can be used to fit the data. For molecules large compared to the "solvent" phospholipid (i.e. proteins) with surface areas greater than about 3 nm^2, continuum

hydrodynamic models can be employed (9, 10, 11, 12).

It is not yet certain what description to use when the size of diffusant falls in the intermediate region between the diffusive behaviour described adequately by free area or continuum theories. The region of uncertainty is schematically drawn in Figure 2.2. We wanted to establish whether the free area theory can be extended to molecular areas exceeding 0.65 nm^2 or whether the hydrodynamic description can be exploited at molecular areas smaller than about 3 nm^2. To address this question, Paprica had synthesized a series of intermediately sized macrocyclic polyamide amphiphiles with a fluorescent nitrobenzoxadiazole (NBD) attached to the macrocyclic ring (28) (Figure 2.3). Their surface areas were determined by monolayer techniques to span the transition region between 0.3 nm^2 and 3 nm^2 discussed above. These molecules would be ideal for this work since the only difference is the molecular size.

2.1.3 Fluorescent NBD-labelled molecules

The choice of NBD as a fluorophore was obvious for several reasons. Fluorescent NBD derivatives are easily prepared by allowing compounds containing amino groups to react with (non-fluorescent) nitrobenzoxadiazoyl chloride (NBD-Cl) (28). The structures of fluorescent NBD-labelled macrocyclic polyamide amphiphiles are represented in Figure 2.3. The NBD group is one of the smallest fluorescent probes known which has a λ_{max} value in the visible region and NBD compounds are among the most commonly used fluorescent probes in biological systems (29). NBD-nitrogen derivatives also have favourable optical properties, with molar absorptivity coefficients of approximately 20,000 $cm^{-1}mol^{-1}L$ (30, 31). Their λ_{max} values typically range between 450-490 nm and derivatives are therefore readily excited by the 476.5 nm line of an argon ion laser. NBD phosphatidyl ethanolamine (NBD-PE), an NBD-derived phospholipid, is the single most commonly used probe for determination of lateral diffusion coefficients in lipid bilayer membranes. In addition, NBD-labelled lipids or NBD-labelled macrocyclic polyamide amphiphiles are lipid analogs whose fluorophores are not as bulky as many other dyes, such as fluorescein or rhodamine.
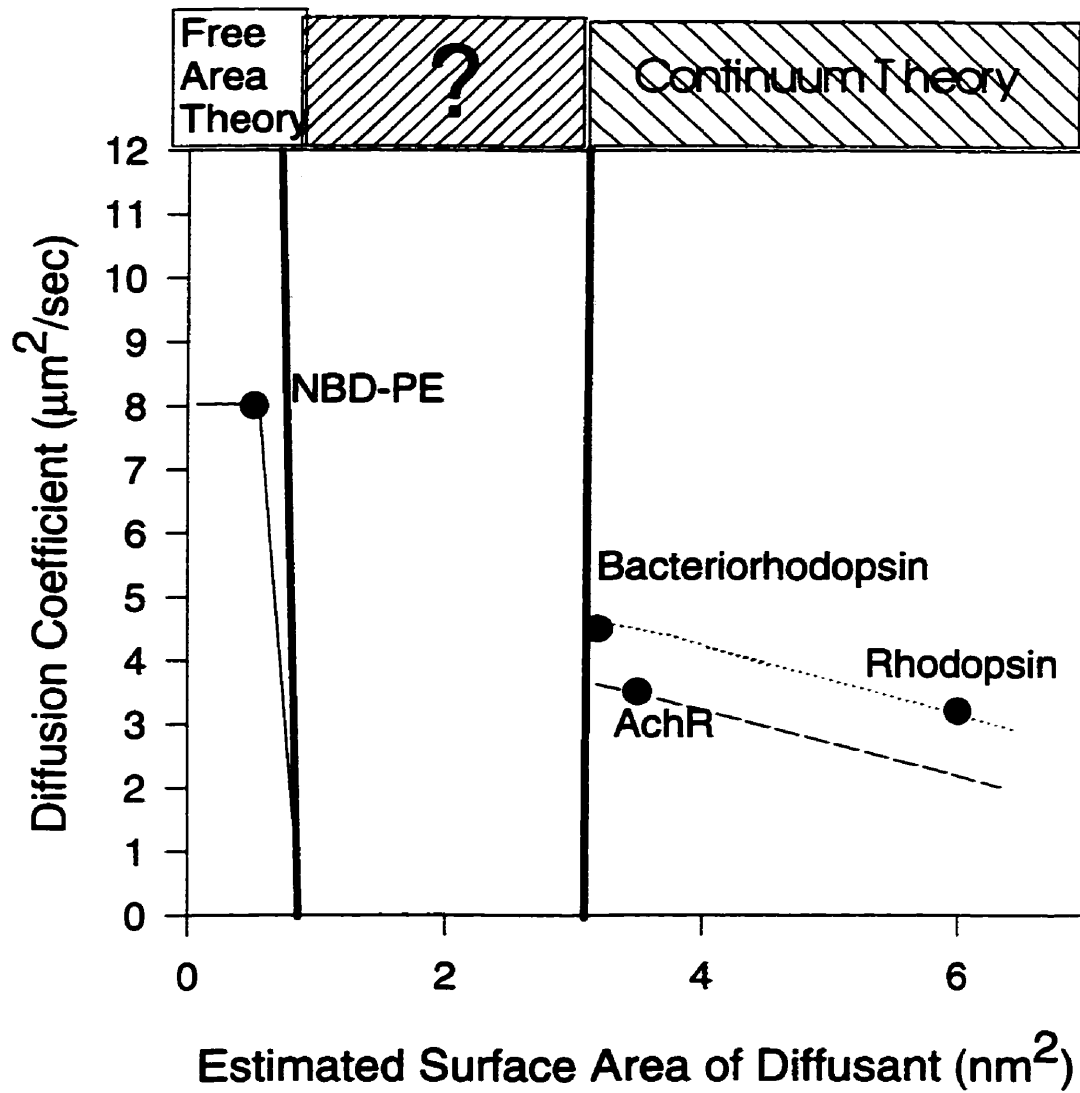
Figure 2.2: Graphical representation of free area and continuum theory. The diffusion of molecules (e.g. NBD-PE) with surface area less than or equal to $0.5\ nm^2$ can be interpreted by free area theory (___). The diffusion of molecules with surface areas greater than or equal to $3\ nm^2$ can be described by continuum theory, such as Saffman-Delbrück theory (......), or Evans-Sackmann model (------). It is not certain what theory can interpret the diffusion behaviour of molecules with surface area ranging from $0.5\ nm^2$ to $3\ nm^2$.

22

NBD: R:

N₂L[NBD] (1)   N₃L₂[NBD] (2)   N₄L₃[NBD] (3)

N₅L₄[NBD] (4)   N₆L₅[NBD] (5)
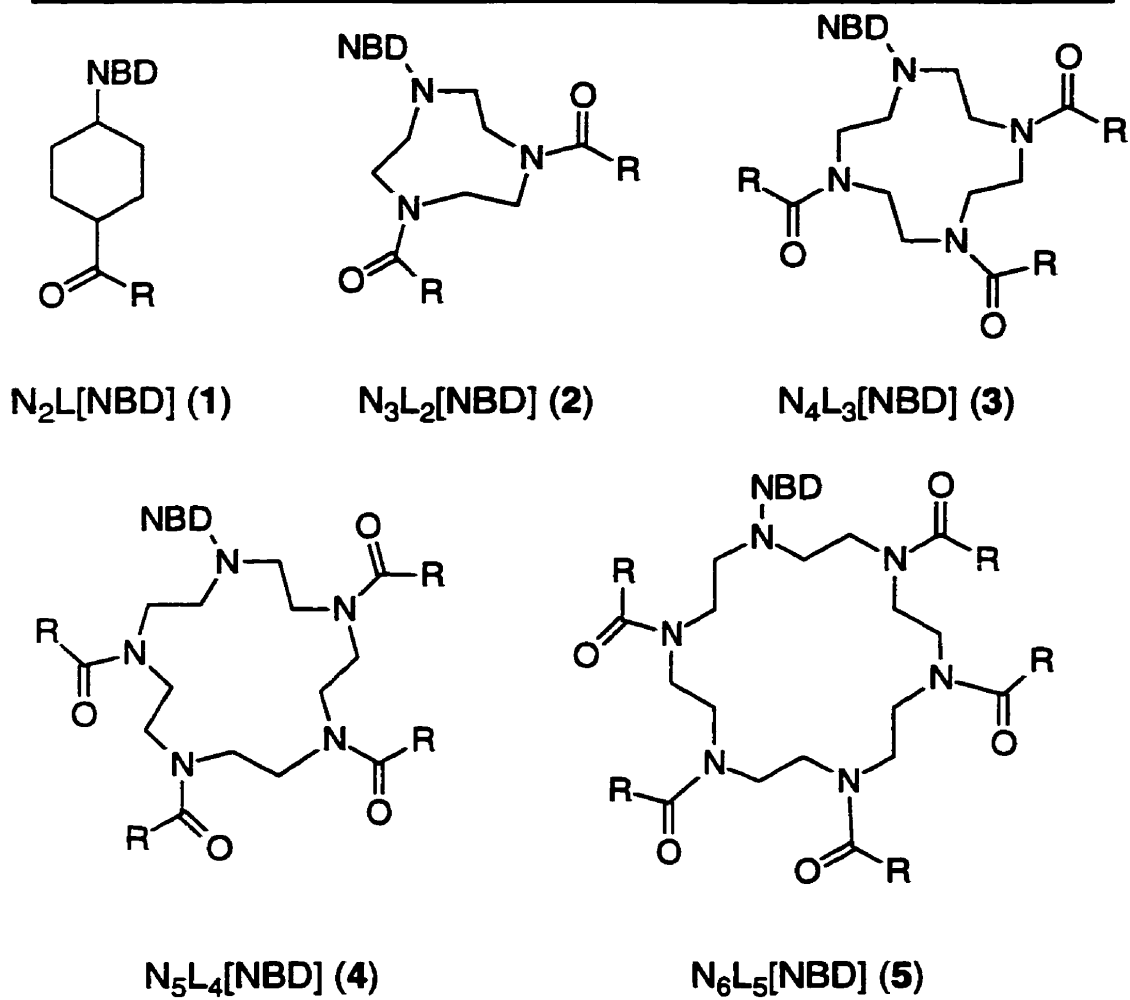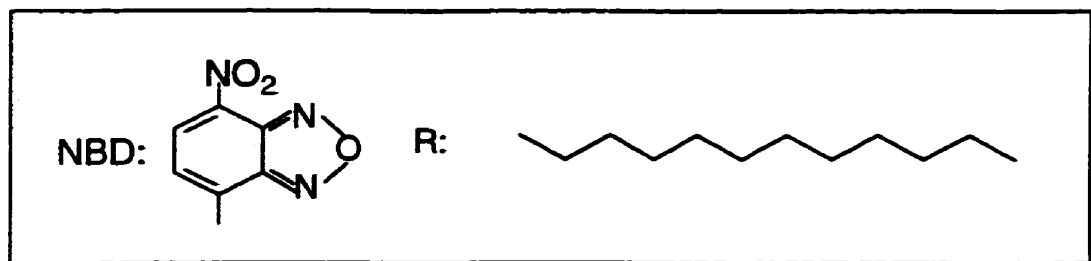
Figure 2.3: The structures of NBD-labelled macrocyclic polyamide amphiphiles.

Each fluorescent amphiphile bears a polar head ring, which is attached by a relatively more rigid NBD group. The tails of amphiphiles are hydrophobic hydrocarbon chains which are flexible. So these NBD-labelled amphiphiles are considered to be easily integrated into the membrane bilayer. As the amphiphile is incorporated into membrane, NBD fluorophore lies near the surface of the bilayer and disrupts the packing of lipid acyl chains in its vicinity (32). More importantly the NBD fluorophore is oriented at the interface when the molecule is inserted into membranes and the emitted fluorescence is polarized. Finally, NBD was chosen as the fluorescent probe since our group has several years experience working with NBD derivatives (28, 29, 31). Paprica found that the diffusion coefficients of NBD-labelled macrocyclic polyamide derivatives are dependent on their sizes (33) at one temperature (36°C). In order to further confirm this result, we have used these NBD-labelled amphiphiles to determine their diffusion coefficients in dimyristoylphosphatidylcholine (DMPC) model membranes by fluorescence photobleaching recovery (FPR) measurements at various liquid-crystalline temperatures.

2.2 Fluorescence photobleaching recovery (FPR)

2.2.1 FPR review

The experimental technique that has so far provided the most information on the lateral diffusibility of cell surface constituents is fluorescence photobleaching recovery (FPR), also termed fluorescence recovery after photobleaching (FRAP). The broad range of biological systems studied by FPR has been described in numerous reviews (34, 35, 36, 37, 38). The membrane component of interest is labelled with a fluorescent tag. Often, this tag is created by conjugating the fluorescent moiety to an antibody that binds specifically to surface protein of interest. Once labelled, the sample is exposed in an epifluorescence microscope with an excitation source to observe the fluorescence at low power. At a predetermined time, a bright light pulse of a wavelength absorbed by the fluorophore (*the bleach pulse*) selectively destroys a fraction of the fluorophores in a small region of the cell or model membranes leaving a gradient of fluorescence on the surface. The diffusion of the labelled species permits that bleached region to recover its fluorescence through the

exchange of molecules from the region of the cell where is not bleached. This fluorescence recovery is observed with the original attenuated light source or the *monitor beam*. Since a gradient of fluorescence is established, the decay of this gradient depends on the transport processes available to the labelled species.

The essence of spot photobleaching is the use of a laser beam to define a bleach region on the fluorescently labelled membrane of about 1 μm^2. An attenuated laser beam is used to monitor fluorescence in the region before the bleach pulse. The bleach pulse typically lasts a few miniseconds and is 3-4 orders of magnitude more intense. After the bleach, the same attenuated laser beam is used to detect the recovery of the fluorescence intensity as a function of time. The transverse intensity profile of the laser beam is Gaussian and the intensity of the laser (I) varies with position in the optical plane according to Equation 2.6

Equation 2.6
$$I(r) = I_o \exp(\frac{-2r^2}{\omega^2})$$

Where I_0 is the intensity of the beam at the centre, and ω is the radius of the beam, defined as the *r* value at which the intensity falls to e^{-2} of its maximum value.

Our home-made FPR instrument couples a laser light source and a photomultiplier detector to a standard microscope (Figure 2.4 and Figure 2.5). A simple beam-splitting device was used to produce co-axial monitor bleach beams and an auxiliary lens is positioned to focus the laser in a secondary image plane so that the objective brings it into sharp focus at the object plane. An aperture is placed between the object and the photomultiplier tube to limit the depth of field. This reduces the amount of fluorescence collected from fluorophores not in the focal plane. The details of the equipment have been described in the descriptions of Figure 2.4 and Figure 2.5.

2.2.2 Measurement of lateral diffusion coefficients

Large multilamellar vesicles (LMV's) were prepared as model phospholipid membrane structures. These structures are essentially vesicular "sacs" which form closed impermeable membrane barriers enclosing distinct intravesicular spaces. They may be as
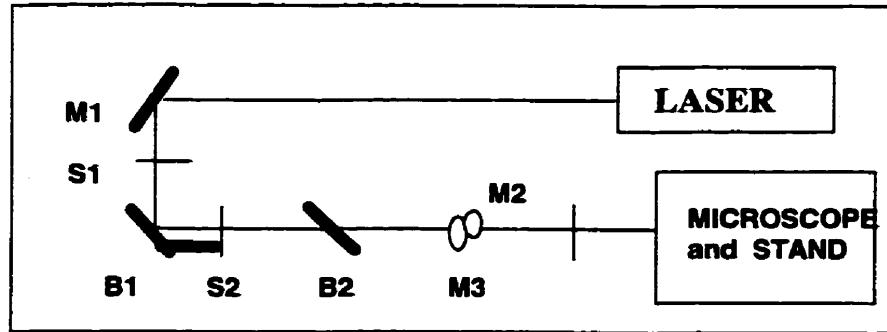
Figure 2.4: Schematic representation of optical FPR setup. The beam splitters, B1 and B2 yield a pair of Gaussian beams with intensities that differ by three or four orders of magnitude. The path of bleach (stronger) beam was indicated by the thicker line. When shutter 2 (S2) is open, the bleach beam is directed into the rear iris of the microscope. Mirrors, M1, M2 and M3 direct the beam, when shutter 1 (S1) limits the incident beam. Figure is not drawn in scale.
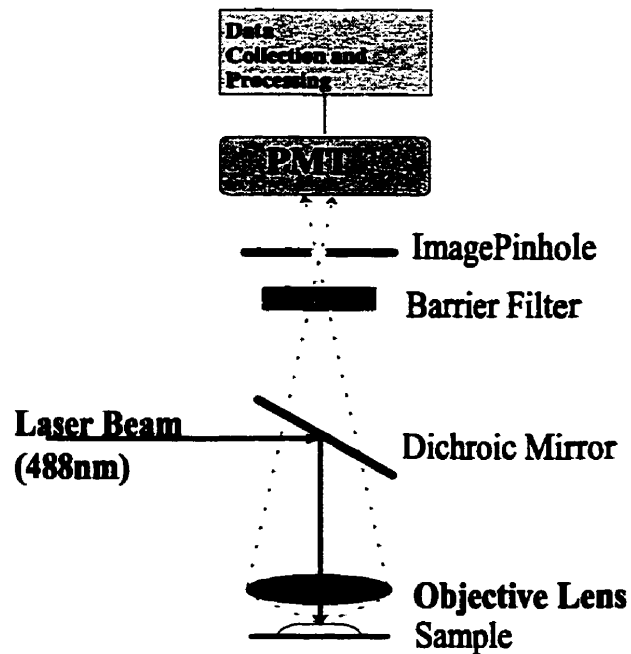
Figure 2.5: Schematic representation of FPR microscope. Fluorescence emission was collected in the objective lens, passes through a dichroic mirror and barrier filter and is focussed on the aperture of an image pinhole. Figure is not drawn to scale.

large as 300 μm in diameter but contain only a few layers. They are prepared by hydration of thin films of phospholipids in solutions of very low ionic strength. A typical protocol includes washing the lipids with deionized water or extracting the lipid solution in organic solvents with deionized water to remove residual ions, drying the lipid over a large surface area and hydrating with distilled water at a temperature above the melting temperature of the hydrated lipid. Within a few hours large vesicles begin to form. LMVs can be observed by fluorescence microscopy and by transmission phase-contrast microscopy at 100-400 × magnification.

In the first step of a typical FPR experiment, the fluorescence intensity of the spot defined by the monitor beam is measured. This fluorescence intensity is refered to as F(-) and corresponds to the average measured fluorescence intensity as labelled amphiphiles diffuse in and out of the monitor beam spot. In the second step, the sample is quickly irradiated with the bleach beam to effect irreversible photolysis (photobleaching) of 30-50% of the fluorescent species within the region defined by the beam spot. The fluorescence intensity immediately after the bleaching process is defined as F(0). After bleaching, the lipids and fluorescent amphiphiles continue to diffuse in and out of the monitor beam spot. As time elapes, the concentration gradient between the bleached and labelled molecules is reduced through the process of lateral diffusion, and eventually the fluorescence intensity returns to a constant level defined as F(∞). The processes of FPR are depicted in Figure 2.6. The mobile fraction (X_m) of fluorescent molecules undergoing lateral diffusion is defined as in Equation 2.7. In model membrane systems, this is expected to be close to unity. In cell membranes, the membrane components appear to be restrictive to diffusion, X_m can be much less than one. The fluorescence recovery curve (Figure 2.6) can be analysed by a curve fitting process (34) to extract the mobile fraction and the beam size. The latter is used as an internal check for the quality of the data.

Equation 2.7 $$X_m = \frac{F(\infty) - F(0)}{F(-) - F(0)}$$

(A)

(1) F(-)

(2) F(0)

(3) F(∞)

PE2009.FPR 95-11-15 12:08:10

(B)

F(-)   F(∞)

F(0)

DC = 0.807E-11 M~2/SEC
XM = 0.968

INTENSITY

1682.

791.

0.

0.   250.   600.

CHANNEL
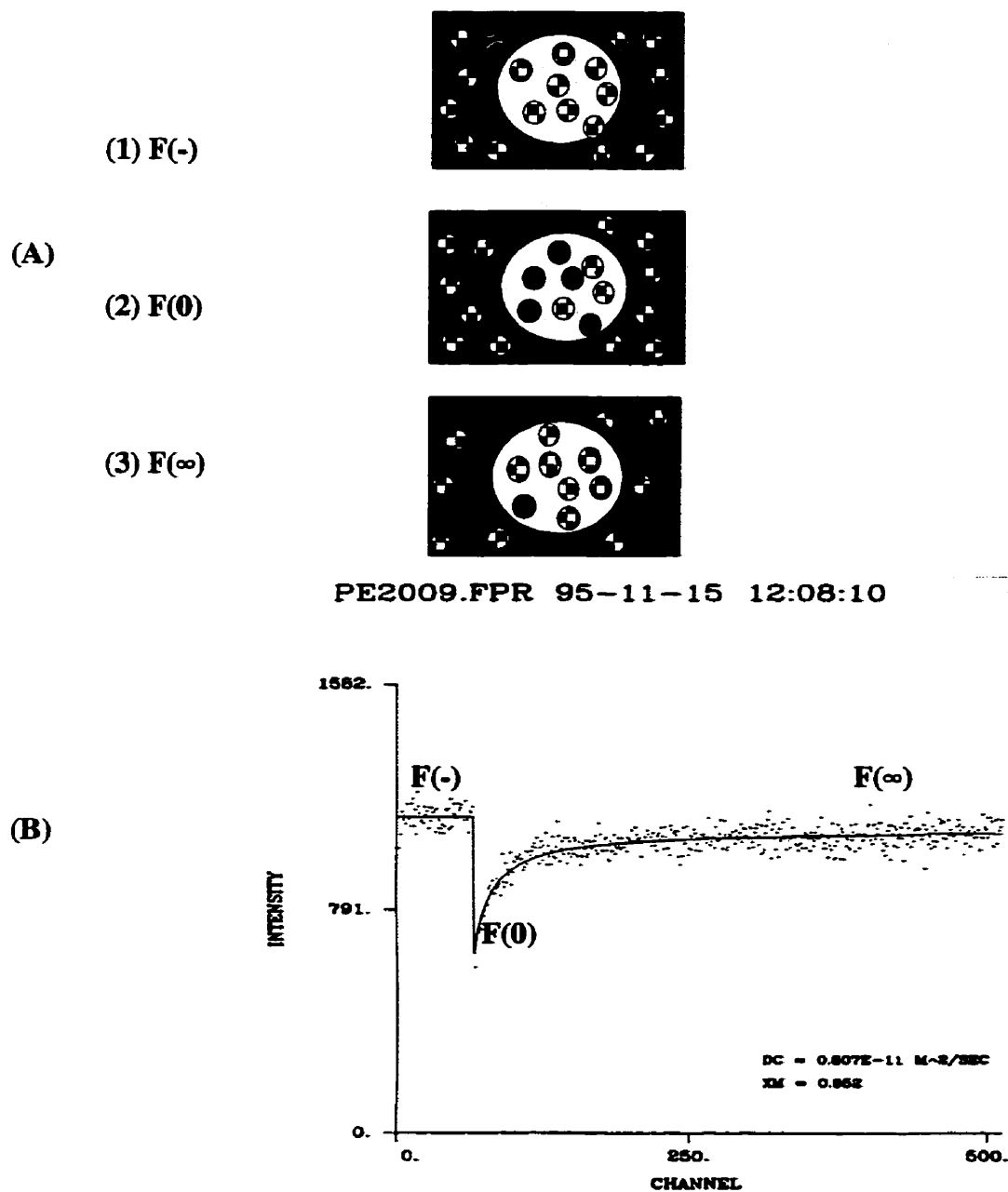
Figure 2.6: (A) Illustrated diagram of an FPR experiment. The black-white dots represent fluorescently labelled molecules. The black dot represents a bleached molecule. Step 1, fluorescence from labelled diffusant within the monitor beam spot (white circle) is monitored. Step 2, the sample is bleached by a brief pulse of light. A concentration gradient produced. Step 3, the fluorescence returns to a constant level. Figure is not drawn in scale. (B) Fluorescence recovery curve for NBD-PE at 32°C. The steps of a FPR experiment are illustrated.

2.2.3 Data analysis and curve fitting

Analysis of FPR recovery curves from the typical experiment is complicated by the Gaussian intensity profile of the laser beam which bleaches a corresponding Gaussian profile in the fluorescence in the spot of interest. There are three parameters to be extracted from a comparison of theoretical and experimental curves. These are the diffusion coefficient, D., the mobile fraction X_m, and the bleach parameter K. The recovery curve was best fitted by nonlinear least square methods (34). The diffusion coefficients can be calculated from the shape of the recovery curve in a spot FPR measurement as represented in Figure 2.6B. This depends on the measured area defined by the focussed laser beam. Measurement of the size of the laser spot is critical to the evaluation of D. We have measured the size of beam by moving a gold scratched coverslip through the laser beam while recording the position. The radius of the beam spot turned out to be about 1.2 μm.

2.3 Materials and Methods
2.3.1 Materials

Dimyristoylphosphatidylcholine (DMPC) was purchased from Fluka (Ronkonkoma, New York). Nitrobenzoxadiazole (NBD) labeled phosphatidylethanolamine (NBD-PE), was obtained from Avanti Polar Lipids (Alabaster, AL). Both were used without further purification. Other NBD-labelled macrocyclic polyamide amphiphiles were prepared by A. P. Paprica (28). The structures of these compounds are shown in Figure.2.3. The compounds are named as 1-(nitrobenzoxadiazoyl)-4-lauroyl-1,4-diazacyclohexane ($N_2L[NBD]$, 1), 1-(nitrobenzoxadiazoyl)-4,7-dilauroyl-1,4,7-triazacyclononane ($N_3L_2[NBD]$, 2), 1-(nitrobenzoxadiazoyl)-4,7,10-trilauroyl-1,4,7,10-tetraazacyclododecane ($N_4L_3[NBD]$, 3), 1-(nitrobenzoxadiazoyl)-4,7,10,13-tetralauroyl-1,4,7,10,13-pentaazacyclopentadecane ($N_5L_4[NBD]$, 4), 1-(nitrobenzoxadiazoyl)-4,7,10,13,16-pentalauroyl-1,4,7,10,13,16-hexaazacyclooctadecane ($N_6L_5[NBD]$, 5). They were repurified and their purity was confirmed by thin-layer chromatography before use. All solutions of DMPC and NBD-labelled compounds were prepared with glass-distilled chloroform.

2.3.2 Vesicle preparation

DMPC lipid vesicles were prepared by a modification of the method of Balcolm and Petersen (39). Typically 2 mg of DMPC was mixed with the NBD molecule at a probe to lipid molar ratio of 1/1000 or less in chloroform solution and allowed to stand for 30 minutes at room temperature. A sample of 200 μL of this solution was deposited as a single drop in the centre of a 22 mm diameter clean (sonified in ethanol for 30 min) and dry glass coverslip heated to 70°C. The chloroform was allowed to evaporate at 70°C and the sample was dried under house vacuum at room temperature for at least two hours. The sample was then heated to 70°C for 5 minutes and a 200 μL drop of doubly distilled deionized water was placed on top of the dry lipid. An 18 mm diameter clean, dry glass coverslip was gently placed on top of the water droplet. The two coverslips, forming a glass/water/glass sandwich, were put in an oven at 70°C for 12 - 15 minutes. After cooling the sample, the edge of the coverslips was sealed with paraffin wax to prevent further evaporation of water. The samples were incubated overnight in the dark at 40°C. Finally the samples were cooled slowly in the oven over a period of several hours and resealed. The lipid vesicles were large with diameters in the range of 10 -100 μm. Only symmetrical, circular or elliptical vesicles were selected for diffusion measurements.

2.3.3 Selection of vesicles

It is very easy to confuse vesicles with other structures and it requires experience to identify them. Here are a few tips for identifying large and good vesicles. Vesicles do not have to look round as seen through the microscope—in fact, if they look perfectly circular, they are probably not vesicles. The shape of the vesicles encountered in the work ranged from slightly oval-like to extremely oblong. They were often irregular (completely asymmetrical) and they varied in size from 10 to 100 nm. Vesicles have extremely faint edges in appearance. Many other structures, such as water droplets, have bright edges due to refraction. Vesicles in contrast, have a low refractive index and have consequently dark (although faint) edges. Vesicles have characteristic focal behaviour in 3-dimensions. They can be focused at a range of depths but their size will appear to change. Paprica described

them as looking like soap bubbles. The fluorescence of vesicles was located at their surfaces, since the probes reside in the lipid bilayers. The vesicle appears in focus at its outermost edges, but the laser's fluorescent focus is usually found at the very top and bottom of the vesicle. Thus, it is easy to test whether or not a vesicle is found by doing the following: position the laser beam through the centre of the vesicle; find the vesicle's best optical focus; reduce the trans illumination in order to observe fluorescence; raise the microscope stage slightly to find the upper focus; lower the microscope stage to find the lower focus. If there are two fluorescent foci that are observed above and below the optical plane of focus, then a real vesicle has been found.

2.3.4 Diffusion measurement

Diffusion measurements were performed with a home-built spot fluorescence photobleaching recovery instrument (34). A Coherent Inc. Innova 70 Four Watt Argon Ion Laser was used as the illumination source. The laser was operated in light regulation mode with an output of approximately 50 mW at 476.5 nm. Timing of the bleach and monitor beams was controlled by a locally designed computer control unit interfaced to a Zenith computer. The microscope used was a Zeiss Universal model fitted for epi-illumination. Fluorescent emission was detected using an RCA 31034A photomultiplier tube which was fitted to the top of the optical column and cooled with dry ice. Data files were saved in ASCII format, then transferred to the VAX or CRAY mainframe computer, where the fluorescence recovery curves were fit and the diffusion coefficients were extracted from the recovery curve of best fit. The objective lens was a 40x water immersion lens with a numerical aperture of 0.75. A laser beam of 1.2 μm radius was produced at the focal plane of the microscope by the combination of a 140 mm focusing lens and the x40 objective lens. The intensity of the bleach and monitor beams was attenuated using neutral density filters of 0.6–1.4 O.D.

Samples were inverted and mounted in a hollow copper holder that contained an axially symmetric hole in the centre which was covered with an 18 mm glass coverslip and sealed with silicone sealant. The holder was filled with water, covering the sample coverslip,

and a light film of thermally conducting grease was applied to the bottom copper holder. The temperature was regulated with a Cambion Bipolar temperature controller (Cambion Division of Midland Ross, Brampton, Ontario) with a microscope stage subassembly. The temperature of the sample was monitored by dipping a small 100 kΩ thermistor into the water and calculating the temperature from a resistance vs. temperature calibration curve provided by the manufacturer (Yellow Springs Instrument Co.). The temperature control is accurate to within $\pm 0.5°C$.

2.4 Results

2.4.1 Correlation of diffusion coefficients with surface areas of NBD-labelled amphiphiles

The lateral diffusion coefficients of five NBD-labelled macrocyclic polyamides (N$_2$L[NBD], 1, N$_3$L$_2$[NBD], 2, N$_4$L$_3$[NBD], 3, N$_5$L$_4$[NBD], 4, N$_6$L$_5$[NBD], 5), and NBD-PE as a control for lipid-diffusion, were determined by photobleaching experiments in DMPC multilamellar vesicles at different temperatures (27-38°C) in the liquid-crystalline phase. The results are shown in Table 2.1. The mean values of the diffusion coefficients were determined with a standard error of the mean of 4-10% at a 95% confidence level. For all NBD-labelled molecules and at all temperatures, the mobile fraction, X_m, was close to unity, which allowed for multiple experiments on the same vesicle. This mobile fraction also confirms that homogeneous incorporation of the probes in the bilayer was achieved. The molar ratio of fluorescent probe : lipid for all diffusion measurements was in the range of 1:1000 to 1:1500. This concentration is low enough for the sample to behave as a nearly ideal system and high enough to allow for good signal-to-noise ratio in the collection of experimental data. The mobile fraction of unity also attests to a nearly ideal mixing of the probe and the lipids in the liquid-crystalline phase. The lateral diffusion of NBD-labelled molecules in fluid DMPC bilayers was studied in the temperature range from 27°C to 38°C. There is no phase transition in the bilayer of DMPC in this temperature range.

Table 2.1: Summary of diffusion measurements of NBD-labelled amphiphiles

NBD-labelled Probe	$D^{\S}$ (n¶) ($\mu m^2/s$)				
	27°C	30°C	32°C	35°C	38°C
NBD-PE	6.5 ± 0.6(32)	7.3 ± 0.4(35)	8.8 ± 0.7(34)	9.1 ± 0.6(38)	11.1 ± 0.6(34)
N_2L[NBD]	6.8 ± 0.5(32)	7.3 ± 0.5(30)	9.2 ± 0.4(37)	9.4 ± 0.6(37)	11.5 ± 0.8(30)
N_3L_2[NBD]	6.3 ± 0.3(40)	7.2 ± 0.8(32)	8.6 ± 0.6(35)	8.7 ± 0.6(36)	11.0 ± 0.8(38)
N_4L_3[NBD]	5.2 ± 0.3(34)	5.9 ± 0.5(36)	6.3 ± 0.4(32)	6.8 ± 0.6(35)	8.8 ± 0.5(35)
N_5L_4[NBD]	5.0 ± 0.3(38)	5.4 ± 0.3(35)	5.7 ± 0.4(38)	5.8 ± 0.2(37)	7.2 ± 0.6(34)
N_6L_5[NBD]	4.6 ± 0.2(39)	5.0 ± 0.2(36)	5.3 ± 0.3(34)	5.4 ± 0.3(38)	6.9 ± 0.2(39)

§ Values of diffusion coefficients measured by photobleaching technique at lipid liquid-crystalline temperatures, were given as mean ± SEM at a confidence of 99%.

¶ The number of measurements.

In our lab Paprica had previously determined the surface areas of NBD-labelled macrocyclic polyamide amphiphiles using Langmuir Film Balance technique (28) under a surface pressure of 30 mN / m. This value of surface pressure is the best estimate available to describe the surface pressure in each monolayer of a bilayer membrane (40, 41). These data were adopted as shown in Table 2.2.

Table 2.2: Surface area measured by Langmuir film balance technique

Probe	1	NBD-PE	2	3	4	5
Surface area (nm^2)	0.33 ± 0.03	0.51 ± 0.05	0.77 ± 0.08	1.00 ± 0.10	1.56 ± 0.16	2.24 ± 0.22

Surface area was measured at surface pressure of 30 mN / m, and was given by the standard error of the mean (SEM). These data were adopted from Paprica's thesis work (33).

Combining the data from Table 2.1 and Table 2.2, we plot diffusion coefficient as a function of surface area for these NBD-labelled amphiphiles at the five temperatures. Figure 2.7 shows the correlation of diffusion in fluid DMPC model membranes with the surface areas of NBD-labelled macrocyclic polyamides at 30 mN/m of surface pressure (28). It is very clear that the rate of lateral diffusion depends on molecular area in the region from 0.3 nm^2 to 3 nm^2. It is also seen that the relative effect of the size of the diffusing molecule is almost independent of temperature. These experiments indicate that the diffusion of smaller molecules with areas comparable to the lipid is faster than that of larger molecules. The rate of diffusion for NBD-PE (as in Table 2.1) is almost identical to literature values (21, 22, 23, 24, 25, 26). In contrast, the larger molecules (N_5L_4[NBD], N_6L_5[NBD]) have diffusion rates about two-thirds of that of NBD-PE. These results provide an indication that the diffusive mechanism is different as the size of the molecule changes.

Vaz and co-workers (16) have treated the diffusion of NBD-PE as typical self-diffusion of lipids, since it has approximately the same surface area as DMPC. The surface area of lipids is reported to be about 0.65 nm^2 for a variety of saturated acyl chain lengths at corresponding lipid crystalline phase temperatures of lipids (42). Our values of the surface areas of the NBD-labelled molecules, N_2L[NBD], NBD-PE and N_3L_2[NBD] are thus comparable to that of DMPC. Also, both NBD-PE and N_3L_2[NBD] contain two acyl chains. While the latter is two methylene segments shorter than the chains in DMPC, the acyl chain length has been found to not affect the diffusion coefficient (16). Vaz has argued that the diffusion behaviour of lipid-like molecules can be expected to be described best by a free area theory of lipid self-diffusion. To confirm this expectation, we used the interfacial viscosity limited free area theory (16), developed from the free-volume theory of Cohen and Turnbull (13, 43) for diffusion in liquid, glass-forming materials. This model takes into account the viscous drag forces experienced by a particle in a membrane due to its contact with water at the aqueous interface and with the ends of the lipid molecules of the opposing monolayer at the bilayer midplane. In this model, the diffusion coefficient is given by Equation 2.8.
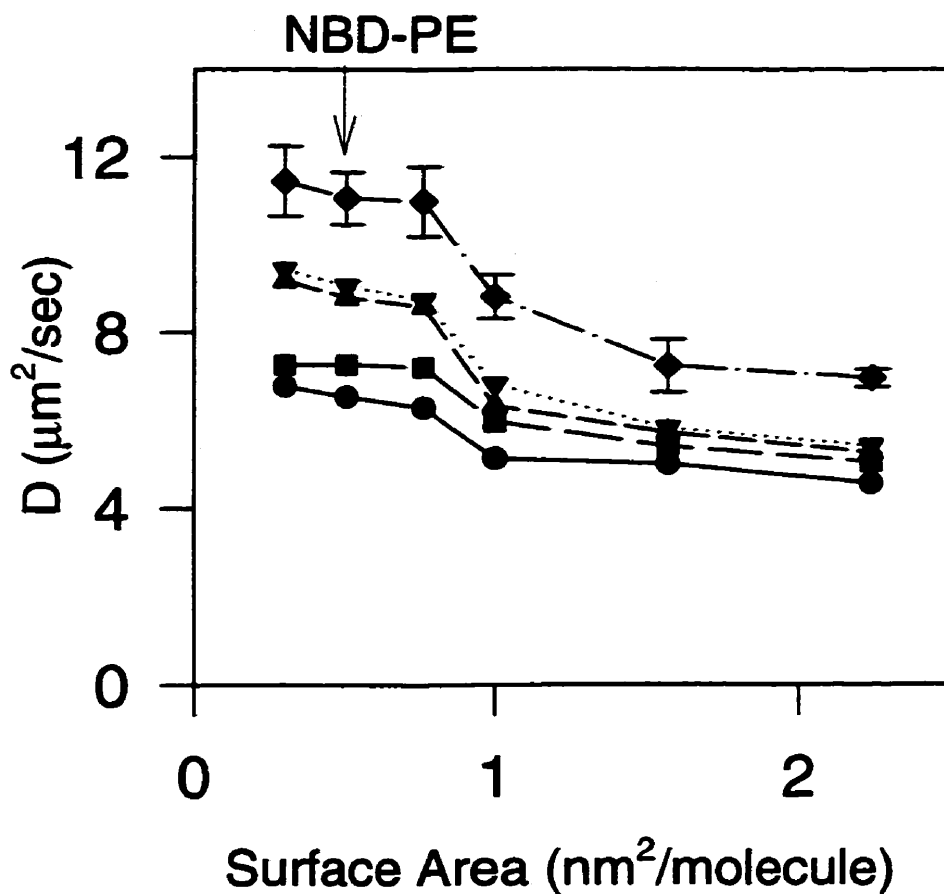
Figure 2.7: Dependence of the lateral diffusion coefficients of NBD-labeled amphiphiles as a function of their surface areas at five temperatures, 27°C (●), 30°C (■), 32°C (▲), 35°C (▼), 38°C (◆). The reference molecule (NBD-PE) used as standard control is indicated by the arrow. For simplicity the set of standard errors are shown only for measurements at 27°C.

Equation 2.8

$$D = (\frac{kT}{f})\exp[(-\varsigma a^*)/(a_0[\beta + \alpha_a(T-T_m)])]$$

Where k is Boltzmann's constant, T is the temperature in Kelvin, f is the translational friction coefficient resulting from drag forces at the membrane-water interface and at the bilayer midplane, T_m is the lipid bilayer main phase transition temperature in Kelvin, ς is a numerical factor that accounts for the overlap of free area (ς has values between 0.5 and 1.0), a^* is the critical free area, a_0 is the van der Waals area per lipid molecule, $a_0\beta$ is the free area at T_m, and α_a is the lateral thermal expansion coefficient in the liquid-crystalline phase. We have used previously published values of $\varsigma a^*/a_0 = 0.4$, $\alpha_a = 2.3 \times 10^{-3}$ K^{-1}, $\beta = 0.148$, and for the DMPC bilayers $T_m = 23.9°C$ (7, 16) for our theoretical calculations. The friction coefficient was considered to contain two terms, $f = f_1 + f_2$, where f_1 is due to the interaction of the lipid polar head group with the aqueous phase at the bilayer-water interface, and f_2 is due to the interaction of the acyl chain ends of the lipid with the other half of the bilayer. Generally, friction coefficients have the form, $f_i = C_i\eta_i$, where C_i is a constant that is equal to 4π times a radius of a particle and η_i is the viscosity of corresponding liquid. Thus, $f_1 = 4\pi\eta_w R$, where R is the protruding radius of the particle, and η_w is the viscosity of water, which is itself a function of temperature. There is no appropriate estimate for f_2 since it is difficult to pick a value for the radius of the acyl chain end, which is embedded within the bilayer, and can not be treated well as a sphere. Here, the value for f_2 was used as an adjustable parameter in the model calculation of the diffusion coefficients. The values of f_2 used are shown in the caption of Figure 2.8 and found to have a value of about 4×10^{-11} Ns / m (16). Using all of these values in Equation 2.8, we calculate the diffusion coefficients which are expected for molecules with surface areas up to 0.8 nm^2, the results are shown as the dotted line in Figure 2.8. The diffusion coefficients calculated from Equation 2.8 with the outlined values are in good agreement with the experimentally determined diffusion coefficients at all temperatures shown in Figure 2.8. This appears to be an excellent
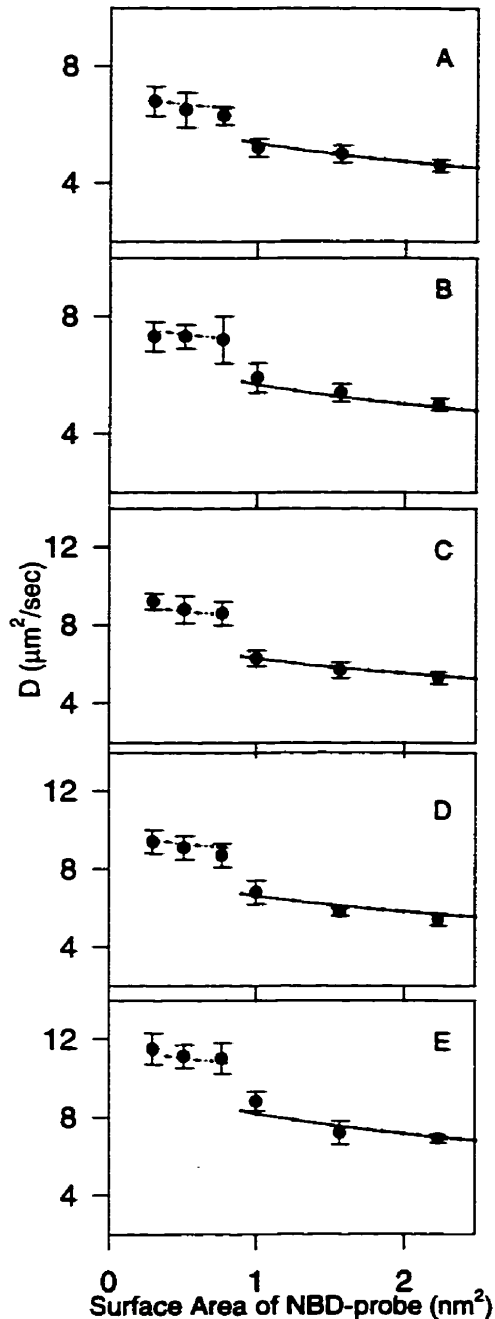
Figure 2.8: Comparision of measured values (●) of lateral diffusion coefficients for NBD-labelled cyclic polyamide amphiphiles with calculated values. The model calculations use the modified free area theory (Equation 2.9) for small molecules (dotted line) and the Evans-Sackmann hydrodynamic model (Equation 2.11) for larger molecules (solid line). The error bar represents standard error of the mean of the measurements. The simulations were performed with the following fixed parameters: $\gamma a^*/a_0 = 0.4$, $\beta = 0.148$, $\alpha_a = 2.3 \times 10^{-3}$ K^{-1}, $T_m = 23.9$ °C, $h = 1.05$ nm, $b_1 = 3 \times 10^6$ Ns/m^3, $b_1/b_2 = 1/2.5$. The adjustable parameters were μ_M, μ_w, f_2. These were set to obtain the best apparent fit for each temperature as follows: (A) 27°C, $\mu_w = 0.0088$ Poise, $\mu_M = 1.25$ Poise, $f_2 = 4.35 \times 10^{-11}$ Ns/m; (B) 30°C, $\mu_w = 0.00808$ Poise, $\mu_M = 1.1$ Poise, $f_2 = 4.4 \times 10^{-11}$ Ns/m; (C) 32°C, $\mu_w = 0.00765$ Poise, $\mu_M = 1.05$ Poise, $f_2 = 4.0 \times 10^{-11}$ Ns/m; (D) 35°C, $\mu_w = 0.00728$ Poise, $\mu_M = 1.0$ Poise, $f_2 = 4.2 \times 10^{-11}$ Ns/m; (E) 38°C, $\mu_w = 0.007$ Poise, $\mu_M = 0.78$ Poise, $f_2 = 3.9 \times 10^{-11}$ Ns/m.

description of diffusion for small molecules with areas as large as 0.8 nm^2.

The hydrodynamic property of diffusing molecules with radius much greater than 1 nm was originally described by the Saffmann and Delbrück model (9). The relevant equation for lateral diffusion of a cylinder in a thin viscous sheet, such as for an integral membrane protein (bacteriorhodopsin and rhodopsin) in a lipid bilayer, is given by Equation 2.9, which was actually derived from Equation 2.2.

Equation 2.9 $$D = \frac{kT}{4\pi\eta_M h}[\ln\left(\frac{\eta_M h}{\eta_w R}\right) - 0.5772]$$

In this equation, h is the thickness of the viscous sheet (the membrane), which is equal to the height of the cylinder. η_M and η_w are the viscosities for the membrane and the surrounding aqueous solution, respectively, and R is the radius of the diffusing cylinder. Equation 2.9 has been tested experimentally and has been found to describe adequately the lateral diffusion of some large membrane proteins (area > 3 nm^2) which span the phospholipid bilayer completely (14, 43). According to Equation 2.9, D value depends only weakly on the radius of the particle.

The Saffmann-Delbrück model is strictly only applicable to molecules which span a symmetric membrane entirely (44, 45). Evans and Sackmann have extended the hydrodynamic approach (11) by treating the diffusing particle as a cylinder inserted into an asymmetric phospholipid bilayer. Thus the bilayer is a pseudo-two dimensional fluid continuum but with different boundary conditions above and below the diffusant. A schematic diagram (Figure 2.9) clearly shows two hydrodynamic theories of the Saffmann-Delbrück model and the Evans-Sackmann model. About ten years ago, the Evans-Sackmann model was applied to membranes by Tamm and his co-workers (46). Thus, the lateral diffusion can be expressed as Equation 2.10 according to the derivation of Tamm from the Evans-Sackmann model.

Equation 2.10 $$D = \frac{kT}{4\pi\eta_m h}\times[\frac{\varepsilon^2}{4}\times(1+\frac{b_1}{b_2}) + \varepsilon\times\frac{K_1}{K_0}]^{-1}$$
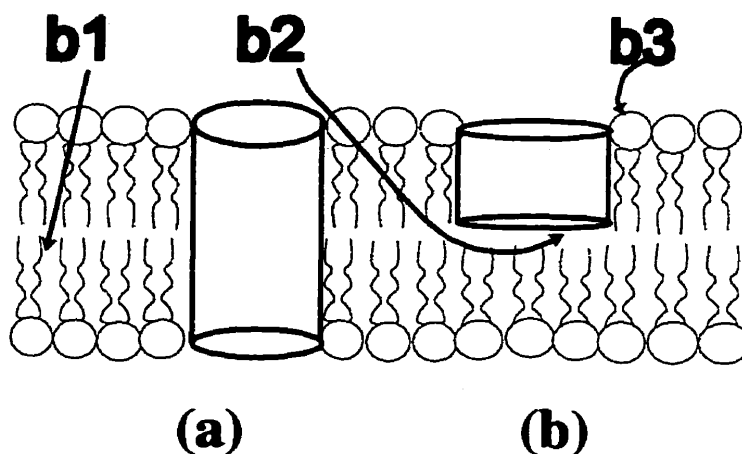
Figure 2.9: Schematic representation of continuum models of protein in bilayer membranes. (a) The diffusant (cylinder) spans the membrane (Saffman-Delbrück and Evans-Sackmann theories). (b) The diffusant (cylinder) partially penetrates the membrane (Evans-Sackmann model only and adapted by Tamm). b1 is frictional coefficient for the frictional force between the two layers of the membrane. b2 represents the frictional coefficient for the frictional force applied by the bathing phase (water) on the membrane (and the diffusant). b3 stands for the frictional coefficient for the frictional force applied by the membrane on the diffusant.

Here $\eta_m = \eta_M h$, is the two-dimensional membrane viscosity, h is the height of diffusing particle, K_0 and K_1 are modified Bessel functions, ε is a dimensionless particle radius given by Equation 2.11, with b_1 and b_3 representing the viscous coefficients of friction for the diffusant with the substrate and water, respectively, and b_2 reflecting the drag between the two monolayers.

Equation 2.11 $$\varepsilon = R\left(\frac{b_2 + b_3}{\eta_m}\right)^{\frac{1}{2}}$$

Equations 2.10 and 2.11 were derived originally to describe the diffusion of a cylinder in a bilayer membrane which is supported by a solid substrate giving rise to an assymmetry. The Evans-Sackmann model was subsequently adapted by Tamm to describe the diffusion of a cylinder inserted into only one monolayer of the bilayer (Figure 2.10) (46). In this interpretation, the frictional coefficients refer to the drag at the aqueous interface (b_3), at the interior of the bilayer (b_2) and at the bottom (b_1) of the diffusant against the other monolayer. The approach by Tamm can be applied to our experiments, since our NBD-labelled amphiphiles are not long enough to span the whole bilayer membrane and therefore they are asymmetrically embedded in the bilayer. Conceptually, this hydrodynamic model is related to the size and shape of the diffusing molecule, the viscosity of the continuous membrane sheet and the interfacial aqueous phase, the mutual friction of diffusant with the interior of the membrane and with the interface of membrane. For cylindrical molecules inserted partially into one monolayer of a membrane, Equations 2.10 and 2.11 should still be valid. As a matter of fact, these two equations are derivations of Equation 2.5. If we assume $b_1/b_2 \ll 1$ for Equation 2.10, then Equation 2.10 becomes Equation 2.5. Hence, ε parameter of Equation 2.11 represents the dimensionless radius which is consistent with the value of ε in Equation 2.5.

The diffusion coefficients were calculated according to Equation 2.10 for molecular surface areas greater than 1 nm^2 and are shown in Figure 2.8 as the solid lines. The parameters used for this theoretical calculation are listed in the caption for Figure 2.8. The

membrane viscosity (η_M) is set to be approximately 1 Poise, and the viscosity of water (η_w) is generally around 0.01 Poise (47). The viscosities of water and membrane should vary with temperature in a predictable manner. The membrane viscosity (η_M) is predicted to be consistent with the value η_M in the diffusion measurement of rubrene, which yields 1.15 poise at 29°C (39). Rubrene is a nearly spherical molecule with a radius of 0.5 nm according to its crystallographic dimensions (49). Its diffusion coefficient at 29°C in the centre of a DMPC bilayer is 5.8×10^{-12} m²/s, which would correspond to a membrane viscosity of 1.15 poise at this temperature. The value for the frictional coefficient between layers of the bilayer membrane, b_2 has been measured to be 7.5×10^6 N s/m³ or smaller (50), which is 2.5 times the value of b_1. The frictional coefficient between the aqueous phase on the membrane and diffusant, $b_3 \sim \mu_w^2 / \eta_M$ is of the order of 10^3 -10^4 N s/m³ (11). For the best calculations, we assume a height of the diffusant of 1.05 nm. This estimation for the height of our NBD-labelled macrocyclic polyamides containing lauroyl groups is consistent with theoretical calculations and experimental studies of chain packing and conformational statistics in lipid bilayers (42, 51, 52, 53, 54). For the calculations of diffusion coefficients, we used the same parameters at all temperatures (h = 1.05 nm, $b_1 = 3 \times 10^6$ N s/m³, $b_1/b_2 = 1/2.5$). The calculation at each temperature was only adjusted for the temperature dependence of the viscosities of water and membrane. It is clear from the solid lines in Figure 2.8 that the experimental data are described very well by the Evans-Sackmann model as modified by Tamm for molecular surface areas greater than about 1 nm².

It is important to reiterate that the calculations shown in Figure 2.8 use the same values for each set of parameters at all temperatures and it is therefore the explicit temperature dependence of these parameters (f_2, η_M, η_w) which accounts for the variation in diffusion coefficient from 27°C to 38°C. For example, the known temperature dependence of the viscosity of water (η_w) was used in these calculations (47). The temperature dependence of viscosity of membrane (η_M) is less well characterized but the values used here follow a trend quite similar to that of water as might be expected. The variation in f_2 is too small to provide a good sense of the temperature dependence but it is decreasing slightly, reflecting the interdependence of f_2 and η_M. The calculations are internally consistent and

their compatibility with the experimental data for all the probes at all the temperatures provides the strongest evidence for the applicability of an Evans-Sackmann type model as used here. It also should be noted that there appears to be a discontinuity in both the experimental data and in the theoretical calculations at molecular areas between 0.8 nm^2 and 1 nm^2. This now defines the transition region between free area and hydrodynamic descriptions of diffusion in model membranes. It should be recognized that there are experimental errors associated with the area measurements and that the absolute area values reflect the choice of 30 mN/m as the bilayer surface pressure. While the absolute areas may be open to some uncertainty and interpretation, the relative areas are determined sufficiently. Thus the data presented here provide the best description of the area dependence of molecular diffusion in membranes available to date. Moreover, these molecules are designed as a homologous series to ensure that they have similar chemical, physical and structural properties. The molecular modeling suggests that these molecules contain circular rings which are rigid and fairly incompressible (28) and therefore vary in size but not in shape.

2.4.2 Activation energy for the diffusion of NBD-labelled amphiphiles

We have obtained the apparent activation energies (E_a) of above NBD-labelled amphiphiles (1-5) by using Arrhenius plotting as shown in Figure 2.10. The corresponding value for each molecule is listed in Table 2.3. In terms of these values and their standard errors. It is clear that the activation energies of larger size particle (N_5L_4[NBD] and N_6L_5[NBD]) are smaller than that of small size molecules (N_2L[NBD], N_3L_2[NBD]) for the lateral diffusion in model membranes. The correlation coefficients of a linear regression of the experimental points for NBD-PE, N_2L[NBD], N_3L_2[NBD], N_4L_3[NBD], N_5L_4[NBD], N_6L_5[NBD] are 0.96, 0.94, 0.95, 0.95, 0.88, 0.87, respectively. The uncertainty is estimated from the variation in E_a obtained from systematically eliminating one of the five data points in the fitting. For the lipid probe (NBD-PE), the Arrhenius plot (Figure 2.10) is linear and yields an apparent activation energy of 36.4 kJ/mol, which compares favourably to 36.8 kJ/mol reported by Vaz (22). The diffusion coefficients of the five other NBD-labelled amphiphiles also exhibit linear Arrhenius plots with the apparent activation energies shown
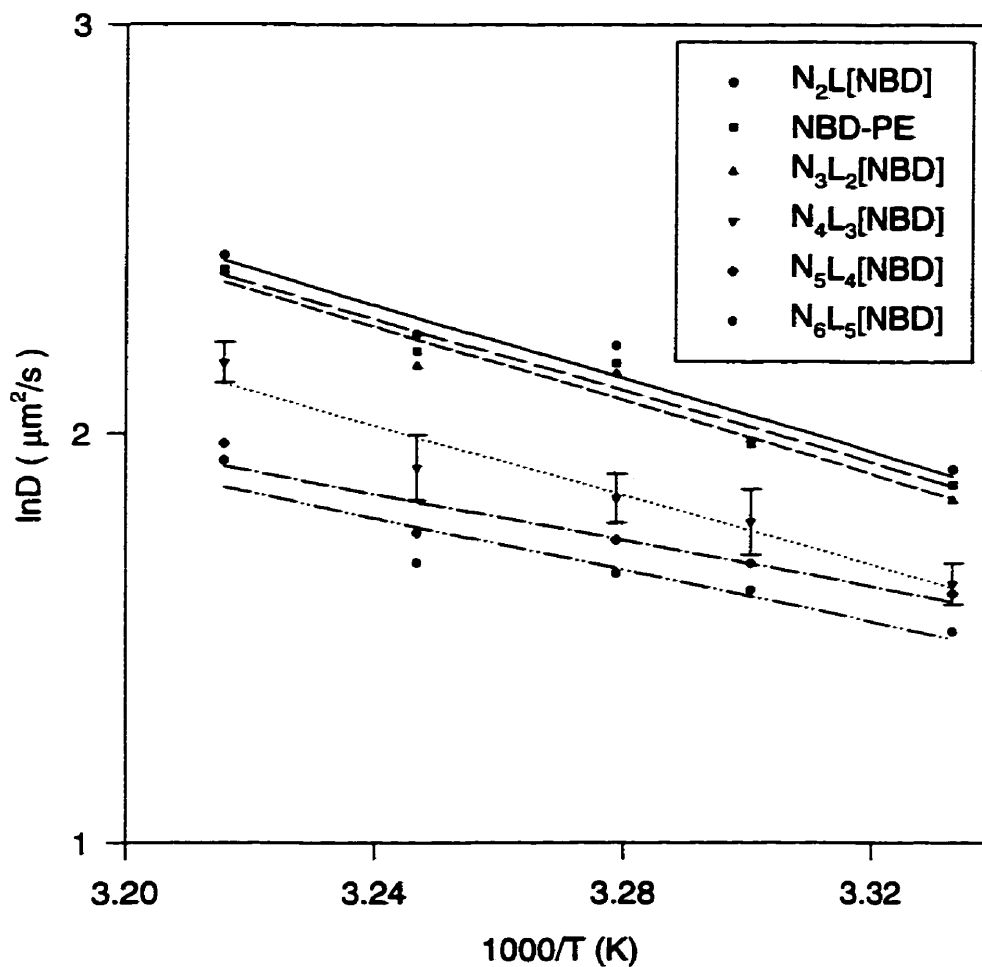
Figure 2.10: Arrhenius plots for the apparent activation energy of the diffusion of NBD-labelled amphiphiles. The experimental data were depicted at the right top description, and were fitted by first order regression for each compound. The slope for $N_2L[NBD]$, NBD-PE, $N_3L_2[NBD]$, $N_4L_3[NBD]$, $N_5L_4[NBD]$, $N_6L_5[NBD]$ was -4.0, -4.1, -4.0, -4.0, -3, -3.1, respectively. For ease, only the SEM of $N_4L_3[NBD]$ was shown in the plot.

in Figure 2.10.

The apparent activation energy for the smaller molecules ($N_2L[NBD]$, $N_3L_2[NBD]$, $N_4L_3[NBD]$), is very close to that of the lipid probe. In contrast, the apparent activation energy for large molecules is relatively lower than those lipid-like molecules. The variation of E_a values for the two size group molecules would be consistent with their different diffusion mechanisms.

Table 2.3 Activation Energy of Various NBD-Labelled Molecules

Numerical NBD-labeled molecules	Activation energy (J/mol)
NBD-PE	37.2 ± 1.5
$N_2L[NBD]$, 1	36.4 ± 1.8
$N_3L_2[NBD]$, 2	37.4 ± 2.0
$N_4L_3[NBD]$, 3	35.2 ± 4.0
$N_5L_4[NBD]$, 4	23.4 ± 4.0
$N_6L_5[NBD]$, 5	26.1 ± 4.8

2.5 Discussion

We have found that the lateral diffusion of NBD-labelled macrocyclic polyamide amphiphiles is dependent on the size and shape of these molecules in the liquid-crystalline phase of model membranes. The surface areas of the NBD-labeled amphiphiles span the transition region of interest from 0.3 nm^2 to 3 nm^2. Now it is very clear that the diffusion behaviour of these intermediately size molecules can be described by different models. The diffusion behaviour of small lipid-like molecules (surface area < 1 nm^2, radius < 0.56 nm) having dimensions similar to the lipids in the bilayer, can be described by an expression of interfacial viscosity limited free area theory (16, 22) while that of larger molecules (surface area $\geq$ 1nm^2, radius $\geq$ 0.56 nm) are much slower than lipid self-diffusion and can be fitted

by a continuum hydrodynamic model recently developed by Tamm (46) based on the Evans and Sackmann model (11). We also observed that the apparent activation energies of diffusion for smaller molecules (surface area < 1 nm^2) are similar to those of lipid molecules, but the apparent activation energies of diffusion for larger molecules (Surface area ≥ 1 nm^2) are smaller than those of lipids. The peculiar observation that N_4L_3[NBD] moves slowly but has a high apparent activation energy may reflect the fact that this molecule is situated in the middle of the transition region.

As we believed, hydrodynamic interactions play an important role in protein diffusion in lipid bilayers. Also numerous experimental results have shown that hydrodynamic variables such as the viscosities of membrane and aqueous phase (water) are critical determinants of diffusion rates (26, 55, 56, 57). Here, it is evident that the hydrodynamic description is appropriate for the larger molecule even though they span only part of the membrane. In fact, it appears that the diffusion is controlled only by the size of the molecule in the region of the membrane closes to the aqueous interface. The question remains why there is an apparent discontinuity in the diffusion behaviour at molecular areas above 1 nm^2. For smaller molecules, density fluctuations in the interface region can generate free area (or volume) thereby permitting the small molecules to move in a diffusive process along the surface. The relatively large apparent activation energy suggests that the temperature dependence of the fluctuations in the equilibrium density is quite large. On the other hand, for large molecules the fluctuations in the equilibrium density is not the only constraint on the diffusive motion. Rather, the frictional forces generated when the molecules move past one another appear to dominate and cause a reduction in the observed diffusion rate. The smaller apparent activation energy indicates that these frictional forces, which are interpreted as the viscosity, are much less sensitive to temperature.

The current data show that the diffusion coefficient is sensitive to a change in size of a molecule at the surface of the membrane. This is in marked contrast to the observations by Balcom and Petersen (39) that the diffusion coefficient of amphiphilic molecules is insensitive to a change in size in the interior of the membrane. In that work, it was shown that the diffusion of derivatives of citronellol, solanosol and dolichols, were identical even

though the volume of the molecule in the interior was increased by more than an order of magnitude. Thus increasing the area at the surface affects the diffusion while increasing the volume in the interior does not. Still, molecules such as tetracene and rubrene, which are entirely in the interior of membrane, exhibit a Stokes-Einstein type dependence on diffusion, i.e. the diffusion depends on the size (49).

These observations suggest that the surface interface region of the bilayer membrane is more restrictive to diffusion than is the middle of the bilayer. The best view of the membrane may then be as a triple layer (Figure 2.11), a region close to the aqueous interface which is more restrictive to diffusion and the middle region which is more fluid and less restrictive to diffusion. In this view, any molecule penetrating into the more rigid interface region (all those studied in this work and the isoprenol derivatives studied earlier) will move laterally in a manner controlled by this region irrespective of the size of the molecule in the aqueous region or in the middle region. Thus lipid-anchored proteins and dolichols share the feature that there are large bulky groups extruding into regions of lower viscosity, where the additional drag influences the diffusion minimally. Moreover, molecules residing only in the interior experience a more fluid environment and diffusion may be more rapid than that of the host lipid as exemplified with tetracene (39).

It is intriguing to speculate that the high viscosity region of the triple layer membrane corresponds to the region with large acyl chain order parameters. This region is about eight to ten carbons deep corresponding to about 1.0 nm thickness (52, 53, 54) (coincidentally the height used to fit the diffusion data). In that case, the more fluid middle region would correspond to the region with relatively small chain order parameters in the layer where the two monolayers meet. This region is from six to eight carbons deep for each monolayer corresponding to a one to two nanometer thick middle layer. This region is sufficiently large to accomodate large hydrophobic chain segments, such as in dolichol, without impeding the diffusion significantly.

Thinking about a membrane functionally as a triple layer may be useful from a number of perspectives. Diffusion of lipids and proteins will differ mostly because the latter span two viscous regions. Diffusive transport across the membrane will be dominated by
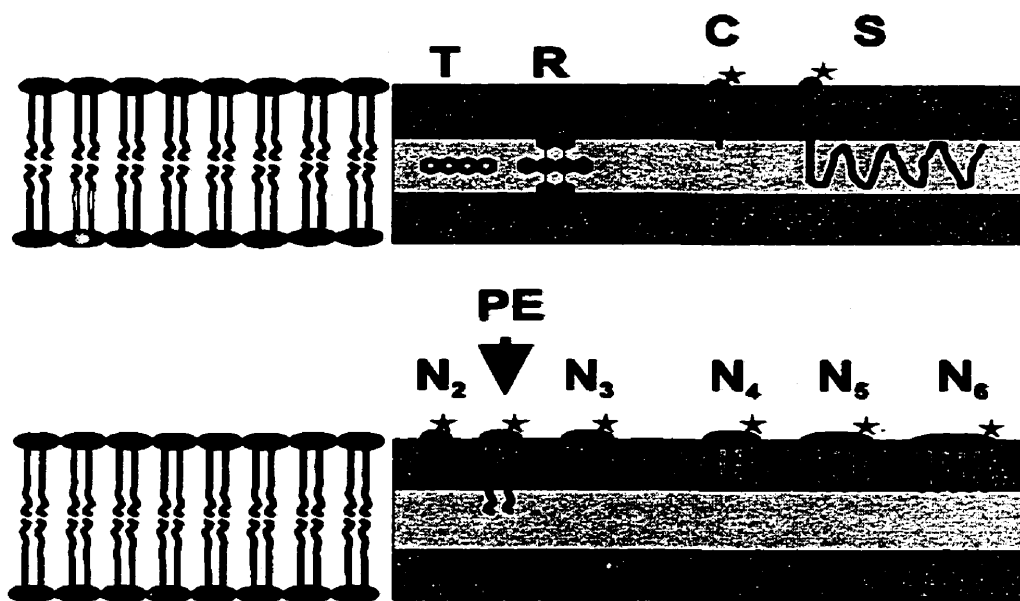
Figure 2-11: Diagrammatic representation of the 'triple layer' model for a membrane. The darker region represents the approximately 1 nm thick viscous region close to the surface and the lighter region represents the 1-1.5 nm thick fluid region in the hydrophobic interior. A series of molecules are depicted as T for tetracene; R for rubrene; C for NBD-labeled citronellol; S for NBD labeled solanosol; PE for the NBD-labeled phospholipid analog; N_n for the NBD-labeled macrocycle with n nitrogens in the ring (see text). The diffusion data suggest that C, S, PE, N_2 ($N_2L[NBD]$) and N_3 ($N_3L_2[NBD]$) have the same diffusion coefficient since they are comparable in size to the lipid molecule and the bulk in the interior is of no consequence. The diffusion of N_4 ($N_4L_3[NBD]$), N_5 ($N_5L_4[NBD]$) and N_6 ($N_6L_5[NBD]$) are slower because their size in the viscous region of the membrane are larger than the host lipid.

penetration through the approximately 1.0 nm thick layers at each surface. Once in the middle region of the membrane, the lateral diffusion would be facile and perhaps more rapid than escape across the other, more viscous region.

2.6 Summary

A series of NBD-labelled macrocyclic polyamide amphiphiles ($N_2L[NBD]$, $N_3L_2[NBD]$, $N_4L_3[NBD]$, $N_5L_4[NBD]$, $N_6L_5[NBD]$, or numerically named as 1-5) and standard fluorescent phospholipid (NBD-PE) have been used to solve the question: How do we describe the dynamic properties of particular molecules of interest, the size of these molecules just span in the transition region with surface area from 0.3 nm^2 to 3.0 nm^2. Spot FPR technique was applied to determine their diffusion coefficients on model membranes. The diffusion coefficients of $N_2L[NBD]$, $N_3L_2[NBD]$, $N_4L_3[NBD]$, $N_5L_4[NBD]$, $N_6L_5[NBD]$, and NBD-PE were correlated with their surface areas. This is the first example of size dependence of lateral diffusion for a series of structurally similar macrocyclic polyamide amphiphiles. The lateral diffusion of molecules which have surface areas smaller than or equal to that of the phospholipids, can be best modelled using viscosity modified free-area theory. In contrast, the lateral diffusion of molecules which have larger surface areas than that of phospholipids can be best explained by hydrodynamic Evans-Sackmann theory.

In summary, we predict that an amphiphile which resides partly in the membrane region, closest to the surface will exhibit lateral diffusion at the rate of the lipids if it is small (surface area $< 1 nm^2$) or slightly slower if it is large (surface area $> 1 nm^2$). The size of the molecule in the aqueous region, or in the hydrophobic interior is of little consequence since the viscous drag will be less. Any hydrophobic molecule which resides exclusively in the interior may diffuse more rapidly than the solvent (i.e. lipid), but will exhibit a dependence on size similar to that observed in three-dimensional diffusion. Any molecule which spans both bilayers should be reduced in diffusion by a factor of two relative to a molecule of comparable cross-sectional area present only in one monolayer, this prediction is yet to be tested rigorously. The diffusive properties of those amphiphiles which have a central head part located in the interface of the membrane, can be described best by the hydrodynamic

model. Amphiphiles such as $N_5L_4[NBD]$ and $N_6L_5[NBD]$, occur at surface areas as low as 1 nm^2 and provide further evidence for the use of the hydrodynamic models for diffusions of molecules other than lipids. Finally, molecules larger than 1 nm^2 are adequately described by the hydrodynamic models provided that the effective height is understood to be the thickness of the viscous layers.

Currently, much effort has been focussed on the size effect of membrane protein aggregates on their diffusion rates in a number of research groups (26, 55, 56). Our results would predict that aggregates would be restricted by hydrodynamics, but good experimental data is needed to verify this prediction.

2.7 References

1. Adam, G., Delbrück, M. Reduction of dimensionality in biological diffusion processes. *In* Structural Chemistry and Molecular Biology. A. Rich and N. Davidson, eds. W. H. Freeman and Company, San Francisco and London. California. **1968**, 198-222.

2. Clegg, R. M., and Vaz, W. L. C. Translational diffusion of proteins and lipids in artificial lipid bilayer membranes. A comparision of experiment with theory. *In* Progress in Protein- Lipid Interactions. A. Watts and J. J. H. H. M. DuPont, editors. Elsevier Science Publishing Co., Amsterdam. **1985**, 173-229.

3. Hackenbrock, C. R.. Lateral diffusion and electron transfer in the mitochondrial inner membrane. *Trends Biochem. Sci.* **1981**, 6, 151-154.3.

4. Koppel, D. E. Measurement of membrane protein lateral mobility. *Tech. Life Sci.* B4/I. B4 **1982**, 25, 1-25.

5. Sackmann, E. Supported membranes: scientific and practical applications. *Science,* **1996,** 271, 43-48.

6. Edidin, M., Rotational and lateral diffusion of membrane proteins and lipids, *Current Topics in Membranes and Transport,* **1989**, 29, 91-127.

7. Galla, H. J., Hartmann, W., Theilen, U., and Sackmann, E. On two-dimensional passive random walk in lipid bilayers and fluid pathways in biomembranes. *J. Membr. Biol.* **1979**, 48, 215- 236.

8. Hildebrand, J. H. Motions of molecules in liquids: Viscosity and diffusivity. *Science.* **1971,**174, 490-493.

9. Saffman, P. G. and Delbrück, M. Brownian motion in biological membranes. *Proc. Natl. Acad. Sci. USA.* **1975**, 73, 3111-3113.

10. Hughes, B. D., Pailthorpe, B. A., White, L. R. and Sawyer, W. H. Extraction of membrane microviscosity from translational and rotational diffusion coefficients. *Biophys. J.* **1982**, 37, 673-676.

11. Evans, R., and Sackmann, E. Translational and rotational drag coefficients for a disk moving in a liquid membrane associated with a rigid substrate. *J. Fluid Mech.* **1988**,

194, 553- 561.

12. Tamm, L. K. Membrane insertion and lateral mobility of synthetic amphiphilic signal peptides in lipid model membranes. *Biochim. Biophys. Acta.* **1991**, 1071, 123-148.

13. Cohen, M. H., and Turnbull, D. Molecular transport in liquids and gases. *J. Chem. Phys.* **1959**, 31, 1164-1169.

14. Vaz, W. L. C., Goodsaid-Zalduondo, F. and Jacobson, K. Lateral diffusion of lipids and proteins in bilayer membranes. *FEBS Letters.* **1984**, 174, 199-207.

15. McCown, J.T., and Galla, H.J., Pressure variation of the lateral diffusion in lipid bilayer membranes, *Biochim. Biophys. Acta,* **1983**, 733, 291-294.

16. Vaz, W. L. C., Clegg, R. M. and Hallmann, D. Translational diffusion of lipids in liquid crystalline phase phosphatidylcholine multibilayers. A comparision of experiment with theory. *Biochemistry.* **1985**, 24, 781-786.

17. Hughes, B.D., Pailthorpe, B.A. and White, L.R. The translational and rotational drag on a cylinder moving in a membrane, *J. Fluid Mech.* **1981**, 110, 349-372.

18. Saffman, P.G., Brownian motion in thin sheets of viscous fluid. *J. Fluid. Mech.* **1976**, 73, 593-602.

19. Einstein, A., Investigations on the theory of the Brownian movement, ed. R. Fürth (Dover, New York), **1956**, 36-37.

20. Wiegel, F.W., Fluid flow through porous macromolecular systems, Lecture notes in physics, **1980**, vol. 121 (Springer, Berlin)

21. Vaz, W. L. C., Criado, M., Madeira, V. M. C., Schoellmann, G. and Jovin, T.M. Size dependence of the translational diffusion of large integral membrane proteins in liquid-crystalline phase lipid bilayers. A study using fluorescence recovery after photobleaching. *Biochemistry.* **1982**, 21, 5608-5612.

22. Vaz, W. L. C., Derzko, Z.I., and Jacobson, K.A. Photobleaching measurements of the lateral diffusion of lipids and proteins in artificial phospholipid bilayer membranes. *Cell Surface Rev.,* **1982**, 8, 83-135.

23. Vaz, W. L. C., Hallmann, D., Clegg, R.M., Gambacorta, A. and DeRosa, M. A comparision of the translational diffusion of a normal and a membrane-spanning

lipid in Lα phase 1-palmitoyl-2-oleoylphosphatidylcholine bilayers. *Eur. Biophys. J.* **1985**, 12, 19-24.

24. Edidin, M., Rotational and lateral diffusion diffusion of membrane proteins and lipids. *Current Topics in Membranes and Transport.* **1989**, 29, 91-127.

25. Johnson, M. E., Berk, D.A., Blankschtein, D., Golan, D.E., Jain, R.K. and Langer, R.S.. Lateral diffusion of small compounds in human stratum corneum and model lipid bilayer systems. *Biophys. J.* **1996**, 71, 2656-2668.

26. Kucik D. F., Elson, E.L., and Sheetz, M.P. Weak dependence of mobility of membrane protein aggregates on aggregate size supports a viscous model of retardation of diffusion. *Biophys. J.* **1999**, 76, 314-322.

27. Nir, S., and Stein, W.D. Two modes of diffusion in liquids. *J. Chem. Phys.* **1971**, 55, 1598-1603.

28. Paprica, P. A., and Petersen, N. O. Monolayers of polylauroyl macrocyclic polyamides and nitrobenzoxadiazole (NBD) labeled polyauroyl macrocyclic polyamides at the air-water interface. *Langmuir.* **1994**, 10, 4630-4636.

29. Paprica, P.A., Baird, N.C., and Petersen, N.O. Theoretical and experimental analysis of optical transitions of Nitrobenzoxadiazole (NBD) derivatives, *J. Photochem. Photobiol. A: Chemistry*, **1993**, 70, 51-57.

30. Chattopadhyay, A., Chemistry and biology of N-(7-nitro-benz-oxa-1,3-diazole-4-yl)-labelled lipids: fluorescent probes of biological and model membranes, *Chemistry and Physics of Lipids*, **1990**, 53, 1-15.

31. Petersen, N.O., Intramolecular fluorescence energy transfer in nitrobenzoxadiazole derivatives of polyene antibiotics. *Can. J. Chem.*, **1985**, 63, 1, 77

32. Chattopadhyay, A. and London, E., Parallax method for direct measurement of membrane penetration depth utilizing fluorescence quenching by spin-labelled phospoholipids. *Biochemistry*, **1987**, 26, 39-45.

33. Paprica, A.P. Evidence for a continuum model of diffusion in lipid membranes: Synthesis and studies of macrocyclic polyamides in monolayer and lipid bilayer systems. The University of Western Ontario, Ph.D. thesis, London, Ontario, Canada.

1994.

34.   Petersen, N. O., Felder, S. and Elson, E.L. Measurement of lateral diffusion by fluorescence photobleaching recovery. *In Handbook of Experimental Immunology.* Weir, D. M. editor. Blackwell, Edinburgh. **1986,** 24.1-24.3.

35.   Axelrod, D. Fluorescence photobleaching techniques and lateral diffusion. *in Spectrosc. Dyn. Mol. Biol. Syst.* P. Bayley and R. Dale, Editors, Academic Press, Toronto. **1985,** 163-175.

36.   Axelrod, D., Koppel, D.E., Schlessinger, J. Elson, E. and Webb, W.W. Mobility measurement by analysis of fluorescence photobleaching recovery kinetics. *Biophys. J.* **1976,** 16, 1055-1069.

37.   Edidin, M., Zagyansky, Y. and Lardner, T.J. Measurement of membrane protein lateral Diffusion in single cells, *Science.* **1976,** 191, 466-468.

38.   Wolf, D.E., Designing, building and using a fluorescence recovery after photobleaching instrument, *Methods Cell Biol.* **1989,** 30, 271-306.

39.   Balcom, B. J., and Petersen, N.O. Lateral diffusion in model membranes is independent of the size of the hydrophobic region of molecules. *Biophys. J.* **1993,** 65, 630-637.

40.   Seelig, A. Local anesthetics and pressure: A comparison of dibucaine binding to lipid monolayers and bilayers. *Biochim. Biophys. Acta.* **1987,** 899, 196-205.

41.   Jones, M. N. and Chapman, D. Micells, Monolayers and Biomembranes. Wiley-Liss, Inc. New York. **1995.**

42.   Lewis, B. A., and Engelman, E.W. Lipid bilayer thickness varies linearly with acyl chain length in fluid phosphatidylcholine vesicles. *J. Mol. Biol.* **1983,** 166, 211-217.

43.   Grest, G. S. and Cohen, M.H. Liquids, glasses and the glass transition: A free-volume approach. *Adv. Chem. Phys.* **1981,** 4, 455-525.

44.   Peters, R. and Cherry, R.J. Lateral and rotational diffusion of bacteriorhodopsin in lipid bilayers: Experimental test of the Saffman-Delbrück equations. *Proc. Natl. Acad. Sci. USA.* **1982,** 79, 4317-4321.

45.   Cherry, R. J. and Godfrey, R.E. Anisotropic rotation of Bacteriorhodopsin in lipid

Membranes. *Biophys. J.* **1981**, 36, 257-276.

46. Frey, S., and Tamm, L.K. Membrane insertion and lateral diffusion of fluorescence-labelled cytochrome C oxidase subunit IV signal peptide in charged and uncharged phospholipid bilayers. *Biochem. J.* **1990**, 272, 713-719.

47. Levine, I. Physical Chemistry. McGraw-Hill, Inc. U. S. A. **1988**.

48. Bergmann, E. and Herlinger, E.I. The structure of rubrene and some remarks on the "ortho- effect". *J. Chem. Phys.* **1936**, 4, 532-534.

49. Edward, J. T. Molecular volumes and the Stokes-Einstein equation. *J. Chem. Edu.* **1970**, 4, 261- 269.

50. Merkel, R., Sackmann, E. and Evans, E. Molecular friction and epitactic coupling between monolayers in supported bilayers. *J. de Physique.* **1989**, 50, 1535-1555.

51. Fattal, D. R., and Ben-Shaul, A. Mean-field calculations of chain packing and conformational statistics in lipid bilayers: Comparision with experiments and molecular dynamics studies. *Biophys. J.* **1994**, 67, 983-995.

52. Derzko, Z., and Jacobson, K. Comparative lateral diffusion of fluorescent lipid analogues in phospholipid multibilayers. *Biochemistry.* **1980**, 19, 6050-6057.

53. Lu, D., I. Vavasour, and M. R. Morrow. Smoothed acyl chain orientational order parameter profiles in dimyristoylphosphatidylcholine-distearoylphosphatidylcholine mistures: A ^{2}H-NMR study. *Biophys. J.* **1995**, 68, 574-583.

54. Hyvönen, M.T., Rantala, T.T. and Ala-Korpela, M. Structure and dynamic properties of diunsaturated 1-palmitoyl-2-linoleoyl-*sn*-glycero-3-phosphatidylcholine lipid bilayer from molecular dynamics simulation. *Biophys. J.* **1997**, 73, 2907-2923.

55. Bussell, S.J., Koch, D.L. and Hammer, D.A. Effect of hydrodynamic interactions on the diffusion of intergral membrane proteins: Tracer diffusion in organelle and reconstituted membranes. *Biophys. J.* **1995**, 68, 1828-1835.

56. Saxton, M.J. and Jacobson, K. Single-particle tracking: applications to membrane dynamics. *Annu Rev Biophys Biomol Struct* **1997**, 26, 373-399.

CHAPTER 3 SYNTHESIS OF DENDRITIC CHELATING AGENTS CONTAINING MULTIPLE TERMINAL NITRILOTRIACETIC ACID (NTA) GROUPS

3.1 Introduction

As introduced in Chapter 1, our long term goal of the entire project is to study the dynamic properties of biological membranes, such as diffusion and aggregation of membrane components in solutions and in model membranes. In Chapter 2, several factors including the size and shape of molecules, the viscosities of membrane and surrounding media (i.e. water), and the temperature of the system, have been revealed to affect the rate of diffusion on model membranes in different ways. In the next few chapters, we aim to address several questions about the aggregation of proteins: how to approach multiprotein complex systems, how to achieve protein aggregates in solution and model membranes, how to control the size and shape of large protein complexes specifically and selectively. The first step is to develop a series of molecules which can be used to bind proteins in a specific way. It is well known that the most popular way to approach multiprotein complexes is to create specific chelating agents. It is expected that macromolecule complexes can be generated using these chelating agents by selective and predominant interactions between proteins and chelating agents through central metal ions.

In recent years, a variety of bifunctional chelating agents have been attached to tumour-specific monoclonal antibodies (mAbs) to bind radioactive ions for imaging and therapy (1, 2, 3, 4, 5). This type of conjugation of antibodies to radiometal complexes represents a versatile strategy for selective delivery of diagnostic or therapeutic radiation to primary or metastatic tumours. The first bifunctional chelators to find widespread use were ethylenediaminetetraacetic acid (EDTA) analogues derived at a methylene carbon atom of the diamine backbone with phenyl (6), benzyl (7), or phenethyl (8) moieties bearing a protein-reactive substituent on the aromatic ring. In addition, more stable mAb-radiometal conjugates modified with derivatives of diethylenetriaminepentaacetic acid (DTPA) (4) and polyazamacrocyclic chelating agents (9) have made considerable progress in this field. Our special interest falls on the type of chelating agent, nitrilotriacetic acid (NTA) derivatives,

which have been widely used in protein engineering.

3.1.1 Rationale of nitrilotriacetic Acid (NTA) chelating agents

Immobilized metal affinity chromatography (IMAC) has become a widely used technique in molecular biology and protein engineering since it was first reported by Porath in 1975 (10). In particular, it has been used for the isolation of proteins, peptides, and nucleic acids. With IMAC, a metal ion, such as Ni^{2+}, Zn^{2+}, or Cu^{2+}, is complexed and immobilized by a chelator which is covalently linked to a solid matrix. The most frequently used metal chelators contain three or four electron-rich groups, leaving three or two metal coordination sites available to interact with additional ligands. Tridentate chelators, e.g., iminodiacetic acid (IDA) may be useful under narrowly defined conditions and when durability (metal retention) of the chromatographic matrix is not of great concern. However, tetradentate chelators are generally superior because they firmly bind and retain the metal ion through repeated use and under harsh conditions (11). The metal complex contains free coordination sites, which can be occupied by additional electron donor groups. Numerous interests are in the use of nitrilotriacetic acid (NTA) derivative such as such as N-(1-carboxy-5-aminopentyl)iminodiacetic acid 17 (12), which has been employed as a chelator to purify proteins since 1987 (12, 13, 14). NTA chelates a Ni(II) ion by using of four of its potential six coordination sites (Figure 3.1). The remaining sites can be occupied by two electron donor groups such as histidine residues of a protein to form an octahedral complex through a nickel (II) ion. Proteins containing two to six histidine residues can act efficiently as electron donor for the formation of this complex. This principle has been applied to purify recombinant proteins with terminal histidines rapidly and effectively. The protein is genetically incorporated two to six histidines at either the amino or carboxyl terminus of the protein. The incorporation of protein of interest is normally tagged with six histidines, thus the protein has an affinity tag and is named as $(His)_6$, 6xHis or His-tagged. The His-tagged protein serves as a high affinity binding sequence for the purification of any fusion protein via metal chelating adsorbent. During IMAC, the His-tagged protein is specifically bound to the immobilized Ni-NTA resin, since the histidine residues bind to the Ni-NTA resin with
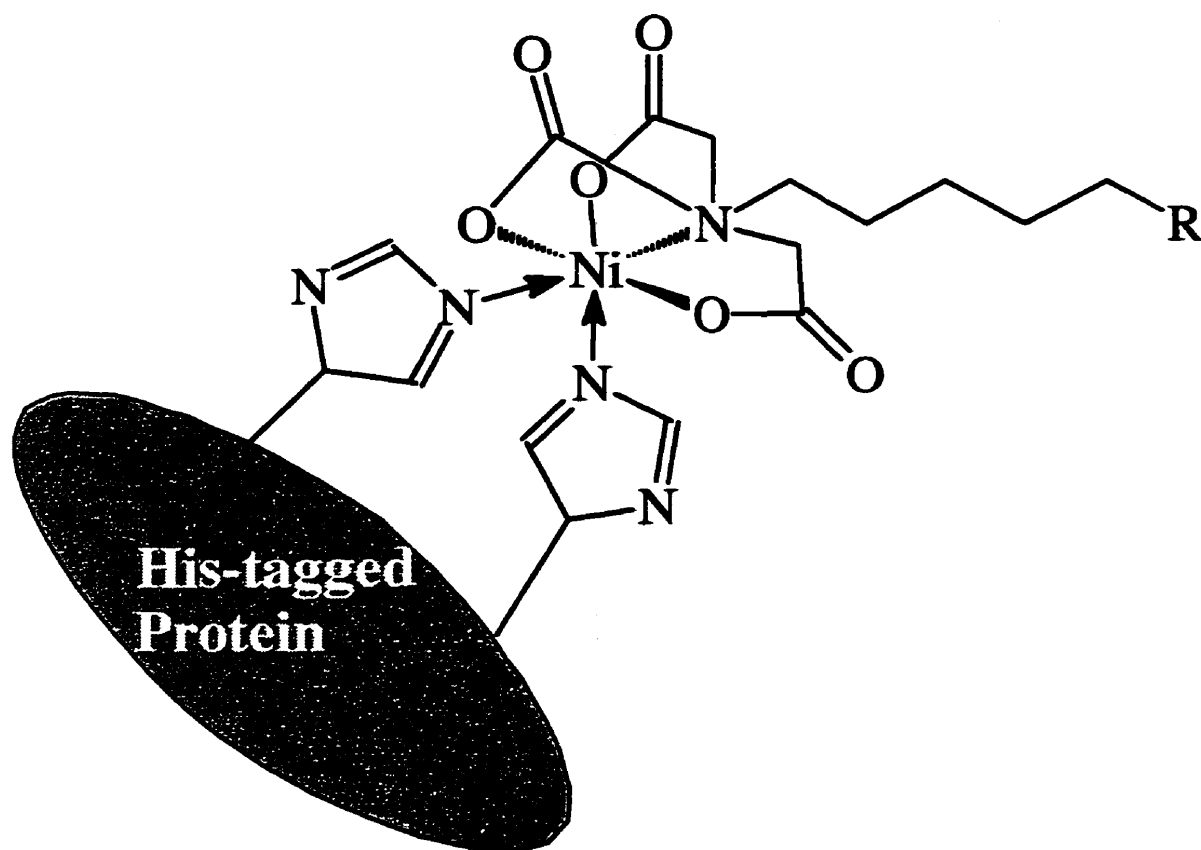
Figure 3.1: Schematic diagram for octahedral complex of NTA-Ni-Protein. The shaded oval represents a His-tagged protein which has two adjacent histidine residues. These two hisditines can donate two pairs of electrons for the octahedral coordinate complex. Nitrilotriacetic acid (NTA) groups provide four pairs of electrons to the complex. R can be any substituents. The drawing is not in scale. In immobilized metal affinity chromatography (IMAC), nickel ion is immobilized in lysine-NTA matrix. When His-tagged protein is eluted, it is specifically coordinated by nickel ion and NTA to form this octahedral complex.

an affinity constant of $K_a = \sim 10^{13}$ at pH 8.0. This strong binding is far greater than the affinity between most antibodies and antigens, or enzymes and substrates (14, 15). Therefore, any other proteins that bind nonspecifically to the NTA resin can be easily washed away under relatively stringent conditions, without affecting the binding of the 6xHis-tagged proteins. The high binding constant also allows proteins in very dilute solutions, such as those expressed at low levels or secreted into the media, to be efficiently bound the resin. IMAC employs a small, uncharged, nonantigenic, protein affinity tag (histidine tag), this tag does not interface with the biological activity of the recombined protein. In most cases, the functionality of the His-tagged protein is preserved.

Additionally, it was reported that the binding of Ni (II) by NTA is reversible, and the protein complex can be dissociated at low pH, or by the addition of competitor of histidine such as imidazole instead of the His-tagged protein, or a competitive chelator such as ethylenediamine tetraacetic acid (EDTA) (15, 16). Based on the high affinity and reversible properties of NTA-Ni-Protein complex, we initiated this work by design of appropriate target molecules. Hence, the approaches of this project are to develop chelating agents with multiple NTA groups and to apply these reagents to protein which has 6xhis tag. The synthesis of target chelating agents has been achieved in this chapter, and its application to His-tagged proteins would be carried out in Chapter 4 and Chapter 5.

3.1.2 Target molecules

The synthetic target molecules must comply to the following criteria. (i) They should be a series of compounds which have common structural features at the molecular level. This is particularly for the systematic comparison of their sizes and shapes. (ii) The bindings of these molecules to proteins must not only be of high affinity but also must be reversible. NTA analogues just perfectly meet this requirement. (iii) The target molecules must have multiple binding sites and these sites should be equivalently but independently bound by proteins. For example, all the sites of bindings must posses the same functional groups, but these functional groups are not affected by each other. (iv) To satisfy the above requirements (i) and (iii), the target molecules must be dendritic chelating agents. This is usually designed

starting from macrocyclic polyamine derivatives. The polyamine analogues usually have various sizes, which are easily varied by their nitrogen atoms in the macrocyclic ring. (v) The core of the synthetic dendrimer must have restricted conformations, such that the geometry and size of the central heads can be determined without too much ambiguity. (vi) The dendritic molecules must have a different number of pendant arms which are attached to the central ring. These arms should have equivalent length of linkers, and each linker should have chemical flexibility. (vii) The target molecules must define the size and shape of corresponding protein aggregates specifically and selectively by controlling the number of dendritic arms. The tightness of protein clusters could be manipulated by the length of each linker. (viii) The last criteria for the target molecules is that they must be capable of governing the stoichiometry of protein aggregates in a specific way.

Accordingly, two sets of target dendrimers were designed as represented in Figure 3.2. These two series of compounds are macrocyclic polyamide derivatives with similar head structure as that of amphiphiles 1-5, which were used to determine their diffusion coefficients in model membranes in Chapter 2. They are dendritic chelating agents with desired features as met by above criteria. First, these dendrimers have similar structures: the central head of each molecule is a macrocyclic polyamide. For example, target molecules in the first set (Figure 3.2A) are diamide 6a, triamide 6b, tetraamide 6c, pentaamide 6d, and hexaamide 6e. The target molecules in the second set (Figure 3.2B) are similar polyamide derivatives (12a and 12b) with the first set but the length of linkers is different. It is generally thought the rotation of (O)C-N bond in amide derivative is restricted at room temperature, thus the macrocyclic polyamide has a rigid but planar structure. From this point of view, the designed polyamide derivatives should have defined size and shape. We wish to take this advantage to control the size and shape of protein clusters if they were bound by multiple proteins. Second, the terminal pendants of these dendrimers are attached by bifunctional NTA groups, which can chelate to a His-tagged protein through a nickel ion. NTA not only has a character of high affinity binding to His-tagged protein, but also has a reversible ability from NTA-Ni-Protein complex to His-tagged protein itself if EDTA is added. Changing the size of the central ring will give a corresponding change in the number of dendritic arms. As
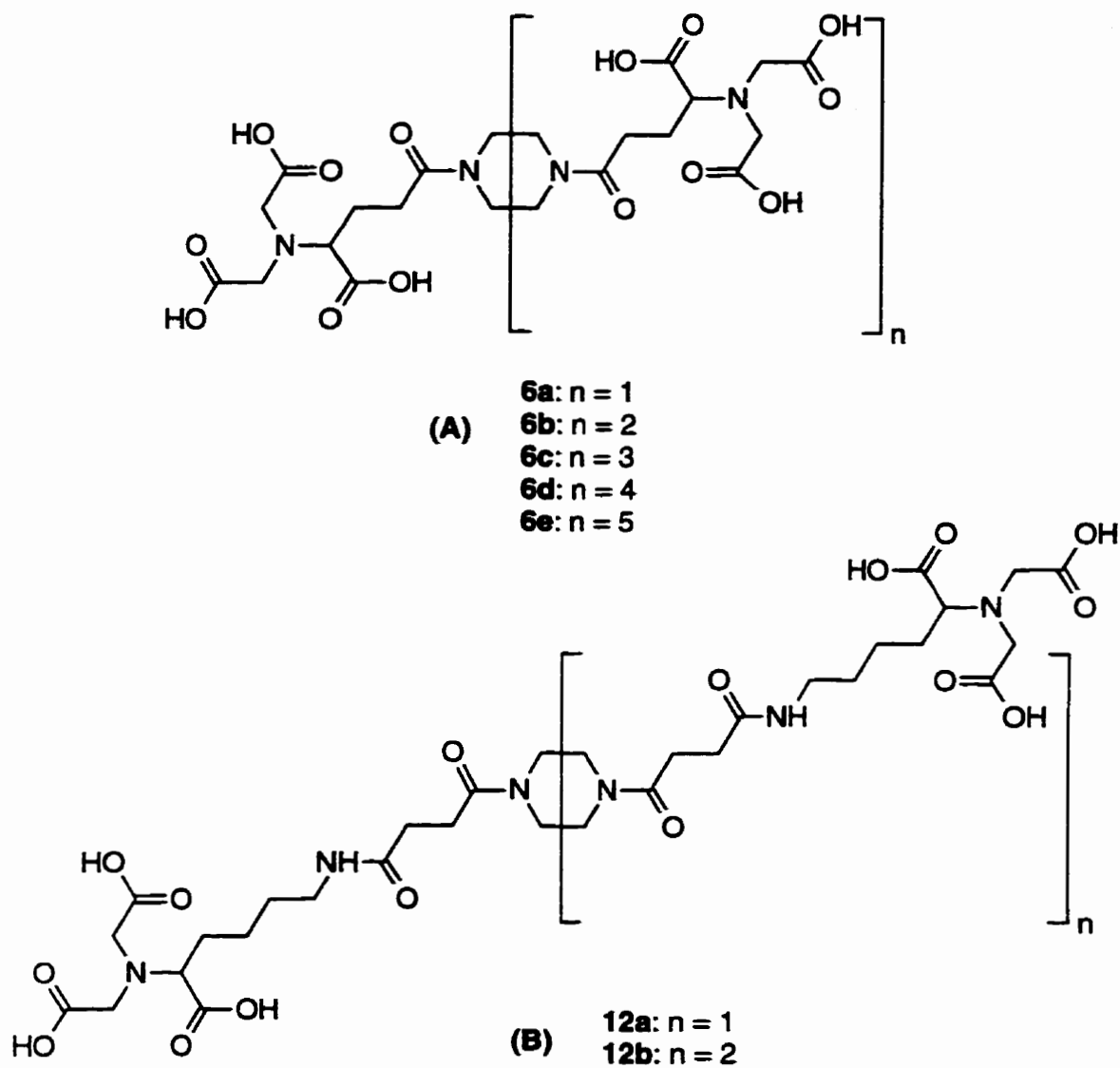
Figure 3.2: The structures of two sets of target dendritic chelating agents: compounds **6a-e** (A), and compounds **12a-b** (B).

a consequence, the number of NTA groups can be varied with the number of nitrogen atoms in the polyamine rings. These terminal NTA groups will chelate various numbers of proteins so that various sizes of protein clusters can be obtained. Thirdly, it may also be possible to control the tightness of the clusters formed by varying the length of the linker chain. This would be important to the future diffusion and aggregation studies in biological membranes. By using these chelating agents, we hope to get some information about the interactions between each protein monomer in solution and model membranes. In this chapter, the synthesis and identification of these target dendritic chelating agents are presented. The uses of these ligands to assemble dimers, trimers, tetramers, pentamers, or hexamers of His-tagged proteins are reported in the subsequent chapters.

3.2 Sequential synthesis of dendritic ligands 6a-e

The first set of macrocyclic polyamide derivatives (**6a, 6b, 6c, 6d, 6e**) with multiple NTA functional groups represented in Figure 3.2 were synthesized as outlined in Scheme 3.1. The sequential strategy for the preparations of **6a-e** was to synthesize the macrocyclic polyamide derivatives **8a-e** containing protected terminal amino acid groups first. The protecting groups in compounds **8a-e** were then cleaved to generate polyamino acid intermediates **9a-e**. These polyamino acid derivatives were finally alkylated with bromoacetic acid to the symmetric multiple acids which are the final chelating agents desired.

All of the syntheses started from cyclic polyamines **7a-e**, some of which are not commercially available as free bases, such as 1,4,7,10,13-pentaazacyclopentadecane **7d** and 1,4,7,10,13- hexaazacycloocadecane **7e**, but can be isolated as such easily from 1,4,7,10,13-pentaazacyclopentadecane pentahydrochloride and hexacyclen trisulphate, respectively. These five macrocyclic polyamines, also called azacrowns, have been widely used for a variety of purposes. For example, studying macrocyclic chelating agents is very important to the characterization of the metal cation binding properties. The related work about macrocyclic polyamine derivatives is an active area of research which spans the disciplines of inorganic chemistry, organic chemistry and biochemistry (4, 17, 18). Most of the
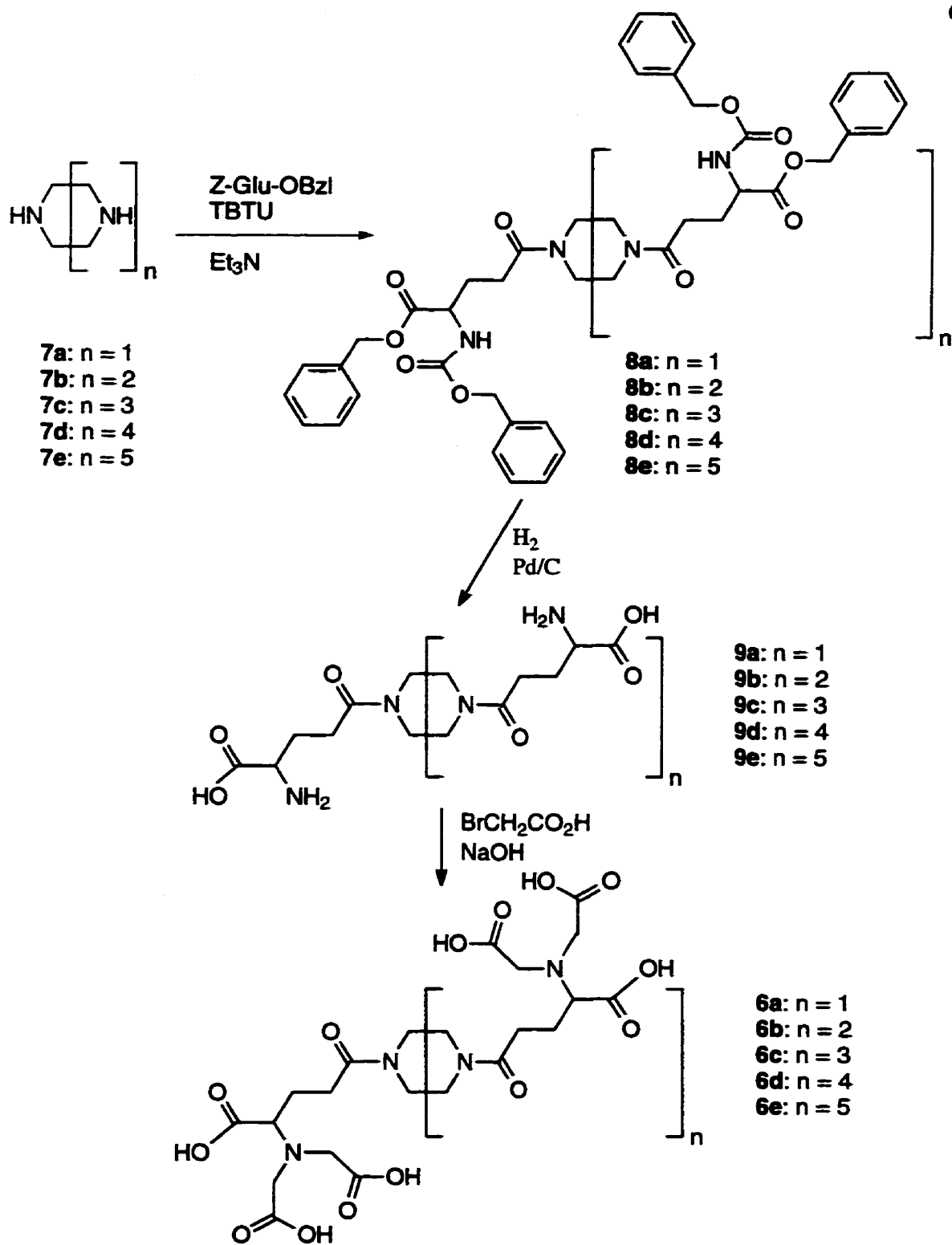
Scheme 3.1: Sequential synthetic strategy to target molecules **6a-e**. TBTU: 2-(1H-benzotriazole-1-yl)-1,1,3,3-tetramethyluronium tetrafluoroborate; Z-Glu-OBzl: L-glutamic acid N-(benzyloxycarbonyl)-1-(benzyl) ester.

derivatives of macrocyclic polyamines are used to enhance the signal intensity of images in resonance imaging through the action of paramagnetic metals in the polyamine complex (3). In a polyamine-metal complex, the ring acts as a chelator for radiolabelled monoclonal antibodies (mAbs), and the complex is used as a radioactive carrier in cancer chemotherapy (1, 2, 3). Research has also shown that certain macrocyclic polyamine derivatives which are completely N-alkylated, or N-acylated, form stable monolayers at the air-water interface (19). Although the purchase of these azacrown are expensive, except for piperazine 7a stored in a large scale, we select them as our starting materials for the synthesis of two sets target molecules.

3.2.1 Formation of macrocyclic polyamide derivatives 8a-e

Two, three, four, five and six glutamic acid substituents (N-benzyloxycarbonyl-1-benzyl ester, or N-α-Z-L-glutamic acid α-benzyl ester, abbreviated as Z-Glu-OBzl) were directly introduced to the secondary macrocyclic polyamine systems by the amidation of side carboxy group of Z-Glu-OBzl. The preparations of polyamide derivatives 8a-e are outlined in Scheme 3.2, and the amidations afforded reasonable conversions for these five compounds 8a-e. The commercially available derivative of glutamic acid (Z-Glu-OBzl) is protected by benzyloxycarbonyl (Z) at the N-terminus and benzyl at the C-terminus. The amidations were achieved efficiently and completely using coupling agent, 2-(1H-benzotriazol-1-yl)1,1,3,3-tetramethyluronium tetrafluoroborate (TBTU) in good yields. The yields of compounds 8a, 8b, 8c, 8d, 8e are 86%, 65%, 44%, 38%, 33%, respectively, according to the corresponding limiting reagents of polyamines 7a-e. The reactions were monitored by Thin Layer Chromatography (TLC) under UV light and analysed by High Performance Liquid Chromatography (HPLC) at wavelength of 258 nm. Each coupling of polyamine and Z-Glu-OBzl was completed after stirring for overnight when the reaction temperature was increased from 25°C to 45°C. The reaction mixtures were worked up by aqueous/organic extractions, and the organic layers were combined. After evaporation of the organic solutions, the resulting reaction residues were separated by column chromatography and preparative TLC. Table 3.1 summarizes the appearance, melting points and percentage yield of compounds
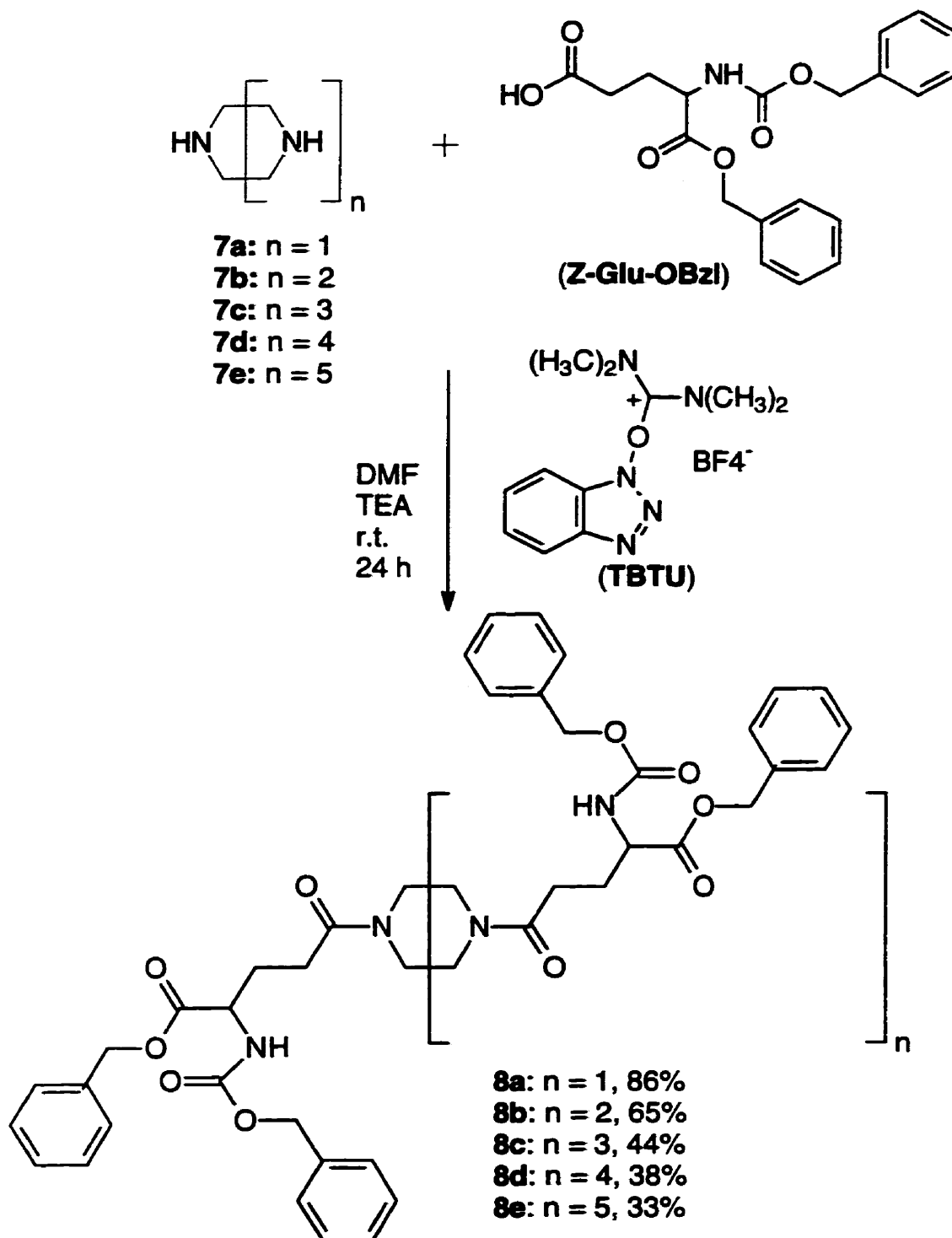
Scheme 3.2: Preparation of macrocyclic polyamide derivatives **8a-e**. The yields of products **8a-e** are calculated from the limiting reagents **7a-e**.

8a-e, and also lists the conditions for the five coupling reactions.

Table 3.1 Summary of the preparation of macrocyclic polyamides 8a-e

Compd	Appearance	m.p. (°C)	Limiting reagent	r_m	t (h)	T (°C)	Yield (%)
8a	w.s.	39-40	7a	1:3:3:3	24	25	86
8b	w.s.	40-43	7b	1:4.5:4.5:4.5	30	35	65
8c	w.s.	60-62	7c	1:6:6:6	36	35	44
8d	w.s.	56-58	7d	1:7.4:7.4:7.4	48	40	38
8e	w.s.	56-58	7e	1:10:10:10	48	45	33

Where w.s.= white solid, m.p. represents melting point, r_m is the molar ratio of polyamine: Z-Glu-OBzl:TBTU:TEA, t is the reaction time in hour, T is the reaction temperature in celsius, the percentage yield is calculated for a pure product from the corresponding limiting reagent.

In the step to polyamides 8a-e, the starting material of macrocyclic polyamines 7a-e allows Z-Glu-OBzl, TBTU and triethy amine (TEA) to react each other in dry N,N'-dimethylformamide (DMF). The couplings were achieved by mixing the macrocyclic polyamines 7a-e with an excess of Z-Glu-OBzl, TBTU and TEA but in proportion to the molar number of reactive amines. For example, for the preparation of 8a, 8b, 8c, 8d, 8e, the molar ratio of 7a, 7b, 7c, 7d, 7e with Z-Glu-OBzl, TBTU and TEA corresponds to 1:3:3:3, 1:4.5:4.5:4.5, 1:6:6:6, 1:7.4:7.4:7.4, 1:10:10:10, respectively. The molar amount of Z-Glu-OBzl used was always equivalent to that of TBTU and TEA. The equivalent molar ratio of triethylamine (TEA) was used as a super-acylation catalyst during the coupling reactions. DMF was chosen as the best solvent for these condensation reactions, since the coupling reagent TBTU is water-soluble and has a higher solubility in this polar solvent. This is the key step for the synthesis of the dendritic chelating agents 6a-e. For the direct formations of 8a-e, one-pot procedure in anhydrous polar organic solvent (DMF) has been established.

The coupling agent, TBTU played an important role in this step. TBTU was first used in peptide synthesis by Knorr in 1989 (20). It is reported that TBTU is very effective for

couplings that involve a proline nitrogen, which is similar to the secondary, cyclic polyamines used in our study. TBTU is an activating reagent of hydroxybenzotriazolyl ester types. The coupling reactions (Scheme 3.2) proceeded smoothly using TBTU. In these reactions, byproducts, such as 1-hydroxybenzotriazole (HOBt), tetrafluoroborate, and tetramethyl urea (TMU) were liberated. But the byproducts are harmless, and completely soluble both in water and in organic solvent. It is assumed that an opening of the 3,4-hydro-4-oxo-1,2,3-benzotriazine ring may occur under these reaction conditions. The opening of the 3,4-hydro-4-oxo-1,2,3-benzotriazine ring generates an activated ester of 2-azido-benzoic acid, which then acts as an effective blocking reagent for free amino functions. Tetrafluoroborate acts as a nonnucleophilic counterion, which has no influence either in coupling rate or in racemization. Among a number of coupling agents which have been used by others for the formation of peptides *in situ* conditions (20, 21, 22), TBTU is tested as the lowest racimization agent in extremely sensitive Z-Glu-OBzl coupling reactions.

The macrocyclic polyamide derivatives **8a-e** were purified by standard procedures (evaporation, extraction, column chromatography and preparative TLC). The increasing size of the polyamines resulted in a greater difficulty in purification, but it is possible to isolate the last TLC band or the last fraction in column chromatography which contained the desired product. The last band in TLC and last fraction of column chromatography usually are easily contaminated by the neighbouring components which have polarity close to the desired compounds. So it is necessary to repeat the separation procedures in order to obtain compounds which have higher purity. The desired products were collected as white flake-like solids with low melting points after removing solvents. These pure compounds **8a-e** are readily soluble in organic solvents.

The characterization of the intermediates **8a-e** was performed by NMR, UV, FTIR, and MS spectroscopy. The ^{1}H-NMR spectrum of **8a-e** in deuterium chloroform (CDCl$_3$) shows the expected signals for all hydrogens and deserves a few remarks. Figure 3.3 depicts the structure (Figure 3.3A), the ^{1}H-NMR spectrum (Figure 3.3B) and the ^{13}C-NMR spectrum (Figure 3.3C) of compound **8a**. All the peaks can be assigned and account for the structure
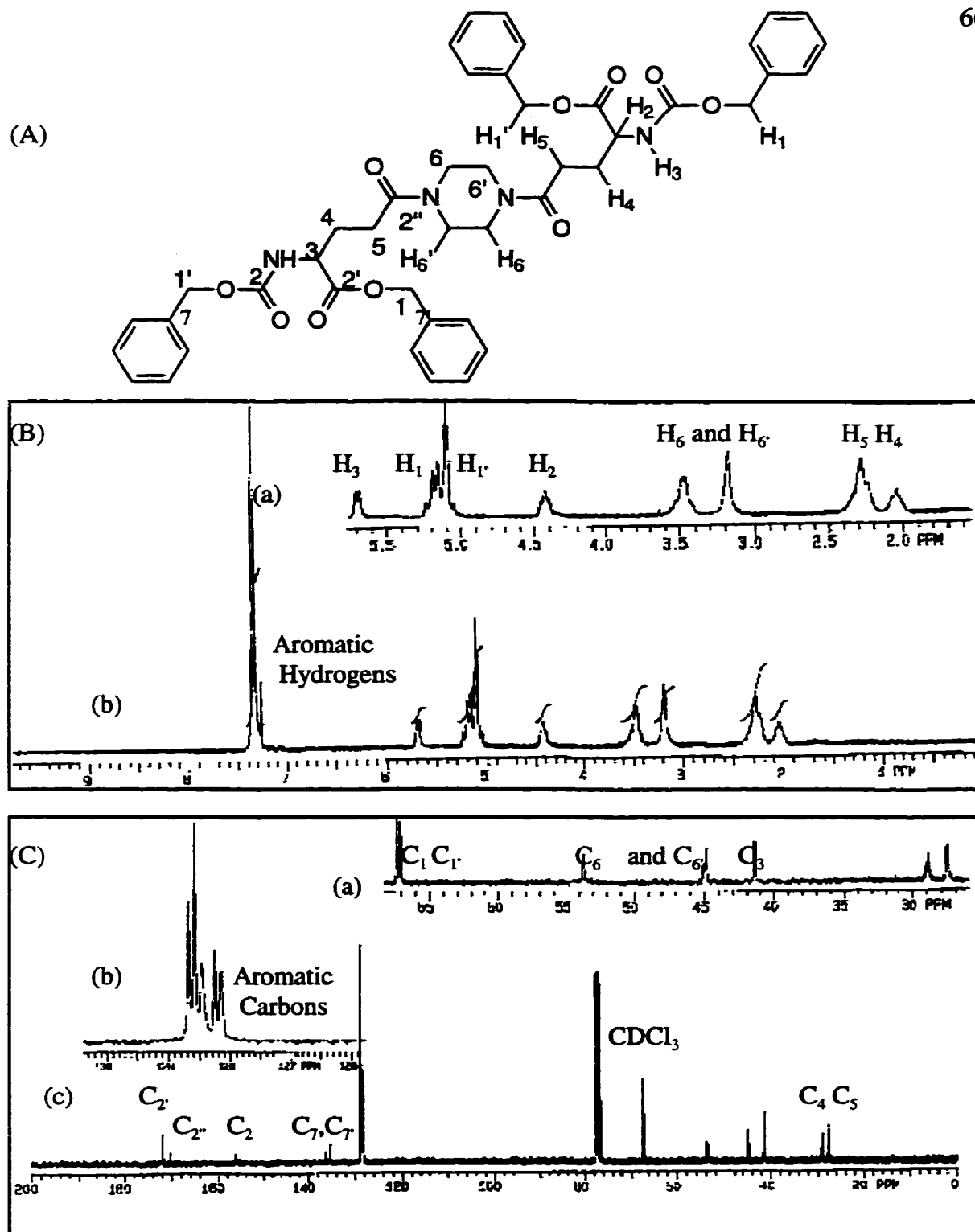
Figure 3.3: Schematic structure (A), ¹H-NMR (B) and ¹³C-NMR (C) spectrum of compound 8a. The carbons are labelled on the left and the hydrogens are labelled on the right. All the peaks are assigned for the hydrogens in (B) and for the carbons in (C).

of **8a**. At room temperature, the two benzylic CH_2 protons have chemical shifts (δ) of 5.10 ppm and 5.18 ppm because of different environments. One of the two benzylic CH_2 peaks causes multiplet splitting (δ 5.18 ppm), this peak is attributed to the benzylic CH_2 which is nearer to the cabamoyl (oxycarboamide) group. The other benzylic CH_2 which is nearer to the oxycarbonyl group gives rise to one signal only at 5.10 ppm. The NH and CH protons were assigned to the peaks at δ 5.70, 4.42 ppm, respectively. The NH signal (δ 5.70 ppm) is a doublet due to the coupling with a neighbouring CH and appears to the lower field due to its amide-type environment. The latter CH behaves as a doublet of triplet with a coupling constant J = 15 Hz. The signal at the lowest field δ 7.32 ppm is assigned to two aromatic benzene hydrogens. It is clear that two cyclic methylene (CH_2) signals occur at δ 3.48, 3.20 ppm with equivalent ratio of peak areas. The CH_2 which is close to the carbonyl group in the glutamic side chain is assigned to the peak at δ 2.30 ppm, and the other CH_2 is assigned to the peak δ 2.05 ppm. The ratio of protons of these two CH_2 signals is not 1:1 but 3:1, because they locate in different chemical and magnetic environments. The assignments of ^{13}C-NMR peaks are also shown in Figure 3.3C. In Figure 3.3C, the expansion (a) shows that two CH_2 of benzyl groups are separated with a minor difference at δ 66.25 ppm and 66.02 ppm. The signals of two cyclic CH_2 carbons occur at δ 53.85 ppm and 45.02 ppm, but there are two pair peaks at each location due to the conformational isomers. The multiple peaks in expansion (b) are identified for two aromatic carbons. The other signals are clearly assigned in Figure 3.3C.

It is well known that the rotation of the (O)C-N bond of amides is restricted (23) and this phenomenon is attributed to the fact that the (O)C-N bond of amides has some double bond character due to the contribution of resonant structures. Here Figure 3.3 and Figure 3.4 show that the proton ratios of cyclic CH_2 groups in compound **8a**, **8b** and **8c** are 1:1 (Figure 3.3A), 1:3 (Figure 3.4B), 1:1 (Figure 3.4C), respectively. These various ratios of peaks indicate that the protons of cyclic methylene groups are not symmetrically equivalent and there are *cis* and *trans* amide rotamers that exist in these compounds due to the (O)C-N restricted rotation. The structures of compounds **8b** and **8c** are represented in Figure 3.4A The signals of two cyclic methylene groups are indicated in Figure 3.4B and Figure 3.4C.

Figure 3.4: Comparison of ^{1}H-NMR spectrum for compounds **8b** (B) and **8c** (C). The schematic structures of compounds **8b** and **8c** are shown on the top (A). The signals of all hydrogens are indicated in (B) and (C) separately. The different integration of cyclic methylene protons is 1:3 for **8b** and 1:1 for **8c**. This phenomena suggests that the (O)C–N bond rotations are restricted in both *cis* and *trans* rotamers for these compounds.
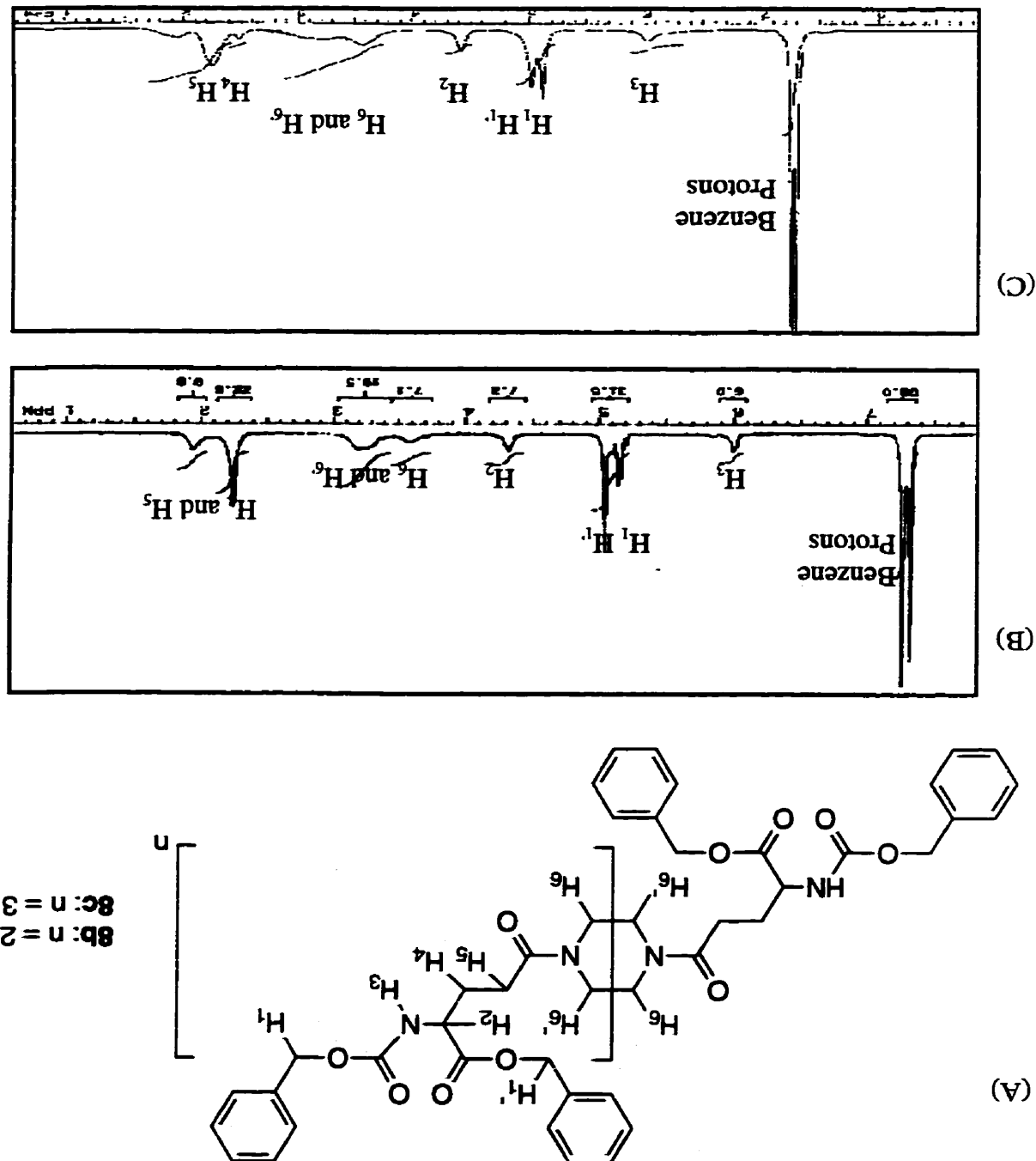
Also the other peaks are assigned in a similar way as Figure 3.3, and they are indicated in Figure 3.4.

3.2.2 Preparation of polyamino acid derivatives 9a-e

Removal of the protecting benzyloxycarbonyl (Z) and benzyl groups from the carbamoyl moieties of compounds 8a-e by catalytic hydrogenation, readily affords polyamino acid derivatives 9a-e as shown in Scheme 3.3. The compounds were hydrogenated for 24 hours at room temperature under normal atmosphere with 10% Pd/C catalyst. The solvent for the cleavage reaction is varied from methanol to a mixture of water and methanol (1:4) as the macrocyclic ring size increased. This is due to the decreasing solubility of products in pure methanol from 9a to 9e. The hydrogenolysis removed the protecting groups cleanly and provided crude polyamino acids 9a-e. After filtration of the catalyst and evaporation of the solvent, the crude products were readily purified by crystallization from ethanol or a mixture of ethanol and water in 80-95% yield. Table 3.2 lists a summary of the appearance, melting point, percentage yield, and the hydrogenolysis conditions of compounds 9a-e.

Table 3.2 Summary of the preparation of compounds 9a-e

Compound	Appearance	m.p. (°C)	t (h)	T (°C)	Solvent	Yield (%)
9a	w. n.	168-170	12	25	MeOH	90
9b	w. n.	210 (dec.)	24	25	MeOH	86
9c	w. n.	210 (dec.)	24	25	MeOH/water	82
9d	w. s.	200 (dec.)	24	25	MeOH/water	80
9e	w. s.	200 (dec.)	24	25	MeOH/water	80

Where w.n. stands for white needle, w.s. represents white solid, m.p. is melting point, t is the hydrogenation time in hour, MeOH is methanol, T is the reaction temperature in celsius. The percentage yield was obtained for each pure product from the starting reagents 8a-e.

8a: n = 1
8b: n = 2
8c: n = 3
8d: n = 4
8e: n = 5

H₂ | Methanol
Pd/C | r.t.
1 atm | 24 h

9a: n = 1, 90%
9b: n = 2, 86%
9c: n = 3, 82%
9d: n = 4, 80%
9e: n = 5, 80%
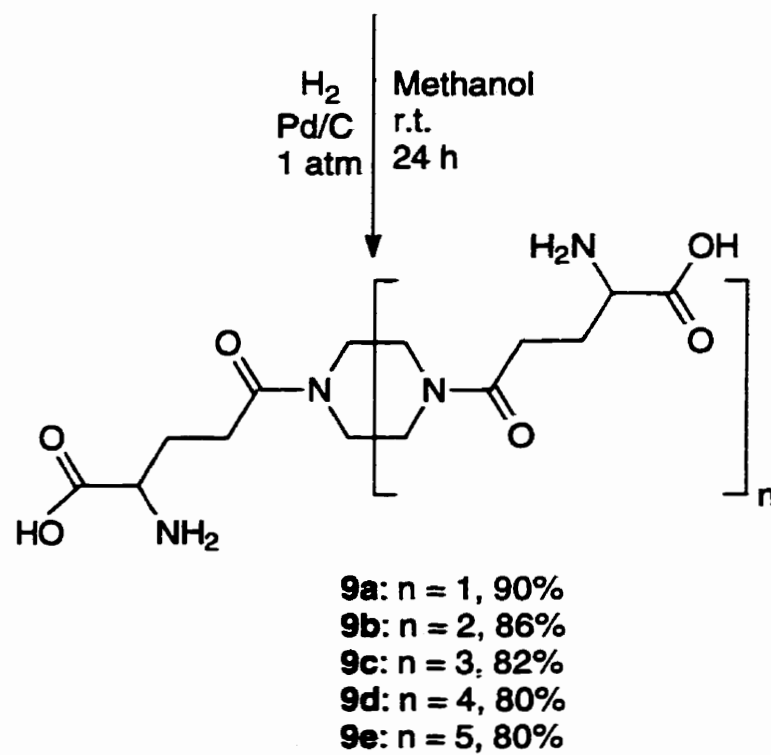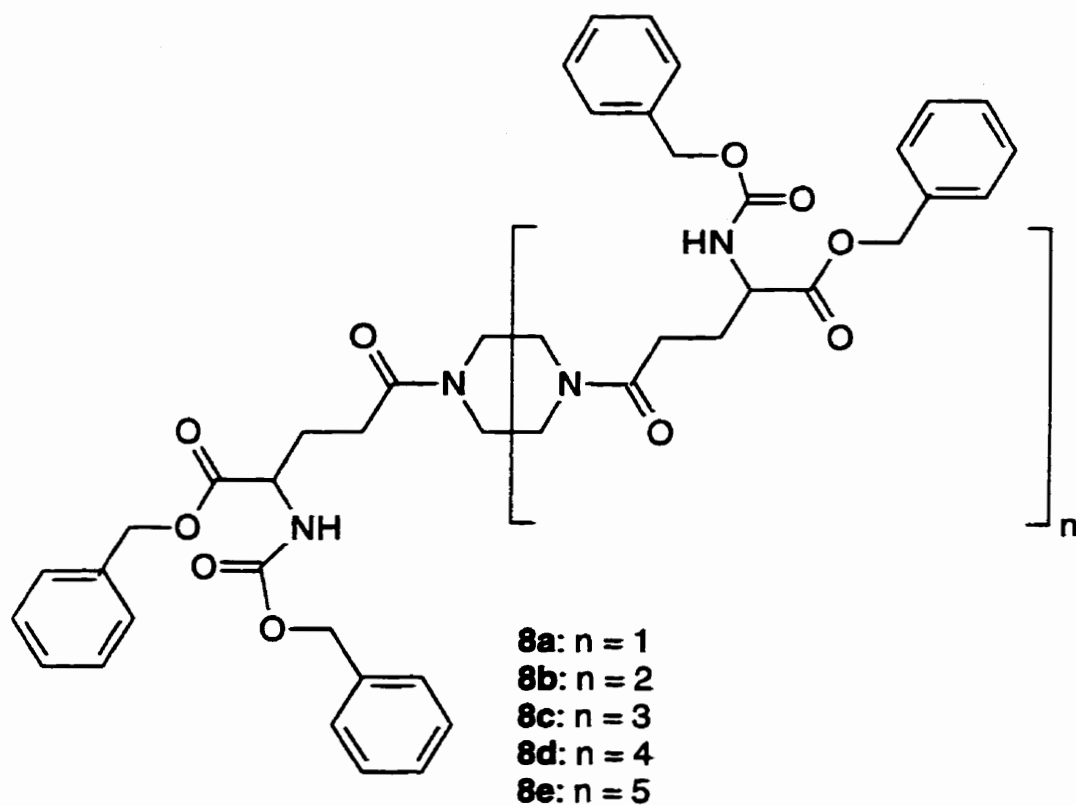
Scheme 3.3: Intermediates **9a-e** were prepared by hydrogenolysis of compounds **8a-e**.

As an example of the ^{1}H-NMR spectrum in D_2O, the ^{13}C-NMR spectrum in D_2O and the FTIR of these types of compounds, Figure3.5 characterizes the identity of compound **9a**, such as the structure (Figure 3.5A), the assignment of protons (Figure 3.5B), the assignment of carbons (Figure 3.5C) and main functional groups (Figure 3.5D). In Figure 3.5B, at room temperature two cyclic CH_2 signals occur at δ 3.50 ppm and 3.45 ppm due to the existence of its rotamers. The tertiary CH signal appears as a triplet peak at the lowest field δ 3.64 ppm with a coupling constant of 7.5 Hz. One CH_2 which is close to the amide bond in the glutamic side chain is assigned to the triplet peak δ 2.49 ppm due to the coupling (J = 9 Hz) to the adjacent CH_2 group. Another CH_2 group is represented as the doublet of triplet peak δ 1.98 ppm due to the coupling (J = 8 Hz) of adjacent CH_2 and CH groups. Figure 3.5C shows the signals of compound **9a** in ^{13}C-NMR spectrum. The two carbonyl carbons are assigned to the peak δ173.0 ppm and δ174.0 ppm, which are indicated the amino acid carbon and amide carbon correspondingly. The signals of two cyclic CH_2 carbons are expanded as in Figure 3.5C (a) and actually appear as two separate peaks at each position such as δ 44.8 ppm, 41.5 ppm. This phenomena also indicate the existence of two different *cis* and *trans* rotamers due to the amide bond restricted rotation. The other three peaks are assigned to the carbons of glutamic side chain as indicated in Figure 3.5C. The FTIR of compound **9a** in Figure 3.4D indicates the vibration of amine (-NH_2) and carboxy (-COOH) at broad absorption 3000-3500 cm^{-1}, and the vibration of carbonyl (C=O) at strong absorption1715 cm^{-1}, 1630 cm^{-1}.

3.2.3 Synthesis of the final dendritic chelating agents 6a-e by carboxymethylation

The last step in the preparation of the multiple NTA-containing compounds with shorter chain length, **6a-e,** was the direct carboxymethylation of the polyamino acids **9a-e** with bromoacetic acid. This was successfully carried out by reaction of **9a-e** with appropriate amounts of bromoacetic acid in the aqueous solution under basic conditions for a few days (Scheme 3.4), followed by acidification with the addition of 6 M hydrochloric acid to pH 1.0. The alkylation step of the polyamino acids **9a-e** with bromoacetic acid was slow but sufficient. The molecules containing numerous primary amine groups are desired
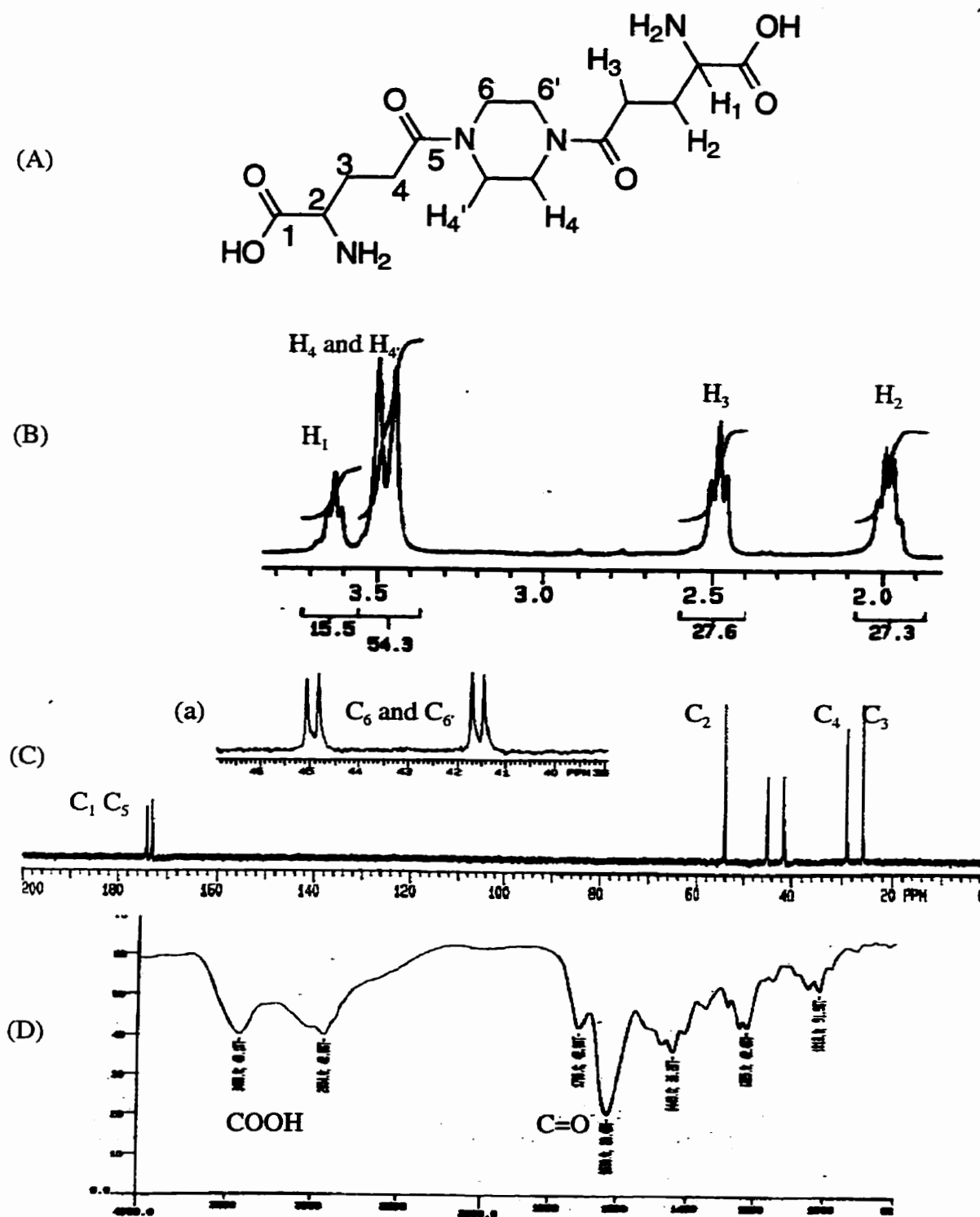
Figure 3.5: Schematic structure (A), ^{1}H-NMR (B), ^{13}C-NMR spectrum, and FTIR of compound **9a**. The carbon atoms are labelled on the left of structure (A), and hydrogen atoms are labelled on the right side. All of peaks are assigned as shown in (B) for hydrogens and in (C) for carbons. The functional groups of carboxy and carbonyl are indicated in (D).

9a: n = 1
9b: n = 2
9c: n = 3
9d: n = 4
9e: n = 5

1: BrCH$_2$CO$_2$H/NaOH
40-60 °C, several days

2: 6 M HCl

6a: n = 1, 46%
6b: n = 2, 38%
6c: n = 3, 37%
6d: n = 4, 34%
6e: n = 5, 29%
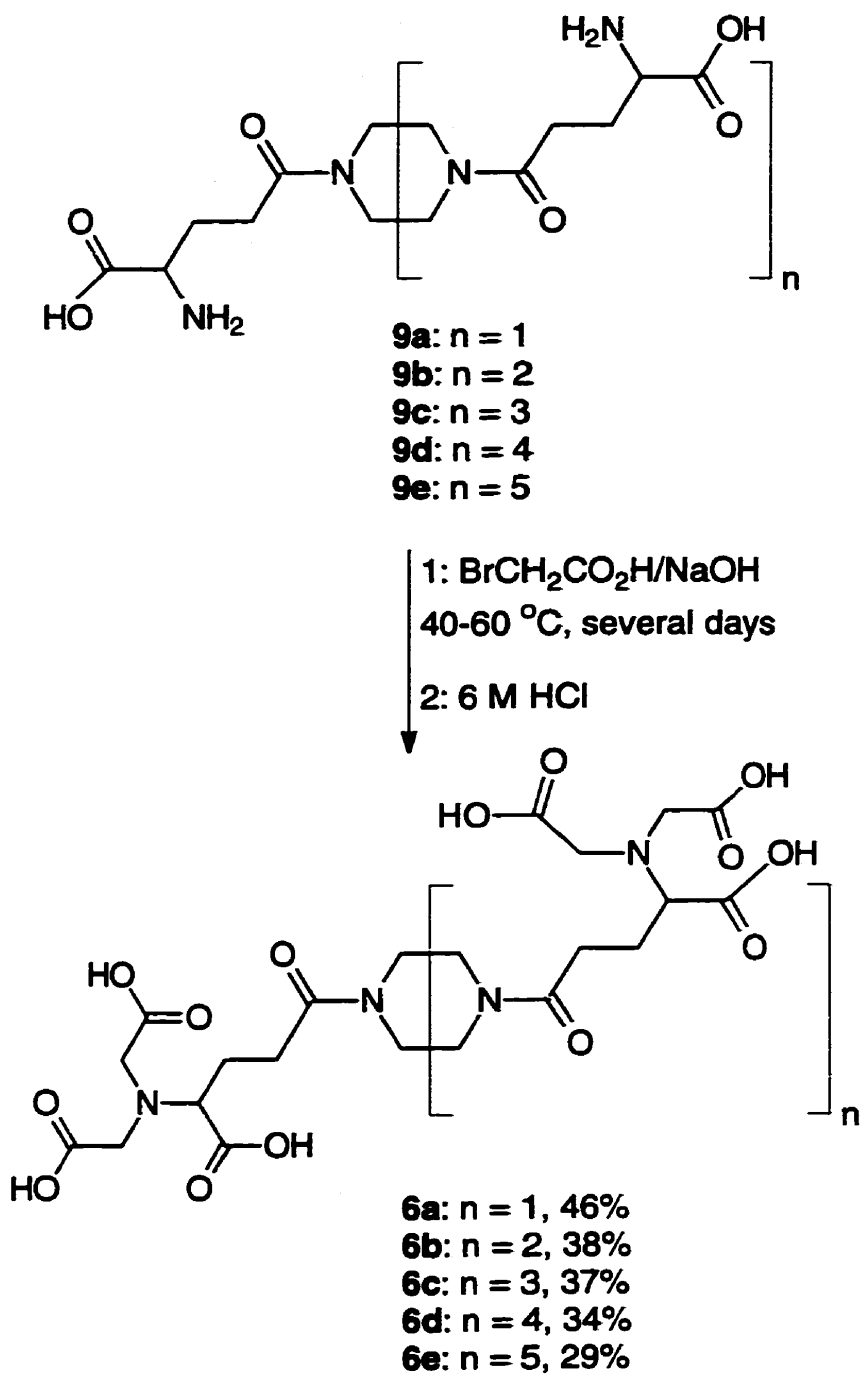
Scheme 3.4: Preparation of final products **6a-e**. The yields were obtained using limiting reagents **9a-b**.

to be alkylated thoroughly by *H*-substitutions at the amine group (-NH$_2$), but an overalkylation to the corresponding ammonium salts in these polyamino acid compounds had to be avoided. After some optima, the alkylations were done mildly by using a slight excess of bromoacetic acid (1.1 mol equivalent to per *N*-carboxymethylation) in aqueous solution with sodium hydroxide as the base. In route to compounds **6a-e**, the carboxymethylation of these polyamino acid **9a-e**, were controlled by maintaining pH and monitored by TLC. Thus the fully substituted species in reaction mixtures were the major products **6a-e** as desired. The reaction mixtures were worked up by acidification, evaporation, neutralization. Finally, anion-exchange chromatography was applied for the purification of the desired products **6a-b**, and the final compounds **6c-e** were purified by crystallization. As a result, this pathway to compounds **6a-e** is practical and easy to perform. The final products **6a-e** were obtained as white solids in 46-29% yields. Table 3.3 lists the physical properties, reaction conditions and yields for compounds **6a-e** .

Table 3.3 Summary of synthesis of dendritic ligands 6a-e

Product	Appearance	m.p. (°C)	Limiting reagent	# of BrCH$_2$CO$_2$H	t (day)	T (°C)	Yield (%)
6a	w.s.	210 (dec.)	**9a**	4.5	1	40	46
6b	w.s.	210 (dec.)	**9b**	6.6	2	40	38
6c	w.s.	210 (dec.)	**9c**	9.0	4	50	37
6d	w.s.	220 (dec.)	**9d**	11.0	5	55	34
6e	w.s.	230 (dec.)	**9e**	13.5	8	60	29

Where, *w.s.* stands for white solid, *m.p.*= melting point, *# of BrCH$_2$CO$_2$H* = molar ratio to the limiting reagent, *t* = reaction time in day, *T* is the reaction temperature in celsius, the percentage yield is calculated from the limiting reagent **9a-e**.

Being concerned about the polarity of the final compounds **6a-e**, we tried another route to obtain **6a-e** by reacting **9e** with methanol to give compound **10e**, followed by alkylation of **10e** with methyl bromoacetate to give compound **11e**, and subsequent hydrolysis of the esters **11e** to give final compounds **6a-e** under basic conditions. This
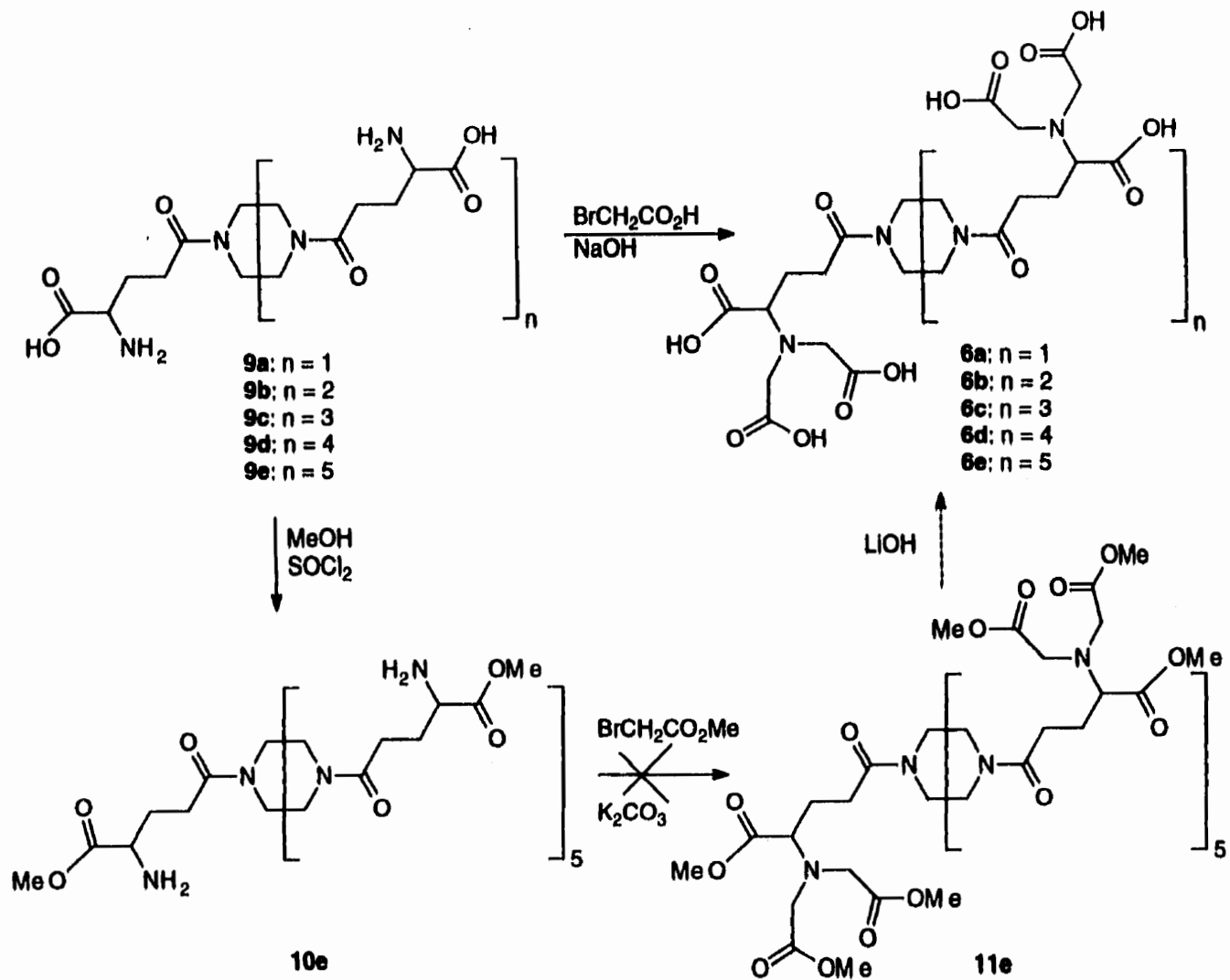
Scheme 3.5: Alternative pathway to dendritic chelating agents **6a-e**.

9a: n = 1
9b: n = 2
9c: n = 3
9d: n = 4
9e: n = 5

6a: n = 1
6b: n = 2
6c: n = 3
6d: n = 4
6e: n = 5

BrCH$_2$CO$_2$H
NaOH

MeOH
SOCl$_2$

LiOH

BrCH$_2$CO$_2$Me
K$_2$CO$_3$

10e

11e

alternative pathway is shown in Scheme 3.5. However, it proved difficult to control the tertiary alkylation of the amine **10e** and it appeared that the quaternary ammonium product formed too easily in organic solvents.

The final compounds **6a-e** are extremely polar, and subsequent isolation by standard chromatographic techniques (silica gel column chromatography, preparative TLC) was cumbersome. Anion exchange chromatography was used for the purification of **6a-b**. The desired products existed as several ionized species after neutralization. The neutralized reaction mixture was adjusted to pH 10 with 6 M NaOH, and the reaction residues were applied to a Bio-Rad Ag1-X4 anion-exchange column. The Ag1-X4 anion-exchange resin was first transferred to a formate form by eluting the resin with formic acid. When the column was saturated with formate, the reaction residues were applied to the column, and eluted successively with water and a gradient concentration of formic acid. The collected fractions were evaluated by TLC on silica plates developed in 25% aqueous mixture of NH_4OH : 75% EtOH. The R_f values of the desired multi-alkylated products are different from the starting materials and the byproducts. Since the desired product has the most polarity, so they can be isolated with the lowest R_f components. If the collected fraction was contaminated with some higher R_f materials, then this fraction had to be repeatedly purified. All fractions containing the lowest R_f materials were combined, and the combined solution was evaporated to dryness. The resulting residue was repeatedly redissolved in water and evaporated to dryness until a solid residue was obtained. The solid residues of **6a** and **6b** were then dried under vacuum over P_2O_5. The final compounds **6a** and **6b** were collected in the form of a white power in yield of 46%, 38%, respectively.

As the number of NTA groups in compounds **6c-e** increases, the solubility decreases in aqueous solution. Thus the crude compounds **6c-e** precipitate out from the acidic aqueous solutions, and the collection of crude compounds **6c-e** can be performed with simple filtration. Ethanol was added to the acidic aqueous solutions containing **6c-e** and the desired crude products precipitated out. The resulting white precipitates were collected and then dried under vacuum. Finally the crude products of **6c-e** were further purified by crystallization from methanol in 37-29% yield. These simple procedures turned out to work

well for the purification of the more polar compounds **6c-e**.

The identities of the final compounds **6a-e** are confirmed by NMR, MS and FTIR. While the structures of these compounds are simple, the characterization is complicated by multiple ionic forms. No single, simple signals are observed in their ^{1}H-NMR spectra. Figure 3.6 shows the identification of compound **6b** and **6c**, such as the structures (Figure 3.6A), ^{1}H-NMR spectrum of **6b** (Figure 3.6B), ^{1}H-NMR spectrum of **6c** (Figure 3.6C), and FAB-MS spectrum of **6b**. The peaks of methylenes which are close to carboxyl groups in each dendritic NTA ligand are overlapped and broad at δ 3.7-4.0 ppm. As the size of dendritic compounds **6a-e** increases, the signals of cyclic methylene groups approach closer to those of methylene groups which are near carboxyl groups. We can not distinguish which peak belongs to which CH_2 group as the size of macrocyclic ring increases. This phenomenon is obviously indicated in Figure 3.6B and Figure 3.6C. In Figure 3.6B, two CH_2 groups of the glutamic side chain in compound **6b** can be assigned to peak at δ 2.59 ppm and δ 1.85 ppm. The cyclic CH_2 signals appear at δ 3.59 ppm and δ 3.40 ppm, and signals of two CH_2 groups and one CH group, which are close to carboxyl groups, are overlapped and assigned to the broad peak at δ 3.86 ppm. In Figure 3.6C, all signals of compound **6c** are similar to that of compound **6a**. Two cyclic CH_2 groups in amide ring, two CH_2 and one CH groups which are close to carboxyl groups, can be assigned to the two broad peaks at δ 3.80 ppm and δ 3.60 ppm. The peaks at δ 2.69 ppm and δ 2.08 ppm are attributed by the two CH_2 groups of the glutamic side chain. While the ^{1}H-NMR spectra of compounds **6a-e** provide us useful information about the identification of their structures, the MS spectra of compounds **6a-e** are helpful to further confirm their structures. For example, Figure 3.6D shows the FAB-MS spectrum of compound **6b**. The molecular weight of compound **6b** is 864, there is a peak at m/z 865 and this corresponds to the molecular ion with one proton transfer $[M+H]^+$ of compound **6b**.

The ^{1}H-NMR spectra of compounds containing multiple NTA groups are pH dependent. Figure 3.7 presents the ^{1}H-NMR spectra of **6a** at four different pH in D_2O solution. These variations, we believe, arise from many possible ionization states of NTA groups in the solution. Altering the pH of the solution, changes the ratio of molecules with
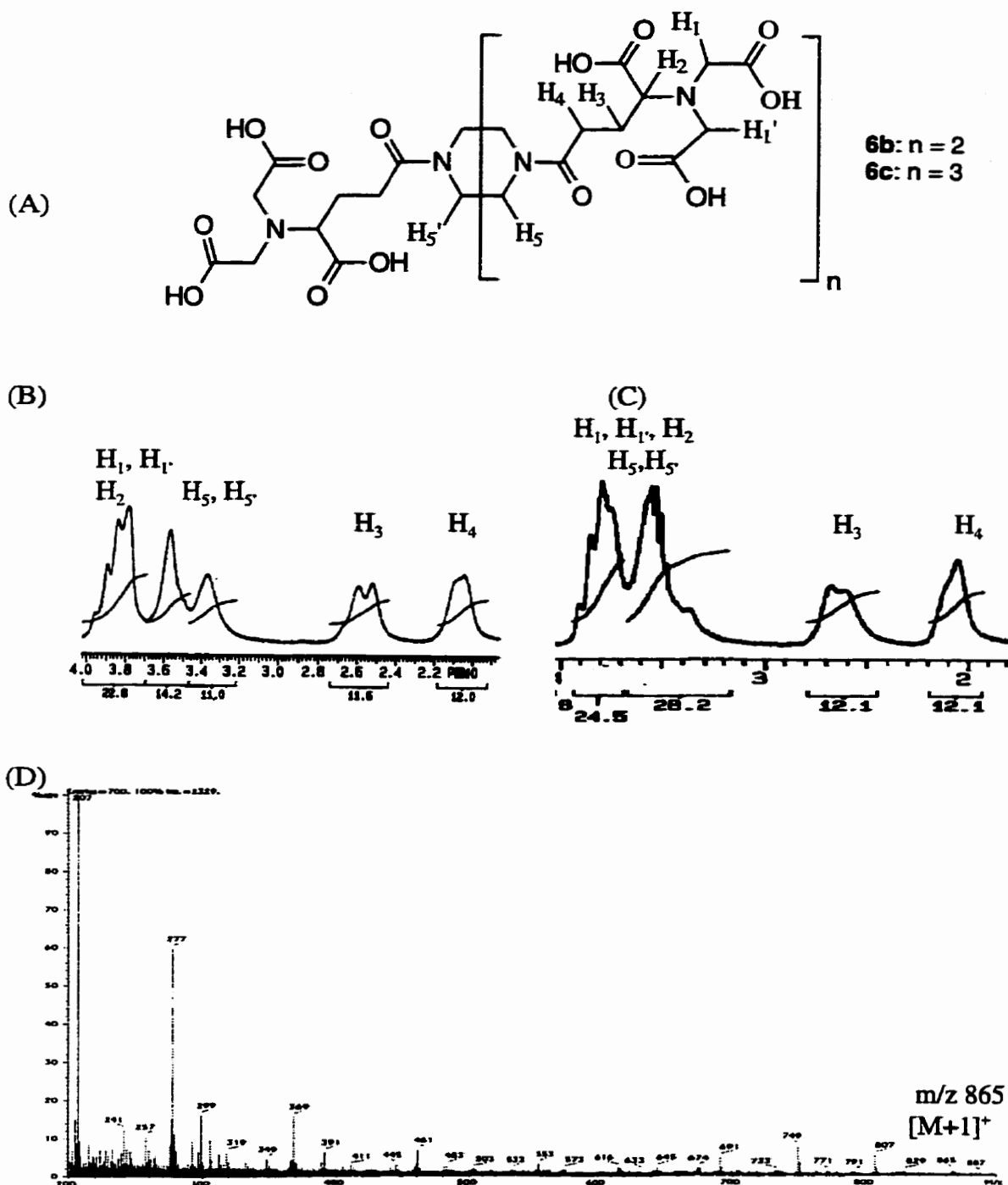
Figure 3.6: Structures of compounds **6b** and **6c** (A), ^{1}H-NMR spectrum of **6b** (B), ^{1}H-NMR spectrum of **6c** (C), FAB-MS spectrum of **6b** (D) was obtained under the matrix of glycerol / oxalic acid with a molecular ion m/z of 865 [M+1]$^+$. Only one unit of hydrogens of **6b** and **6c** are labelled in (A). All peaks in ^{1}H-NMR spectrum of compounds **6b** and **6c** are indicated in (B) and (C), respectively.
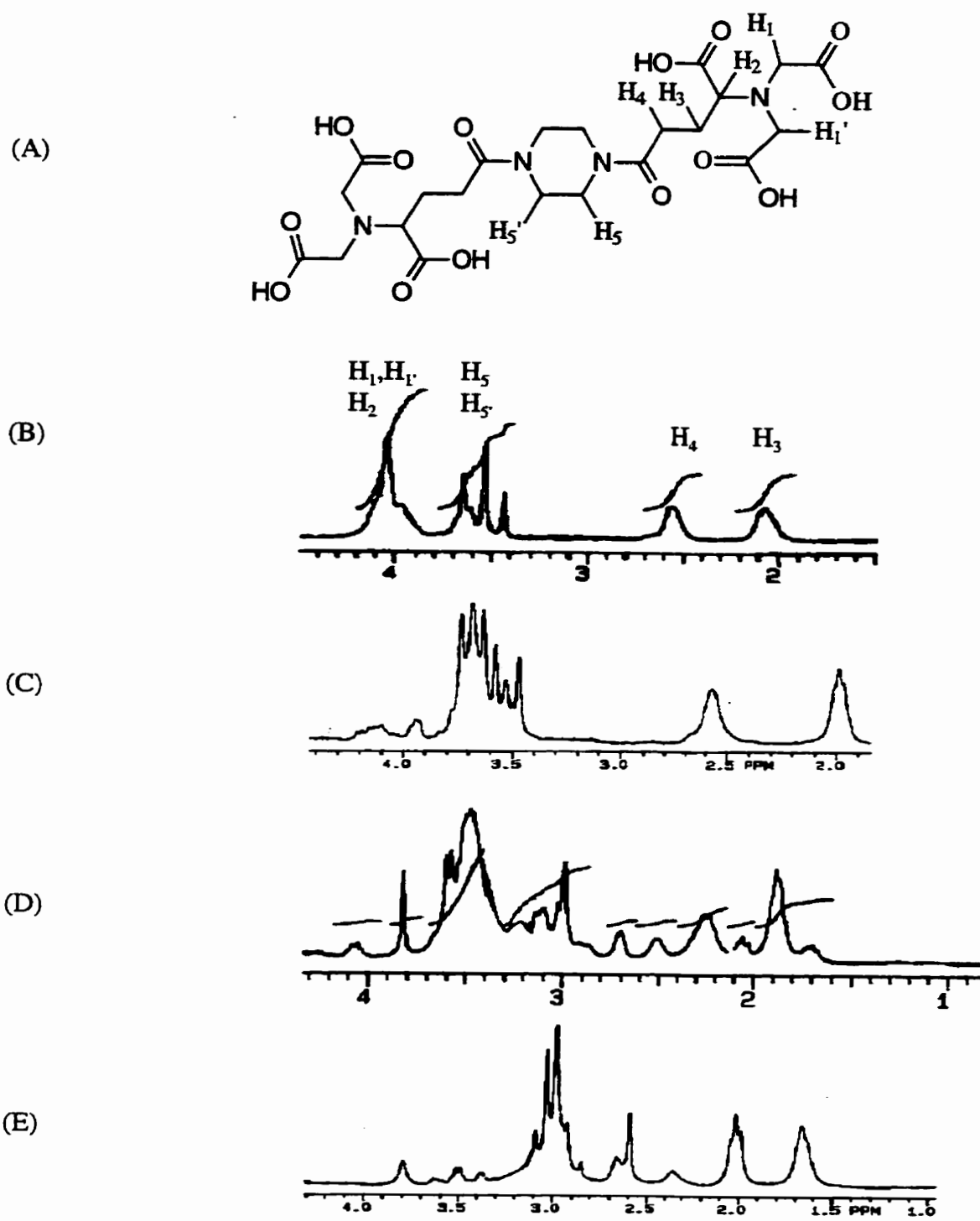
Figure 3.7: Schematic structure (A), ^{1}H-NMR spectrum at pH 1.0 (B), pH 5.0 (C), pH 9.0 (D), pH 11.0 (E) of compound **6a** in D_2O. Protons of **6a** in different environments are labelled on the right of (A), and are assigned to the corresponding signals (B). Various ionic states of **6a** exist in solution when the pH of solution is increased.

different ionizations. We have not determined the individual signals from each component at a given pH. But changing pH environments would affect the signal positions of both cyclic CH_2 and neighbouring CH, CH_2 of multiple carboxyl groups as depicted in Figure 3.7. The two CH_2 peaks are less influenced by pH.

3.3 Convergent synthesis of dendritic ligands 12a-b

As an alternative approach to making compounds with multiple NTA groups, we used lysine-NTA (17) which was generated according to Hochuli's method (11, 12, 13). Compound 17 was then coupled with tetrafluorophenyl activated esters (14a-b) to give final chelating agents 12a-b as shown in Scheme 3.6. This convergent strategy provides a longer linker between the macrocyclic polyamide head and the terminal NTA groups. This pathway gives an opportunity to change the length of linkers by using lysine-NTA and succinic anhydride. Lysine-NTA 17 has been used previously as a convenient reactant for lipid-NTA derivatives (15, 24).

3.3.1 Macrocyclic succinyl polyamides 13a-b

With the first step of the convergent synthesis outlined in Scheme 3.7, 13a and 13b were prepared by reacting 7a and 7b with succinic anhydride in benzene under refluxing condition for two days using the method of Izatt and Kung (25, 26). The products were purified as white needles by crystallization from ethanol in yields of 45-65%. However, only the two smallest succinyl amides were successfully obtained. This route failed for the larger cyclic polyamide derivatives, possibly because of steric factors or decreased reactivity.

The structure proposed for compounds 13a and 13b are consistent with those determined from NMR, FTIR, FAB-MS spectra. Figure 3.8 shows the structure (Figure 3.8A), the ^{1}H-NMR spectrum in D_2O (Figure 3.8B) and the ^{1}H-NMR spectrum in DMSO-d_6 (Figure 3.8C) of compound 13a. The ^{1}H-NMR spectrum of this compound is interesting. For example, the peaks of ethylene hydrogens in the succinic acid portions of the molecules in ^{1}H-NMR spectrum exhibit distinctly at δ 2.68 ppm and 2.54 ppm in D_2O and at δ 2.54 ppm and 2.42 ppm in DMSO. The cyclic methylene signals are seen as a triplet at 3.58 ppm in
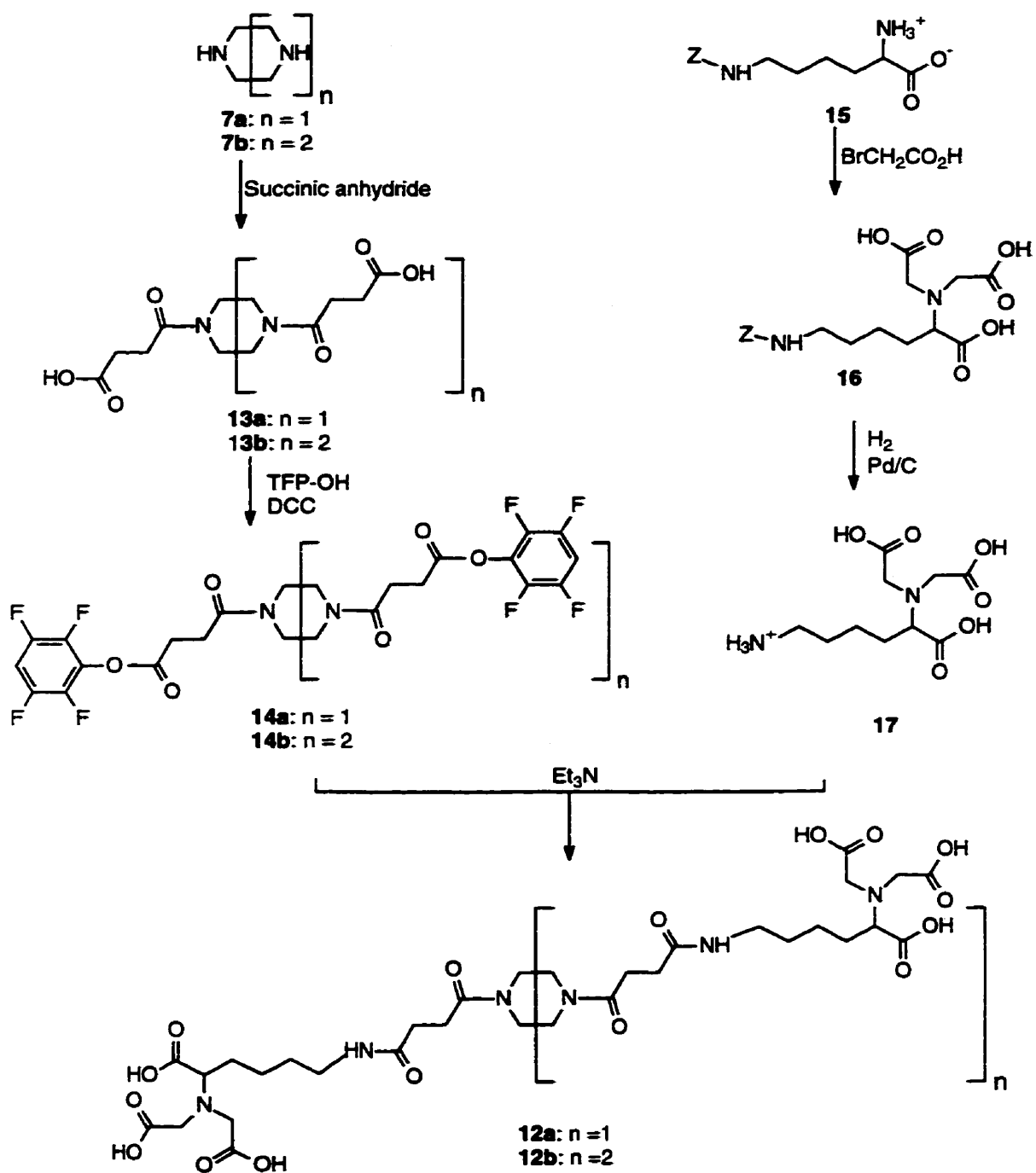
Scheme 3.6: Convergent synthetic strategy to target molecules **12a-b**.

7a: n = 1
7b: n = 2

Benzene
Reflux for two days

13a: n = 1, 65%
13b: n = 2, 45%
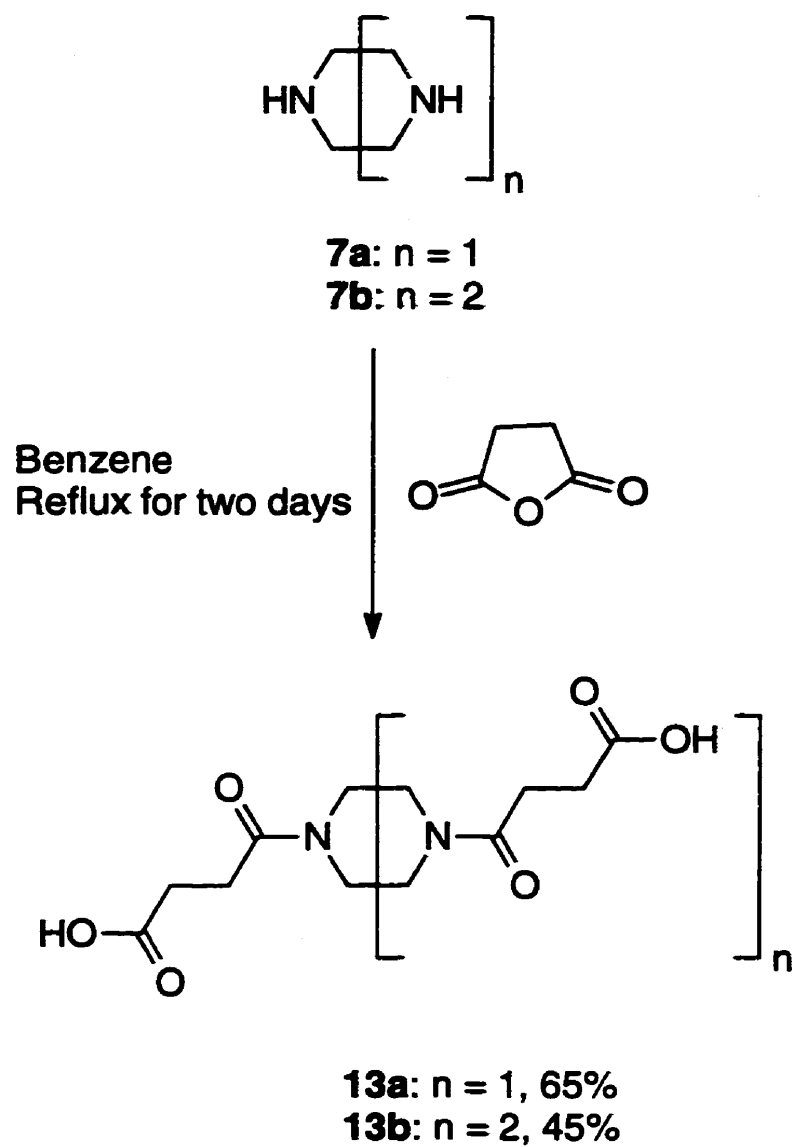
Scheme 3.7: Preparation of polyamide derivatives **13a** and **13b**. The yields were obtained from limiting reagents **7a-b**.

(A)

(B)

(C)
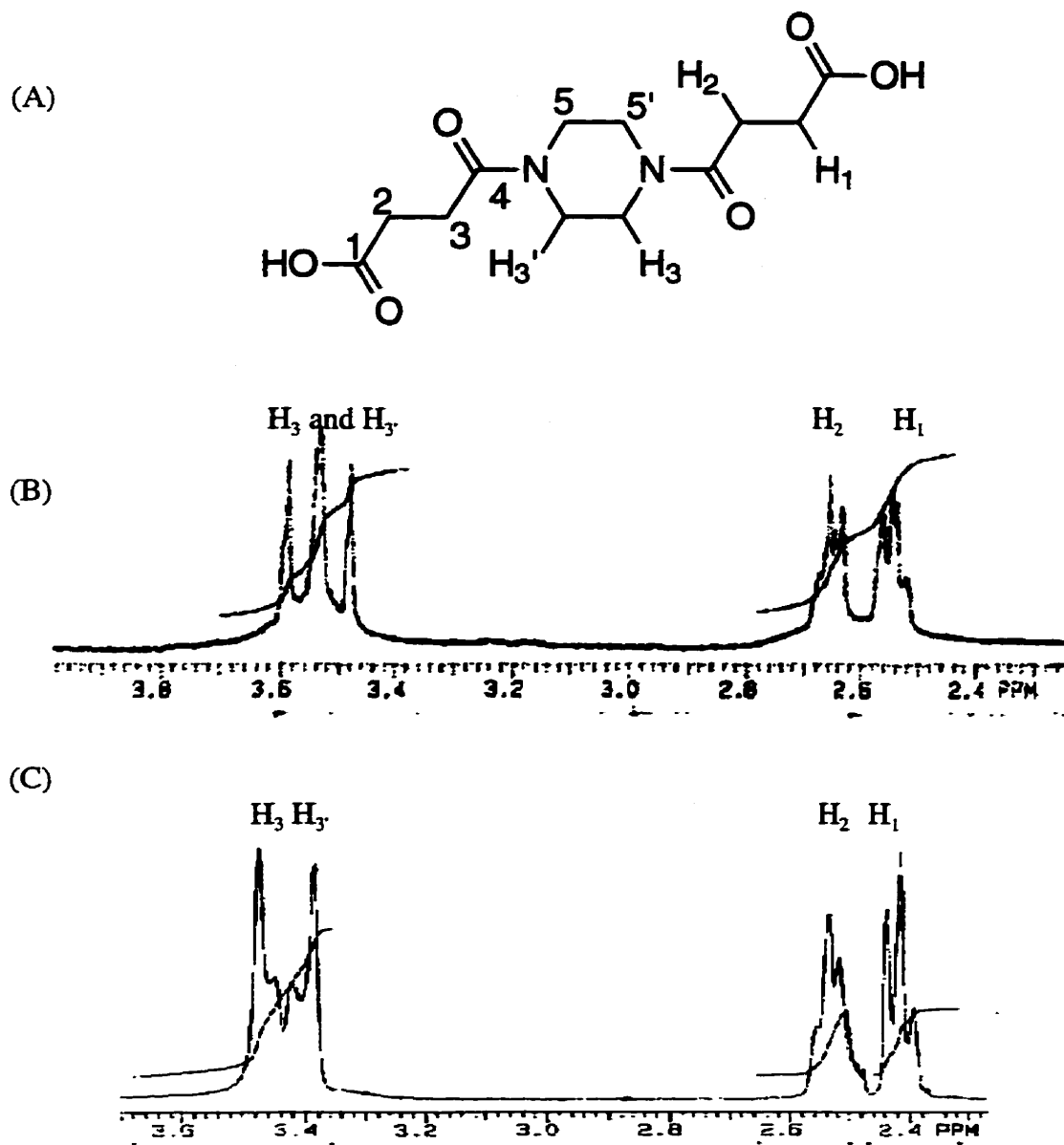
Figure 3.8: Schematic structure (A), ^{1}H-NMR spectrum in D_2O (B) and ^{1}H-NMR spectrum in DMSO (C) of compound **13a**. The hydrogens are labelled on the right of (A). All of peaks are assigned as indicated in (B) and (C). The cyclic methylene groups in ^{1}H-NMR spectrum of compound **13a** is influenced by solvent.

D_2O, but two deformed peaks at δ 3.48 ppm and 3.40 ppm in DMSO at room temperature. The total intensities of peaks at δ 3.48-3.40 ppm corresponds to eight hydrogens. In an ^{1}H-NMR study of N,N-disubstituted piperazine derivatives, Spragg found *cis*- and *trans*- isomers with the *trans*- form in most abundant (27). Variable NMR temperature experiments on compound **13a** show that the splitting of the cyclic methylene groups arise from conformational isomers. This will be discussed further in Section 3.4. The diacids and triacids (**13a** and **13b**) exhibit an IR band at 1690-1720 cm^{-1}, indicative of carboxylic acid carbonyl groups. They all possess the amide character and contain bands at 1620-1600 and 1550-1500 cm^{-1} which are indicative of the amide group.

3.3.2 Tetrafluorophenyl activated esters (14a-b)

In this step, we tried to activate the carboxyl group which is located at the ends of the previous products **13a** and **13b**. The desired activated compounds must be readily obtained, and is stable to environment moieties (15, 24). We have found tetrafluorophenol (TFP-OH) is a very good activating reagent for the formation of the corresponding TFP ester, even if the TFP ester is normally not as active as N-hydroxysuccinic imide (NHS) ester. The requisite activated macrocyclic polysuccinyl amide derivatives were prepared as the tetrafluorophenyl (TFP) esters **14a** and **14b** as white power in 86-67% yield. The processes in this step are outlined in Scheme 3.8. We have followed the procedure described by Wilbur et al (28, 29, 30) for these two reactions. Compounds **13a** and **13b** were mixed with proportional molar ratios of dicyclohexylcarbodiimide (DCC) and TFP-OH in dry DMF. The reaction mixtures were stirred for overnight at 50°C. The reaction was monitored by TLC and the developing components were visualized by bromophenol blue solution. After filtration of the white precipitates (dicyclohexyurea), the reaction mixtures were evaporated to give crude products as white solids. The resulting solids were triturated with a mixture of acetonitrile and ethylacetate, and the pure compounds **14a-b** were obtained by vacuum filtration and washing with diethylether.

TFP esters are preferred over other activated esters in this work, since they are less sensitive to ambient moisture and they are stable to hydrolysis to provide good aminolysis
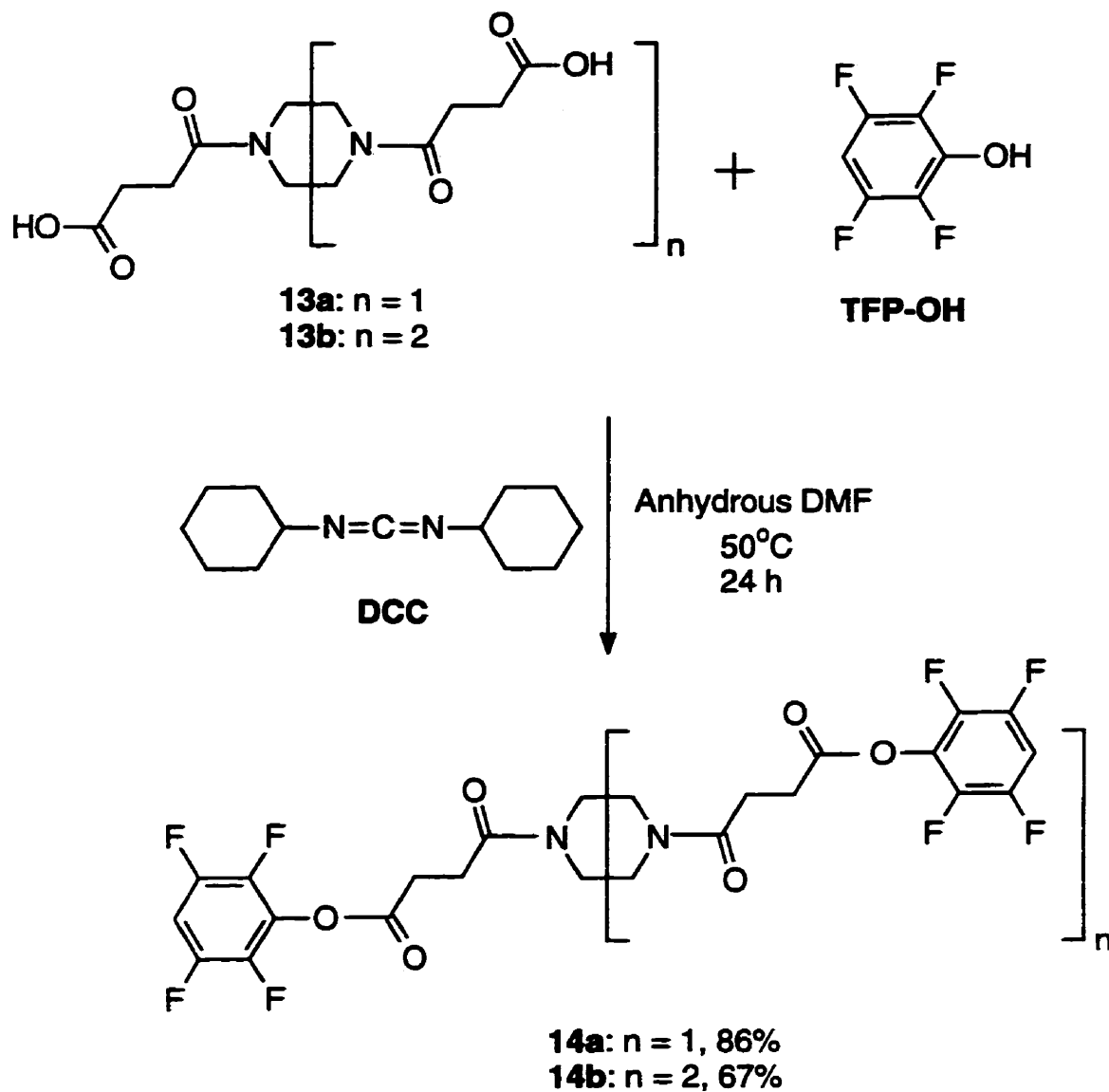
Scheme 3.8: Formation of tetrafluorophenyl (TFP) activate ester **14a** and **14b**. The yields were obtained from limiting reagents **13a** and **13b**.

yield in the final coupling step. In the process of seeking the best activating group for the next coupling reaction, carbonyldiimidazole (CDI) and N-hydroxylsuccinic imide (NHS) had been tested for this purpose. CDI had been successfully used to produce diimidazole activated diamide compound in the process of synthetic work. But using the activated CDI amide was not successful to obtain the final desired product in the next coupling step with the addition of lysine-NTA. It also proved difficult to isolate the activated NHS esters of **13a** and **13b**. It is not clear yet why the NHS activated esters were difficult to isolate. More efforts are needed to work out the CDI and NHS activated pathway. Although tetrafluorophenoxy is a not good leaving group as NHS, it is sufficient for the next reaction.

The two activated tetrafluorophenyl esters, **14a** and **14b** were identified by NMR, IR and MS as well (Figure 3.9). Figure 3.9 presents the structure (Figure 3.9A), the ^{1}H-NMR spectrum in $CDCl_3$ (Figure 3.9B), and MS spectrum (Figure 3.9C) of compound **14a**. In Figure 3.9B, the benzene hydrogens (H_1) appear at lowest field δ 6.98 ppm as a multiplet peak. The multiplet splitting (J = 4.7 Hz) is due to the heteronuclear coupling of neighbouring fluorine resonance as seen in the expansion (a) of Figure 3.9B. The signals of two cyclic methylene groups are also observed as two deformed peaks at δ 3.70 and 3.55 ppm, this separation is caused by the restricted (O)C-N bond rotation and indicated the existence of conformational (*cis* and *trans*) isomers. The other two triplet peaks at δ 3.04 and 2.80 ppm are assigned for two CH_2 groups in succinyl portion. These two CH_2 signals occur at relatively lower field than that of starting materials **13a** and **13b** due to the electron-withdrawing effect of the surrounding fluorines. The broad peak at highest field δ 1.65 ppm is attributed to the water in $CDCl_3$. Figure 3.9C depicts the MS spectrum of compound **14a** with a molecular ion at m/z 582 [M]$^+$, which equals the calculated molecular weight of **14a**. The most abundant peak is at m/z 417 and this is equivalent to the fragment which loses the tetrafluorophenyloxy group. This information provides an evidence that tetrafluorophenoxy acts as both good activating and leaving group.
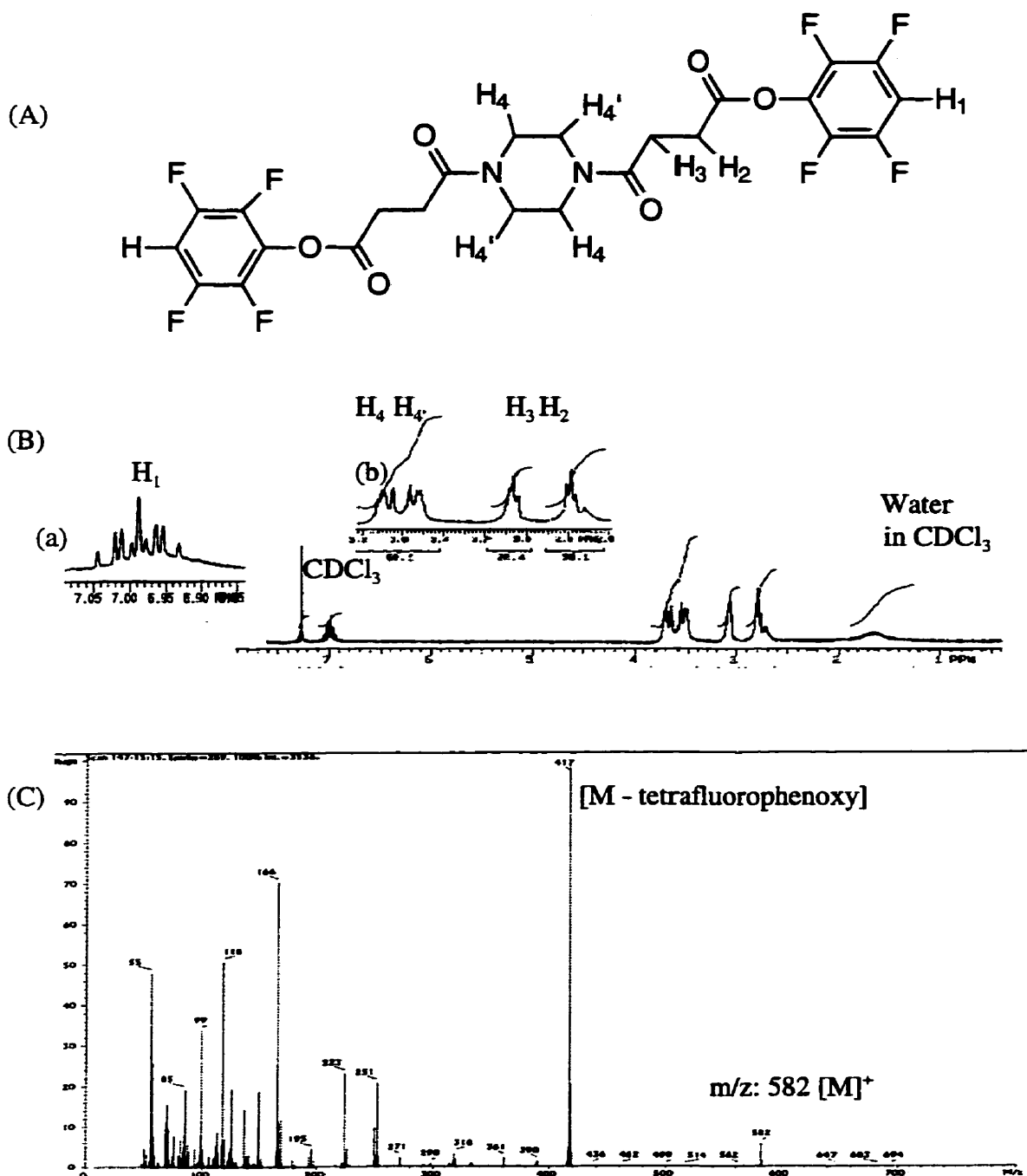
Figure3.9: The structure (A), ^{1}H-NMR spectrum (B) and MS spectrum (C) of compound
14a. The protons which are labelled on the right of (A) are assigned in (B). The MS spectrum
yields a molecular ion at m/z = 582, this equals to the expected MW of compound 14a.

3.3.3 Preparation of lysine-NTA 17

The NTA derivative 17 was synthesized according to the method of Hochuli (11, 12) as outlined in Scheme 3.9. The starting material, $N(\epsilon)$-benzyloxycarbonyl-L-lysine 15 was carboxymethylated at 45°C for overnight, under basic condition using sodium hydroxide as a base. The product 16 was precipitated out after acidifying the basic reaction mixture. The white solids were collected by vacuum filtration and purified by crystallization from ethanol in 89% yield. The protecting group of compound 16 was cleaved by hydrogenolysis in basic solution, but the precipitation of product 17 from an aqueous solution was problematic according to Hochuli's procedure. To solve this problem, many researchers have modified the method of Hochuli's cleavage at the protecting group. For example, Paborsky and his coworkers have modified the reductive removal of the Z group. The removal was carried out with ammonium formate and 5% Pd/C at 70°C in water for 15 h (31). Schmitt's lab cleaved the protecting Z group in 95:5 mixture of methanol:acetic acid (15). We found that a very small amount (5% in volume) of iso-propanol was added into the solution and the product lys-NTA precipitated out from the saturated solution after being stored for two days at - 4°C. Finally, pure lys-NTA 17 was isolated as white crystals in 76% yield from crystallization in a mixture of ethanol and water. The purity of lys-NTA is determined by TLC, FTIR and NMR, and is found to agree with previously published data.

3.3.4 Final dendritic chelating agents 12a and 12b

Syntheses of 12a and 12b (Scheme 3.10) were readily accomplished by reaction of 2.5 molar or 3.5 molar equivalent of lysine-NTA 17 with 1,4-Bis[3'-(2,3,5,6-tetrafluophenoxycarbonyl)-propanoyl]diazacyclohexane 14a and 1,4,7-Tris[3'-(2,3,5,6-tetrafluorophenoxycarbonyl)propanoyl]triazacyclononane 14b in a mixture of an acetonitrile and water solvents. The mixed solvent system was used in this final step of convergent strategy to address the problem of differential solubility of the TFP esters and lysine-NTA 17. The coupling was conducted under conditions that resulted in a slow reaction, but elevating the reaction temperature to 50°C resulted in reasonable yields of 12a and 12b. TEA was found to be the best base for this reaction, even through it was difficult to
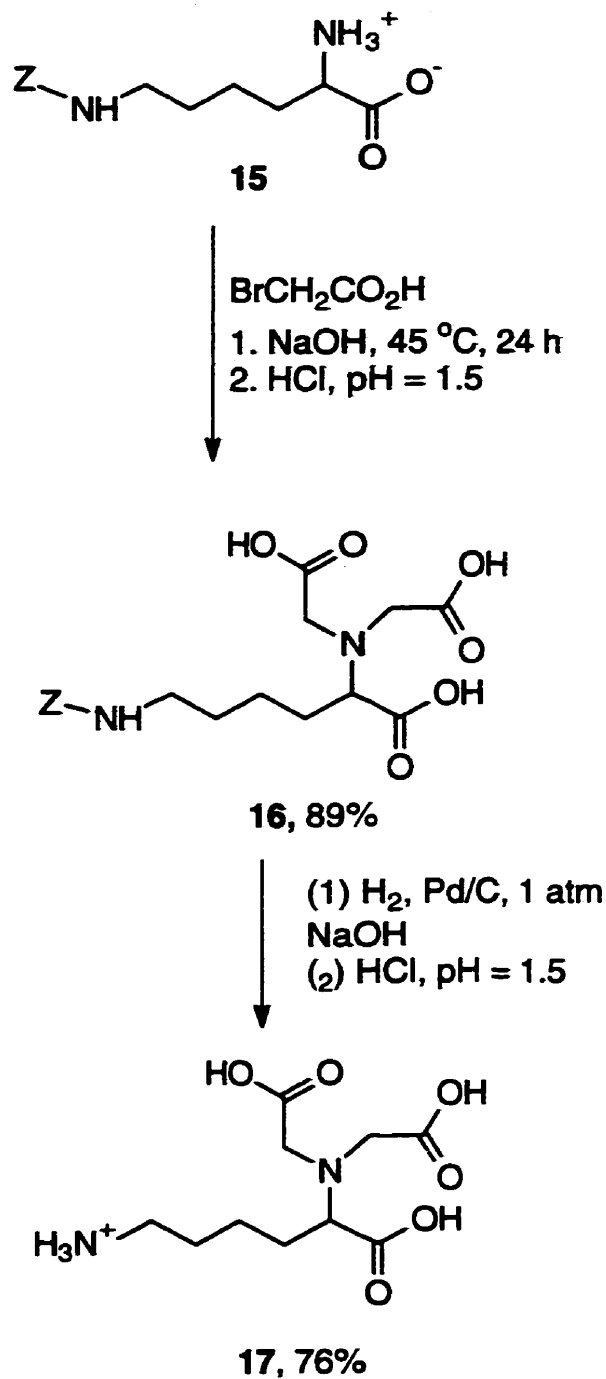
Scheme 3.9: Two steps to compound **17** from starting material $N(\varepsilon)$-Z-lysine (**15**).
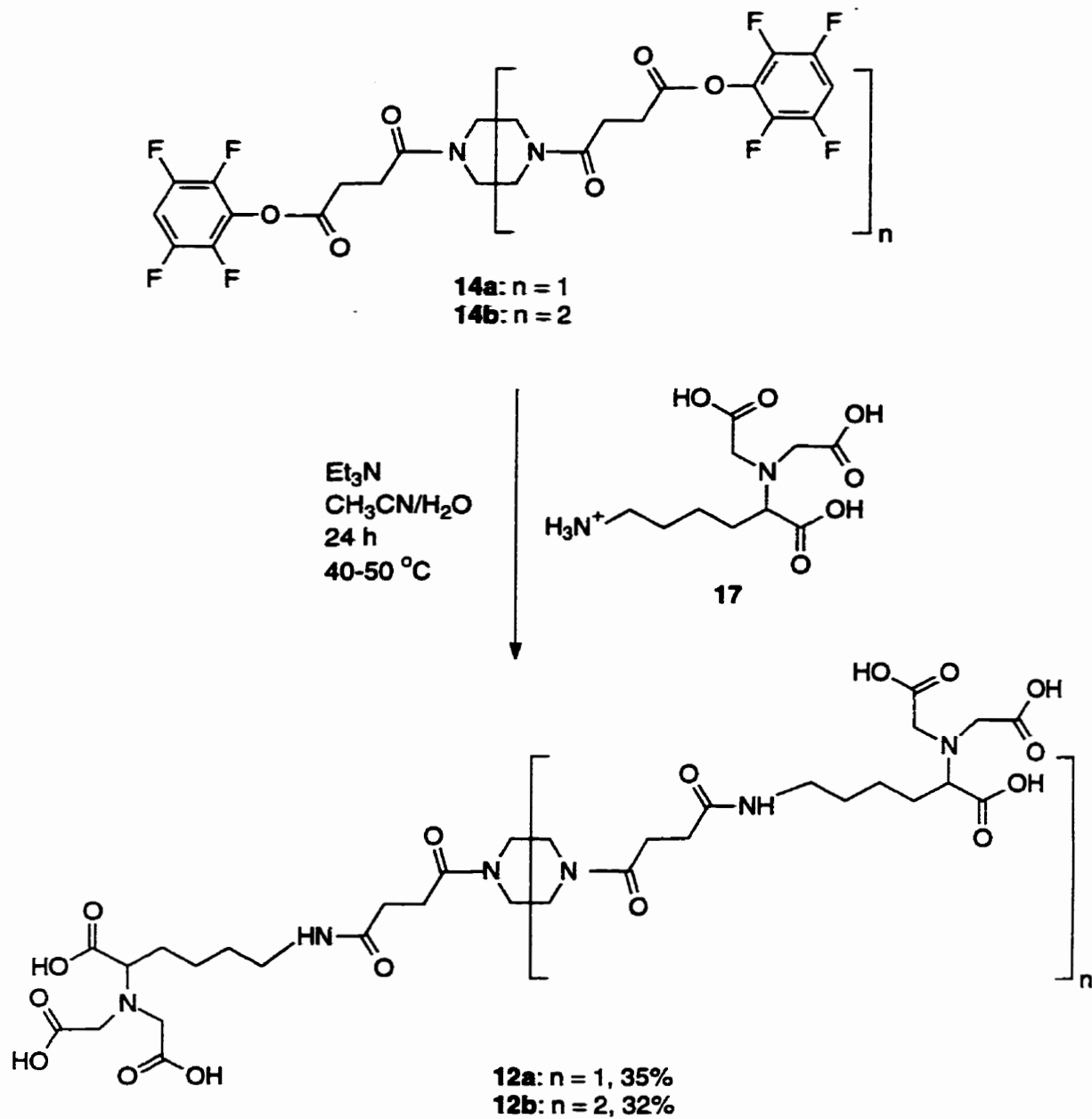
Scheme 3.10: Coupling step to final compounds **12a** and **12b**. The yields were obtained from limiting reagents **14a** and **14b**. Et₃N: triethylamine.

remove afterwards. The coupling was monitored by TLC, and the developing components were visualized by ninhydrin spray.

The purification of the final compounds **12a** and **12b** is cumbersome. After the reaction was completed, appropriate amounts of 6 M HCl were added to acidify the reaction mixtures. The desired products were expected to crystallize out from water, but no precipitations from the solution were observed. The resulting reaction mixture was concentrated to an oil using a rotatory evaporator. The solvents were removed as an azeotrope by adding water and evaporating *in vacuo*. Then the reaction residue was dried as a viscous solid. This solid was dissolved in water and the solution was adjusted to pH 9. This mixture was then applied to ion-exchange chromatography (32) and the final desired products **12a** and **12b** were collected in the last fraction subsequently. The purification procedure of products **12a** and **12b** was similar to that used in the purification of **6a** and **6b**. A summary of the experimental conditions for the synthesis of **13a** and **13b**, **14a** and **14b**, **12a** and **12b** is given in Table 3.4.

Table 3.4 Summary for experimental convergent synthesis

Compounds	Appearance	m.p. (°C)	Limiting Reagent	t (h)	T (°C)	Solvents	Yield (%)
13a	w.n.	156-158	**7a**	24	60-70	Benzene	65
13b	w.n.	126-130	**7b**	48	60-70	Benzene	45
14a	w.p.	140-142	**13a**	20	50	DMF	86
14b	w.p.	120-122	**13b**	24	50	DMF	67
12a	w.s.	170 (dec.)	**14a**	12	25	CH_3CN-H_2O	35
12b	w.s.	200 (dec.)	**14b**	20	45	CH_3CN-H_2O	32

Where, *w.n.* = white needle, *w.p.* = white powder, *w.s.* = white solid, *m.p.* = melting point in Celcius, *t* is the reaction time in hour, *T* is the reaction temperature in Celsius, the yields were calculated for pure compounds from the corresponding limiting reagents.

As before, these two final chelating agents **12a** and **12b** were identified by NMR, FTIR and MS. Figure 3.10 presents the structure (Figure 3.10A), the ^{1}H-NMR in D_2O (Figure 3.10B) and the ^{13}C-NMR spectrum (Figure 3.10C) of compound **12a**. The carbons are labelled on the left, and hydrogens are indicated on the right of Figure 3.10A. In Figure 3.10B, two peaks at δ 3.60 ppm and 3.40 ppm are assigned to the cyclic methylene groups. The signals of δ 2.58 ppm and 2.40 ppm correspond to two CH_2 groups between two amide bonds. One peak at δ 3.08 ppm is assigned to the terminal NH of the lysine side chain. The triplet peak at δ 2.80 ppm is attributed by the CH_2 which is located near to the secondary amide. The large broad peak at δ 4.20 - 4.10 ppm is attributed to the two CH_2 and one tertiary CH which are adjacent carboxylic acids. The multiplet peaks at δ1.90 and 1.60-1.40 ppm clarify the aliphatic methylene groups in the lysine side chain. In the ^{13}C-NMR spectrum of compound **12a**, there are five peaks which correspond to the carbonyl carbons in three carboxy and two amide groups. The other peaks of the ^{13}C-NMR spectrum are assigned as indicated in Figure 3.10C.

3.4 The structures of cyclic polyamides in solution characterized by temperature NMR experiments

It is evident from the NMR spectra of all the polyamides that there is restricted rotation. This phenomenon is also observed for the polyamides **1-5** used in the diffusion work (33). Here we take an interest in the characterization of amide derivatives by ^{1}H-NMR temperature experiments. It is expected, that NMR spectroscopy could make significant contributions to the problem of structural isomerism involving restricted rotation in any amide derivatives. When the barrier hindering of internal rotation is very high, as in isomers which are *cis* and *trans* with respect to a double bond, the rotamers can usually be isolated and have distinguishable NMR spectra. In some cases, where isolation is not possible, the resonance spectrum may consist of a superposition of the spectra due to the two forms in equilibrium.
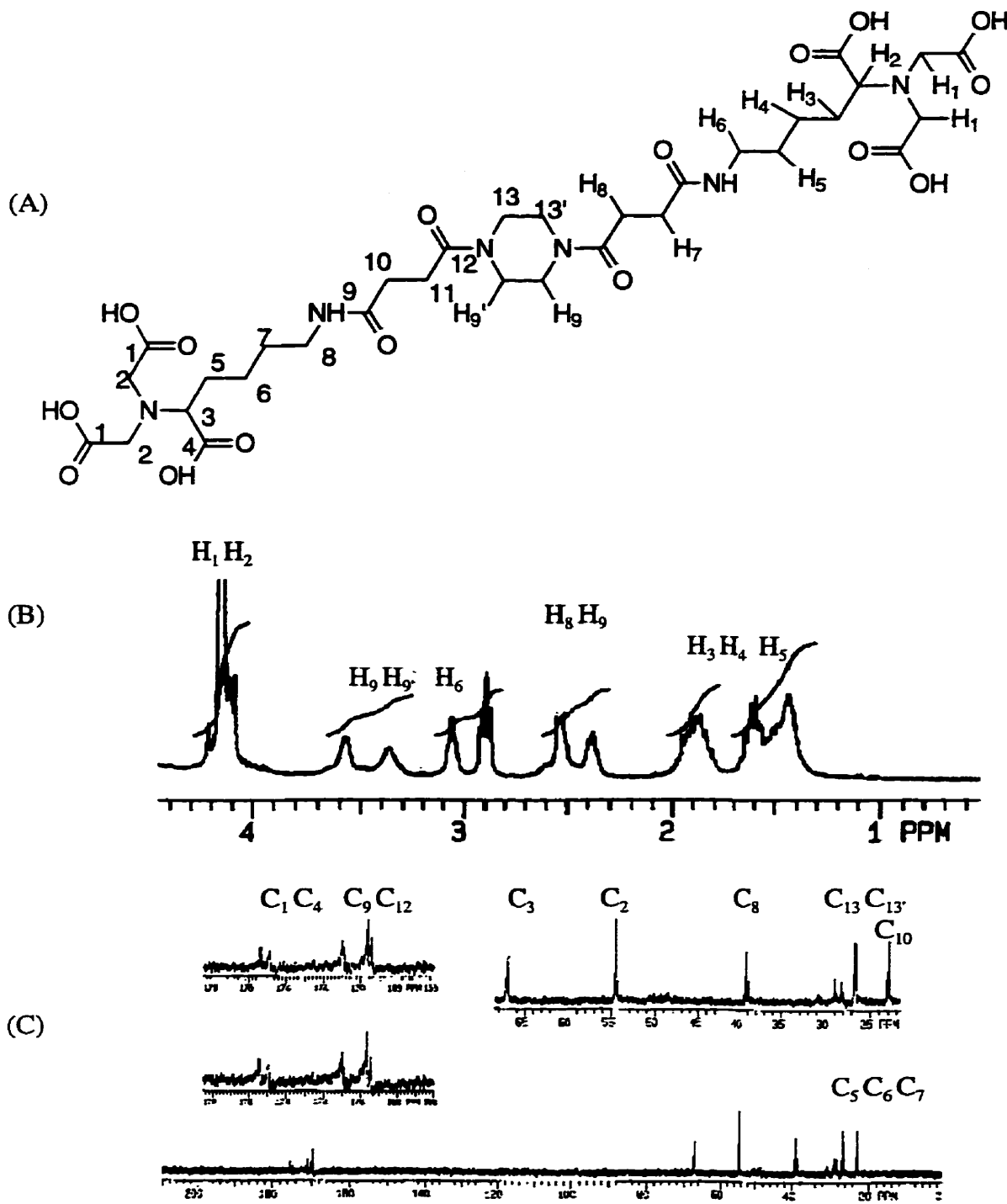
Figure 3.10: Structure (A), ^{1}H-NMR spectrum (B) and ^{13}C-NMR spectrum (C) of compound **12a**. The carbon atoms which are labelled on the left of (A) are assigned in (C), and the peaks in (C) are attributed to the hydrogens which are indicated on the right of (A).

3.4.1 Introduction and theory

According to resonance theory (34), we can assume that the C-N bond in amides have double bond character owing to the types of resonance structures as shown in Figure 3.11A. The partial double-bond character would be expected to impart a planar configuration to such a system. The barrier to hindered rotation might well be quite high but usually not so high that the *cis* and *trans* isomers can be physically separated by organic methods. NMR spectroscopy is often the tool of choice for the study of molecular dynamic properties, because the timescale of the interconversion of one isomer to the other may be slow enough to allow two separate spectra to be obtained. This specifically requires the rate of interconversion to be less than the chemical shifts between signals from the two isomers.

The *cis* and *trans* rotational isomers are not magnetically equivalent because of the shielding and deshielding effects of the amide group as illustrated in Figure 3.11B. Accordingly, the ^{1}H-NMR spectra of most amides exhibit two different signals for the sp^3 carbons bound to nitrogen. As amides in solution are heated, the rate of rotation about the (O)C-N bond increases, and eventually the two signals may coalesce to a single peak which has a frequency mid-way between the two signals observed at room temperature.

In this section, we shall discuss some of the variable temperature NMR results obtained for the isomers of the same class of compounds (**9a** and **13a**). They have partial double-bond character but different variation of piperazine diamide derivatives.

3.4.2 Variable temperature NMR of 1,4-bis(4'-amino-4'-carboxybutanoyl)-diazacyclohexane (9a)

In the ^{1}H-NMR spectrum of cyclic diamide **9a**, there is a clear splitting due to the nonequivalence of axial and equatorial protons of the methylene groups in the six member ring. The chemical shifts of the methylene groups occur between δ 3.68-3.58 ppm due to their different environments in the planar structure. The variable temperature ^{1}H-NMR spectra of two cyclic methylene hydrogens in D$_2$O of compound **9a** are illustrated in Figure 3.12 at 70°C (A), 65°C (B), 50°C (C), 35°C (D), 21°C (E). Three ^{13}C-NMR spectra of
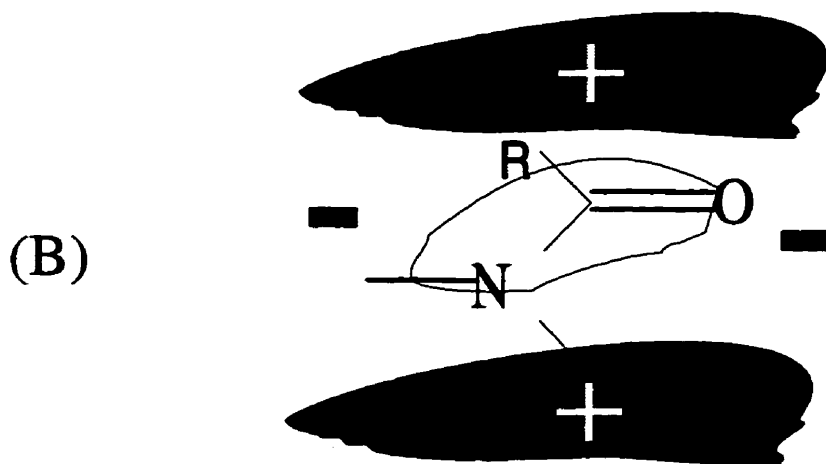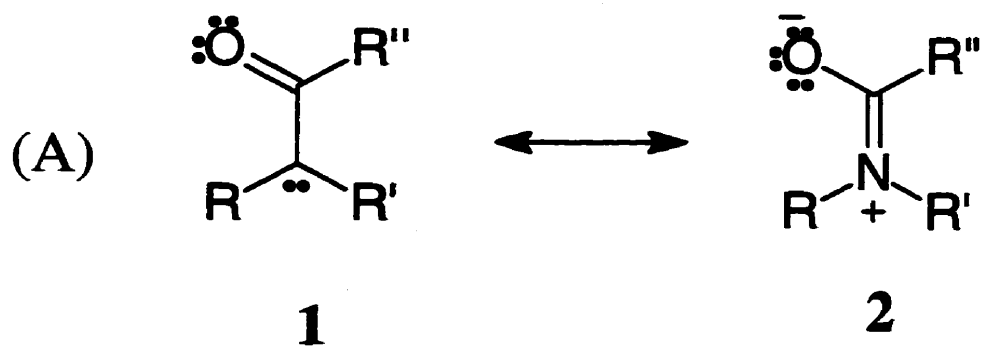
Figure 3.11: (A) Resonance structures (**1** and **2**) of amides. (B) Diagram showing shielded

(+) and deshielded (-) regions around the amide bond.
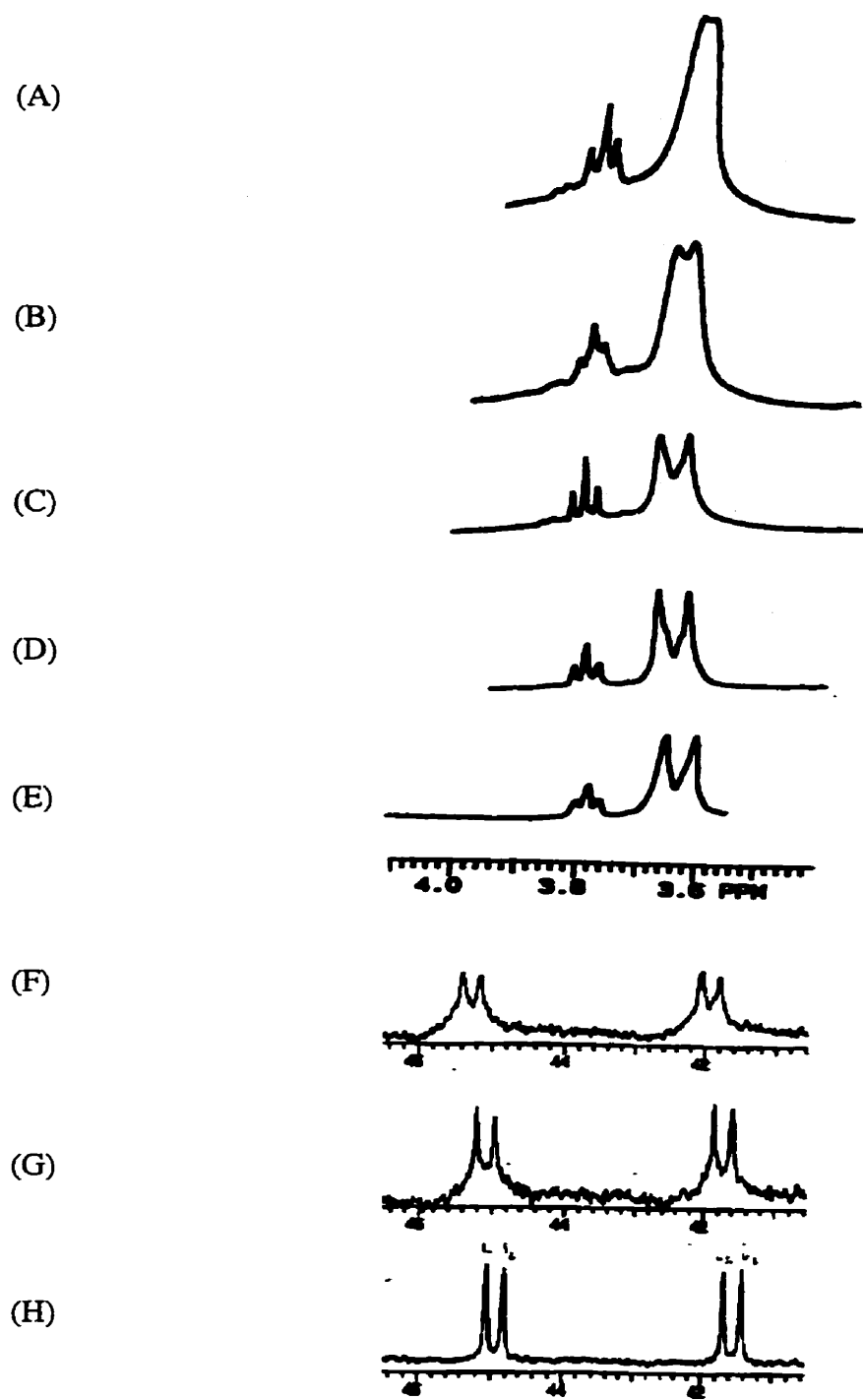
Figure 3.12: Temperature ¹H-NMR experiments of diamino acid **9a** in D₂O at 70°C (A), 65°C (B), 50°C (C), 35°C (D), 21°C (E). ¹³C-NMR spectrum of two cyclic CH₂ of compound **9a** in D₂O at 50°C (F), 35°C (G), 21°C (H).

compound **9a** in D_2O are also recorded in Figure 3.12 at 50°C (F), 35°C (G), 21°C (H).
At lower temperature, the signals of the cyclic methylene groups are separated in two peaks,
and have peak areas of 1:1 ratio. At higher temperatures, these two peaks are overlapping and
eventually coalesce when the temperature is raised to 70°C. Besides these two broad peaks,
there is a triplet peak which corresponds to the tertiary methylene (CH) hydrogen atoms with
a coupling constant of 12 Hz. The decreasing bandwith phenomenon was also observed in
the ^{13}C-NMR spectrum in D_2O of compound **9a**. The peaks of two cyclic methylene carbons
occur at δ 45.0 ppm and δ 41.6 ppm in two pairs, and overlap as the solution temperature
increases.

We applied the method described by Gutowsky to quantitatively determine the rates
of hindered internal rotations (35). This method was based on correlating decreases in signal
bandwidth with increases in exchange rates. The NMR signals are shown for two
interchanging species A and B when the populations are equal in Figure 3.12. The rate
constants for dynamic processes can be calculated from NMR spectra based on the observed
peak separation as a function of temperature in Equation 3.1

Equation 3.1 $$k = k_0 e^{-E_a / RT}$$

Where k_0 is the frequency factor and E_a is the potential barrier hindering the internal rotation.
k is the rotation rate constant and R is the universal constant (8.314 J K^{-1} mol^{-1}).

When no exchange is detectable in an exchanging system between two sites having
frequency v_A and v_B in Hz, the difference in frequency between two species (A and B) is
defined as $\delta v = v_A - v_B$. In a similar way, the observed difference in frequency between two
signals which are undergoing exchange is defined as $\delta v_e = v_{e(A)} - v_{e(B)}$. If frequency between
two signals in an exchange system is large enough for two species to be resolved at low
temperature, then the rate of exchange (k) or rate constant for exchange can be calculated as
Equation 3.2 at any temperature.

Equation 3.2 $$k = \frac{\pi}{\sqrt{2}} \sqrt{(\delta v^2 - \delta v_e^2)}$$

At the coalescence temperature, when an average signal for A and B is observed in the NMR

spectrum, Equation 3.2 then simplifies to:

Equation 3.3 $$k = \frac{\pi \delta v}{\sqrt{2}}$$

In our case, ^{1}H-NMR spectra of cyclic diamide **9a** were recorded at five temperatures as shown in Figure 3.12. These experiments clearly indicate that the coalescence temperature for amide bond rotation in **9a** is 70°C. The rate constants are calculated according to Equation 3.2 and Equation 3.3, and they are represented in Table 3.5.

Table 3.5 Rate constants for rotation of the (O)C-N bond in diamide 9a

Temperature (°C)	Rate constant k (sec^{-1}) for (O)C-N bond rotation
21	7
35	13
50	27
65	33
70	53

According to Equation 3.1, an Arrhenius plot of ln$k$ vs 1/T should produce a straight line with a slope equal to -E$_a$/R. This plot is presented in Figure 3.13 from the data in Table 3.5. The experimental data (solid dot) of Figure 3.13 are fitted by first-order regression line (solid line). The straight line results in a slope of -3.90, which corresponds to the potential barrier or activation energy E$_a$ to be 32 ± 2 kJ/mol. The fitted straight line yields a correlation coefficient of 0.97.

For comparison, the activation energy is 40 kJ/mol for dilauroyl piperazine (33) and 29 kJ/mol and 50 kJ/mol activation energy barrier for the (O)C-N bond rotation in N,N'-dimethylformamide and N,N'-dimethylacetamide, respectively (23). The E$_a$ value of 32 ± 2 kJ/mol calculated for diamide **9a** is in reasonably agreement with these systems: lower than that of N,N'-dimethylacetamide, but higher than N, N'-dimethylformamide.
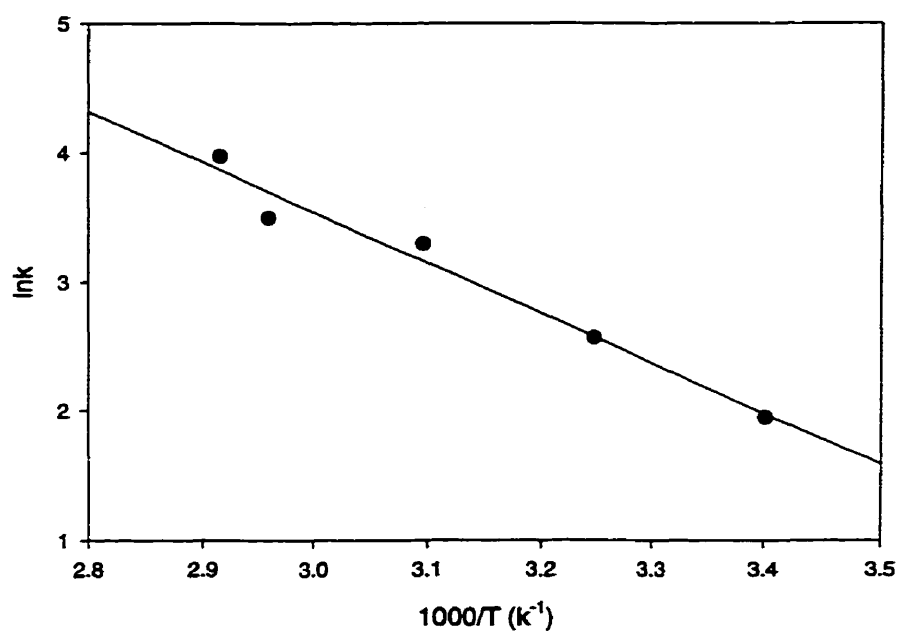
Figure 3.13: Arrhenius plot for the rate of rotation of the (O)C-N bond in compound **9a**. The experimental data are represented as solid dot (●). The solid line is the first order regression fitting and yields a slope of -3.90 with a correlation coefficient of 0.97.

3.4.3 Variable temperature NMR of 1,4-bis(3'-carboxypropanoyl)diazacyclohexane (13a)

Several representative ^{1}H-NMR spectra of cyclic diamide **13a** were recorded in DMSO-d$_6$ and shown in Figure 3.14 at five different temperatures. It is observed that the signals of cyclic methylene carbons coalesce at 55°C. Using Equation 3.2 and Equation 3.3, the rate constants of rotation are calculated and outlined in Table 3.6. The activation energy is obtained from a linear regression of ln$k$ as a function of 1/T (Figure 3.15). The value of the apparent activation barrier is 36 ± 2 kJ/mol, which indicate that the rotation of **13a** is a little bit higher than that of compound **9a**.

Table 3.6 Rate constants for the (O)C-N bond rotation in di(succinoyl)piperazine 13a

Temperature (°C)	Rate constant k (sec^{-1}) for the rotation of (O)C-N
20	13
30	27
40	33
45	47
55	70

These variable temperature ^{1}H-NMR spectra of two simple diamides **9a** and **13a**, illustrate that the amide groups make the cyclic rings fairly rigid and planar structures. The variable temperature NMR analysis of larger macrocyclic polyamides are not simple since the lines broadened in their ^{1}H-NMR spectra. However, the ^{1}H-NMR spectral data for all of our compounds support the hypothesis that the macrocyclic rings are fairly planar and rigid, because the nitrogens of amide bonds have some sp^2 hybridization characteristics. The dynamic properties of cyclic amide derivatives provided by variable ^{1}H-NMR spectra support that the macrocyclic polyamide head rings can control the shape of molecules as well as the size of molecules.

3.50   3.45   3.40   PPM35
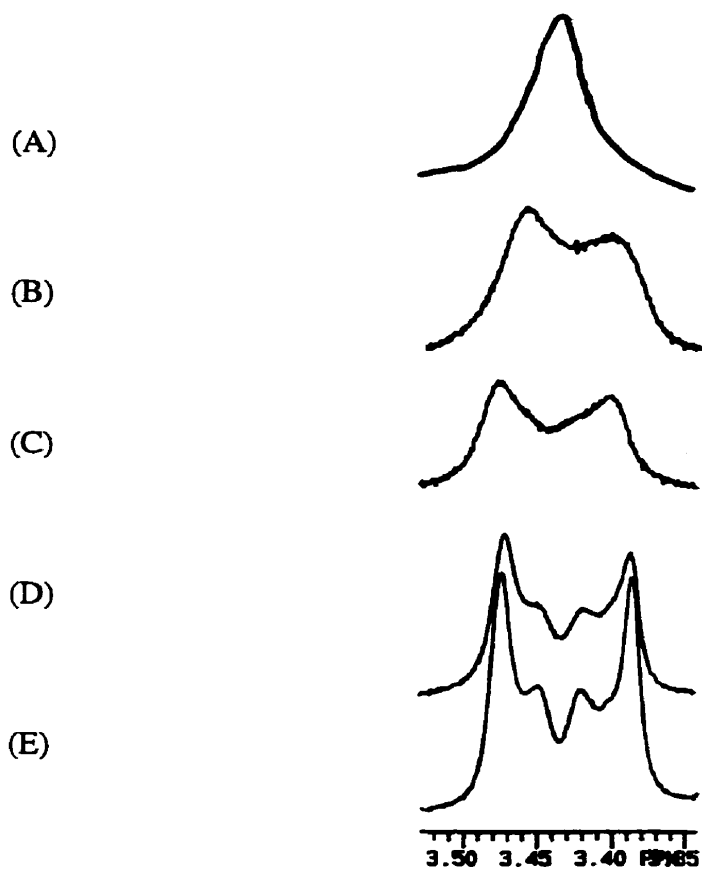
Figure 3.14: Temperature ^{1}H-NMR experiments of diamide acid **13a** at 55°C (A), 45°C (B), 40°C (C), 30°C (D), 20°C (E).
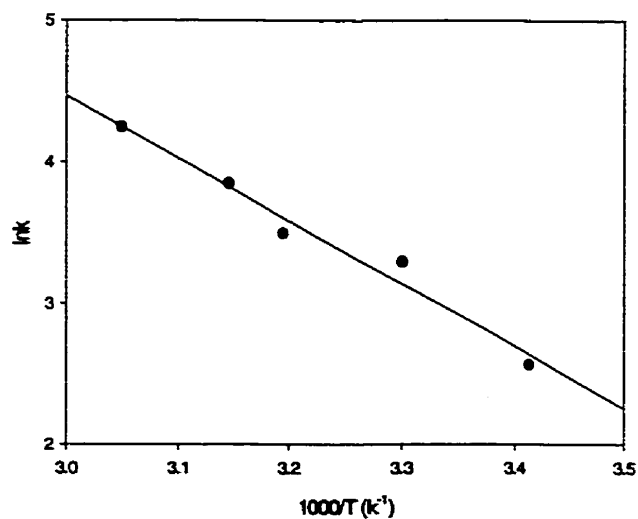
Figure 3.15: Arrhenius plot for the rate of rotation of (O)C-N bond in compound **13a**. The data points are represented as solid dots (●). The solid line is calculated as the least square with a correlation coefficient of 0.97. The straight line yields a slope of -4.42.

3.5 Summary and discussions

In summary, only compounds **13a, 16** and **17** have previously been reported in the literature. A total of twenty new compounds (**8a-e, 9a-e, 13b, 14a-b, 6a-e** and **12a-b**) including intermediates and final products, have been prepared in the course of this work. More importantly, two sets of dendritic NTA ligands were obtained through mult-step sequential and convergent strategies. The dynamic properties of representative cyclic diamides have been investigated by variable temperature ^{1}H-NMR experiments. The ^{1}H-NMR analysis shows the macrocyclic heads are fairly rigid and not freely rotated. The syntheses of these dendritic chelators are in principle straight-forward, but in practice, difficult because of solubility, ionization and completion of reactions. The strategy adopted here was to use two different pathways such as sequential and convergent routes to provide versatility.

According to the criteria which we aimed to achieve, we believe that the two different strategies proved successful. First of all, macrocyclic polyamines are selected as the central head because they are available in different sizes and provide a symmetric building block. Secondly, the polyamide ring structure is useful, since the restricted motions result in fairly planar ring structures and different sizes of macrocyclic polyamides. Thirdly, the NTA is the easiest to be derived from amino acid analogues. We successfully used protected esters of glutamic acid (Z-Glu-OBzl) and $N(\epsilon)$-benzyloxocarbonyl lysine as starting materials in each strategy. These two amino acid derivatives are commercially available, so they provided a convenient and straightforward start for the two routes to the final target ligands. The different pathways could be used to obtain shorter and longer chains. Unfortunately, the longer chain derivatives were not as easily prepared.

It is possible to improve these synthetic strategies. In the synthesis of the first set of ligands **6a-e**, more efforts are needed to increase the solubility of the intermediates in organic solvents. Even if our synthesis as outlined in Scheme 3.5 is unsuccessful, this strategy principally is better than the direct carboxylmethylation as shown in Scheme 3.4. In the case of the second set of chelating agents (**12a-b**), it is probably worthwhile to make NTA
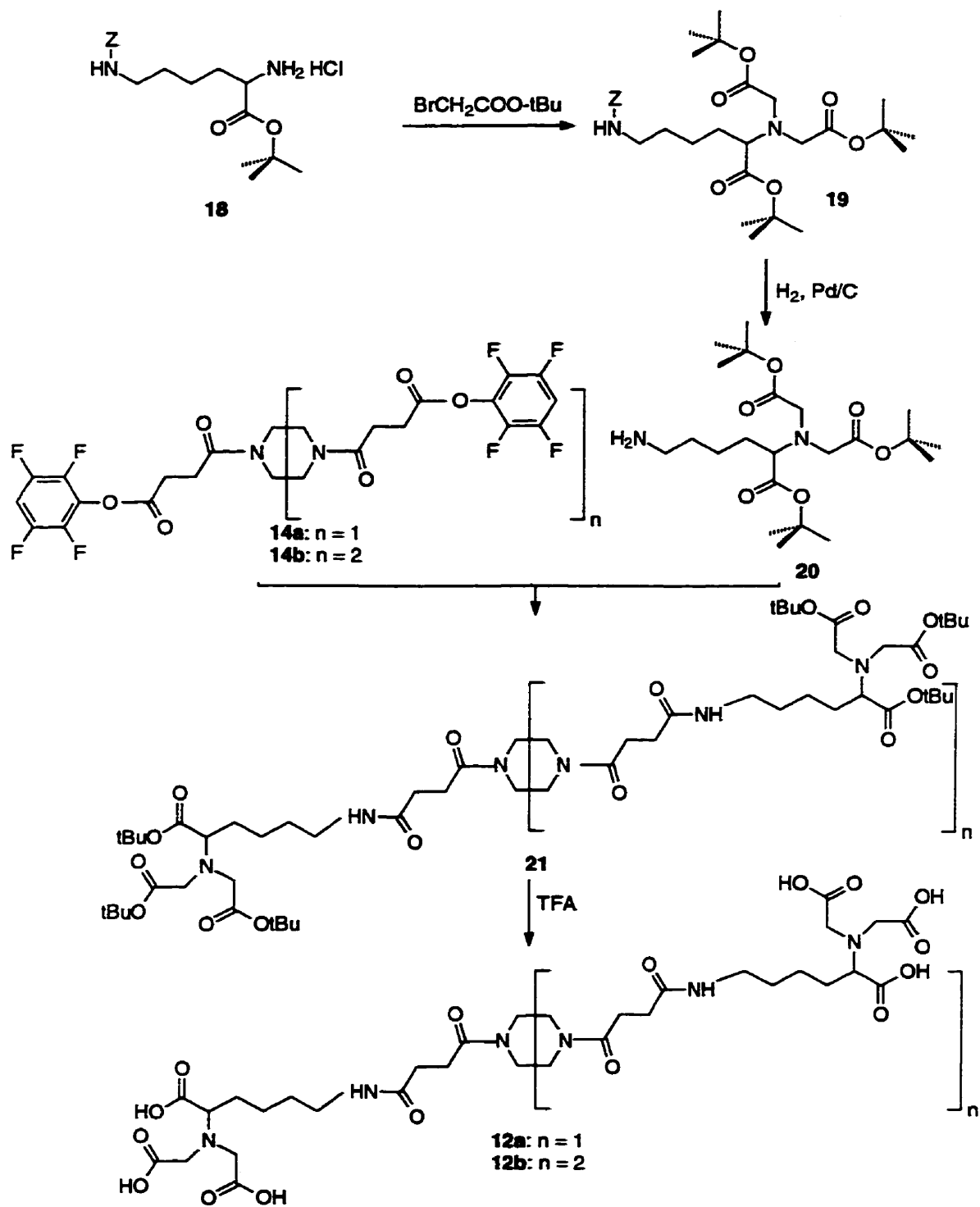
Scheme 3.11: Potential synthetic strategy for dendritic ligands containing longer linker, such as compounds **12a** and **12b**.

intermediates less polar as shown in Scheme 3.11, for example by the method which was reported recently by Dorn's group (24). Scheme 3.11 outlines a potential synthetic pathway with a different starting material (18) named as N^ϵ-benzyloxycarbonyl-L-lysine *tert*-butyl ester hydrochloride. The compound 18 may be then alkylated by *tert*-butyl bromoacetate ester and the alkylation leads to a product 19. This compound has higher solubility in organic solvents and consequently yields a product 20 through the next coupling step. Thus the compounds 20 may be coupled with TFP activated esters 14a-b, and these coupling reactions result in the formation of compounds 21a-b, which are fully *tert*-butyl esters of 12a-b. In the last step, compounds 21a-b can be cleaved with trifluoroacetic acid (TFA) and the final products 12a-b can be easily isolated by complete sonication or hydrolysis under basic conditions.

Common FTIR, ^{1}H-NMR, ^{13}C-NMR and MS spectroscopic methods have been used to characterize the desired intermediates and the final chelating agents. Particularly, fast atomic bombardment (FAB) MS spectra, which were performed by Mr. Doug Harrison, plays a critical role in the identification of those compounds containing carboxyl terminal groups under very difficult conditions. The magic conditions are varied with the different multicarboxy compounds, and will be given in the "experimental" section.

We expect that these compounds may have several potential applications (see Chapter 4 and Chapter 5). Access to appropriate ligands with multiple binding features may be a useful step in many aspects of molecular biology or cell biology and protein engineering. The formation constants for 1:1 trivalent metal complexes of NTA (typically 10^{13}) may be inadequate for *in vivo* applications, but the ability to form protein-NTA-metal-NTA-protein linkages may provide nondenaturing and readily reversible means for cross-linking two proteins, such as antibody and enzyme, for *in vitro* use (5, 36, 37). The bifunctional NTA ligands may also prove useful for tethering ternary metal complexes to proteins, as was done by Kline (37). The ability to introduce a protein-reactive substituent into any polyamino polycarboxylate chelator by the two ways described here should facilitate the identification of additional areas where an interface between coordination chemistry and protein biochemistry may bear fruit.

3.6 Experimental

3.6.1 Synthesis of dendritic chelating agents

Piperazine, 1,4,7-triazacyclononane, 1,4,7,10-tetraazacyclododecane, hexacylen trisulphate, 2,3,5,6-tetrafluorophenol (TFP-OH), dicyclohexylcarbodiimide (DCC), bromoacetic acid, and succinic anhydride were obtained from Aldrich Chemical Co. 1,4,7,10,13-Pentaazacyclopentadecane pentahydrochloride was purchased from Parish Chemical Co. TBTU and Z-Glu-OBzl were from Novabiochem. $N(\varepsilon)$-Z-L-Lysine was obtained from Fluka. All solvents are distilled in glass or reagent grade and were used without purification. Column chromatography was performed from 230-400 mesh silica gel supplier. Preparative TLC Kieselgel F_{254} plates were obtained from EM Separation Technology. Melting points (uncorrected) were determined using a Thomas-Hoover model capillary melting points apparatus. Proton and carbon-13 NMR spectra were recorded on a Varian Gemini-300 spectrometer operating at 300 MHz (^{1}H) and 75 MHz (^{13}C). Infrared spectra were recorded as KBr pellets on a Perkin Elmer System 2000 FTIR. Fast atom bombardment (FAB) mass spectra were obtained on a Finigan MAT 8320 mass spectrometer. Reactions were monitored by TLC (precoated plates 0.25 mm silica gel 60 F_{254}) and visualized by UV (Z and benzyl groups), ninhydrin (amino group), bromocresol blue (acids and bases), or iodine vapour.

1,4-Bis[4'-(N-benzyloxycarbonyl)amino-4'-benzyloxycarbonylbutanoyl]diazacyclohexane (8a)

Z-Glu-OBzL (2.5 g, 6.0 mmol) and TBTU (1.9 g, 6.0 mmol) were dissolved in 4 mL dimethylformamide (DMF), followed by the addition of triethylamine (TEA) (0.8 mL, 6.0 mmol). To this solution, a warm solution of piperazine (0.206 g, 2 mmol in 2 mL DMF) was added. After stirring overnight, the reaction mixture was evaporated to dryness. The viscous residue was dissolved in 80 mL chloroform, then washed twice with 5% $NaHCO_3$, saturated NaCl, and H_2O, sequentially. The organic layer was dried with anhydrous Na_2SO_4, and the solvent was removed by rotary evaporator. The residue was subjected to silica gel column chromatography, and the desired product was isolated by preparative TLC. The fourth band

was collected (R_f = 0.32, developed by a (5:2:5:1) mixture of ethyl acetate, chloroform, hexane, and methanol). The product was obtained as a white solid in 86% yield, mp 39–42°C. IR 3300 (NH stretch), 3033 (CH stretch for aromatic compound), 2947 (CH stretch for alkane), 1721 (C=O stretch for ester), 1636 (C=O stretch for tertiary amide), 1530 (C=C stretch), 1455 (CH$_2$ deformation), 1215 (C-O-C stretch), 699 (CH out of plane deformation) cm^{-1}; ^{1}H-NMR (CDCl$_3$) δ 7.34–7.25 (bs, 20H, $C_6H_5CH_2$), 5.70 (d, J = 7.5 Hz, 2H, CHNHCO), 5.16 (q, J = 2.5 Hz, 4H, NCOOCH_2C$_6$H$_5$), 5.06 (s, 4H, C$_6$H$_5CH_2$OCO), 4.45 (t, J = 6.5 Hz, 2H, CH$_2CH$COO), 3.48 (bs, 4H, OCNCH_2CH_2NCO), 3.20 (bs, 4H, OCNCH_2CH_2NCO, isomer), 2.26 (t, J = 6.5 Hz, 4H, COCH_2CH$_2$), 2.05 (q, J = 3.5 Hz, 4H, CH$_2CH_2$CH); ^{13}C-NMR δ 171.67, 170.42, 156.80, 136.27, 135.30, 128.69, 128.47, 128.16, 67.35, 67.07, 53.68, 45.04, 41.43, 29.08, 27.56; HRMS (FAB, oxalic acid/glycerol/thioglycerol) m/z Found: 792.3505 [M]$^+$, Calcd for: C$_{44}$H$_{48}$N$_4$O$_{10}$ 792.3370 [M]$^+$.

1,4,7-Tris[4'-N-benzyloxycarbonylamino-4'-benzyloxycarbonylbutanoyl]triazacyclononane (**8b**)

Compound **8b** was obtained as a white solid from 1,4,7-triazacyclononane **7b** (0.10 g, 0.80 mmol) and Z-Glu-OBzl (1.35 g, 3.60 mmol), TBTU (1.15 g, 3.60 mmol) according to the procedure of **8a** in 65% yield, mp 40–43°C. IR 3305 (NH stretch), 3031 (CH stretch for aromatic compound), 2948 (CH stretch for alkane), 1725 (C=O stretch for ester), 1634 (C=O stretch for tertiary amide), 1528 (C=C stretch), 1458 (CH$_2$ deformation), 1215 (C-O-C stretch), 700 (CH out of plane deformation) cm^{-1}; ^{1}H-NMR (CDCl$_3$) δ 7.33–7.25 (bs, 30H, $C_6H_5CH_2$), 6.01 (d, J = 8.1 Hz, 3H, CHNHCO), 5.15 (m, J = 2.0 Hz, 6H, C$_6$H$_5CH_2$OCON), 5.05 (s, 6H, C$_6$H$_5CH_2$OCO), 4.38 (t, J = 7.5 Hz, 3H, CH$_2CH$COO), 3.64 (bs,3H, OCNCH_2CH_2NCO), 3.30 (bs, 9H, OCNCH_2CH_2NCO, due to isomer), 2.25 (bs, 6H, COCH_2CH$_2$), 1.95 (bs, 6H, COCH$_2CH_2$CH); ^{13}C-NMR (CDCl$_3$) δ 173.35, 172.23, 158.12, 136.27, 128.80, 128.56, 128.33, 67.31, 67.12, 54.01, 50.90, 46.01, 30.04, 26.53; HRMS (FAB, glycerol/thioglycerol/oxalic acid) m/z Found: 1188.5167 [M]$^+$, Calcd for: C$_{66}$H$_{72}$N$_6$O$_{15}$ 1188.5056 [M]$^+$.

1,4,7,10-Tetrakis[4'-(N-benzyloxycarbonyl)amino-4'-benzyloxycarbonylbutanoyl]-tetraazacyclododecane (**8c**)

Compound **8c** was obtained from cyclen or 1,4,7,10-tetraazacyclododecane (**7c**, 0.043 g, 0.24 mmol) and Z-Glu-OBzl (0.54 g, 1.44 mmol), TBTU (0.46 g, 1.44 mmol) according to the procedure of **8a** as a white solid in 44% yield, mp 60-62°C. IR 3310 (NH stretch), 3023 (CH stretch for aromatic compound), 2946 (CH stretch for alkane), 1720 (C=O stretch for ester), 1638 (C=O stretch for tertiary amide), 1533 (C=C stretch), 1456 (CH$_2$ deformation), 1205 (C-O-C stretch), 698 (CH out of plane deformation) cm^{-1}; ^{1}H-NMR (CDCl$_3$) δ 7.33-7.25 (bs, 40H, *C$_6$H$_5$CH$_2$*), 6.04 (bs, 4H, CH*NH*CO), 5.15 (m, J = 2 Hz, 8H, *C$_6$H$_5$CH$_2$*OCON), 5.05 (s, 8H, C$_6$H$_5$*CH$_2$*OCO), 4.43 (b, 4H, CH$_2$*CH*COO), 3.71-3.13 (two bs, 16H, OCN*CH$_2$CH$_2$*NCO), 2.50 (b, 8H, CO*CH$_2$*CH$_2$), 1.95 (b, 8H, COCH$_2$*CH$_2$*CH); ^{13}C-NMR (CDCl$_3$) δ 172.47, 171.85, 156.48, 136.23, 128.88, 128.42, 128.21, 67.35, 67.03, 53.49, 49.68, 38.68, 29.77, 26.89; HRMS (FAB, glycerol/3-nitrobenzylalcohol/oxalic acid) m/z Found: 1584.6812 [M]$^+$, Calcd for: C$_{88}$H$_{96}$N$_8$O$_{20}$ 1584.6741 [M]$^+$.

1,4,7,10,13-Pentaazacyclopentadecane (**7d**)

Pentaaza-15-crown-5 pentahydrochloride (0.17 g) was dissolved in 1 mL 0.1 M HCl, to which a large excess of 6M NaOH was added. The solution was extracted with chloroform (40 mL × 4) and dried by anhydrous Na$_2$SO$_4$. Removal of the solvent gave **7d** in 75% yield.

1,4,7,10,13-Pentakis[4'-(N-benzyloxycarbonyl)amino-4'-benzyloxycarbonylbutanoyl]-pentaazacyclopentadecane (**8d**)

Compound **8d** was prepared as a white solid from 1,4,7,10,13-pentaazacyclopentadecane (**7d**, 0.06 g, 0.28 mmol) and Z-Glu-OBzl (0.77 g, 2.06 mmol), TBTU (0.66 g, 2.06 mmol) according to the procedure of **8a** as a white solid in 38% yield, mp 56-58°C. IR 3305 (NH stretch), 3030 (CH stretch for aromatic compound), 2948 (CH stretch for alkane), 1719 (C=O stretch for ester), 1630 (C=O stretch for tertiary amide), 1528 (C=C stretch), 1456 (CH$_2$ deformation), 1210 (C-O-C stretch), 697 (CH out of plane deformation) cm^{-1}; ^{1}H-NMR (CDCl$_3$) δ 7.35-7.25 (bs, 50H, *C$_6$H$_5$CH$_2$*), 5.96 (d, J = 7.8 Hz, 5H, CH *NH*CO), 5.15 (b, 10H,

was introduced to the flask at room temperature under normal pressure. The reaction progress was monitored by TLC, visualized by illumination with UV light. The catalyst was filtered off and washed with water. The filtrate was dried *in vacuo*. The resulting precipitate was redissolved in hot ethanol, and crystallizes at 0°C. The crystals were filtered off and dried *in vacuo* in 90% yield, mp 168-170°C. IR 3435 (NH and OH stretch), 2934 (CH stretch for alkane), 1716 (C=O stretch for carboxylic acid), 1630 (C=O stretch for tertiary amide), 1530 (NH_3^+ deformation), 1443 (CH_2 deformation), 1427 (COO⁻ sym stretch) cm⁻¹; ¹H NMR (D_2O) δ 3.74 (t, J = 7.5 Hz, 2H, CH_2CHCOO), 3.60-3.46 (two bs, 8H, CH_2CH_2NCO), 2.48 (t, J = 6.5 Hz, 4H, $COCH_2CH_2$), 1.99 (q, J = 6.0 Hz, 4H, CH_2CH_2CH); ¹³C-NMR (D_2O) δ 174.11, 173.03, 54.18, 45.07, 41.72, 28.35, 25.21; HRMS (FAB, oxalic acid/glycerol) m/z Found: 345.1801 [M+H]⁺, Calcd for: $C_{14}H_{24}N_4O_6$ 345.1691 [M+H]⁺.

1,4,7-Tris(4'-amino-4'-carboxybutanoyl)triazacyclononane (9b)

Compound **9b** was obtained from **8b** (0.30 g, 0.25 mmol) according to the procedure of **9a** as a white solid, which was deliquescent, but could be recrystallized from hot ethanol in 86% yield, mp 210°C (dec.). IR 3436 (NH and OH stretch), 2936 (CH stretch for alkane), 1723 (C=O stretch for carboxylic acid), 1638 (C=O stretch for tertiary amide), 1445 (NH_3^+ deformation), 1429 (COO⁻ sym stretch) cm⁻¹; ¹H NMR (D_2O) δ 3.69 (t, J = 7.5 Hz, 3H, CH_2CHCOO), 3.67-3.37 (two bs, 12H, $OCNCH_2CH_2NCO$), 2.42 (t, J = 6.5 Hz, 6H, $COCH_2CH_2$), 2.02 (q, J = 6.0 Hz, 6H, CH_2CH_2CH); ¹³C-NMR (D_2O) δ 175.27, 174.54, 50.48, 48.63, 44.10, 29.49, 25.73; HRMS (FAB, glycerol/oxalic acid) m/z Found: 517.2690 [M+H]⁺, Calcd for: $C_{21}H_{36}N_6O_9$ 517.2544 [M+H]⁺.

1,4,7,10-Tetrakis(4'-amino-4'-carboxybutanoyl)tetraazacyclododecane (9c)

Compound **9c** was obtained from **8c** according to the procedure of **9a** as a white solid in 82% yield, mp 210°C (dec.). IR 3432 (NH and OH stretch), 2933 (CH stretch for alkane), 1720 (C=O stretch for carboxylic acid), 1634 (C=O stretch for tertiary amide), 1442 (NH_3^+ deformation), 1430 (COO⁻ sym stretch) cm⁻¹; ¹H NMR (D_2O) δ 3.67 (t, J = 7.4 Hz, 4H, CH_2CHCOO), 3.63-3.43 (two b, 16H, $OCNCH_2CH_2NCO$), 2.44 (t, J = 6.5 Hz, 8H,

COC*H₂*CH₂), 2.05 (q, J = 6.0 Hz, 8H, CH₂*CH₂*CH); ¹³C-NMR (D₂O) δ 175.02, 174.24, 51.42, 48.63, 45.67, 29.49, 25.60; HRMS (FAB, glycerol/oxalic acid) m/z Found: 689.2305 [M+H]⁺, Calcd for: $C_{28}H_{48}N_8O_{12}$ 689.3392 [M+H]⁺.

1,4,7,10,13-Pentakis(4'-amino-4'-carboxybutanoyl)pentaazacyclopentadecane (9d)

Compound **9d** was obtained from **8d** (0.30 g, 0.15 mmol) according to the procedure of **9a** as white solid in 80% yield, mp 200°C (dec.). IR 3430 (NH and OH stretch), 2931 (CH stretch for alkane), 1716 (C=O stretch for carboxylic acid), 1640 (C=O stretch for tertiary amide), 1448 (NH₃⁺ deformation), 1430 (COO⁻ sym stretch) cm⁻¹; ¹H-NMR (D₂O) δ 3.67 (t, J = 7.2 Hz, 5H, CH₂*CH*COO), 3.63-3.43 (two b, 20H, OCN*CH₂CH₂*NCO), 2.42 (t, J = 6.5 Hz, 10H, COC*H₂*CH₂), 2.01 (q, J = 6.4 Hz, 10H, CH₂*CH₂*CH); ¹³C-NMR (D₂O) δ 175.07, 174.20, 50.85, 47.94, 45.63, 29.20, 25.23; HRMS (FAB, glycerol/oxalic acid) m/z Found: 861.4325 [M+H]⁺, Calcd for: $C_{35}H_{60}N_{10}O_{15}$ 861.4240 [M+H]⁺.

1,4,7,10,13,16-Hexakis(4'-amino-4'-carboxybutanoyl)hexaazacyclooctadecane (9e)

Compound **9e** was obtained from **8e** (0.11 g, 0.05 mmol) according to the procedure of **9a** as a white solid in 80% yield, mp 200°C (dec.). IR 3436 (NH and OH stretch), 2933 (CH stretch for alkane), 1717 (C=O stretch for carboxylic acid), 1635 (C=O stretch for tertiary amide), 1447 (NH₃⁺ deformation), 1426 (CH₂ deformation) cm⁻¹; ¹H NMR (D₂O) δ 3.78 (t, J = 7.5 Hz, 6H, CH₂*CH*COO), 3.56-3.46 (two b, 24H, OCN*CH₂CH₂*NCO), 2.64 (b, 12H, COC*H₂*CH₂), 2.02 (b, 12H, CH₂*CH₂*CH); ¹³C-NMR (D₂O) δ 174.68, 173.89, 53.87, 50.99, 46.09, 28.45, 25.54; HRMS (FAB, glycerol/oxalic acid) m/z Found: 1033.5458 [M+H]⁺, Calcd for: $C_{42}H_{72}N_{12}O_{18}$ 1033.5088 [M+H]⁺.

1,4-Bis[4'-N,N-di(carboxymethyl)amino-4'-carboxylbutanoyl)]diazacyclohexane (6a)

A solution of bromoacetic acid (0.24 g, 1.72 mmol) in 2 mL NaOH (1.5 M) was cooled to 0°C and was added dropwise to a solution of 0.13 g **9a** (0.38 mmol) in 2 mL of NaOH (2 M). The pH of the resulting solution was adjusted to 12. Then the reaction mixture was stirred at 45°C for seven days. The pH was maintained in the range of 11-12 by periodic addition

of 2 M NaOH. The reaction progress was monitored by TLC. After cooling to room temperature, the reaction was evaporated to dryness under vacuum to give a white solid. The solid was redissolved in water, pH adjusted to 10, and applied to a Bio-Rad AG1-X4 anion-exchange column (formate ion). The column was eluted successively with water, 4M formic acid and 5 M formic acid. The fraction containing the desired product determined by TLC was applied to a second Bio-Rad AG1-X4 anion-exchange column that was eluted with water, 5 M formic acid, 6 M formic acid. The desired product was eluted slowly in the 5 M formic acid fractions and these fractions were combined, evaporated to dryness under vacuum, and redissolved in 4 M HCl. The resulting solution was again evaporated to dryness, and the residue was repeatedly redissolved in water. The solution was dried to form a solid in 56% yield, mp 210°C (dec.). IR 3436 (OH stretch), 1733 (C=O stretch for carboxylic acid), 1631 (C=O stretch for tertiary amide), 1365 (N-C stretch) cm^{-1}; ^{1}H-NMR (D$_2$O) δ 3.89 (bs, 10H, NCH$_2$COOH and CH$_2$CHCOOH), 3.65-3.43 (two bs, 8H, OCNCH$_2$CH$_2$NCO), 2.54 (bs, 4H, NCOCH$_2$CH$_2$), 2.06 (bs, 4H, CH$_2$CH$_2$CH); ^{13}C-NMR (D$_2$O) δ 176.63, 175.28, 171.16, 170.08, 65.68, 54.06, 49.23, 40.57, 30.34, 22.47; HRMS (FAB, glycerol/oxalic acid) m/z Found: 599.1042 [M+H+Na]$^+$, Calcd for: C$_{22}$H$_{32}$N$_4$O$_{14}$ 599.1813 [M+H+Na]$^+$.

1,4,7-Tris[4'-N,N-di(carboxymethyl)amino-4'-carboxybutanoyl]triazacyclononane (**6b**)

Compound **6b** was obtained from **9b** (0.02 g, 0.04 mmol) and bromoacetic acid (0.034 g, 0.25 mmol) according to the procedure of **6a** as a white solid in 48% yield, mp 210°C (dec.) IR 3435 (OH stretch), 1735 (C=O stretch for carboxylic acid), 1630 (C=O stretch for tertiary amide), 1367 (N-C stretch) cm^{-1}; ^{1}H-NMR (D$_2$O) δ 3.92-3.74 (two b, 15H, NCH$_2$COOH and CH$_2$CHCOOH), 3.58-3.35 (two b, 12H, OCNCH$_2$CH$_2$NCO), 2.54 (b, 6H, NCOCH$_2$CH$_2$), 2.05 (b, 6H, CH$_2$CH$_2$CH); ^{13}C-NMR (D$_2$O) δ 175.29, 174.97, 169.82, 66.57, 60.88, 54.66, 48.66, 30.43, 24.52; HRMS (FAB, glycerol/oxalic acid) m/z Found: 865.2821 [M+H]$^+$, Calcd for: C$_{33}$H$_{48}$N$_6$O$_{21}$ 865.2873 [M+H]$^+$.

1,4,7,10-Tetrakis[4'-N,N-di(carboxymethyl)amino-4'-carboxybutanoyl]-tetraazacyclododecane (**6c**)

Compound **6c** was obtained from **9c** (0.056 g, 0.081 mmol) and bromoacetic acid (0.10 g, 0.73 mmol) according to the procedure of **6a** as white solid in 43% yield, mp 220°C (dec.). IR 3430 (OH stretch), 1723 (C=O stretch for carboxylic acid), 1634 (C=O stretch for tertiary amide), 1387 (N-C stretch) cm^{-1}; ^{1}H NMR (D$_2$O) δ 3.85-3.45 (two b, 36H, N*CH$_2$*COOH, CH$_2$*CH*COOH and OCN*CH$_2$CH$_2$*NCO), 2.54 (b, 8H, NCOC*H$_2$*CH$_2$), 2.01 (b, 8H, CH$_2$C*H$_2$*CH); ^{13}C-NMR (D$_2$O) δ 175.43, 174.25, 171.04, 169.32, 66.81, 57.90, 54.95, 47.44, 29.57, 24.66; HRMS (FAB, oxalic acid) m/z Found: 1153.3538 [M+H]$^+$, Calcd for: C$_{44}$H$_{64}$N$_8$O$_{28}$ 1153.3830 [M+H]$^+$.

1,4,7,10,13-Pentakis[4'-N,N-di(carboxymethyl)amino-4'-carboxybutanoyl]-pentaazacyclopentadecane (**6d**)

Compound **6d** was obtained from **9d** (0.07 g, 0.08 mmol) and bromoacetic acid (0.12 g, 0.88 mmol) according to the procedure of **6a** as a white solid in 38% yield, mp 220°C (dec.). IR 3433 (OH stretch), 1730 (C=O stretch for carboxylic acid), 1637 (C=O stretch for tertiary amide), 1364 (N-C stretch) cm^{-1}; ^{1}H-NMR (D$_2$O) δ 3.86-3.45 (two b, 45H, N*CH$_2$*COOH, CH$_2$*CH*COOH and OCN*CH$_2$CH$_2$*NCO), 2.70 (b, 10H, NCOC*H$_2$*CH$_2$), 2.01 (b, 10H, CH$_2$C*H$_2$*CH); ^{13}C-NMR (D$_2$O) δ 175.22, 174.81, 171.04, 170.20, 66.47, 64.84, 58.46, 54.66, 48.63, 30.42, 26.51; HRMS (FAB, glycerol/oxalic acid) m/z Found: 1441.3256 [M+H]$^+$, Calcd for: C$_{55}$H$_{80}$N$_{10}$O$_{35}$ 1441.4788 [M+H]$^+$.

1,4,7,10,13,16-Hexakis[4'-N,N-di(carboxymethyl)amino-4'-carboxybutanoyl]-hexaazacyclooctadecane (**6e**)

Compound **6e** was obtained from **9e** (0.023 g, 0.022 mmol) and bromoacetic acid (0.04 g, 0.30 mmol) according to the procedure of **6a** as a white solid in 33% yield, mp 230°C (dec.). IR 3430 (OH stretch), 1729 (C=O stretch for carboxylic acid), 1628 (C=O stretch for tertiary amide), 1360 (N-C stretch) cm^{-1}; ^{1}H-NMR (D$_2$O) δ 3.86-3.46 (two b, 54H, N*CH$_2$*COOH, CH$_2$*CH*COOH and OCN*CH$_2$CH$_2$*NCO), 2.72 (b, 12H, NCOC*H$_2$*CH$_2$), 2.01 (b, 12H,

CH_2CH_2CH); ^{13}C-NMR (D_2O) δ 175.22, 174.81, 171.02, 169.56, 66.46, 65.82, 57.43, 54.23, 48.65, 31.44, 27.51; HRMS (FAB, glycerol/oxalic acid) m/z Found: 1729.5821 [M+H]$^+$, Calcd for: $C_{66}H_{96}N_{12}O_{42}$ 1729.5745 [M+H]$^+$.

1,4-Bis(3'-carboxypropanoyl)diazacyclohexane (13a)

Piperazine (0.87 g, 10 mmol) was dissolved in 10 mL of benzene and heated to 60-70 °C. Succinic anhydride (2.10 g, 20 mmol) in 20 mL benzene was added at this temperature and then the solution was refluxed for 48 hours. After this period, the benzene was removed under vacuum. The product **13a** was purified by crystallization from ethanol in 90% yield, mp 156.6-158.5°C. IR 3030 (OH stretch), 1720 (C=O stretch for carboxylic acid), 1600 (C=O stretch for tertiary amide), 1490 (CH_2 deformation) cm^{-1}; ^1H-NMR (D_2O) δ 3.62-3.48 (t, at room temperature; bs, at 55 °C, due to the existence of rotamers. 8H, OCNCH_2CH_2NCO), 2.66 (deformed t, J = 7.5 Hz, 4H, NCOCH_2CH$_2$), 2.56 (deformed t, J = 7.5 Hz, 4H, CH$_2CH_2$COOH); ^{13}C-NMR (DMSO) δ 174.28, 170.28, 52.36, 44.49, 29.29, 27.73; HRMS (FAB, oxalic acid/glycerol) m/z Found: 287.1646 [M+H]$^+$, Calcd for: $C_{12}H_{18}N_2O_6$ 287.1165 [M+H]$^+$.

1,4,7-Tris(3'-carboxypropanoyl)triazacyclononane (13b)

Compound **13b** was prepared from 1,4,7-triazacyclononane (**7b**) (0.14 g, 1.08 mmol) and succinic anhydride (0.33 g, 3.24 mmol) according to the procedure of **13a** in 85 % yield as a white solid, mp 126-130°C. IR 3010 (OH stretch), 1718 (C=O stretch for carboxylic acid), 1602 (C=O stretch for tertiary amide), 1486 (CH_2 deformation) cm^{-1}; ^1H-NMR (DMSO) δ 3.68-3.38 (two b, 12H, OCNCH_2CH_2NCO, conformational isomer), 2.58 (t, J = 7.5 Hz, 6H, NOCCH_2CH$_2$), 2.46 (t, J = 6.0 Hz, 6H, OCCH$_2CH_2$COOH); ^{13}C-NMR (DMSO) δ 174.08, 170.18, 52.12, 40.38, 29.19, 27.63; HRMS (FAB, oxalic acid/glycerol) m/z Found: 430.1468 [M+H]$^+$, Calcd for: $C_{18}H_{27}N_3O_9$ 430.1747 [M+H]$^+$.

1,4-Bis[3'-(2,3,5,6-tetrafluophenoxycarbonyl)-propanoyl]diazacyclohexane (14a)

To a stirred solution (0.28 g, 0.98 mmol) of compound **13a** in 10 mL of dimethylformamide

(DMF) under argon was added 0.41 g (2.50 mmol) of 2,3,5,6-tetrafluorophenol (TFP-OH) at 50°C. A solution of 0.45 g (2.04 mmol) dicyclohexylcarbodiimide (DCC) in 10 mL DMF was added dropwise at this temperature. The reaction was stirred overnight, and the solution was cooled to room temperature. The white precipitate of dicyclohexylurea was filtered out, and the solvent of the filtrate was removed under vacuum. The residue of reaction was triturated with 15 mL of 1:1 acetonitrile/ethyl acetate. A white solid was collected by vacuum filtration in 86% yield, mp140-142°C. IR 3422, 3086 (CH stretch for aromatic compound), 2970, 2930, (CH stretch), 1778 (C=O stretch for ester), 1696 (C=C stretch), 1651 (C=O stretch for tertiary amide), 1485, 1451 (CH$_2$ deformation), 1216 (C-F stretch), 851 (CH out of plane deformation)cm^{-1}; ^{1}H-NMR (CDCl$_3$) δ 6.98 (m, J = 4.7 Hz, 2H, C$_6$HF$_4$), 3.76-3.52 (two m, J = 5.6 Hz, 8H, CONCH$_2$CH$_2$NCO, conformational isomer), 3.08 (t, J = 5.5 Hz, 4H, NCOCH$_2$CH$_2$COO), 2.80 (t, J = 6.0 Hz, 4H, NCOCH$_2$CH$_2$COO); ^{13}C-NMR (CDCl$_3$) δ 173.19, 172.02, 135.20, 135.08, 128.56, 48.32, 41.13, 30.31, 26.39; HRMS (EI) m/z Found: 582.1040 [M]$^+$, Calcd for: C$_{24}$H$_{18}$N$_2$F$_8$O$_6$ 582.1037 [M]$^+$.

1,4,7-Tris[3'-(2,3,5,6-tetrafluorophenoxycarbonyl)propanoyl]triazacyclononane (**14b**)
Compound **14b** was obtained from 1,4,7-tris(3'-carboxypropanoyl)triazacyclononane (**13b**, 0.11 g, 0.25 mmol) and TFP-OH (0.15 g, 0.88 mmol) and DCC (0.18 g, 0.82 mmol) according to the procedure of **14a** as a white solid in 67% yield, mp 120-122°C. IR 3412, 3085 (CH stretch for aromatic compound), 2950 (CH stretch), 1776 (C=O stretch for ester), 1686 (C=C stretch), 1650 (C=O stretch for tertiary amide), 1480, 1450 (CH$_2$ deformation), 1216 (C-F stretch), 850 (CH out of plane deformation) cm^{-1}; ^{1}H-NMR (CDCl$_3$) δ 6.97 (m, J = 4.5 Hz, 3H, C$_6$HF$_4$), 3.72-353 (two m, J = 6.5 Hz, 12H, CONCH$_2$CH$_2$NCO , conformational isomer), 3.07 (t, J = 7.5 Hz, 6H, NOCCH$_2$CH$_2$COO), 2.82 (t, J = 7.5 Hz, 6H, NOCCH$_2$CH$_2$COO); ^{13}C-NMR (CDCl$_3$) δ 174.20, 172.28, 135.26, 128.65, 128.04, 45.46, 41.54, 30.84, 27.26; HRMS (FAB, oxalic acid/glycerol) m/z Found: 873.1658 [M]$^+$, Calcd for: C$_{36}$H$_{27}$N$_3$F$_{12}$O$_9$ 873.1556 [M]$^+$.

N-(5-Benzyloxycarbonylamino-1-carboxypentyl)iminodiacetic acid (*N*(ε)-Z-lys-NTA, **16**)

Bromoacetic acid (4.17 g, 30 mmol) was dissolved in 15 mL of 2 M sodium hydroxide solution and cooled to 0 °C. $N(\varepsilon)$-benzyloxycarbonyl-L-lysine (15, 4.20 g, 15 mmol) in 22.5 mL of 2 M sodium hydroxide solution was added dropwise at 0 °C with stirring. After 2 h, the ice bath was removed and the mixture was stirred overnight at room temperature. The mixture was then enhanced to 50 °C for 2 h and 45 mL of 1 M hydrochloric acid was added. After the mixture had been cooled, the crystals that formed were filtered off, and redissolved in 1 M NaOH solution again. The product precipitated out by the dropwise addition of 1 M HCl solution and were collected by filtration. 16 was obtained as a white solid in 89% yield, mp 172-174°C. mp 172-174°C. IR 3206 (OH stretch), 1720 (C=O stretch for carboxylic acid), 1652 (C=O stretch for O(C=O)NH), 1640 (C=O stretch for tertiary amide), 1594 (C=C stretch), 1464 (CH_2 deformation), 1431, 1287 (C-N stretch) cm⁻¹; ¹H NMR (DMSO) δ 7.33 (bs, 5H, $C_6H_5CH_2$), 4.98 (s, 2H, $C_6H_5CH_2$), 3.55 (bs, 5H, NCH_2COOH and NCHCOO), 2.02 (q, J = 6.0 Hz, 2H, $NHCH_2CH_2$), 1.76-1.36 (b, 6H, $NHCH_2CH_2CH_2CH_2CH$); ¹³C-NMR (DMSO) δ 174.82, 173.21, 158.45, 128.46, 118.34, 117.65, 65.15, 64.21, 59.85, 54.65, 46.43, 28.64, 27.80, 23.27.

5-Aminopentylnitrilotriacetic acid or N^α,N^α-Bis[carboxymethyl]-L-lysine (17)

$N(\varepsilon)$-Z-Lys-NTA (16, 3.02 g, 7.50 mmol) was dissolved in 50 mL of 1 M sodium hydroxide solution. After the addition of a spatula tip of 10% Pd/C, the mixture was hydrogenated at room temperature and normal atmosphere. The reaction was complete after 6 hr as monitored by TLC (CH_3CN/H_2O = 4:1) and visualized with UV, I_2, and ninhydrin. The catalyst was filtered off, and solvent was removed *in vacuo*. The resulting residue was redissolved in 25 mL of EtOH, the product crystalized at 0°C within two days. The crystals were filtered and dried in vacuum, in 76% yield of lysine-NTA, mp 202 - 204°C (dec.). IR 3016 (OH stretch), 1724 (C=O stretch for carboxylic acid), 1710 (COO⁻ antisym stretch), 1464 (CH_2 deformation), 1381, 1287 (C-N stretch) cm⁻¹; ¹H-NMR (D_2O) δ 3.84-3.50 (bs, 5H, NCH_2COOH and NCHCOO), 2.88 (t, J = 6.5 Hz, 2H, $NHCH_2CH_2$), 1.91-1.52 (b, 6H, $NHCH_2CH_2CH_2CH_2CH$); ¹³C-NMR (D_2O) δ 175.80, 174.65, 70.83, 59.12, 42.85, 32.64, 28.90, 26.34.

1,4-Bis[5'-N,N-di(carboxymethyl)amino-5'-carboxypentylamino-3-oxo-propanoyl]diazacyclohexane (**12a**)

Lysine-NTA (**17**) (0.26 g, 0.99 mmol) was dissolved in 4 mL water. To this solution was added 0.3 mL triethylamine, followed by a solution of 0.29 g (0.49 mmol) **14a** in 5 mL warm acetonitrile. The reaction solution turned to cloudy immediately and was stirred at room temperature for 12 h . The reaction was monitored by TLC, the developed component was visualized by ninhydrin. When the reaction was complete, it was quenched by the addition of 1M HCl to pH = 1. After extraction with chloroform, the aqueous layer was dried under high vacuum and redissolved in water. The resulting residue was purified twice by anion exchange column chromatography and collected to give **12a** in 35% yield, mp 170°C (dec.). IR 3330 (OH stretch), 2948, 2854 (CH stretch), 1730 (C=O stretch for carboxylic acid),1680 (C=O stretch for tertiary amide), 1436 (CH$_2$ deformation), 1380 (C-N stretch) cm^{-1}; ^{1}H-NMR (D$_2$O) δ 3.89-3.80 (bs, 10H, NCH$_2$COOH and CH$_2$CHCOOH), 3.56-3.46 (two b, 8H, CH$_2$CH$_2$NCO), 3.10 (t, J = 6.0 Hz, 4H, NHCH$_2$CH$_2$), 2.58 (t, J = 7.2 Hz, 4H, NCOCH$_2$ CH$_2$), 2.38 (t, J = 7.4 Hz, 4H, CH$_2$CH$_2$CO), 1.85-1.37 (b, 12H, CH$_2$CH$_2$CH$_2$CH$_2$ CH); ^{13}C-NMR (D$_2$O) δ 172.50, 171.63, 170.51, 168.05, 66.83, 63.86, 54.41, 46.77, 38.76, 30.82, 28.23, 26.69, 22.96; HRMS (FAB, oxalic acid/glycerol) m/z Found: 775.3386 [M+H]$^+$, Calcd for: C$_{32}$H$_{50}$N$_6$O$_{16}$ 775.3283 [M+H]$^+$.

1,4,7-Tris(5'-N,N-di(carboxymethyl)amino-5'-carboxypentylamino-3'-oxo-propanoyl)triazacyclononane (**12b**)

Compound **12b** was obtained from **14b** (0.25 g, 0.28 mmol)and lysine-NTA (**17**, 0.28 g, 1.17 mmol) according to the method of **12a** as a white solid in 32% yield, mp 200°C (dec.). IR 3331 (OH stretch), 2945, 2857 (CH stretch), 1732 (C=O stretch for carboxylic acid), 1685 (C=O stretch for tertiary amide), 1434 (CH$_2$ deformation), 1381 (C-N stretch) cm^{-1}; ^{1}H-NMR (D$_2$O) δ 3.89 (b, 15H, NCH$_2$COOH and CH$_2$CHCOOH), 3.55-3.45 (bs, 12H, OCNCH$_2$CH$_2$NCO), 3.18 (t, J = 6.5 Hz, 6H, NHCH$_2$CH$_2$), 2.80 (t, J = 6.5 Hz, 6H, NCOCH$_2$CH$_2$), 2.44 (t, J = 6.0 Hz, 6H, CH$_2$CH$_2$CONH), 1.85-1.37 (b, 18H, CH$_2$CH$_2$CH$_2$CH$_2$

117

CH); ^{13}C-NMR (D$_2$O) δ 172.31, 171.36, 170.01, 168.56, 66.87, 64.84, 54.45, 46.78, 38.08, 30.83, 28.21, 27.02, 23.01, 22.86; HRMS (FAB, oxalic acid/glycerol) m/z Found: 1162.4702 [M+H]$^+$, Calcd for: C$_{48}$H$_{75}$N$_9$O$_{24}$ 1162.4925 [M+H]$^+$.

3.6.2 Dynamic NMR

Approximately 20 mg of sample **9a** was dissolved in D$_2$O. Sample **13a** for dynamic NMR experiments was prepared by dissolving ~ 20 mg of solid material in ~ 1 mL of D$_6$ DMSO-d$_6$. The resulting solutions were transfered to 5 cm o.d. NMR tubes, evacuated under vacuum and sealed with an acetylene torch. Samples were tested at high temperatures prior to NMR analysis to ensure the stability of the samples. All ^{1}H-NMR spectra were performed with a Varian XL-300 spectrometer operating at 300 MHz. The NMR spectrometer was equipped with a Gemini Variable Temeprature Control unit which had been calibrated using ethylene glycol. Temperature was controlled within ± 0.2°C.

In each experiment the sample was allowed to equilibrate for at least 20 minutes after the probe had reached the desired temperature. Once the sample had reached equilibrium, shimming was performed and 100 transients were collected. Fourier transforms on spectral data were made without signal enhancement or line broadening functions. DSS was used as an internal standard of chemical shift for sample **9a**. ^{1}H-NMR chemical shifts for sample **13a** are reported in ppm relative to TMS as an internal standard.

3.7 References

1.   Gansow, O.A. Newer approaches to the radiolabeling of monoclonal antibodies by use of metal chelates. *Int. J. Radiat. Appl. Instrum. Part B Nucl. Med. Biol.* **1991**, 18, 369-381.

2.   Liu, Y., and Wu, C. Radiolabeling of monoclonal antibodies with metal chelates. *Pure Appl. Chem.* **1991**, 63, 427-463.

3.   Martin, V. V., Ralston, W.H., Hynes, M.R., and Keana, J.F.W. Gadolinium (III) di- and tetrachelates designed for *in Vivo* noncovalent complexation with plasma proteins: A novel molecular design for blood pool MRI contrast enhancing agents. *Bioconjugate Chem.* **1995**, 6, 616-623.

4.   Ali, M. S. And Quadri, S.M. Maleimido derivatives of diethylenetriaminepentaacetic acid and triethylenetetraaminehexaacetic acid: Their synthesis and potential for specific conjugation with biomolecules. *Bioconjugate Chem.* **1996**, 7, 576-583.

5.   Moreau, P.; Tinkl, M.; Tsukazaki, M.; Bury, P.S.; Griffen, E.J.; Snieckus, V.; Maharajh, R.B.; Kwpk, C.S., Somayaji, V.V., Peng, Z., Sykes, T.R., Noujaim, A.A. Synthesis of the bifunctional chelating agent 6-(4-aminobenzyl)-1,4,8,11-tetraazacyclotetradecane-*N,N',N'',N'''*-tetraacetic acid (H₂NBn-TETA) *Synthesis* **1997**, 1010-1012.

6.   Sundberg, M.W., Meares, C.F., Goodwin, D.A., and Diamanti, C.I. Selective binding of metal ions to macromolecules using bifunctional analogues of EDTA. *J. Med. Chem.* **1974**, 17, 1304-1307.

7.   Yeh, S.M., Sherman, D.G., and Meares, C.F. A new route to :bifunctional" chelating agents: conversion of amino acids to analogs of ethylenediaminetetra-acetic acid. *Anal. Biochem.* **1979**, 100, 152-159.

8.   Altman, J., Shoef, N., Wilchek, M., and Warshawsky, A. Bifunctional chelating agents. Part 1. 1-(p-aminophenethyl)-ethylenediaminetetra-acetic acid. *J. Chem. Soc. Perkin Trans.* **1983**, 365-368.

9.   Lewis, M.R. and Shively, J.E. Maleimidocysteineamido-DOTA derivatives: New reagents for radiometal chelate conjugation to antibody surfhydryl groups undergo

pH-dependent cleavage reactions. *Bioconjugate Chem.* **1998**, 9, 72-86.

10. Porath, J., Carlsson, J., Olsson, I., Belfrage, G. Metal chelate affinity chromatography, a new approach to protein fractionation. *Nature* **1975**, 258, 598-599.

11. Hochuli, E.; Döbeli, H.; Schaher, A. New metal chelate adsorbent selective for proteins and peptides containing neighboring histidine residues. *J. Chrom.* **1987**, 411, 177-184.

12. Hochuli, E., Bannwarth, W., Döbeli, H., Gentz, R., and Stüber, D. Genetic approach to facilitate purification of novel recombinant proteins with a novel metal chelate adsorbent. *Bio'Technology*, **1988**, 6, 1321-1325.

13. Hochuli, E. Purification of recombinant proteins with metal chelate adsorbent. *Gen. Eng.* **1990**, 12, 87-98.

14. Crowe, J., Doböli, H., Gentz, R., Hochuli, E., Stüber, D., Henco, K. 6xHis-Ni-NTA chromatography as a superior technique in recombinant protein expression/purification *Methods Mol. Biol.* **1994**, 31, 371-387.

15. Shmitt, L., Dietrich, C., Tampé, R. Synthesis and characterization of chelator-lipids for reversible immobilization of engineered proteins at self-assembled lipid interfaces. *J. Am. Chem. Soc.* **1994**, 116, 8485-8491.

16. Qiagen, The QIAexpressionist. A handbook for high-level expression and purification of 6xHis-tagged proteins. CLONTECH Laboratories, Inc, Palo Alto, CA, USA. March, **1997**.

17. Akkaya, E.U., Huston, M.E., and Czarnik, A.W., Chelation-enhanced fluorescence of anthrylazamacrocycle conjugate probes in aqueous solutions. *J. Am. Chem. Soc.*, **1990**, 11, 3590-3593.

18. Bernhard, P.V., and Lawrance, G.A., Complexes of polyaza macrocycles bearing pendent coordinating groups, *Coord. Chem. Rev.*, **1990**, 104, 297-343.

19. Mertesdorf, C., Plesnivy, T., Ringsdorf, H., and Suci, P.A., Monolayers of amphiphilic azacrowns: Characterization of monolayer behaviour and specific interaction with nucleotides. *Langmuir*, **1992**, 8, 2531-2537.

20. Knorr, R., Trzeciak, A., Bannwarth, W. and Gillessen, D. New coupling reagents in peptide chemistry. *Tetrahedron Lett.* **1989**, 30, 1927-1930.

21. Carpino, L.A. and El-Faham, A. Efficiency in peptide coupling: 1-Hydroxy-7-azabenzotriazole vs 3,4-dihydro-3-hydroxy-4-oxo-1,2,3-benzotriazine. *J. Org. Chem.* **1995**, 60, 3561-3564.

22. Hudson, D. Methodological implications of simultaneous solid-phase peptide synthesis 1. Comparison of different coupling procedure. *J. Org. Chem.* **1988**, 53, 617-626.

23. Stewart, W.E., and Siddall III, T.H. Nuclear magnetic resonance studies of amides, *Chem. Rev.*, **1970**, 70, 517-551.

24. Dorn, I.T., Neumaier, K.R. and Tampé, R. Molecular recognition of His-tagged molecules by metal-chelating lipids monitored by fluorescence energy transfer and correlation spectroscopy. *J. A. Chem. Soc.* **1998**, 120, 2753-2763.

25. Asay, R.E., Bradshaw, J.S., Nielsen, S.F., Thompson, M.D., Snow, J.W., Masihdas, D.R.K., Izatt, R.M., and Christensen, J.J. The synthesis of novel macrocyclic multidentate compounds from dioxodioic acids. *J. Heterocyclic Chem.* **1977**, 14, 85-90.

26. Kung, V.T.; Redemann, C.T. Synthesis of carboxyacyl derivatives of phosphatidylethanolamine and use as an efficient method for conjugation of protein to liposomes. *Biochim. Biophys. Acta* **1986**, 862, 435-439.

27. Spragg, R.A. Nuclear magnetic resonance studies of six-membered rings part II, chemical shifts and coupling constants in morpholine and piperazine derivatives. *J. Chem. Soc.*, (B) **1968**, 1128-1132.

28. Wilbur, D.S., Hamlin, D.K., Pathare, P.M., Weerawarna, S.A. Biotin reagents for antibody pretargeting. Synthesis, radioiodination, and *in vitro* evaluation of water soluble, biotinidase resistant biotin derivatives. *Bioconjugate Chem* **1997**, 8, 572-584.

29. Wibur, D.S., Pathare, P.M., Hamlin, D.K., Weerawarna, S.A. Biotin reagents for antibody pretargeting. 2. Synthesis and *in vitro* evaluation of biotin dimers and

trimers for cross-linking of streptavidin. *Bioconjugate Chem.* **1997**, 8, 819-832.

30. Pathare, P.M., Wilbur, D.S., Hamlin, D.K., Heusser, S., Quadros, E., McLoughlin, P., Morgan, A.C. Synthesis of cobalamin dimers using isophthalate cross-linking of corrin ring carboxylates and evaluation of their binding to transcobalamin II. *Bioconjugate Chem.*, **1997**, 8, 161- 172.

31. Paborsky, L.R., Dunn, K.E., Gibbs, C.S., and Dougherty, J.P. A nickel chelate microtiter plate assay for six histidine-containing proteins. *Anal. Biochem.* **1996**, 234, 60-65.

32. Small, H., Stevens, T.S. and Bauman, W.C., Novel ion exchange chromatographic method using conductimetric detection. *Anal. Chem.*, **1975**, 47, 1801-1810.

33. Paprica A.P. Evidence for a continuum model of diffusion in lipid membranes. The University of Western Ontario, London, Ontario, Canada. Ph.D. thesis, **1994**. p88-90.

34. Pauling, L. "The nature of the chemical bond", 2d ed., p. 20. Cornell University Press, Ithaca, N.Y. **1942**.

35. Gutowsky, H.S., and Holm, C.H. Rate processes and nuclear magnetic resonance spectra. II Hindered internal rotation of amides. *J. Chem. Phys.*, **1956**, 25, 1228.

36. Kruper, Jr., W.J., Pollock, D.K., Fordyce, W.A., Fazio, M.J., Inbasekaran, M.N., Muthyala, R. Functionalized polyamine chelants. *U.S. Patent, 5489425*, Issued Feb. 6, **1996**, Filed Mar. 15, 1993.

37. Kline, S.J., Betebenner, D.A., Johnson, D.K. Carboxymethyl-substituted bifunctional chelators: Preparation of Aryl isothiocyanate derivatives of 3-(carboxymethyl)-3-azapentanedioic acid, 3,12-bis(carboxymethyl)-6,9-dioxa-3,12-diazatetradecanedioic acid, and 1,4,7,10-tetraazacyclododecane-N,N',N'',N'''-tetraacetic acid for use as protein labels. *Bioconjugate Chem.* **1991**, 2, 26-31.

CHAPTER 4 FORMATION OF HIS-TAGGED *ESCHERICHIA COLI* THIOREDOXIN AGGREGATES IN SOLUTION

4.1 Introduction

In Chapter 2, we reported on a systematic study of the dependence of molecular size on lateral diffusion in model membranes. That work shows that lateral diffusion depends on the size and shape of molecules. Molecules smaller than or equivalent in size to lipids, diffuse at the rate of the lipid, and their diffusive properties can be described by a free-area model. Molecules located in the transition area between lipids and membrane proteins, diffuse more slowly and their behaviour can be interpreted by hydrodynamic models. Membrane proteins in lipid bilayers move slowly in comparison with lipids (1). Proteins in cell membranes typically diffuse much more slowly than do proteins in artificial lipid bilayers (2, 3). It has not yet been reported how protein aggregates move in model membranes since it is difficult to control the protein clusters selectively and specifically in both solution and in model membranes.

In Chapter 3, we reported the synthesis of two sets of multivalent dendritic chelating agents designed for the purpose of making large protein aggregates. These dendritic ligands are expected to bind a model His-tagged protein with metal affinity coordination. The objective of the work reported in this chapter is to test the molecules described in Chapter 3, using a model protein in solution.

4.2 Approach

We desire the model protein to be water-soluble, heat-stable and of small-size. A His-tagged *Escherichia coli* thioredoxin was available from Dr. E. Ball and was selected as an initial model protein. To demonstrate protein aggregates in solution, we used native (nondenaturing) polyacrylamide gel electrophoresis (native PAGE). A brief description of the protein and native PAGE follows.

4.2.1 Choice of His-tagged *Escherichia coli* thioredoxin as a model protein

Escherichia coli thioredoxin is a well studied, heat-stable enzyme, which contains 108 amino acids (Mr 12,000) and has a central core of five strands of twisted β-pleated sheets flanked by four α-helices and the active site located in a protrusion of the protein (4, 5). The primary structure of *E. coli* thioredoxin is schematically depicted in Figure 4.1A. The three-dimensional structure of *E. coli* thioredoxin (as illustrated in Figure 4.1B) has been determined by NMR for both oxidized and reduced forms, as well as by x-ray crystallography (6, 7). *E. coli* thioredoxin is also a reference model for protein folding and dynamics (8).

Dr. Ball in the Department of Biochemistry at The University of Western Ontario, has successfully placed six histidines at the carboxyl terminus of *E. coli.* thioredoxin. This affinity tag at the carboxyl terminus has only minimum effect on the enzymatic activity (9). The cloning, expression and purification of His-tagged thioredoxin were done by Dr. Ball. Because of its well-defined mixed α/β secondary structure elements, stability, small size and prokaryotic origin, His-tagged *Escherichia coli* thioredoxin would provide an excellent model system for the study of protein aggregation.

4.2.2 Native polyacrylamide gel electrophoresis (native PAGE)

We are seeking a direct, easy technique to demonstrate the formation of large protein complexes by affinity binding of NTA chelating agents with metal and histidine-tagged proteins in solution. Native (nondenaturing) polyacrylamide gel electrophoresis (native PAGE), one of many protein assays, is the first choice because of simplicity, low cost and reasonable sensitivity (10). Native gel electrophoresis under nondenaturing conditions is used in circumstances where the enzymatic activity or the structure of a protein or protein complex under study is to be maintained. Native electrophoresis techniques can be applied to protein samples which are soluble and which will not precipitate or aggregate during electrophoresis (11, 12).

The most common electrophoresis technique uses a detergent, such as sodium dodecylsulfate (SDS), during polyacrylamide gel electrophoresis, thus termed as SDS-PAGE.

(A)

(B)
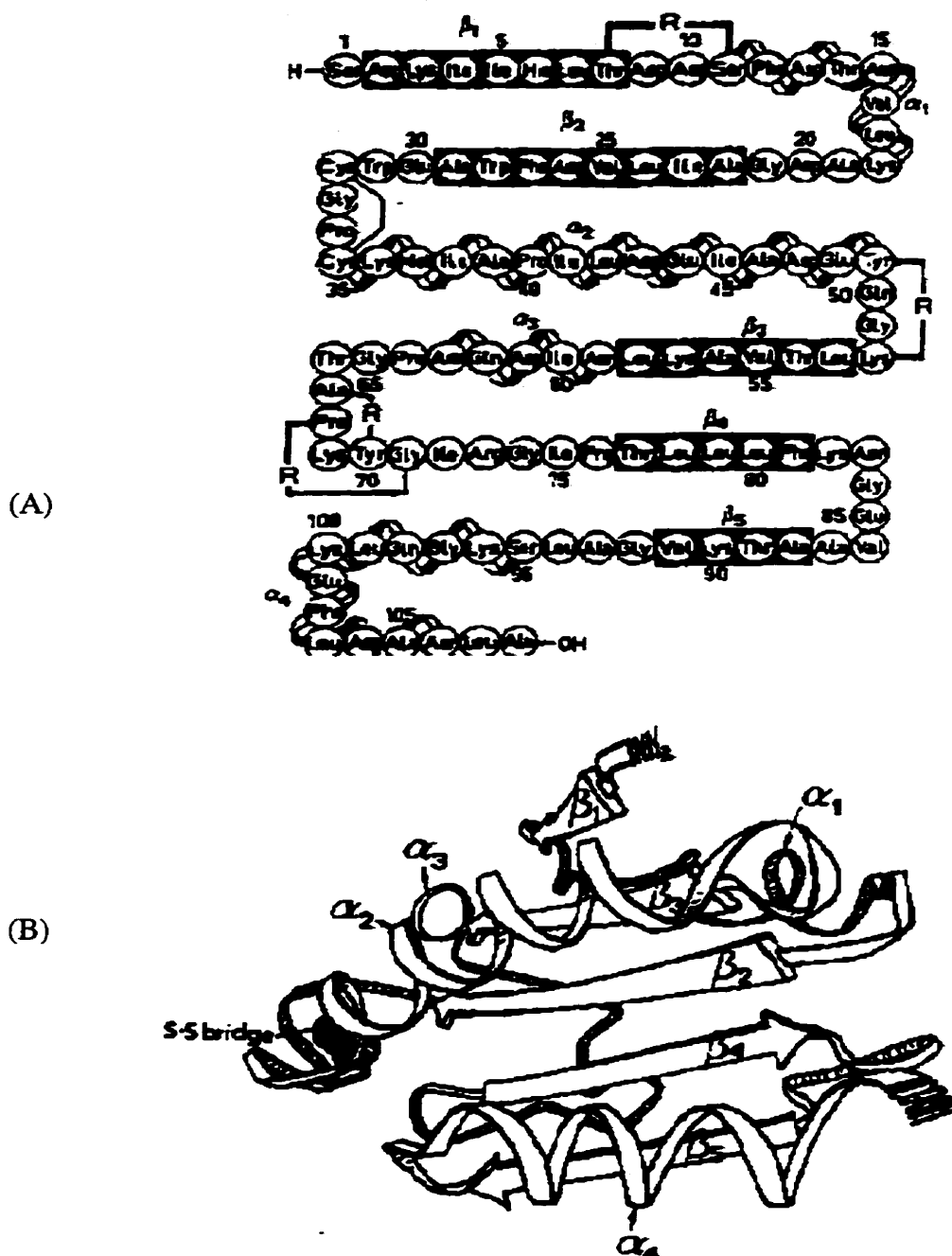
Figure 4.1: (A) The amino acid sequence of reduced thioredoxin-S$_2$ from *E. Coli* and the secondary structure elements. R = reverse turn. (Adapted from Höög, J.-O., von Bahr-Lindström, H., Josephson, S., Wallace, B.J., Kushner, S.R., Jörnvall, H., and Holmgren, A. *Bioscience Rep.* 1984, 4, 917-923.) (B) Schematic drawing of three-dimensional structure of *E. Coli* thioredoxin-S$_2$ (Adapted from Holmgren, A. *Annu. Rev. Biochem.* 1985, 54, 237-271.)

ι

SDS exists in an anion of dodecylsulfate, which binds in large amounts to proteins: at 1.4 g SDS per gram of typical protein, nearly one molecule is bound for every two amino acids. The native protein surface charges are masked by the strong negative charges of the detergent giving a high and constant charge:mass ratio and producing an elongated, flexible rod shape. It is common to include a reducing agent such as mercaptoethanol (ME), or dithiothreitol (DTT). These are used during sample preparation and also in the separation buffer, in order to cleave disulphide bonds. Figure 4.2 summarizes the effects of these various treatments on the structure of typical globular proteins.

With normal SDS-PAGE, the separation of proteins is simplified since it depends only on the size of the protein subunits. Native charges are masked by the SDS and the molecules tend to be elongated and of similar shape. The SDS diminishes the association among individual protein molecules breaking the protein complexes into their subunits. Subsequent electrophoresis of the protein-SDS complexes then gives results which are more easily interpreted, and in any case will provide additional information, since the separated subunits are detected directly. However, information on associations among proteins is lost. The terms dissociating and non-dissociating (or denaturing and nondenaturing) electrophoresis are applied to the two alternative approaches.

In our case, we aim to detect protein monomers and oligomers, such as dimer, trimer, tetramer, pentamer, and hexamer of proteins. These oligomers would be created by association through binding of NTA groups with histidine segments and metal ion to form a metal octahedral complex. Since SDS disrupts non-covalent, weak protein-protein interactions, it is possible that these protein-metal-ligand complexes will also be dissociated. Both SDS-PAGE and native PAGE were tested in our system. As expected, SDS-PAGE dissociated most of the His-tagged thioredoxin complexes, while native PAGE allowed oligomers to be detected. Therefore, we applied native (nondenaturing) PAGE to study protein monomers and oligomers. The native PAGE is performed as usual SDS-PAGE using Bio-Rad mini-protein apparatus.

In normal SDS-PAGE, a plot of the logarithm of the molecular weight of a set of known proteins versus their migration distances is usually linear. The relative migration
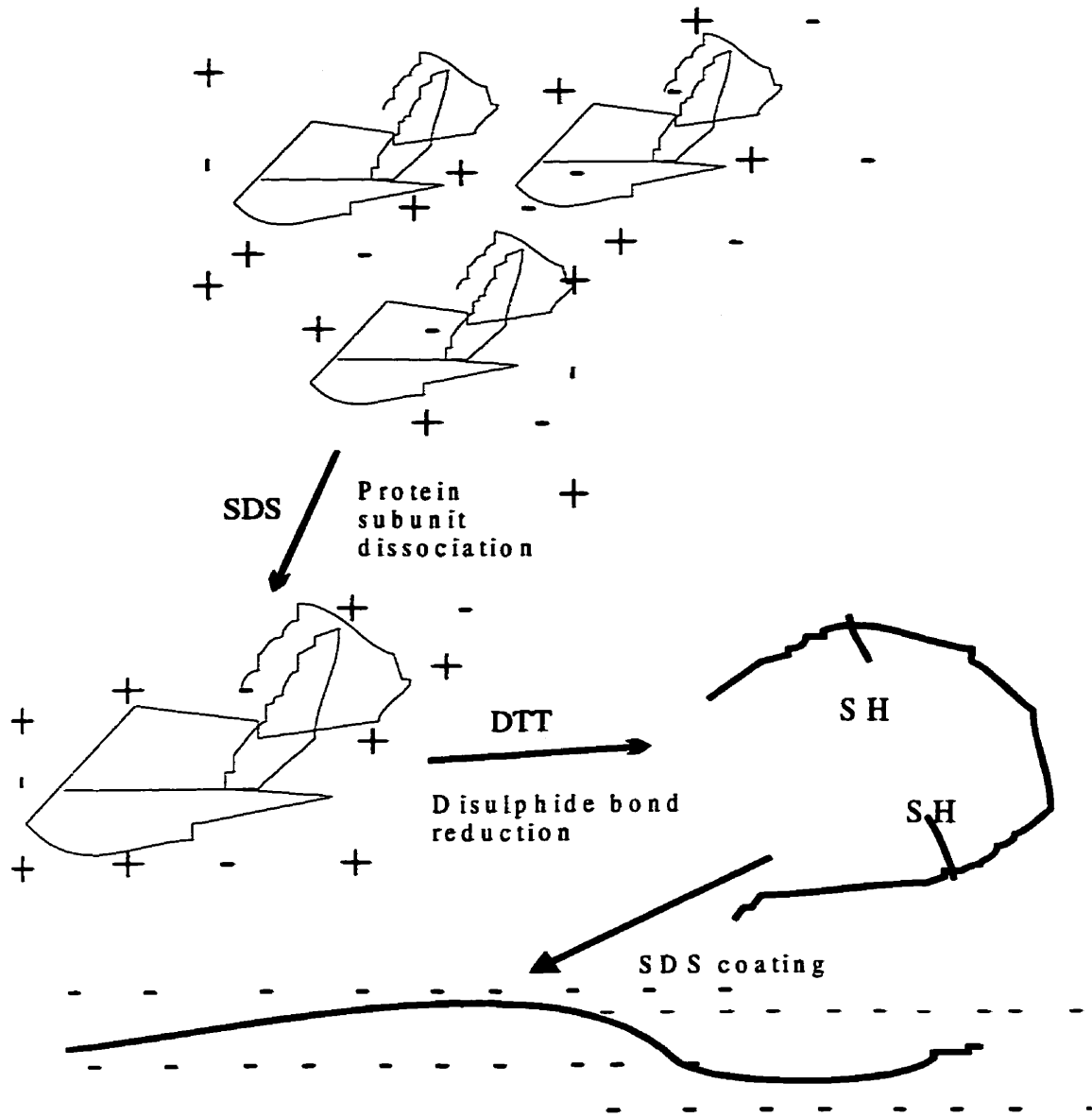
Figure 4.2: The effects of common treatment processes on proteins.

distance R_f, is calculated from the migration distance (from the top of the gel to the centre of the protein band) divided by the migration distance of the bromphenol blue tracking dye. This R_f value is given by Equation 4.1.

$$\text{Equation 4.1} \quad R_f = \frac{\text{protein migration distance (mm)}}{\text{bromophenol blue migration distance (mm)}}$$

The molecular weight (MW) of an unknown protein can be determined from the regression equation or directly from the graph. This approach is valid only under the condition that the charge to mass ratio is a constant.

In native PAGE, the migration distance of proteins is not only dependent on the size, but also on the charge of the protein, thus R_f value usually makes calibration more difficult in native PAGE. But it is possible to use the approach of SDS-PAGE to determine the MW of unknown protein complexes, because the charge to mass ratio remains a constant in our system, as determined by the binding of SDS. Four protein standards for native PAGE were bought from Sigma and calibrated for the determination of molecular weight of the unknown proteins (12, 13). These standards were: a-Lactalbumin 14.2 kDa, Carbonic anhydrase 29 kDa, Chicken egg albumin, 45 kDa, Human Serum albumin, monomer, 66 kDa. Proteins were prepared for native PAGE as described by the manufacturer (Sigma Chemical Co.). The relative mobility (R_f) of standard protein is plotted against the percentage concentration of the gel for each standard and all unknown proteins, and the slopes are calculated. A calibration graph can then be generated by plotting these slopes against the known molecular weights of the standards. The molecular weight of an unknown protein can be determined from this graph, once its mobility is determined as a function of gel concentration.

4.3 Materials and methods

4.3.1 Reagents

The NTA ligands were synthesized as described in Chapter 3 with the structures shown in Figure 3.2. They are: 1,4-bis[4'-N,N-di(carboxymethyl)amino-4'-carboxylbutanoyl)]diazacyclohexane (6a); 1,4,7-tris[4'-N,N-di(carboxymethyl)amino-4'-

carboxybutanoyl]triazacyclononane (**6b**); 1,4,7,10-tetrakis[4'-*N*,*N*-di(carboxymethyl)amino-4'-carboxybutanoyl]tetraazacyclododecane (**6c**); 1,4,7,10,13-pentakis[4'-*N*,*N*-di(carboxymethyl)amino-4'-carboxybutanoyl]pentaaza-cyclopentadecane (**6d**); 1,4,7,10,13,16-hexakis[4'-*N*,*N*-di(carboxymethyl)amino-4'-carboxybutanoyl]hexaaza-cyclooctadecane (**6e**); 1,4-bis[5'-*N*,*N*-di(carboxymethyl)amino-5'-carboxypentylamino-3-oxo-propanoyl]diazacyclohexane (**12a**); 1,4,7-tris(5'-*N*,*N*-di(carboxymethyl)amino-5'-carboxypentylamino-3'-oxopropanoyl) triazacyclononane (**12b**). Acrylamide, *N*,*N*'-methylene-bis-acrylamide, Coomassie brilliant blue R250, tris-hydroxymethylaminomethane hydrogenchloride (Tris-HCl) and glycine were purchased from Life Technologies Inc. Ammonium persulfate, *N*,*N*,*N*',*N*'-tetramethylenediamine (TEMED), bromophenol blue, the native molecular weight marker kit (containing a-Lactalbumin 14.2 KDa, carbonic anhydrase 29 KDa, chicken egg albumin, 45 KDa, Human Serum albumin, monomer, 66 KDa, dimer 132 KDa) were bought from Sigma Chemical Co. Calcium chloride ($CaCl_2$), sodium chloride (NaCl), sodium dodecyl sulphate (SDS), potassium chloride (KCl) and ethylene-diamine tetraacetic acid (EDTA) were bought from BDH Chemicals. Bio-Rad dye reagent and Mini-Protein II sets were obtained from Bio-Rad laboratories. Native gel electrophoresis was run with a Bio-Rad Model 200/2.0 power supply.

4.3.2. Purification of His-tagged thioredoxin and concentration determination

A crude solution of His-tagged thioredoxin obtained from Dr. E. Ball was further dialysed against 20 mM HEPES buffer (20 mM Tris-HCl, 100 mM sodium chloride, and 2 mM calcium chloride), pH 8.0. A Spectra/por1 wet tubing MWCO 1000 was chosen for the purpose of cutting off (1000) low molecular weight molecules. The dialysis tubing was closed to seal the two ends of tubing, and placed in the HEPES buffer (pH 8.0). This dialysis was carried out for two days in a cold room, changing the solution twice. The resulting solution was concentrated with lyophilizer (ETS System, Inc.), and the size and purity were determined by SDS-PAGE. If more than one band is seen in SDS-PAGE, conventional gel filtration is needed to further purify. The size of His-tagged thioredoxin dictates that Sephadex G-50 is the appropriate choice. HEPES buffer (20 mM Tris-HCl, 100 mM sodium

chloride, and 2 mM calcium chloride, pH 8.0) was used as eluent. All fractions were collected and concentrated by lyophilizer (ETS System, Inc.). The pure His-tagged thioredoxin solution was divided into several parts for concentration measurement and stored in freezer (-20°C).

Protein concentration was determined from the absorbance at 595 nm using the Bradford method (14). This measurement was performed at Dr. van Huystee's laboratory in the Department of Plant Science, the University of Western Ontario. The Bradford stock solution was obtained from Bio-Rad. The solution is stable indefinitely at room temperature, and contains 100 mL 95% ethanol, 200 mL 88% phosphoric acid, and 350 mg Serva Blue G. A working buffer was prepared as 425 mL distilled water, 15 mL 95% ethanol, 30 mL 88% phosphoric acid, 30 mL Bradford stock solution. The resulting solution was filtered through Whatman No.1 paper and stored at room temperature in a brown glass bottle. Approximately 10 µL of protein solution was added to a cell and mixed with enough experimental buffer to make a total volume of 100 µL. Then 1 mL of working buffer was added and the solution was mixed with a vortex mixer. After two minutes, the absorbance at 595 nm was measured. Using a standard curve which was generated by Bao Lige, the calculation of protein concentration is accomplished immediately after measuring the absorbance. The concentrated His-tagged thioredoxin was stored at -20 °C for at least two months.

4.3.3 Native PAGE

The conditions for native PAGE were adapted from Weber and Osborn (15). The apparatus routinely used generates an 10.2W cm × 7.3L cm separating gel, 1 mm in thickness. This gel accommodates 12 wells, so a maximum 10 samples can be loaded to electrophoresis. In order to achieve sufficiently high ionic strength, buffer concentrations were adjusted and extra salt was added to the running gel and the electrode buffer. The final concentrations in the running gel were varied from 12% to 16% acrylamide and a varying amount of N,N'-methylene-bis-acrylamide. The compositions of separating gels are listed in Table 4.1. The separating gels were prepared freshly in cassettes and acrylamide

polymerization was allowed to proceed at room temperature. The separating buffer comprised of Tris-HCl, pH 8.8. A small amount of KCl solution was added to increase the ionic strength in the separating environment. The electrode buffer contained 25 mM Tris base, 0.19 M glycine, and 20 mM KCl, pH 8.0. Samples for native PAGE were prepared by mixing one part of the protein sample with five parts of native PAGE sample buffer (15.5 mL of 1 M Tris-HCl pH 8.0, 2.5 mL of a 1% solution of bromophenol blue, 7 mL of water and 25 mL of glycerol). Because of the high ionic strength in the native PAGE system, the gel was run at room temperature for a period of 4 h. The protein samples, as described below, were electrophoresized toward the anode (+) for 30 minutes at 40 V, followed by 210 mins at 70 V until the dye front reached the bottom of the gel. The gel was then placed in a staining solution containing 0.25% Coomassie Blue G-250 (0.25 g Coomassie Blue G-250, 125 mL methanol, 25 mL glacial acetic acid, and 100 mL water) for overnight. Then, the gel was destained in a solution containing 10% methanol and 10% acetic acid for four hours. A piece of white paper towel was placed in the destaining solution in order to remove the blue dyes more efficiently. The resulting gels were expanded flatly between two glass plates using refreshing film (Research Products International Corp.), and finally were dried in the oven at 40°C for overnight.

Table 4.1 The compositions of separating gels in native PAGE

Reagent	Percentage of polyacrylamide gel			
	12	13	15	16
30% stock acrylamide/bis-acrylamide solution (mL)	6	6.5	7.5	8
1.5 M Tris-HCl, pH 8.8 (mL)	3.84	3.34	2.84	2.84
Water (mL)	4	4	3.5	3
10% ammonium persulfate (mL)	0.15	0.15	0.15	0.15
N,N,N',N'-tetramethylethylenediamine (TEMED) (μL)	10	10	10	10
1 M potassium chloride solution (mL)	1	1	1	1
Total volume (mL)	15	15	15	15

4.3.4 Sample preparations for native PAGE

All stock chelating agent solutions were prepared at concentrations ranging from 1 to 10 mM. The weights of ligands were measured very accurately, and they were dissolved in double distilled water. Chelating agents (**6c, 6d, 6e**) dissolved incompletely at room temperature, thus these three reagents were heated for a few minutes until they dissolved completely. All of the solutions were adjusted slowly to pH 8.0 using 1 M sodium hydroxide. The resulting solutions are stable at room temperature for at least one month. Metal ion solutions were prepared as 1 mM $NiCl_2$ or $NiSO_4$, and used instantaneously for protein coordination. Both $NiCl_2$ and $NiSO_4$ solutions work for the formation of protein complexes. The solutions of metal ion and chelating agents were mixed separately for up to 1 hour using the range of molar ratios listed in Table 4.2. The His-tagged thioredoxin solution was combined with the ligand-metal ion solutions in appropriate ratios for 3-4 hours. These protein sample solutions are stable for one month in the freezer (-20°C). The desired conditions are summarized in Table 4.3.

Table 4.2 Optimal condition for ligand-metal ion mixture

Solution	Chelating agent	RM_{L-Ni}	Equilibration time (min)
$N_2[NTA-Ni]_2$	**6a**	1 : 3	20
$N_3[NTA-Ni]_3$	**6b**	1 : 3.5	30
$N_4[NTA-Ni]_4$	**6c**	1 : 5	40
$N_5[NTA-Ni]_5$	**6d**	1 : 6.5	50
$N_6[NTA-Ni]_6$	**6e**	1 : 7.5	60

Where $N_2[NTA-Ni]_2$ represents the mixture of **6a** and $NiCl_2$, $N_3[NTA-Ni]_3$ is the mixture of **6b** and $NiCl_2$, $N_4[NTA-Ni]_4$ is the mixture of **6c** and $NiCl_2$, $N_5[NTA-Ni]_5$ is the mixture of **6d** and $NiCl_2$, $N_6[NTA-Ni]_6$ is the mixture of **6e** and $NiCl_2$. RM_{L-Ni} is the molar ratio of chelating agent : Ni^{2+}. These abbreviations will be used in the rest of my thesis.

Table 4.3 Formation of His-tagged thioredoxin complexes

Protein aggregates	Solution	RM_{L-Ni-P}	Equilibration time (h)
$N_2[NTA-Ni]_2P_2$	$N_2[NTA-Ni]_2$	1 : 2.2	2
$N_3[NTA-Ni]_3P_3$	$N_3[NTA-Ni]_3$	1 : 3.3	2
$N_4[NTA-Ni]_4P_4$	$N_4[NTA-Ni]_4$	1 : 4.4	3
$N_5[NTA-Ni]_5P_5$	$N_5[NTA-Ni]_5$	1 : 5.5	4
$N_6[NTA-Ni]_6P_6$	$N_6[NTA-Ni]_6$	1 : 6.8	4

Where $N_2[NTA-Ni]_2P_2$, $N_3[NTA-Ni]_3P_3$, $N_4[NTA-Ni]_4P_4$, $N_5[NTA-Ni]_5P_5$, $N_6[NTA-Ni]_6P_6$ represent the corresponding His-tagged thioredoxin complexes which were formed by the addition of ligand/metal solution, such as $N_2[NTA-Ni]_2$, $N_3[NTA-Ni]_3$, $N_4[NTA-Ni]_4$. $N_5[NTA-Ni]_5$, $N_6[NTA-Ni]_6$, respectively. RM_{L-Ni-P} is the molar ratio of a mixture of ligand and Ni^{2+} to protein solution. The abbreviations of $N_2[NTA-Ni]_2P_2$, $N_3[NTA-Ni]_3P_3$, $N_4[NTA-Ni]_4P_4$, $N_5[NTA-Ni]_5P_5$, $N_6[NTA-Ni]_6P_6$ for protein complexes will be used in the rest of my thesis.

To prepare the protein samples for dissociation of the protein aggregates, excess EDTA was added to the aggregated protein solution. His-tagged thioredoxin complexes which were formed by chelating agents containing both shorter chain linker and longer chain linker (**12a-b** and **6b-c**) were examined by EDTA. The optimum ratio for the dissociation of protein aggregates into monomers was found to be 1:5 and 1:8 (molar ratio of chelating agent to EDTA) using chelating agents **12a** and **12b**, respectively. The conditions for the formation of protein aggregation and protein dissociation using chelating agents **12a** and **12b** are summarized in Table 4.4. Each component was added sequentially while maintaining pH 8.0, followed by vortexing and standing for at least 1 hour. Finally, protein samples were adjusted to an appropriate concentration, and a total volume of 10-30 μl of each sample was immediately subjected to native PAGE.

Table 4.4: Optimal condition for aggregation and dissociation of His-tagged thioredoxin using ligands 12a and 12b

Solution	L	MR_{L-Ni}	RM_{L-Ni-P}	$RM_{Complex-EDTA}$	Equilibration time (h)
$N_2[NTA-Ni]_2$	**12a**	1 : 3.0			0.5
$N_3[NTA-Ni]_3$	**12b**	1 : 4.5			0.5
$N_2[NTA-Ni]_2P_2$	**12a**		1 : 2.2		2
$N_3[NTA-Ni]_3P_3$	**12b**		1 : 3.3		3
$N_2[NTA-Ni]_2P_2$+ EDTA	**12a**			1 : 5	0.5
$N_3[NTA-Ni]_3P_3$+ EDTA	**12b**			1 : 8	0.5

Where L = chelating agents, $N_2[NTA-Ni]_2$, $N_3[NTA-Ni]_3$ represent the mixture of chelating agent **12a**, **12b** with $NiCl_2$, respectively. $N_2[NTA-Ni]_2P_2$ and $N_3[NTA-Ni]_3P_3$ correspond to the His-tagged thioredoxin complexes formed using **12a** and **12b**. $N_2[NTA-Ni]_2P_2$ + EDTA, $N_3[NTA-Ni]_3P_3$+ EDTA are the protein samples which were caused by the addition of EDTA to samples $N_2[NTA-Ni]_2P_2$ and $N_3[NTA-Ni]_3P_3$. MR_{L-Ni} is the molar ratio of ligand (**12a** and **12b**) and nickel ion solution. RM_{L-Ni-P} is the molar ratio of $N_2[NTA-Ni]_2$, $N_3[NTA-Ni]_3$ with His-tagged thioredoxin solution. $RM_{Complex-EDTA}$ is the molar ratio of $N_2[NTA-Ni]_2P_2$ and $N_3[NTA-Ni]_3P_3$ with EDTA solution. All of these abbreviations will be used for the rest of my thesis.

4.4 Results

4.4.1 Demonstration of the association and dissociation of His-tagged thioredoxin complexes

Evidence for selective His-tagged thioredoxin aggregation is shown in Figure 4.3A for the dendritic ligands **6a-e**. The monomeric protein is observed in the left lane as the fastest running protein with the smallest molecular weight. As the various complexing agents were included, the proteins moved in single bands but more slowly, indicating that His-tagged thioredoxin aggregates were obtained. Although the molecular weight (MW) of these complexes is not determined, this gel provides direct evidence that the size of the His-tagged
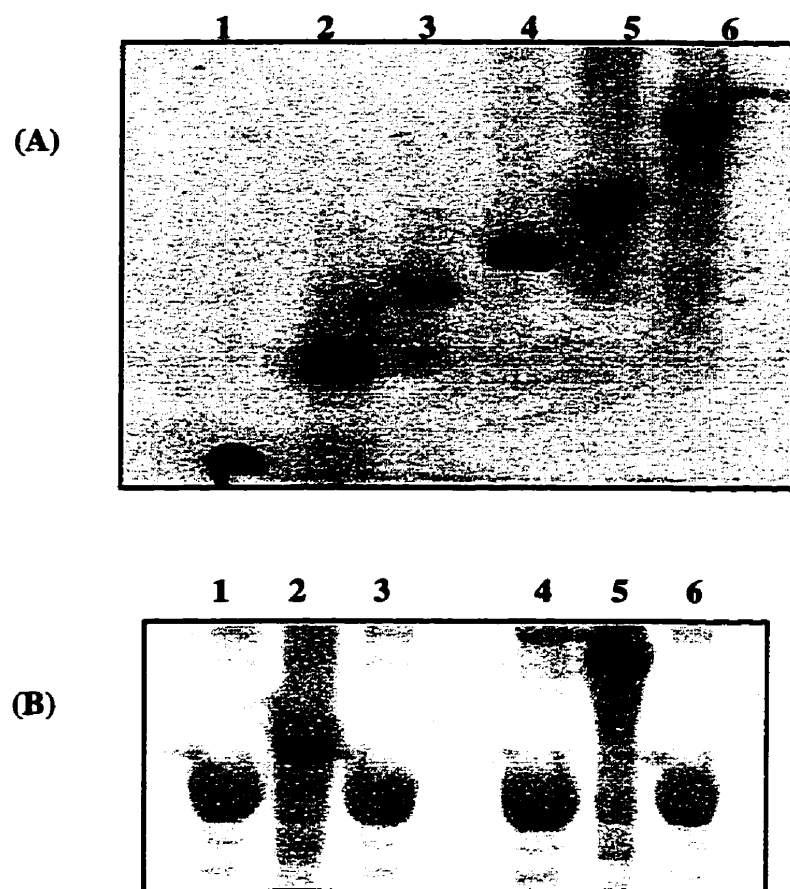
Figure 4.3: Demonstration of the aggregation (A) and the dissociation (B) of His-tagged *E. coli* thioredoxin complexes. (A) Lane 1 is His-tagged thioredoxin monomers and lanes 2, 3, 4, 5, 6 show the complexes which were formed by the combination of ligand **6a, 6b, 6c, 6d, 6e** with NiCl$_2$ and His-tagged thioredoxin. The molar ratio of lane 2, 3, 4, 5, 6 is 1:3.0:2.2; 1:3.5:3.3, 1:4.0:4.4, 1:6.5:5.5, 1:7.5:6.8, respectively. Gel electrophoresis was performed at 14% polyacrylamide. (B) Lane 1 and lane 4 illustrate the protein monomers. Lane 2 and lane 5 show the complexes formed by a combination of ligand **12a, 12b**, NiCl$_2$ and protein with molar ratio of 1:3.0:2.2, 1:4.5:3.3, separately. Lane 3 represents the complex from lane 2 being dissociated by the addition of EDTA with molar ratio of 1:5 for **12a**:EDTA. Lane 6 shows the dissociation of complex from lane 5 into protein monomers by the addition of EDTA with molar ratio of 1:8 for **12b**:EDTA. The gel was performed at 17% polyacrylamide. Both of the gels were stained with Coomassie blue.

thioredoxin oligomers can be controlled by changing the number of NTA groups on the complexing reagents. Each complex of *E. coli* His-tagged thioredoxin is observed as a single oligomeric structure, and not as a mixture of different oligomeric forms as long as the appropriate molar ratios of ligand:Ni^{2+}:protein were used in solutions.

Figure 4.3B shows the corresponding protein complexes formed by using ligands **12a-b**. The migration distances are consistent with those observed for **6a** and **6b** in Figure 4.3A providing evidence that these two complexes are similar molecular weight complexes (may be dimers and trimers respectively for **12a** and **12b**). The addition of excess EDTA following the protein aggregates prior to running the gels shows that the formation of protein complexes is reversible. This proves that the aggregates of His-tagged thioredoxin are NTA-Ni-$(His)_2$ protein complexes. The optimal conditions for formation and dissociation of protein complexes at specific stoichiometric ratios are outlined in Table 4.2, Table 4.3, Table 4.4.

4.4.2 Estimate of molecular weight of protein complexes

For native PAGE, the migration distance of protein samples is sensitive to both charge and size, since the charge of protein is not controlled by binding of SDS. The calibration of molecular weight (MW) of standards therefore requires measurement of the migration distance as a function of gel concentration. The four standards and the complexes of His-tagged thioredoxin which were formed using chelating agents **6a-e**, were run on native PAGE at four polyacrylamide concentrations: 12%, 13%, 15% and 16%. The migration distances of the His-tagged thioredoxin complexes were compared with four standard proteins as shown in Figures 4.4 at each concentration. It is obvious that larger molecular weight of complexes were obtained by using the dendritic ligands **6a-e**. Increasing the acrylamide concentration (i.e. decreasing the pore size) resulted in decreased migration for protein standards as well as the complexes. The $100[\log(R_f \times 100)]$ values of the standard markers and the protein complexes were plotted against the percentage concentration of gels (Figure 4.5A). For each standard protein (14.2 kDa, 29 kDa, 45 kDa, 66 kDa), the slopes were calculated and then plotted as a function of molecular weight to yield a calibration

(A) 12% **(B) 13%**

(C) 15% **(D) 16%**
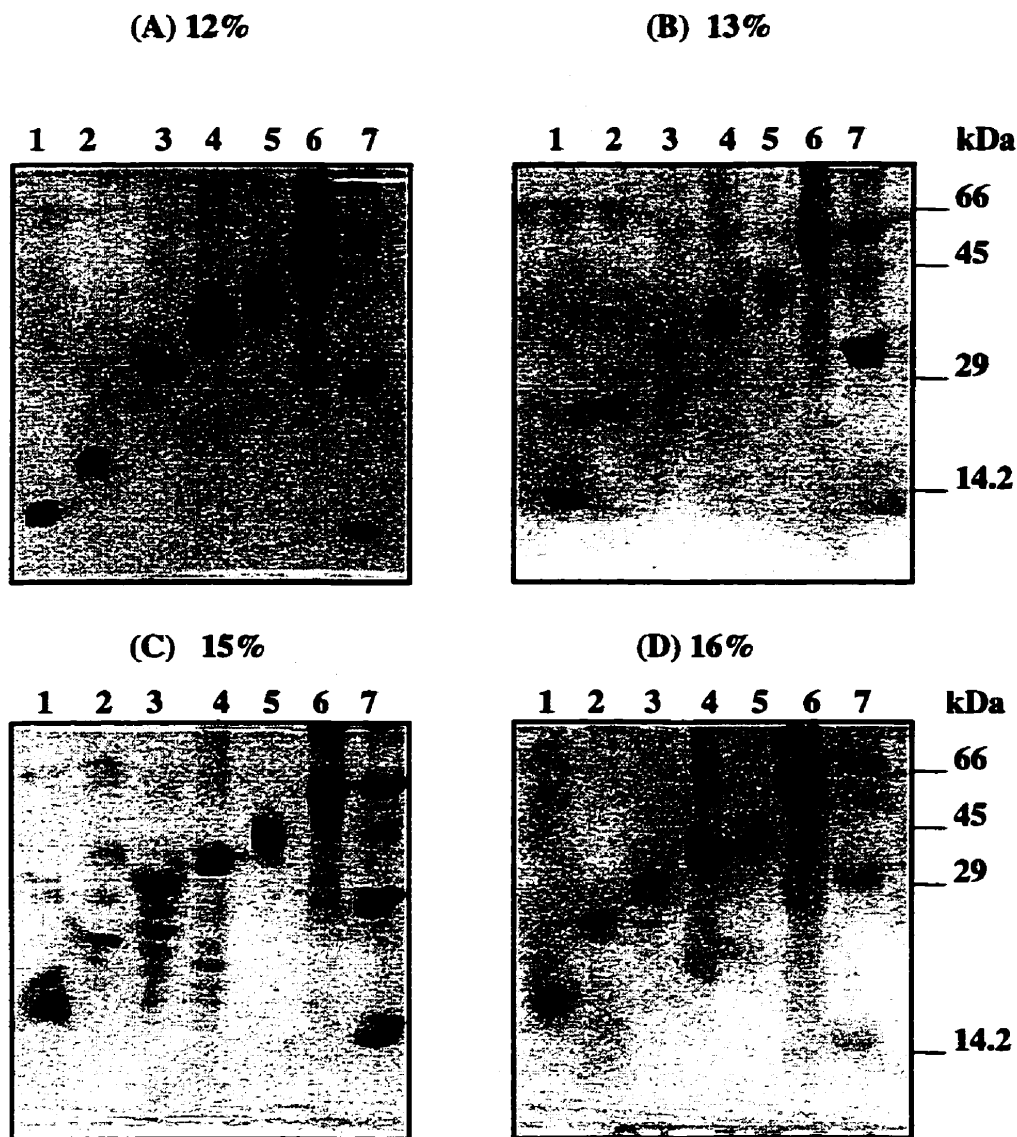
Figure 4.4: Illustration of His-tagged thioredoxin aggregations with Native PAGE at various acrylamide concentration. Gel electrophoresis was performed at 12% (A), 14% (B), 15% (C), 16% (D). The MW of each protein standard is indicated on the right of gels (lane 7). Lane 1 represents only His-tagged thioredoxin monomers, lanes 2, 3, 4, 5, 6 illustrate the protein complexes such as $N_2[NTA-Ni]_2P_2$, $N_3[NTA-Ni]_3P_3$, $N_4[NTA-Ni]_4P_4$, $N_5[NTA-Ni]_5P_5$, $N_6[NTA-Ni]_6P_6$, which were formed with the addition of dendritic ligand **6a, 6b, 6c, 6d, 6e**, respectively. The molar ratios of ligand, $NiCl_2$ and His-tagged thioredoxin are outlined in Tables 4.2 and 4.3. The gels were stained with Coomassie blue.

curve (Figure 4.5B). The slope values for the four standards are listed in Table 4.5 with the corresponding confidence. This calibration curve is nearly a straight line (Figure 4.5B) with a correlation coefficient of 0.82, which is acceptable.

Table 4.5: Calibration of four protein standards

MW of protein standard (kDa)	Slope	Correlation Coefficient
14.2	-1.7	0.83
29	-4.1	0.92
45	-4.9	0.83
66	-7.1	0.84

Similarly, the slopes of the R_f values as a function of gel concentration were calculated for each of the protein complexes as outlined in Table 4.6. These slopes were compared to the calibration curve (Figure 4.5B) to estimate the MW for each protein complex. The estimate values do not correspond well with those expected for the MW of His-tagged thioredoxin monomers and oligomers (Table 4.6). This suggests that either the bands are not the expected complexes or the analysis is inappropriate or inaccurate for this system. For the reasons outlined below, we believe the analysis is inappropriate.

Table 4.6: Estimate of the MW of each protein complex according to Figure 4.5

Protein sample	Slope	Coefficient	MW of complex (kDa)
P	-2.7	0.98	28
$N_2[NTA-Ni]_2P_2$	-3.9	0.89	34
$N_3[NTA-Ni]_3P_3$	-3.0	0.95	25
$N_4[NTA-Ni]_4P_4$	-3.0	0.99	22
$N_5[NTA-Ni]_5P_5$	-1.4	0.92	12
$N_6[NTA-Ni]_6P_6$	-5.0	0.91	43

Where P represents the His-tagged thioredoxin monomers, the slope and confidence values were obtained from the first order regression in Figure 4.5A, and MW values were obtained from the comparison with the calibration curve in Figure 4.5B. The abbreviations of $N_2[NTA-Ni]_2P_2$, $N_3[NTA-Ni]_3P_3$, $N_4[NTA-Ni]_4P_4$, $N_5[NTA-Ni]_5P_5$, $N_6[NTA-Ni]_6P_6$ are defined as the description of Table 4.3.
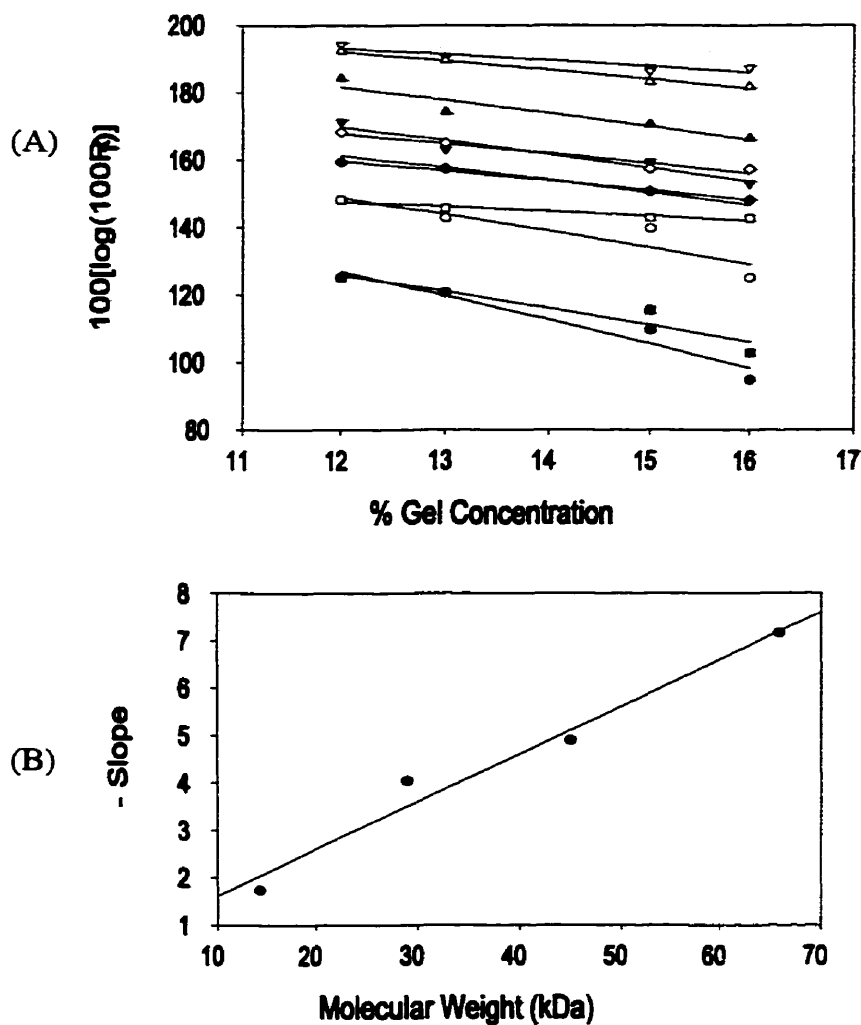
Figure 4.5: (A) 100Log(R_f×100) of four standard proteins and His-tagged thioredoxin complexes were plotted against the percentage concentration of polyacrylamide gels. •: standard 66 kDa; o: standard 45 kDa; ▼: standard 29 kDa; ▽: standard 14.2 kDa; ■: His-tagged thioredoxin complex formed by ligand **6e**; □: His-tagged thioredoxin complex formed by ligand **6d**; ◆: His-tagged thioredoxin complex formed by ligand **6c**; ◇: His-tagged thioredoxin complex formed by ligand **6b**; ▲: His-tagged thioredoxin complex formed by ligand **6a**; △: His-tagged thioredoxin monomers. All data points were fitted with first-order regression lines. The slope values are outlined in Table 4.5 and Table 4.6. (B) The negative slope values of four standards were plotted against the corresponding MW values.

In the experiments outlined above, the pH of the protein buffer system is adjusted to 8.0. At this pH, His-tagged thioredoxin is negatively charged because of the large number of asparitic acid residues in the primary structure of *E. coli* thioredoxin (Figure 4.1). Each protein monomer has a given charge-to-mass ratio. Since the protein complexes are formed as multiples of the monomers, it is reasonable to expect that the charge-to-mass ratio of the complex is a constant which is independent of the number of monomers in the complex. The series of protein complexes should therefore behave on native polyacrylamide gel in exactly the same way as most proteins behave in an SDS-PAGE. Therefore the migration distance is only dependent on mass and the logarithm of MW is inversely proportional to the migration distance.

To test this concept, we plotted the log(MW) of the four standards against the R_f value measured at each of the four gel concentrations (Figure 4.6A). Good correlation between mobility and log(MW) is observed for these standards. Using these standard lines, the MW was estimated for each of the protein complexes at each gel concentration. Table 4.7 presents the MW values of each protein complex at each gel concentration. For each protein complex, the MW was estimated using the corresponding calibration curves at four gel concentrations (Figure 4.6A). Also, the mean MW and SEM values of each complex were calculated within a confidence of 99%. The last column of Table 4.7 outlines the mean R_f and SEM values of protein monomers and oligomers. The mean R_f and SEM values were calculated from the relative distances for each sample at each concentration of gels, separately. We plotted the mean MW and logarithm of the mean MW against the mean R_f values and these plots yield a curve and a straight line as shown in Figure 4.6B and Figure 4.6C, respectively. Consequently, the MW value of bands in lanes1, 2, 3, 4, 5, 6 was calculated to be approximate 14.3 ± 0.3 kDa, 25.1 ± 1.3 kDa, 34.1 ± 0.4 kDa, 40.1 ± 0.6 kDa, 46.9 ± 1.7 kDa and 63.6 ± 1.2 kDa, respectively. The MW value for monomeric, dimeric, trimeric, tetrameric, pentameric and hexameric His-tagged thioredoxin is expected to be approximate12 kDa, 24 kDa, 36 kDa, 48 kDa, 60 kDa, 72 kDa. The estimated overall MW values of these oligomers are smaller than the expected ones, but the trend is consistent.
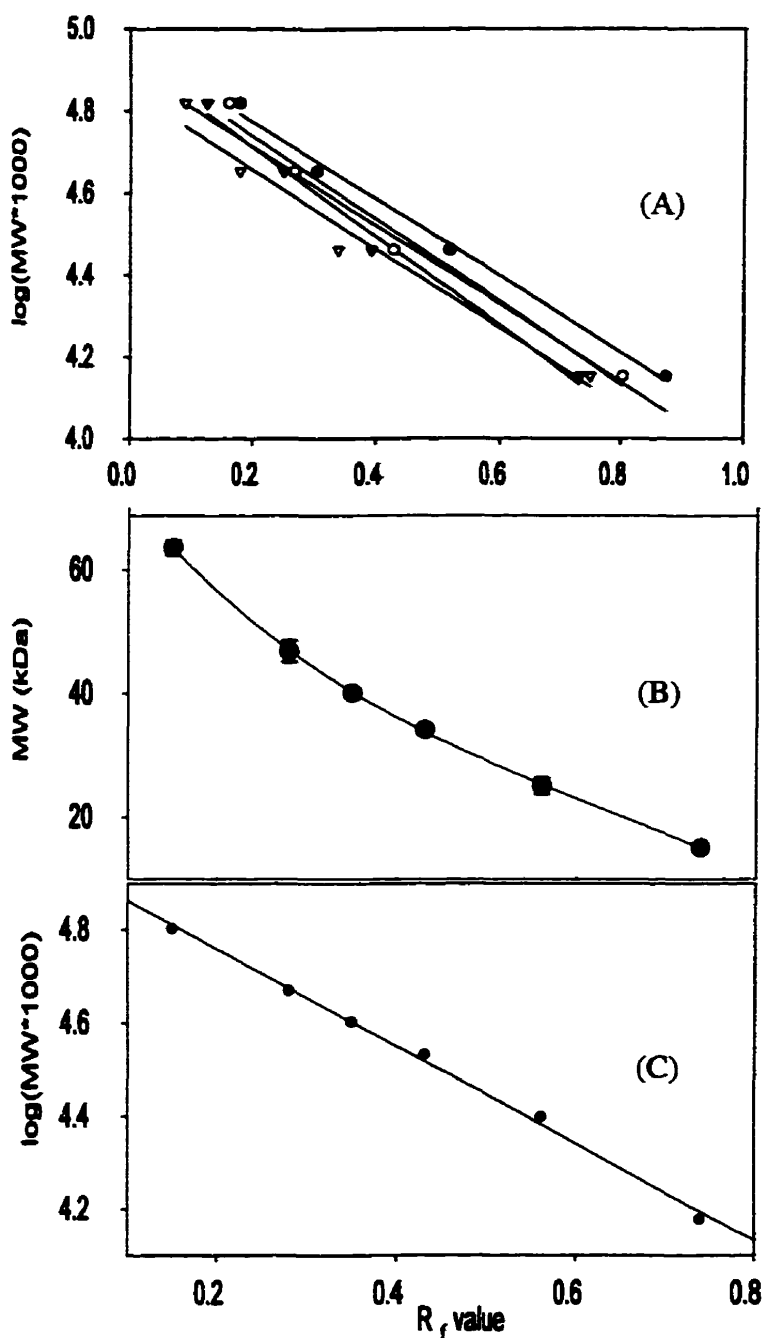
Figure 4.6: Scatter plots of the log(MW×1000) of the four standards (A), the average MW of protein monomers and its aggregates were plotted against the R_f values with SEM bars (B) , the logarithm of the MW of protein and its aggregates is plotted against their relative migrations (C). The MW values of His-tagged thioredoxin monomers and aggregates were obtained in comparison with Figure 4.4 at various concentration of gels. (A) The logarithm of the MW of standards is plotted against the relative migrations (R_f). •: 12%; o: 13%; ▼: 15%; ▽: 16% of polyacrylamides. The points in (C) were fitted by the first-order linear regression with a correlation coefficient of 0.99.

Table 4.7: Estimated MW values of protein complexes at four gel concentrations

Protein sample	MW 12%	MW 13%	MW 15%	MW 16%	Mean MW ± SEM	Mean R_f ± SEM
P	14	15	13	13	13.7 ± 0.3	0.74 ± 0.04
$N_2[NTA-Ni]_2P_2$	22	26	25	28	26.0 ± 1.3	0.56 ± 0.05
$N_3[NTA-Ni]_3P_3$	35	33	35	34	34.1 ± 0.4	0.43 ± 0.02
$N_4[NTA-Ni]_4P_4$	42	39	40	40	40.1 ± 0.6	0.35 ± 0.02
$N_5[NTA-Ni]_5P_5$	51	48	46	43	46.9 ± 1.7	0.28 ± 0.01
$N_6[NTA-Ni]_6P_6$	67	64	63	61	63.6 ± 1.2	0.15 ± 0.01

MW and the mean MW values of each sample were calculated according to the standard curves in Figure 4.6A at four gel concentrations. The mean R_f was calculated from the migration distances from Figure 4.4 at four gel concentrations using Equation 4.1. SEM is the standard error of the mean and is obtained within a confidence of 99%.

It is clear that the MW value increases systematically as protein complexes are induced by ligands 6a-e. The electrophoretic mobilities are not quantitatively accurate but the interpretation assuming a constant charge-to-mass ratio is superior to the analysis by using slope of each protein complex at various concentrations of gels. It is assumed the shape of these complexes is similar to that of protein monomers, because each complex is induced by the corresponding dendritic ligand. As a matter of fact, if the number of protein monomers in each complex is increased, the whole protein complex can be compacted but maintained a constant of charge-to-mass ratio. The compacted protein complex is moving faster than the dispersed one in electrophoresis, thus the MW values of His-tagged thioredoxin oligomers are estimated to be smaller than the expected ones.

The size of protein complexes in lanes 1, 2, 3, 4, 5, 6 gets increasingly larger. We know that the band in lane 1 represents His-tagged thioredoxin monomers. We propose that the band in lanes 2, 3, 4, 5, 6 corresponds to the dimeric, trimeric, tetrameric, pentameric, and hexameric His-tagged thioreoxin complexes which were produced specifically by the addition of the dendritic ligands 6a, 6b, 6c, 6d, 6e. The native PAGE result presented here

provides good evidence that large His-tagged thioredoxin complexes were formed with the affinity ligand-metal-protein (NTA-Ni^{2+}-His-tagged thioredoxin) in solution and that the stoichiometry of these large protein complexes can be controlled by the structure of the dendritic complexing reagents.

4.4.3 Optimization of native PAGE
4.4.3.1 Effect of pH in the separating gel

Polyacrylamide gels (15%) were assembled as described in the "Materials and methods" section with pH 9.2 (Figure 4.7A) and pH 8.8 (Figure 4.7B) for the separating buffer. Lane 1 represents the four protein standards, lanes 2, 3, 4, 5, 6, 7 show the samples of monomers, $N_2[NTA-Ni]_2P_2$, $N_3[NTA-Ni]_3P_3$, $N_4[NTA-Ni]_4P_4$, $N_5[NTA-Ni]_5P_5$, $N_6[NTA-Ni]_6P_6$, respectively. A significant decrease in electrophoretic run time was observed at pH 9.2 presumably because all the proteins are more negatively charged. Electrophoresis at pH 8.8 and pH 9.2 were stopped by monitoring the dye front migration. No substantial difference between the relative migration rate for four protein standards and the His-tagged thioredoxin monomers and oligomers was noted through the 1.0 mm separating gel. The migration rates through the separating gel at pH 8.8 gels are slower than the migrations through pH 9.2 gels but with similar linear correlation between log(MW) and R_f value in all cases. The same trend in the migrations of the protein complexes is observed.

4.4.3.2 Effect of sample preparation

Changing the molar ratios of complexing agent, metal ion and His-tagged protein in solution leads to significant variation in the stoichiometry of the protein complexes (Figure 4.8). Lane 1 is the protein monomer, lane 2 represents a mixture of the protein monomers and dimers, which was formed with a molar ratio of 1:3 for ligand 6a to His-tagged thioredoxin. Lane 3 illustrates three components of protein monomers and complexes which were formed by ligand 6b. Lane 4 shows a single band which was formed by ligand 6c. Lane 5 shows a mixture of proteins which were formed by ligand 6d. Lane 6 illustrates perfectly a single band which was formed by ligand 6e. The detailed conditions are described in the caption
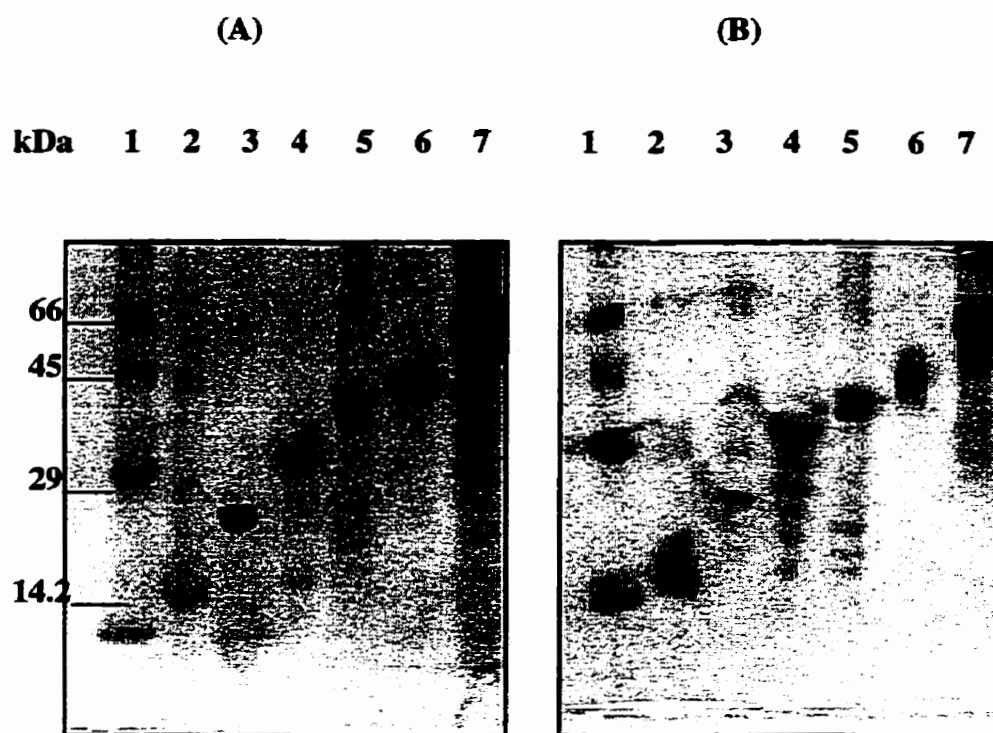
Figure 4.7: Effect of increased pH of separating gel. (A) pH = 9.2, (B) pH = 8.8. Gel electrophoresis was performed at 15% of polyacrylamide. Lane 1 shows the protein standards, and the MW of each standard is indicated on the left. Lane 2 represents His-tagged thioredoxin monomers, lanes 3, 4, 5, 6, 7 illustrate the protein complexes formed with the addition of dendritic ligand **6a, 6b, 6c, 6d, 6e**, respectively. The gels were stained with Coomassie blue.

Figure 4.8: Illustration of incomplete complex formation of His-tagged thioredoxin complexes in native PAGE. Lane 1 represents for protein monomers, lane 2 shows a mixture of protein monomer and complexes which were induced by the $N_2[NTA-Ni]_2$ solution with a molar ratio of 1:3 for **6a** : protein. Lane 3 is a mixture of $N_3[NTA-Ni]_3$ and protein solution with a molar ratio of 1 : 4. Lane 4 is sample $N_4[NTA-Ni]_4P_4$ which was obtained by $N_4[NTA-Ni]_4$ and protein solution with a molar ratio of 1 :4. Lane 5 is a mixture of $N_5[NTA-Ni]_5$ and protein solution with a molar ratio of 1 / 6.5. Lane 6 is sample $N_6[NTA-Ni]_6P_6$ which was formed by mixing $N_6[NTA-Ni]_6$ and protein solution with a molar ratio of 1 : 6. The gels were run at 14% of polyacrylamide and stained with Coomassie blue. No standard markers were compared.

of Figure 4.8. As expected, the molar ratios of the components are critical for the formation of specific stoichiometric protein aggregation. The optimum conditions for the formation of the specific oligomers of the His-tagged thioredoxin are indicated in Table 4.2 and Table 4.3.

All of the native PAGEs were run under continuous gel conditions with no stacking gels. Although continuous buffer gels lack a "stacking gel" to concentrate the protein sample at the onset of electrophoresis, they are capable of good separation if the volume and ionic strength of the sample are low. As the protein molecules enter the gel, they become concentrated simply because the first molecules to enter are immediately retarded. This effect has been enhanced by the weaker ionic strength of the sample than that of gel, so that the proteins that enter the gel first experience a lower electric field. For best results, however, the band of sample applied to a continuous buffer gel should be no more than 2-3 mm thick. If the sample is so dilute that larger volumes must be used, or if the ionic strength of the sample is significantly greater than that of the gel buffer, better results will probably be obtained using a discontinuous buffer system. This is why a small amount of potassium chloride solution was added to the separating buffer.

4.4.4 Dissociation of His-tagged thioredoxin complexes by EDTA

We have shown the dissociation of His-tagged thioredoxin complexes which were formed by ligands **12a** and **12b** (Figure 4.3B). Figure 4.9 is a further demonstration of the dissociation of protein complexes with the addition of excess amount of EDTA. Lane 1 shows the trimeric protein complex which was formed by ligand **6b**. Lane 2 is the same protein sample to which EDTA was added. It is clear that the trimeric protein complex (lane 1) is gone and only monomers are observed in lane 2. Lane 3 represents the formation of His-tagged thioredoxin complexes which were produced by the addition of **6c** and nickel ion solutions. Lane 4 shows the partial dissociation upon addition of insufficient amounts of EDTA, while lane 5 shows the complete dissociation of the NTA-Ni-protein complex with the addition of excess EDTA. The molar ratios of protein, ligand and metal ions are described in the caption of Figure 4.9. This native PAGE affirms that the binding of metal-ligand-protein is reversed and competitive with EDTA at pH 8.8 of separating gel.
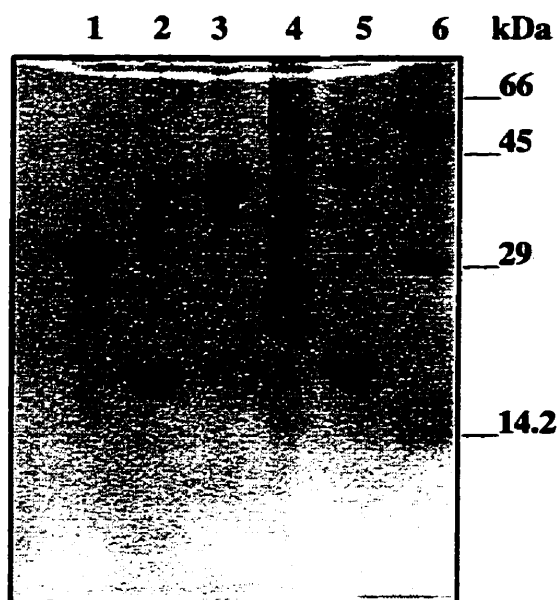
Figure 4.9: Illustration of the dissociation of protein complex with the addition of EDTA in native PAGE. This gel was run at 17% of polyacrylamide. The MW of protein standards is indicated on the right of gel. Lane 1 shows sample $N_3[NTA-Ni]_3P_3$ which was formed with ligand **6b**. Lane 2 shows the sample $N_3[NTA-Ni]_3P_3$ + EDTA which was obtained from the protein complex $N_3[NTA-Ni]_3P_3$. (lane 1). Lane 3 represents the sample $N_4[NTA-Ni]_4P_4$ which was formed with ligand **6c**. Lane 4 shows a partial dissociation of protein complex $N_4[NTA-Ni]_4P_4$ (from lane 3), the molar ratio of $N_4[NTA-Ni]_4P_4$ to EDTA is 1: 6. Lane 5 shows sample $N_4[NTA-Ni]_4P_4$ + EDTA with molar ratio of 1: 10. It is clear that protein complex (lane 3) is dissociated to its monomers. In this case, the molar ratio of EDTA with protein complex is greater than the case of lane 4. The gel was stained with Coomassie blue.

4.5 Discussions

The principle of native PAGE (without SDS) is to separate according to both molecular size, shape and charge. In the present case, the separation is influenced by pH, the use of different ligand and the exact molar ratios of each component (ligand, $NiCl_2$ and protein). However, it becomes clear that the ratio of charge:mass of protein is the same in each protein complex regardless of the increasing size. Hence, it is possible to determine the MW in the same way as used for SDS-PAGE.

Specific oligomers of His-tagged thioredoxin were observed by native polyacrylamide gel electrophoresis. The low molecular weight monomer moves near the front of the gel, while the dimer, trimer, tetramer, pentamer and hexamer move progressively more slowly. The protein complexes were generated by specific molar ratios of ligand (**6a, 6b, 6c, 6d, 6e**), protein and nickel ion. As shown in Tables 4.2 and 4.3, these ratios are 1:3:2.2; 1:3.5:3.3; 1:5:4.4; 1:6.5:5.5; 1:7.5:6.8 for the formation of dimers, trimers, tetramers, pentamers, hexamers at pH 8, respectively. This suggests that the protein aggregates were formed stoichiometrically and one species predominated. These ratios are exactly as expected according to the number of NTA groups for each complexing reagent. It is clear that the size of the oligomers can be controlled and selected by the mixing of appropriate amounts of each component.

The formation of the protein complexes can be considered equivalent to the formation of ligand-protein complexes where multiple ligands can bind to a single receptor. Scatchard analysis (16) can be used to examine such ligand-receptor binding to provide an estimate of association (dissociation) constants and the number of binding sites. This comparison is schematically represented in Figure 4.10. For convenience, L stands for ligand, P designates the protein (In our case, P means His-tagged thioredoxin).

Simple Scatchard analysis is based on two assumptions. (1) Equivalence: the binding to each site of the central molecule is the same, i.e. the equilibrium constant is the same for each site. (2) Independence: the binding at one site is independent of binding to other sites,
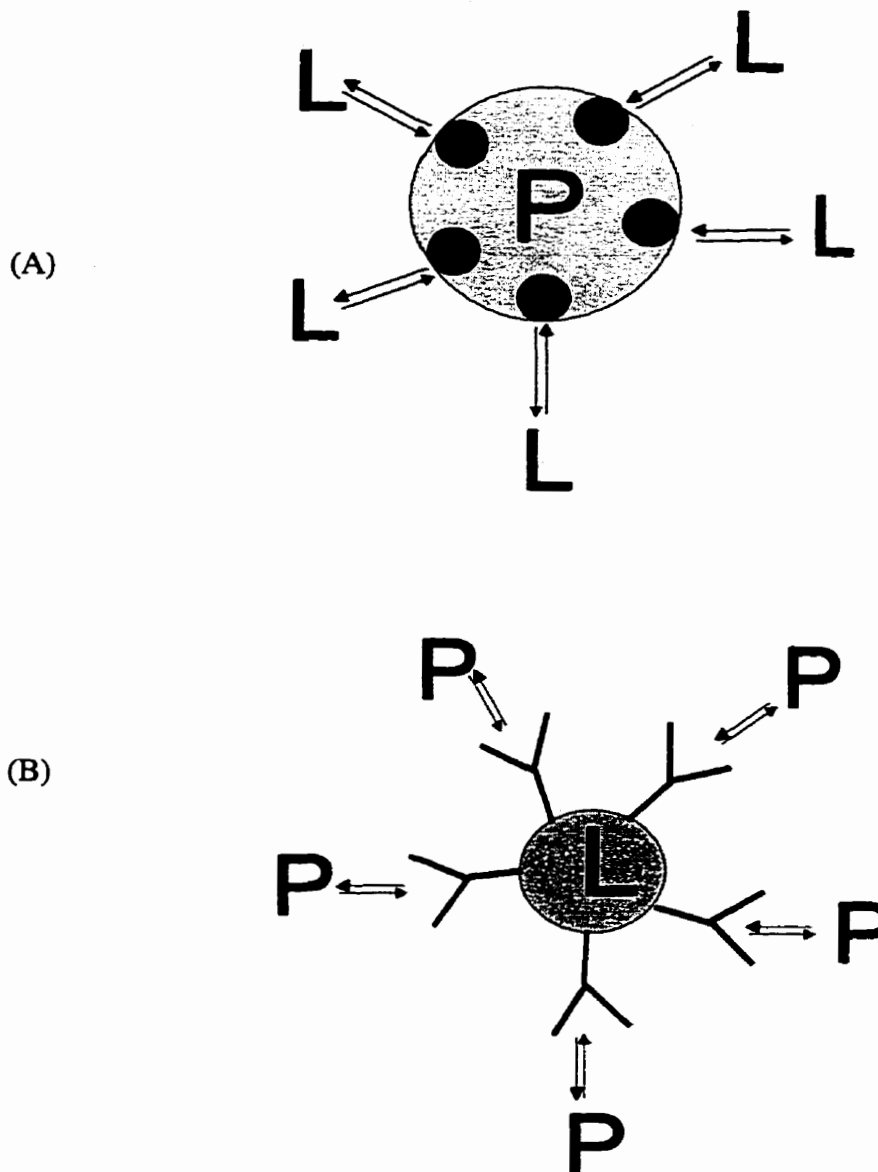
Figure 4.10: Graphical representation of macroprotein bound by multiple ligands (A) and dendritic ligand bound by multiple proteins (B). (A) P is a macroprotein, L is ligand which is bound to protein independently, ●standards for equivalent binding site. These bindings are in equilibrium and can be described by Scatchard Equation. (B) L is dendritic ligand with multiple terminal NTA groups which are independent, and these sites (NTA groups) are bound equivalently by His-tagged proteins, P stands for His-tagged protein. The binding equilibriums are expected to be interpreted by similar Scatchard equation.

i.e. the equilibrium constant at one site is independent of whether a protein is bound at any other site or not. Let γ be the number of sites occupied by protein and N, the total number of NTA groups on the ligand. Then, $\theta = \gamma/N$ is the fraction of binding sites occupied by protein. It is straightforward to show Equation 4.2:

Equation 4.2

$$\theta = \frac{[P]_{bound}}{[L]_{total}} = \frac{[LP]+2[LP_2]+3[LP_3]+\cdots N[LP_N]}{[L]+[LP]+[LP_2]+[LP_3]+\cdots[LP_N]} = \frac{\sum_{i=1}^{N}i[LP_i]}{\sum_{i=0}^{N}[LP_i]}$$

Where $[LP_i]$ = concentration of ligands to which exactly i proteins are bound. In this equation, the top sum starts at $i = 1$, since the concentration of free ligand [L] does not contribute to the total concentration of bound proteins. Also $[LP_i]$ is multiplied by i in the top term, because each ligand has i proteins. In contrast, [L] contributes to the total ligand concentration, so the bottom sum starts at $i = 0$. Also each $[LP_i]$ contributes only one ligand to the sum and there is no multiplicative factors. Using the assumptions of equivalence and independence, some mathematical manipulations give the fraction of each binding site of ligand occupied by proteins (θ) as

Equation 4.3: $\theta = \dfrac{[P]K_a}{1+[P]K_a}$ or $\theta = \dfrac{[P]}{K_d+[P]}$

Where K_a is the association constant for binding a protein to an NTA site and $K_d = 1/K_a$ is the corresponding dissociation constant. Accordingly, a series of Equations 4.4 should be followed.

Equation 4.4: $N\theta = \gamma = \dfrac{N[P]K_a}{1+[P]K_a}$ $\Rightarrow$ $\dfrac{\gamma}{[P]} = -K_a\gamma + NK_a$

$$\text{or} \quad N\theta = \gamma = \frac{N[P]}{K_d + [P]} \quad \Rightarrow \quad \frac{\gamma}{[P]} = -\frac{1}{K_d} \cdot \gamma + \frac{N}{K_d}$$

It has been estimated that the association constant (K_a) for NTA binding Ni^{2+} and a histidine tag is $\sim 10^{13}$ M^{-1} (17, 18, 19). The observations made here suggest that the complexes are saturated with protein (i.e. $\gamma = N$) which will happen whenever the concentration of free protein [P] is greater than 10^{-13} M. Clearly, such low concentrations of monomers are not detectable in the mixture.

The large association constant provides the opportunity to prepare saturated protein complexes. These stoichiometric complexes then have sizes that depend only on the number of NTA groups in the complexing agent. The set of reagents **6a-e** can now be used to specifically and selectively make dimers, trimers, tetramers, pentamers or hexamers. Although there are six histidines on each His-tagged protein, the 6xHis tag appears to bind only one NTA group. Otherwise, there would have been opportunity for higher order polymers to form in an uncontrolled manner.

The native electrophoresis method is presented to observe the formation and separation of multiprotein complexes. The successful resolution of His-tagged thioredoxin complexes is very important to us under non-denaturing conditions. All of the reagents including the protein itself used for protein complexes are water soluble, therefore we perform all the systems in solution. The electrode buffer was found to be suitable for the demonstration of multiprotein complexes, because these complexes were not prone to dissociation. The native PAGE described here is distinct from other literature methods in three respects: the introduction of KCl solution to increase the ionic strength, the running pH of 8.0 to avoid protein denaturation and dissociation of protein complexes, and the optimal combination of ligand, nickel ion solution and protein monomer solution.

It is known the reversibility of NTA-Ni-Histidine complex can be achieved by changing pH of the surrounding environment of this complex, the addition of imidazole at pH 8 or competitive chelator. When the imidazole nitrogen (pKa of 6.0) of histidine residue in protein is protonated, the protein complex will be decomposed, because it generates a

positively charged ammonium ion, which is repelled by the positively charged metal atom (20, 21). Also the bound 6xHis protein can competitively come off at pH 8.0 by simply adding imidazole to the protein solution, since imidazole is identical to the histidine side chain. An alternative EDTA treatment would dissociate the complex, because the binding constant in tetrahedral EDTA-Ni complex is higher than that in octahedral NTA-Ni-protein complex as observed in Figure 4.3B and Figure 4.9 (18, 19). The exhibiting reversibilities of NTA-Ni-Histidine complex are depicted in Figure 4.11.

In summary, the approach in this chapter is to use a relatively small *Escherichia coli* His-tagged thioredoxin to selectively and specifically control the formation of dimeric, trimeric, tetrameric, pentameric, and hexameric complexes by metal ion affinity binding. Not only can the association of proteins be generated by dendritic ligands containing shorter chain linkers (**6a, 6b, 6c, 6d** and **6d**), but also the aggregation of His-tagged thioredoxin has been proved with two other ligands (**12a** and **12b**) containing longer chain linkers. The association of large protein complexes manipulated by NTA ligands has been proved and found the binding can be reversed by the addition of EDTA.

4.6 Significance

We demonstrated that the protein complex can be dissociated following the addition of excess EDTA (Figure 4.3B and Figure 4.9). This phenomena confirms that the dendritic ligands which were synthesized in Chapter 3, can induce the aggregation of proteins in solution through the NTA-Ni-Histidine tag complex. We found this result to be interesting, and it is expected that the results presented here could be very useful for many biological processes. The reversibility also suggests important applications of these reagents. For example, the aggregation of cell surface receptors on cell membranes could be specifically controlled by using dendritic ligands containing a specific number of NTA groups. Thus, we could measure the diffusion coefficients of membrane protein clusters and His-tagged transmembrane polypeptide aggregates of controlled sizes, or we could determine their distributions by fluorescence microscopy. Importantly, we could also determine the dynamic properties of the corresponding monomers in the same sample by the subsequent addition of
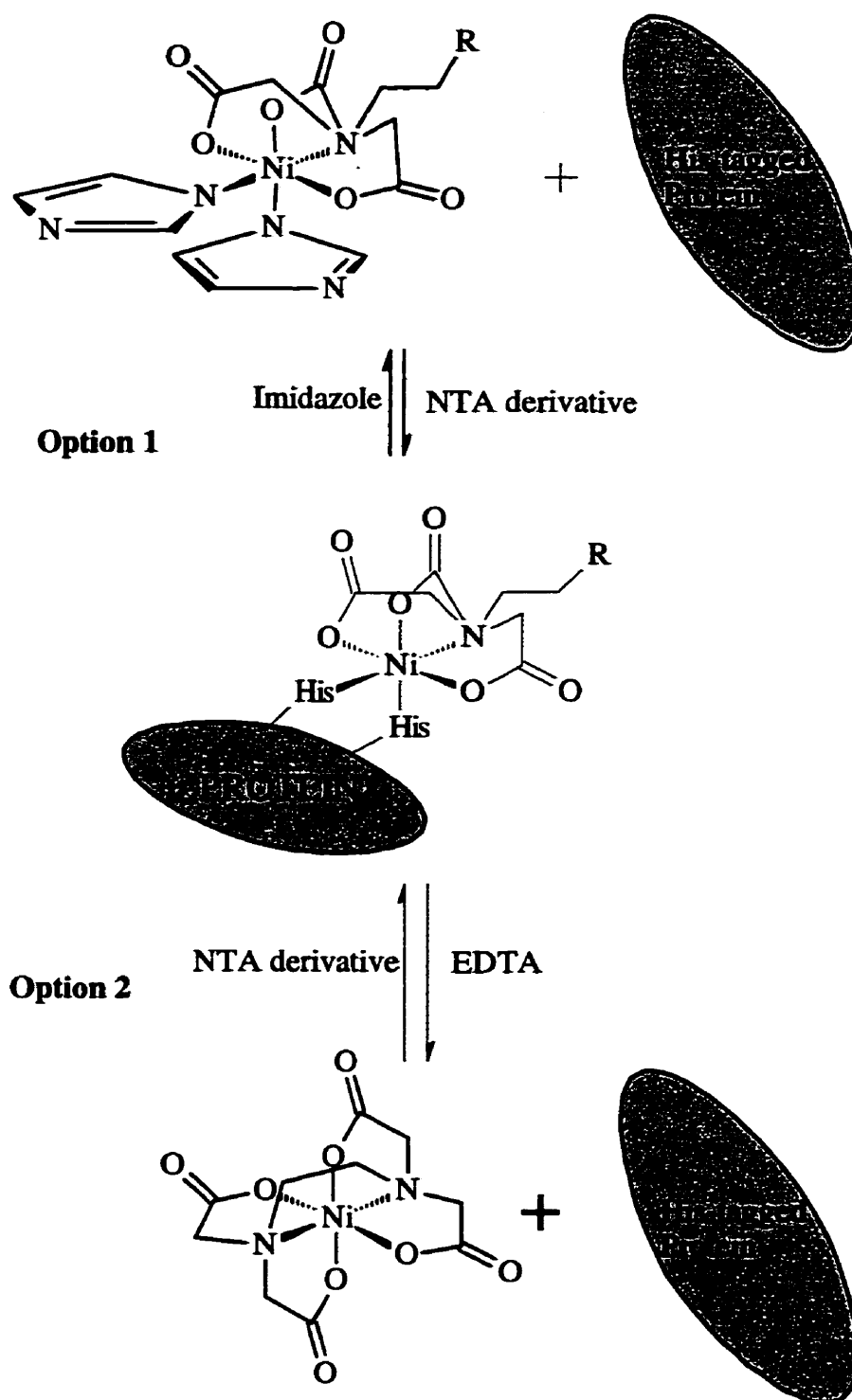
Figure 4.11: The schematic diagram shows the two reversible possibilities of NTA-Ni-Histidine protein complex. The complex is dissociated by imidazole (option 1) and by EDTA (option 2). R could be any substituent.

EDTA. In addition, these compounds (**6a-e** and **12a-b**) could possibly be used as complexing reagents to aggregate membrane receptors and thus to initiate signal transduction events. This would allow us to study the kinetics of activation as a function of aggregate size. Using EDTA would allow for natural control experiments.

We have used a very simple molecular interaction event, ligand-metal-protein complexation, to a particular model protein in complex solutions. The His-tagged thioredoxin molecules can be associated from specific sizes of protein complexes without perturbing protein functions. The uses of His-tagged thioredoxin and our dendritic chelating agents (**6a-e** and **12a-b**) to investigate the protein aggregation in solution, constitutes a proof of principle. We have verified that the binding is reversible and stoichiometric. Since the interaction of NTA with histidines is specific, it is expected that any recombinant His-tagged proteins can be selectively aggregated by these two sets of series of dendritic ligands (**6a-e** and **12a-b**). This is particularly important in the case of recombinant proteins expressed at low levels in biological cells. Numerous proteins have been expressed with His-tag sequences (22, 23, 24). The choice of the 6xHis-tag should not prevent proper folding and function of active protein. This is relevant to immobilize many receptor binding domains at the surface for subsequent interactions with ligand or other proteins. In addition, the 6xHis-tag can be replaced by a metal binding site engineered into the protein, resulting in a protein with a yet higher affinity constant for the formation of the chelating complexes (18, 19, 20). Metal-histidine tag affinity chromatography has been unambiguously used to demonstrate dimer formation of the cytoplasmic domain of transmembrane osmosensor protein (25). It is now possible to probe and manipulate the state of aggregation of these proteins in cells and thereby mimic or affect cellular processes. Ultimately, we believe that the described approach in this chapter, such as generating large protein complexes by metal affinity binding, combined with native PAGE technique, will offer new possibilities for investigation of ligand-protein interaction and protein associations in solutions.

4.7 References

1. Edidin, M. Translational diffusion of membrane proteins. In "The structure of biological membranes" (P. Yeagle, Ed.), **1992**, pp. 539-572. CRC Press, Boca Raton, Florida.

2. Edidin, M. Getting there is only half the fun. *Curr. Top. Membr.* 1996, 43, 1-13.

3. Zhang, F., Lee, G.M., and Jacobson, K. Protein lateral mobility as a reflection of membrane microstructure. *BioEssays*, **1993**, 15, 579-588.

4. Höög, J.-O., von Bahr-Lindström, H., Josephson, S., Wallace, B.J., Kushner, S.R., Jörnvall, H., and Holmgren, A. Nucleotide sequence of the thioredoxin gene from Escherichia coli. *Bioscience Rep.* **1984**, 4, 917-923.

5. Georgescu, R.E., Li, J.-H., Goldberg, M.E., Tasayco, M.L., and Chaffotte, A.F. Prolin isomerization-independent accumulation of an early intermediate and heterogeneity of the folding pathways of a mixed α/β protein, *Escherichia col* thioredoxin. *Biochemistry*, **1998**, 37, 10286-10297.

6. Jeng, M.F., Campbell, A.P., Begley, T., Holmgren, A., Case, D.A., Wright, P.E., and Dyson, H.J. High-resolution solution structures of oxidized and reduced Escherichia coli thioredoxin. *Structure*, **1994**, 2, 853-868.

7. Katti, S.K., LeMaster, D.M. and Eklund, H. Crystal structure of thioredoxin from *Escherichia coli* at 1.68 Å resolution. *J. Mol. Biol.* **1990**, 212, 167-184.

8. Yasukawa, T., Kanei-Ishii, C., Maekawa, T., Fujimoto, J., Yamamoto, T. and Ishii, S. Increase of solubility of foreign proteins in *Escherichia coli* by coproduction of the bacterial thioredoxin. *J. Biol. Chem.* **1995**, 270, 25328-25331.

9. Hochuli, E.; Döbeli, H.; Schaher, A. New metal chelate adsorbent selective for proteins and peptides containing neighboring histidine residues. *J. Chrom.* **1987**, 411, 177-184.

10. Hawcroft, D.M. Electrophoresis: The Basis. Published in the United States by Oxford University Press Inc., New York. Printed in Great Britain by Bath Press Ltd., Bath, Avon, **1997**.

11.   Hames, B.D. and Rickwood, D. (eds) Gel Electrophoresis of Proteins: A Practical Approach (2rd edn). IRL Press at OUP, Oxford. **1990**.

12.   Patel, D. Gel Electrophoresis, Essential Data. John Wiley and Sons Ltd, Chichester and BIOS Scientific Publishers Ltd, Oxford, **1994**.

13.   Neville, D.M. Molecular weight determination of protein-dodecyl sulfate complex by gel electrophoresis in a discontinuous buffer system. *J. Biol. Chem.* **1971**, 246, 6328-6334.

14.   Bradford, M.M. A rapid and sensitive method for the quantitation of microgram quantities of protein utilizing the principle of protein-dye binding. *Anal. Biochem.* **1976**, 72, 248-254.

15.   Weber, K. and Osborn, M. The reliability of molecular weight determinations by dodecyl sulfate-polyacrylamide gel electrophoresis. *J. Biol. Chem.* **1969**, 244, 4406-4412.

16.   Klotz, I.M. *Ligand-Receptor Energetics: a guide for the perplexed.* A Wiley-Interscience Publication, John Wiley & Sons, Inc. New York, **1997**.

17.   Schmidt, A.M., Müller, H.N., Skerra, A. A Zn(II)-binding site engineered into retinol-binding protein exhibits metal-ion specificity and allows highly efficient affinity purification with a newly designed metal ligand. *Chem. Biol.* **1996**, 3, 645-653.

18.   Shmitt, L., Dietrich, C., Tampé, R. Synthesis and characterization of chelator-lipids for reversible immobilization of engineered proteins at self-assembled lipid interfaces. *J. Am. Chem. Soc.* **1994**, 116, 8485-8491.

19.   Dorn, I.T., Neumaier, K.R. and Tampé, R. Molecular recognition of His-tagged molecules by metal-chelating lipids monitored by fluorescence energy transfer and correlation spectroscopy. *J. A. Chem. Soc.* **1998**, 120, 2753-2763.

20.   Müller, K.M., Arndt, K.M., bauer, K., and Plückthun, A. Tandem immobilized metal-ion affinity chromatography/immunoaffinity purification of His-tagged proteins-Evaluation of two anti-His-tag monoclonal antibodies. *Anal. Biochem.* **1998**, 259, 54-61.

21. Qiagen, The QIAexpressionist. A handbook for high-level expression and purification of 6xHis-tagged proteins. CLONTECH Laboratories, Inc, Palo Alto, CA, USA. March, **1997**.

22. Hochuli, E. In *Genetic Engineering*, Ed. By Setlow, J.K. Plenum Press, New York, **1990**.

23. Dolja, V.V., Peremyslov, V.V., Keller, K.E., Martin, R.R., Hong, J. Isolation and stability of histidine-tagged proteins produced in plants via polyvirus gene vectors. *Virology* **1998**, 252, 269-274.

24. Bader, B., Knecht, W., Fries, M., Löffler, M. Expression, purification, and characterization of histidine-tagged rat and human flavoenzyme dihydroorotate dehydrogenase. *Protein Expr Purif* **1998**, 13, 414-422.

25. Hidaka, Y., Park, H., and Inouye, M. Demonstration of dimer formation of the cytoplasmic domain of a transmembrane osmosensor protein, EnvZ, of *Escherichia coli* using Ni-histidine tag affinity chromatography. *FEBS Lett*, **1997**, 400, 238-242.

CHAPTER 5 CONFIRMATION OF THE AGGREGATION OF HIS-TAGGED THIOREDOXIN WITH IMAGE CORRELATION SPECTROSCOPY

In Chapter 4, we used dendritic NTA ligands binding with Ni^{2+} and histidine residues of affinity tagged fusion proteins to form large protein complexes in solution. The formation of His-tagged thioredoxin oligomers was demonstrated with simple native PAGE technique. The objective of this chapter is to confirm the presence of His-tagged thioredoxin aggregates on a surface using a high-resolution biophysical technique, namely image correlation spectroscopy (ICS).

5.1 Fluorescence spectroscopy of single molecules

Recent years have seen significant advances in the characterization and manipulation of individual molecules. Scanning probe techniques allow study of single molecules on surfaces (1, 2, 3, 4, 5) and in solutions (6, 7), and optical techniques enable their characterizations in complicated environments (8, 9). We are particularly interested in single-molecule detection and single-molecule spectroscopy at room temperature. Laser-induced fluorescence coupled with high resolution microscopes offer new tools for the study of individual macromolecules on surfaces and under physiological conditions.

Fluorescence microscopy is very useful for observing small objects. It was demonstrated about fifteen years ago that single actin filaments (double-helical polymers of actin), which were labelled with fluorescent phalloidin, could be seen clearly by fluorescence microscopy in intact cells (10). This finding led to the development of new *in vitro* motility assays that address the elementary process of force generation by actin-myosin interaction directly at the molecular level (11). More recently, observations at the level of individual molecules have become possible by microscopy and spectroscopy (1, 2). Laser-induced fluorescence detection of single fluorescent molecules is one very sensitive tool for fluorescence-based assays in analytical chemistry, biology, and medicine (5, 6, 7, 8, 9). Single-molecule spectroscopy eliminates ensemble averaging and allows individual members of population to be probed, thereby yielding more direct information regarding the

distribution of molecular and kinetic properties. This constitutes a major step toward the study of single-molecule dynamics and molecular recognition in solution and at surfaces.

The number of photons emitted from a single fluorophore excited by a strong light source such as a laser is sufficient for it to be visualized by a commercial, high-sensitivity video camera. Confocal microscope techniques (5, 12) have been used to measure fluorescence bursts caused by individual molecules diffusing through a microscopic measurement volume. Analysis of several bursts results in an averaging of properties over the single-molecule population under analysis. Schmidt et al has measured diffusion using single molecule imaging (1). Elegant techniques, such as single particle tracking (SPT), have been developed to characterize the diffusion and other motions in model membranes and on surfaces of living cells (13, 14, 15).

Conventional fluorescence spectroscopy has been utilized to study macromolecular clustering in both artificial and cell membranes. Early studies provided qualitative evidence of surface reorganization and clustering of receptors after the addition of ligands (16, 17, 18). Fluorescence resonance energy transfer (FRET) techniques have recently provided strong evidence of spatial colocalization of receptor macromolecules on the surface of living cells (19, 20). However, FRET doesn't yield information about the actual size of the aggregates. Fluorescence video imaging microscopy techniques have been successfully used to track the motions of receptor aggregates and simultaneously quantify the distribution of cluster sizes (21). These methods are advantageous in that they provide complete information about the aggregate state in combination with a measurement of receptor motional dynamics. But they are computationally intensive and require operator tracking of fluorophores in each image, making it labor intensive as well.

Fluorescence correlation spectroscopy (FCS) analyzes the fluctuations in fluorescence intensity in a small volume of a system at equilibrium (22, 23, 24). Image correlation spectroscopy (ICS) analyzes the spatial variation of fluorescence intensity across a surface. ICS is an adaptation of the FCS methods used to analyze fluorescence images collected on laser scanning confocal microscope. It is sensitive to and capable of quantifying differences in the aggregation state of fluorescent labelled components at cell surface. In ICS,

instead of observing fluorescent particles as they diffuse in and out of a fixed laser beam, one generates an image of the fluorescence intensity on the surface by scanning a fluorescent labelled sample with a laser beam, recording fluctuations in fluorescence intensity as a function of position rather than of time (25, 26). The analysis provides information about the dynamics of motion of individual molecules, or aggregates of molecules. The amplitude of fluctuations depends on the state of aggregation of the system. This technique has been developed and used in our group to quantify the distribution of cell surface receptors (25, 26, 27, 28, 29, 30). The ICS is an alternative technique to measure the state of aggregation of the His-tagged thioredoxin observed in solution as described in Chapter 4.

5.2 Approach

To use ICS to confirm the His-tagged thioredoxin aggregations, we need to fluorescently label the protein. We then must immobilize the aggregates on a glass surface so that they can be imaged in the confocal microscope. Accumulation of many confocal microscopy images increases sensitivity. Correlation analysis of the magnitude of the intensity fluctuations yields the number of fluorescent particles, or clusters, present per unit area. The total fluorescence intensity reflects the total number of molecules in the same area. Correlation of these values leads to a measure of the degree of aggregation or size of the cluster.

5.2.1 Labeling of His-tagged thioredoxin

Two fluorescent dyes were chosen to covalently label His-tagged thioredoxin. Fluorescein isothiocyanate (FITC), and rhodamine in the form of Rhodamine Red^{TM}-X (RRX), are frequently used in labeling proteins. Their structures are shown in Figure 5.1. FITC is the most commonly used green reagent dye in fluorescence microscopy because it has high absorptivity, a high quantum yield, and it is water soluble so that it can easily be reacted with proteins. The labeling by FITC is through the conjugation of its isocyanate group with the amine side chain of the lysine amino acid residue present in any proteins.
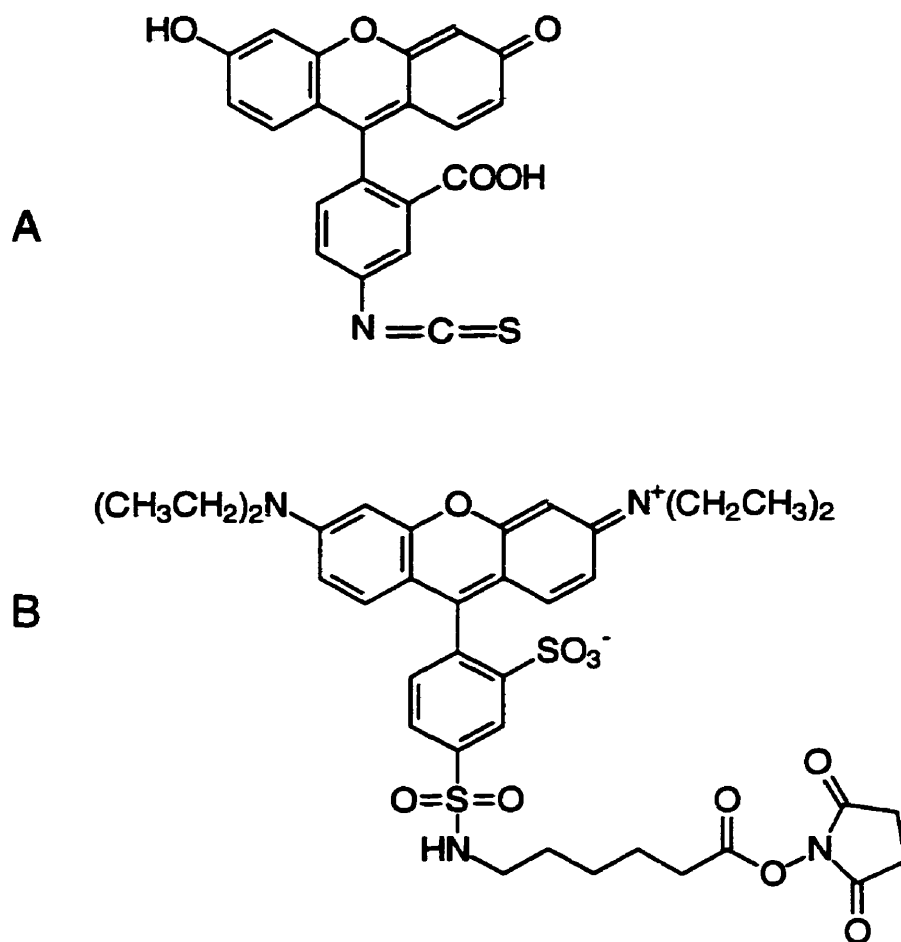
Figure 5.1: A) Chemical structure of the 5-isomer of the fluoresce
reagent dye fluorescein isothiocyanate (FITC); B) and one isomer
of reagent dye Rhodamine Red™-X (RRX).

Since the labeling is easy and the conjugation is stable, there are many FITC labelled antibodies or proteins commercially available. FITC is readily excited by the 488 nm laser line (maximum absorption is 494 nm) of the argon or the Ar/Kr mixed gas laser. FITC is easily photobleached, and the emission is pH sensitive. RRX is a succinimidyl ester of lissamine rhodamine. Succinimidyl esters react efficiently with aliphatic amines to give stable red conjugated products. The RRX-labelled proteins can be excited by the 568 nm laser line with the Ar/Kr laser and exhibit higher intensities at the same degree of dye substitution than FITC conjugates. Both of these dyes were conjugated to His-tagged thioredoxin. The intensity of FITC-labelled species was very low and photobleaching was a problem. Thus RRX (Rhodamine Red^{TM}-X) was the reagent of choice.

5.2.2 Performing image correlation spectroscopy

The fluorescent labelled protein is used to make its complexes. The solutions of fluorescent protein complexes are prepared as described in Chapter 4 and are adjusted to an appropriate concentration for confocal imaging. A drop of each protein complex solution can be deposited on a dry, clean coverslip (22 mm in diameter) and dried to immobilize the proteins on the glass surface. These samples can subsequently be examined and imaged using a confocal scanning laser microscope. Once fluorescent confocal images are collected, ICS technique can be applied to quantitate the stoichiometry of these fluorescent protein complexes.

The ICS is usually used in our research group to characterize the quantitative distribution of cell surface receptors (25, 28, 29). It involves an autocorrelation analysis of the intensity fluctuations within confocal images which, in this case, should arise from the covalently labelled His-tagged thioredoxin complexes which were formed by affinity binding of NTA-Ni-Histidine residues in solution. In ICS, the normalized or relative intensity fluctuation $\delta i(x,y)$, is defined as

Equation 5.1
$$\delta i(x, y) = \frac{i(x, y) - <i(x, y)>}{<i(x, y)>}$$

Where i(x,y) is the intensity of the pixel at the image location in x,y plane, and the angle brackets, < >, indicate an average over all pixels, i.e. <i(x,y)> is the average pixel intensity in the image. An intensity two-dimensional autocorrelation function is obtained as:

Equation 5.2 $\quad g(\xi,\eta) = < \delta i(x, y)\delta i(x + \xi, y + \eta) >$

The autocorrelation function is a function of two independent spatial lag variables which relate to the two independent scan directions (ξ and η) of the image. The limit of the autocorrelation function as ξ and η approach zero, is equal to the variance of the relative intensity fluctuation. This variance can be shown to be inversely proportional to $\bar{N}p$, the average number of particles (molecules) in the observation volume.

Equation 5.3 $\quad \lim_{\xi\to 0,\eta\to 0} g(\xi,\eta) = g(0,0) = \mathrm{var}\,\delta i(x,y) = \dfrac{\dot{1}}{\bar{N}_p}$

Hence the magnitude of the autocorrelation function g(0,0) is a direct measure of the density of the fluorescent particles. The term "particles" refers to any fluorescent species, i.e. a particle can be protein monomer, but a oligomer or aggregate of proteins containing many monomers can also be a particle. The g(0,0) value is an extensive parameter, since it is dependent on the observation area, and it is inversely proportional to the average number of independent particles. In some cases, it is more convenient to use an intensive parameter, the cluster density (CD), which represent the number of protein clusters (independent particles) per unit area.

Equation 5.4 $\quad CD = \dfrac{1}{g(0,0)\pi\omega^2} = \dfrac{\overline{N_p}}{\pi\omega^2}$

The degree of aggregation (DA) may be introduced to represent the average number of monomers per aggregate as shown in Equation 5.5. As above, <i(x,y)> the average intensity, gives an estimate of the total number of protein monomers $\bar{N}_m$, and 1/g(0,0) gives an estimate of the average number of independent protein clusters ($\bar{N}_p$). α is a constant involving instrumental and experimental parameters.

$$\text{Equation 5.5} \quad DA = \langle i(x,y) \rangle g(0,0) = \alpha \frac{\overline{N_m}}{\overline{N_p}}$$

In this Chapter, we use image correlation spectroscopy to determine the cluster density and the degree of aggregation of fluorescent labelled His-tagged thioredoxin deposited on glass surfaces. We confirm the findings from Chapter 4 that complexes of specific stoichiometry can be detected. We also demonstrate that ICS has the sensitivity to make these observations on a surface. This illustrates the potential for using the dendritic NTA probes as reagents to cluster proteins in membranes and ICS to detect their effectiveness.

5.3 Material and Methods

FluoReporter protein labelling kits containing fluorescent dyes Rhodamine Red-X (RRX) were purchased from Molecular Probes. Sephadax G-50 was obtained from Pharmacia. His-tagged *E. coli* thioredoxin was provided by Dr. Eric Ball. The chelating agents 6a-e were synthesized in our laboratory as described in Chapter 3. $NiCl_2$, $NaHCO_3$, NaCl, Na_2HPO_4 were bought from BDH.

5.3.1 Labeling of His-tagged thioredoxin

Labeling of His-tagged thioredoxin was conducted at room temperature for three hours according to the procedure from Molecular Probes. But the spinning column was not used to separate the labelled protein from other non-labelled ones. A small amount (0.2 mL) of protein (His-tagged thioredoxin) solution was transferred to a reaction tube, and followed with an addition of 20 µL of freshly prepared PBS buffer (1 M $NaHCO_3$, 10 mM Na_2HPO_4, 150 mM NaCl, pH 8.3). Dimethylsulphoxide (0.5 mL, DMSO) was added to the vial containing Rhodamine Red-X, to give a concentration of dye of 5 mg/mL. This solution was mixed with the pipet until the dye was completely dissolved. The amount of dye solution required for conjugation was calculated using the following equation (31).

Equation 5.6:

$$mL \ dye \ stock \ solution = \frac{mg/mL \ protein \times 0.2 \ mL}{MW_{protein}} \times 771 \times 200 \times MR$$

Where 0.2 mL is the volume of protein solution, MR is the molar ratio of dye to protein in the reaction mixture, 771 is the MW of dye, 200 is a unit conversion factor. The MW of *E. Coli* His-tagged thioredoxin is 12000. The concentration of protein was determined in a unit of mg/mL with the Bradford method as described in Chapter 4. The calculated amount of dye solution was added to the reaction tube containing protein in PBS buffer. After the conjugation mixture was stirred at room temperature for 3 hours, hydroxylamine solution in DMSO (1/40th of the volume) was added to quench the conjugation. The resulting reaction solution was stirred further for 30 minutes at room temperature. The conjugation mixture was freeze-dried with lyophilizer (ETS System, Inc.) and this concentrated protein residue was applied to gel filtration.

5.3.2 Purification and concentration determination of fluorescent His-tagged thioredoxin

A Sephadex G-50 medium (5 g) was swelled with 50 mL of 20% ethanol solution in water for at least 2 hours. A column (1 cm in diameter) was filled smoothly to 25 cm height with the swollen beads and washed to equilibrate with PBS buffer (1 M $NaHCO_3$, 10 mM Na_2HPO_4, 150 mM NaCl, pH 8.3) for 2 hours. Then the fluorescent sample residue was loaded and eluted with this PBS buffer. Fractions were collected into 2 mL tubes. The required labelled proteins were located in the first fraction, since they are the largest molecule in the mixture of conjugation reaction. Most of the solvent was removed to lyophilize the labelled protein solution. The concentration of the resulting fluorescent His-tagged thioredoxin solution was determined by UV absorption (Cary UV-visible 100 BIA, Varian) at 280 nm using Equation 5.7.

$$mg/mL \ protein = \frac{[A_{280} - (A_{max} \times 0.17)] \times dilution \ factor}{1.4}$$

Equation 5.7

Where 0.17 is a correction factor, 1.4 is the absorbance of protein at 1 mg/mL, dilution factor is the number of the diluted times of fluorescent protein, A_{max} is the absorbance at maxium wavelength (580 nm). 1.4 will be replaced by ϵ, the molar extinction coefficient of the protein at 280 nm if the concentration is calculated as unit of mol/L (M).

To determine the extent of fluorescent labeling for the purified conjugate, the A_{max} at 580 nm in pH 8.0 buffer was measured using the following equation:

$$dye\ per\ molecule = \frac{A_{max} \times dilution\ factor}{\varepsilon} \times \frac{12000}{mg\ /\ mL\ labelled\ protein}$$

Equation 5.8

Where ϵ is the molar extinction coefficient of the conjugated dye, its value is 120,000 at 580 nm for RRX. 12000 is the molecular weight of His-tagged thioredoxin, the dilution factor is the number of the diluted times of fluorescent protein solution, and the concentration of fluorescent protein is calculated in a unit of mg/mL from Equation 5.7.

5.3.3 Sample preparation

The fluorescent protein monomers were obtained as described above. The protein complex solutions were prepared in a similar way as described in Chapter 4 using the fluorescent protein solution, chelating agents 6a-e and $NiCl_2$ solution. After determining the concentration of fluorescent His-tagged thioredoxin with the absorbance at 280 nm (A_{280}) using Equation 5.7, the protein solution was combined with a mixture of NTA chelating agent and nickel chloride solutions according to the molar ratio described in Chapter 4, separately. All concentrations of His-tagged thioredoxin complexes were adjusted at level of 50-60 nM in terms of its monomers, in order to make comparisons and to avoid automatically oligomerization of His-tagged thioredoxin. A drop of 20 μL of the diluted His-tagged thioredoxin complex solution was deposited on dry, clean 22 mm coverslips which were sonicated for half an hour. The coverslip was placed in a laminar flow hood for 3-4 hours until completely dried and immobilized on glass surfaces. Then the samples on the coverslips were mounted on microscope slides using Airvol containing n-propylgallate. All the samples were marked and were ready to be examined and imaged using a confocal

scanning laser microscope.

5.3.4 Laser scanning confocal microscopy

Once the protein complex of interest is prepared, fluorescent images of the protein complexes were collected under a Biorad MRC 600 confocal microscope (Biorad Microscience, Ltd., Hertfordshire, England) at room temperature. The MRC-600 is supplied with all its operating software setup on the hard drive. Each sample of the protein complexes on microscope slide was visualized using an inverted configuration Nikon epifluorescence microscope which was part of the MRC 600 Biorad system. A 60× oil immersion objective (numerical aperture 1.40) was used for all measurements. Samples were examined through this objective using a 25 mW Ar/Kr mixed gas laser as the illumination source. Excitation of the RRX labelled protein was achieved using the 568 nm Kr-line. The fluorescence was detected by the photomultiplier tube operating in the photon counting mode for the rhodamine labelled samples. A filter block for rhodamine imaging was inserted in the scan box of the instrument. The gain knob was set to position 10, this is usually best for preventing saturation and the low black current background. The pinhole aperture was opened to a setting of 5.8 on the Biorad vernier scale corresponding to a beam size at the focus point of about 0.34 μm. The fluorescent specimen of each protein complex on the glass surface was scanned with the laser, using the raster scanning optics of the confocal microscope. Appropriate shutters were closed and opened to switch the microscope from optical to confocal mode. The confocal microscope was controlled using PC based software called COMOS (Biorad). COMOS controls all aspects of the imaging process via icons on a 486 PC's monitor. The program was used to select settings for the 60× objective, to set image size to 512 ×512 pixels. The normal scanning speed (one image or frame per sec.) was selected and the instrument zoom was set at zoom 1 first. The laser scanning was then initiated by clicking with the mouse on the laser icon. The fine focus knob was manually used to bring the scanned image into focus as seen on a second computer display monitor. The laser scanning was then terminated.

A typical confocal image of fluorescent His-tagged thioredoxin aggregate was

produced as shown in Figure 5.2A. Images were collected by accumulation of 25 scans using fast photon counting mode. All the image were collected as square images with 512 ×512 pixels at a zoom factor of 10 corresponding to 15.3 × 15.3 μm^2 areas. Using the fast photon counting feature of the confocal microscope, the calibration procedure was carried out in order to ensure linear amplification of the intensity signal according the outline of Biorad MRC 600 users. Once the photon counting was calibrated, the direct scan mode in microscope was selected. It is necessary to do background measurements to ensure the short noise inherent in the photomultiplier detector of the confocal microscope. The background images were taken in the same procedure as sample (zoom 10, photon counting mode, and an equal number of scan accumulations as the sample). Usually the scanning and the accumulation of images take a total of ~ 30 seconds. Thirty-three to fifty-three images were collected for those samples on different parts of the coverslip, in order to accurately determine the population mean for each data point in an experiment. All confocal microscope images were printed on a Sony video printer and are then submitted for correlation analysis.

5.3.5 Image correlation spectroscopy (ICS)

ICS involves estimation of the autocorrelation function (Equation 5.2) from a two-dimensional array of intensity samples. The variability in the magnitude of the relative intensity fluctuations within the images is related to the variability in the number of proteins found in individual aggregates. A few spatially separated aggregates containing a large number of proteins will give rise to large intensity fluctuations. In contrast, more closely spaced aggregates with a small number of proteins will give rise to small intensity fluctuations. All spots in magnified images collected for our purposes are clusters of protein aggregates which should act as point sources in which case the spots will be comparable with the diameter of laser beam (~ 0.68 μm) (Figure 5.2A), i.e. they appear to be the size of the laser beam.

(A)
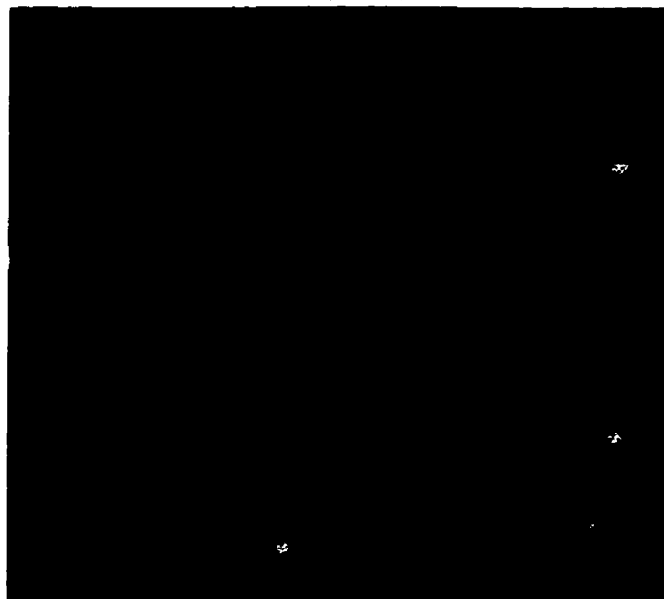
(B)
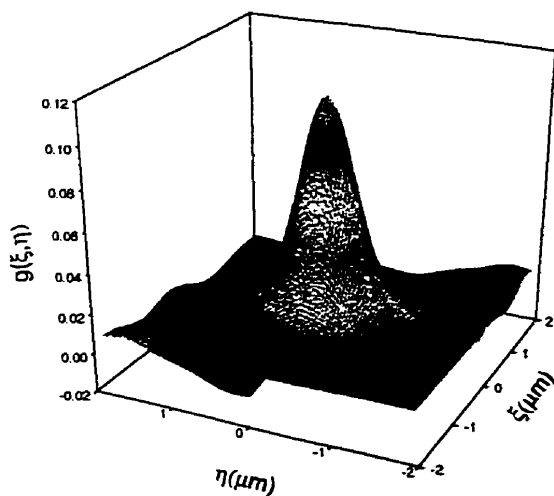
(C)
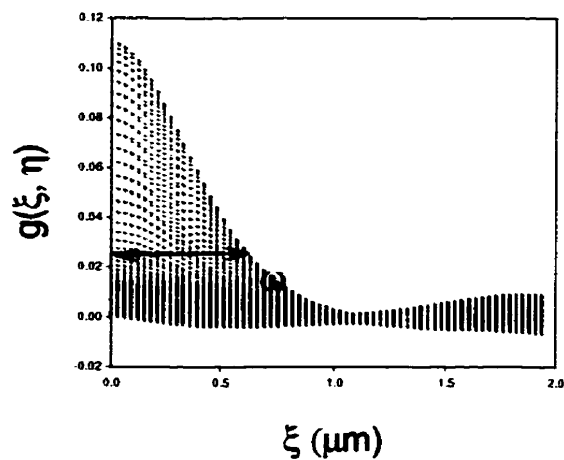
Figure 5.2: (A) Typical fluorescent confocal image of rhodamine-labelled His-tagged *E. coli* thioredoxin complexes which were formed by using of ligand **6b** in the area of 15.3 × 15.3 μm². (B) 2D autocorrelation function calculated from the image in (A). (C) 1D autocorrelation function calculated from the image (A) along the X axis ξ (μm), where ω is the observed laser beam radius.

The discrete normalized two-dimensional fluorescence fluctuation autocorrelation function can be calculated from Equation 5.9.

Equation 5.9:
$$g(\xi,\eta) = \frac{\frac{1}{NM}\sum_{x=1}^{N}\sum_{y=1}^{M} i(x,y)i(x+\xi,y+\eta)}{[\frac{1}{NM}\sum_{x=1}^{N}\sum_{y=1}^{M} i(x,y)]^2} - 1$$

The signal analysis is computationally tedious to calculate the correlation function of the fluorescence intensity fluctuations (Equation 5.9), we therefore use 2D Fourier transform technique. When a single fluorescent labelled component is analyzed, the autocorrelation function, $g(\xi,\eta)$, can be estimated by fitting the correlation function to a two-dimensional Gaussian function determined by the transverse intensity profile of the spots in the image.

Equation 5.10:
$$g(\xi,\eta) = g(0,0)e^{-(\xi^2+\eta^2)/\omega^2} + g_0$$

Where ξ and η are the position coordinates (for the x and y axes, respectively) of the autocorrelation function; ω is the e^{-2} radius of the laser beam; g_0 is an offset parameter, which reflects the finite image in dimensions, because the correlation function does not always vanish at large correlation distance. $g(0,0)$ is the value of the autocorrelation function upon extrapolation of ξ and η to zero (Figure 5.2B). Alternatively, the values of $g(0,0)$, ω, and g_0 can be extracted from the non-linear least squares fitting of the autocorrelation function of Equation 5.10 as represented in Figure 5.2C.

Importantly, as defined in Equation 5.3, $1/g(0,0)$ is equal to $\bar{N}p$, the average number of independent fluorescently labelled particles in the area illuminated by the beam (25, 31). We can expect that aggregation leads to a reduction in $\bar{N}p$, which is measured by the $1/g(0,0)$ value, since the larger the aggregate, the fewer particles. Also we expect to quantitatively detect the stoichiometry of each His-tagged thioredoxin oligomer by the determination of the cluster density (CD) values and the degree of aggregation (DA) values.

The <i> values reported in ICS had been corrected, because the fluorescence measured by confocal microscopy contains contributions from the background intensity, such

as white noise due to stray light and dark current in the photomultiplier tube. The background intensity was measured under conditions of no exposure of the laser beam to the sample. Hence the final average intensity value $<i>$ always has been corrected by subtraction of the black current counts from the measured intensity. Actually, the contribution from the black current to the final $<i>$ value was low, since the intensity recorded from 512×512 pixels by accumulated photon counting (25 scans) was quite high.

5.3.7 Data analysis

Correlation analysis was performed by two-dimentional Fourier transformation of each image, followed by complex conjugate multiplication of the transform by itself and finally reverse Fourier transformation. The resulting correlation function was normalized and the value 1 was subtracted to give the $g(\xi,\eta)$. The data were subjected to a fit for Equation 5.10 to give an estimate of $g(0,0)$, ω and g_0. The results of the ICS calculations were transferred to a PC computer and imported to Sigma Plot 4.01. Using Equations 5.4 and 5.5, the average intensity $<i>$, the frequency value $1/g(0,0)$, the cluster density (CD) and the degree of aggregation (DA) value were obtained in Sigma Plot. Finally the average value and the standard error of the mean (SEM) were calculated for each data point of all ICS measurements in Sigma Plot 4.01. The SEM values are expressed at the 99% confidence level. Each value was compared to the average and outliers were eliminated by z-score analysis. One-tailed student's t-tests for the difference between means were conducted using the formula $SEM = t(S.D./n0.5)$, where S.D. is the sample deviation, n is the number of measurements, t is the t statistic for n-1 degrees of freedom (equal to 2.576 at the 99% confidence level). p values were determined based on a t test for two independent samples with different variance (32). All calculations of the autocorrelation functions were carried out on a massively parallel computer (MasPar MP-2 with 2048 processors) at the Information and Technology Services of the University of Western Ontario (London, Ontario, Canada) for all of the measurements.

5.4 Results

5.4.1 Confocal images of fluorescent His-tagged thioredoxin aggregates

E. coli His-tagged thioredoxin was fluorescently labelled at room temperature by Rhodamine Red™-X (RRX). The rhodamine labelled proteins were purified by gel filtration, and directly used for protein complex formation. The concentration of each protein complex solution was determined in terms of protein monomers according to Equation 5.7. The concentration of fluorescent His-tagged thioredoxin aggregates was adjusted to be close to each other in all the protein complex samples.

Typical confocal images of protein complex are depicted in Figure 5.3. These representative fluorescent images were observed in a 15.3 ×15.3 μm^2 area for His-tagged thioredoxin monomers (A) and complexes, such as $N_2[NTA\text{-}Ni]_2[RP]_2$ (B), $N_3[NTA\text{-}Ni]_3[RP]_3$ (C), $N_4[NTA\text{-}Ni]_4[RP]_4$ (D), $N_5[NTA\text{-}Ni]_5[RP]_5$ (E), and $N_6[NTA\text{-}Ni]_6[RP]_6$ (F). These complexes were formed by using dendritic ligands 6a, 6b, 6c, 6d, 6e and appropriate amounts of $NiCl_2$ and His-tagged thioredoxin solution at pH 8. Each image is a spatial record of the signal, which represents individual fluorescent spots or accumulation of His-tagged thioredoxin aggregates. Qualitative differences can be observed between these images: the fluorescent spot size increases and the signal intensity of each spot increases.

5.4.2 Quantification of the His-tagged thioredoxin complexes

To quantify these differences, confocal images of flat 15.3 ×15.3 μm^2 areas of His-tagged thioredoxin monomers and complexes were collected on the glass surfaces and processed by autocorrelation analysis. Table 5.1 outlines all of the ICS experimental data for those samples which are abbreviated as RP, $N_2[NTA\text{-}Ni]_2[RP]_2$, $N_3[NTA\text{-}Ni]_3[RP]_3$, $N_4[NTA\text{-}Ni]_4[RP]_4$, $N_5[NTA\text{-}Ni]_5[RP]_5$, $N_6[NTA\text{-}Ni]_6[RP]_6$ in column 1. Column 2 contains the concentrations of all samples which were held approximately at 60 nM (0.7μg/mL) in term of the His-tagged thioredoxin monomers. By using the dendritic chelating agents 6a-e, the ω value (beam radius in a unit of μm) ranges from 0.60 to 0.77 and <i> (average intensity) ranges from 28 to33. Both of the 1/g(0,0) and CD (cluster density) values decrease as the size of central ring in the dendritic ligands increases. An increasing trend for the DA
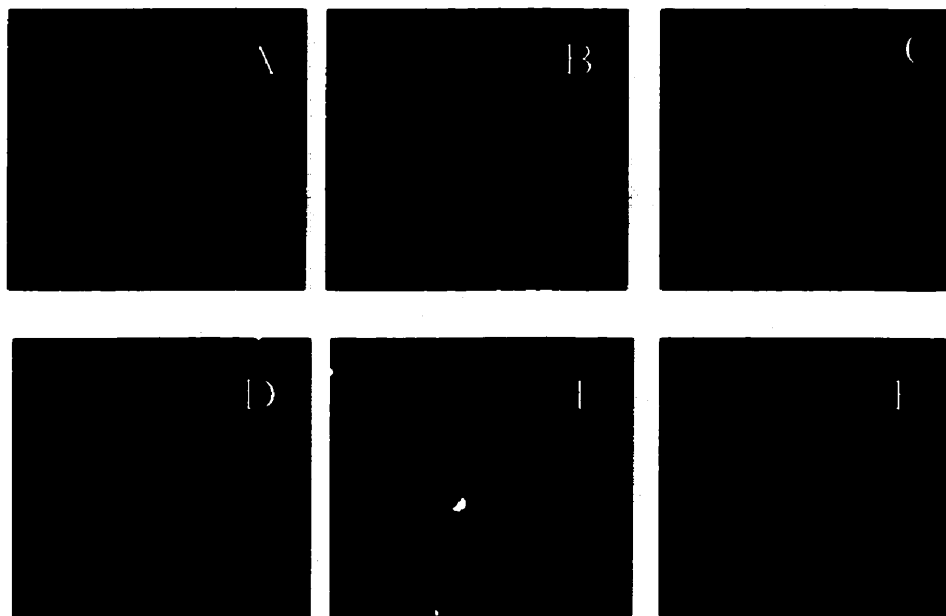
Figure 5.3: Representative confocal images of rhodamine labelled His-tagged thioredoxin monomers and complexes. The whole images were collected in the area of 15.3 μm × 15.3 μm. (A) Typical image of fluorescent His-tagged thioredoxin monomers. (B) Image of His-tagged thioredoxin complexes N₂[NTA-Ni]₂[RP]₂, which were formed by the affinity binding of 6a through NTA-Ni-His-tagged protein. (C) Image of the His-tagged thioredoxin complexes N₃[NTA-Ni]₃[RP]₃, which were formed by ligand 6b. (D) Image of His-tagged thioredoxin complexes N₄[NTA-Ni]₄[RP]₄, which were formed by ligand 6c. (E) Image of complexes N₅[NTA-Ni]₅[RP]₅ which were formed by ligand 6d. (F) Image of complexes N₆[NTA-Ni]₆[RP]₆, which were formed using dendritic ligand 6e. The optimal molar ratios of ligand, NiCl₂ and protein are used as outlined in Tables 4.2 and 4.3.

Table 5.1: Summary of ICS data of fluorescent His-tagged thioredoxin complexes

Sample	[RP] (nM)	L	$\omega \pm$ SEM	$1/g(0,0) \pm$ SEM	$<i> \pm$ SEM	CD $\pm$ SEM	DA $\pm$ SEM	N*
RP	50		0.60 ± 0.01	33.6 ± 3.0	28.3 ± 1.1	31.5 ± 3.0	1.1 ± 0.1	39
$N_2[NTA\text{-}Ni]_2[RP]_2$	55	6a	0.64 ± 0.01	16.0 ± 1.6	30.5 ± 1.3	13.0 ± 1.3	2.8 ± 0.2	53
$N_3[NTA\text{-}Ni]_3[RP]_3$	60	6b	0.62 ± 0.02	11.9 ± 1.2	33.0 ± 1.5	12.8 ± 1.1	3.6 ± 0.3	42
$N_4[NTA\text{-}Ni]_4[RP]_4$	60	6c	0.64 ± 0.03	10.7 ± 1.5	33.8 ± 2.8	10.3 ± 1.8	4.8 ± 0.5	37
$N_5[NTA\text{-}Ni]_5[RP]_5$	62	6d	0.59 ± 0.01	7.1 ± 0.6	33.1 ± 1.9	7.4 ± 0.8	5.2 ± 0.3	33
$N_6[NTA\text{-}Ni]_6[RP]_6$	62	6d	0.77 ± 0.02	5.4 ± 0.7	33.3 ± 1.3	3.2 ± 0.4	8.7 ± 0.5	52

ICS results from each sample of fluorescent His-tagged thioredoxin monomers and aggregates, Where RP represents the monomer of rhodamine-labelled His-tagged thioredoxin. $N_2[NTA\text{-}Ni]_2[RP]_2$, $N_3[NTA\text{-}Ni]_3[RP]_3$, $N_4[NTA\text{-}Ni]_4[RP]_4$, $N_5[NTA\text{-}Ni]_5[RP]_5$, $N_6[NTA\text{-}Ni]_6[RP]_6$ stand for the rhodamine-labelled His-tagged thioredoxin complexes, which were obtained corresponding by mixing protein with the solution of $N_2[NTA\text{-}Ni]_2$, $N_3[NTA\text{-}Ni]_3$, $N_4[NTA\text{-}Ni]_4$, $N_5[NTA\text{-}Ni]_5$, $N_6[NTA\text{-}Ni]_6$, respectively. L is the dendritic chelating agent which has numeric abbreviation of 6a, 6b, 6c, 6d, 6e (See Figure 3.1) containing two, three, four, five, and six NTA terminal groups, respectively. These abbreviations were derived from Chapter 4. SEM is a standard error of the mean. [RP] = the concentration of protein monomers in nM, which was determined by the absorbance at 280 nm using Equation 5.7 in terms of fluorescent His-tagged thioredoxin monomers. $\omega \pm$ SEM is the observed laser beam size with SEM. $1/g(0,0)$ is an estimate of the average number of independent protein clusters. $<i>$ is the average intensity, which had been corrected for the contribution of black current background. CD $\pm$ SEM stands for the cluster density with the standard error of the mean. DA $\pm$ SEM is the degree of aggregation with the standard error of the mean. N* is the number of images and analysed for each data point. SEM values are at 99% confidence.

(the degree of aggregation) values is observed.

5.4.2.1 Constant values of the observed beam size (ω)

In ICS analysis, a three parameter, non-linear least squares fitting routine is used to fit a two-dimensional Gaussian function to the discrete autocorrelation data as represented in Equation 5.10. The three fitting parameters are $g(0,0)$, which is the amplitude of the autocorrelation function; ω, which is the e^{-2} laser beam radius; and g_0 which is an offset as described in section 5.2. The ω values in Table 5.1 remains almost a constant, this means that all the measurements can be best fitted and less rejected. This is reflected in the magnitude of the best fit value for ω, which essentially represents a measurement of the spot size for each protein sample. A series of histograms for the frequency distributions of the ω values are shown in Figures 5.4. No matter what the samples are, protein monomers or complexes, no significant differences of the ω values (~0.66 μm) between the monomers and complexes are observed, except for the ω (0.77 μm) of complex $N_6[NTA-Ni]_6[RP]_6$ is greater than the others. The average values and the frequency distributions of ω values for the protein monomers and complexes (Figure 5.4) show that ICS measures complexes which are physically large compared to the laser beam.

Figure 5.4: Percentage frequency distribution of the ω values for fluorescent His-tagged thioredoxin monomers (A) and oligomeric complexes, such as $N_2[NTA-Ni]_2[RP]_2$ (B), $N_3[NTA-Ni]_3[RP]_3$ (C), $N_4[NTA-Ni]_4[RP]_4$ (D), $N_5[NTA-Ni]_5[RP]_5$ (E), $N_6[NTA-Ni]_6[RP]_6$ (F), respectively. These complexes correspond to the samples which were obtained using specific chelating agents 6a, 6b, 6c, 6d, 6e and proportional molar ratios of protein and nickel ion solutions as outlined in Table 4.3. The vertical dashed lines represent the average ω values for each sample. The percentage frequency was normalized to the number of data points included in the distribution.

5.4.2.2 Consistence of average intensity with the concentration of each sample

The average fluorescence intensity per pixel in an image is denoted as $<i>$. It is directly proportional to the average number ($\bar{N}_m$) of fluorescently labelled molecules in the area illuminated by the laser beam. Table 5.1 gives the average values of $<i>$ for a set of images for each type of protein monomers and complexes. The number of images used vary from 32 to 53. It is evident that the average value of $<i>$ is almost constant for the different experiments. This is consistent with the relatively constant concentration of solutions employed. This is an encouraging observation, since it suggests that the concentration on the surfaces is a good reflection of the concentration in solution. Also if higher order aggregates are formed, there is no evidence for quenching. The distribution of $<i>$ values among the images is shown in Figure 5.5. It is clear that the distribution is independent of how the protein complex is being formed. This observation indicates the total numbers of fluorescent molecules are the same in all cases. Therefore we should be able to determine the stoichiometry of protein aggregates using other parameters such $1/g(0,0)$, CD and DA under the conditions of constant ω and $<i>$ values.

5.4.2.3 Decreasing values of $1/g(0,0)$

According to Equation 5.5, the $1/g(0,0)$ values which are derived from $g(0,0)$, represent the frequency distribution measured in a number of discrete samples, such as RP, $N_2[NTA-Ni]_2[RP]_2$, $N_3[NTA-Ni]_3[RP]_3$, $N_4[NTA-Ni]_4[RP]_4$, $N_5[NTA-Ni]_5[RP]_5$, $N_6[NTA-Ni]_6[RP]_6$ as shown in Figure 5.6. Since in our case the fluorescent labelled particles were located in a single population (26, 29), the $1/g(0,0)$ gives an estimate of the number of independent fluorescent particles ($\bar{N}_p$). With a fixed monomer concentration, aggregation should lead to a reduction in $\bar{N}_p$ (larger and fewer particles), which is indicated by the $1/g(0,0)$ value (26, 33). The average values of $1/g(0,0)$ for each sample are represented as *the dash lines* in Figure 5.6. It was also found that the value of $1/g(0,0)$ had a decreasing
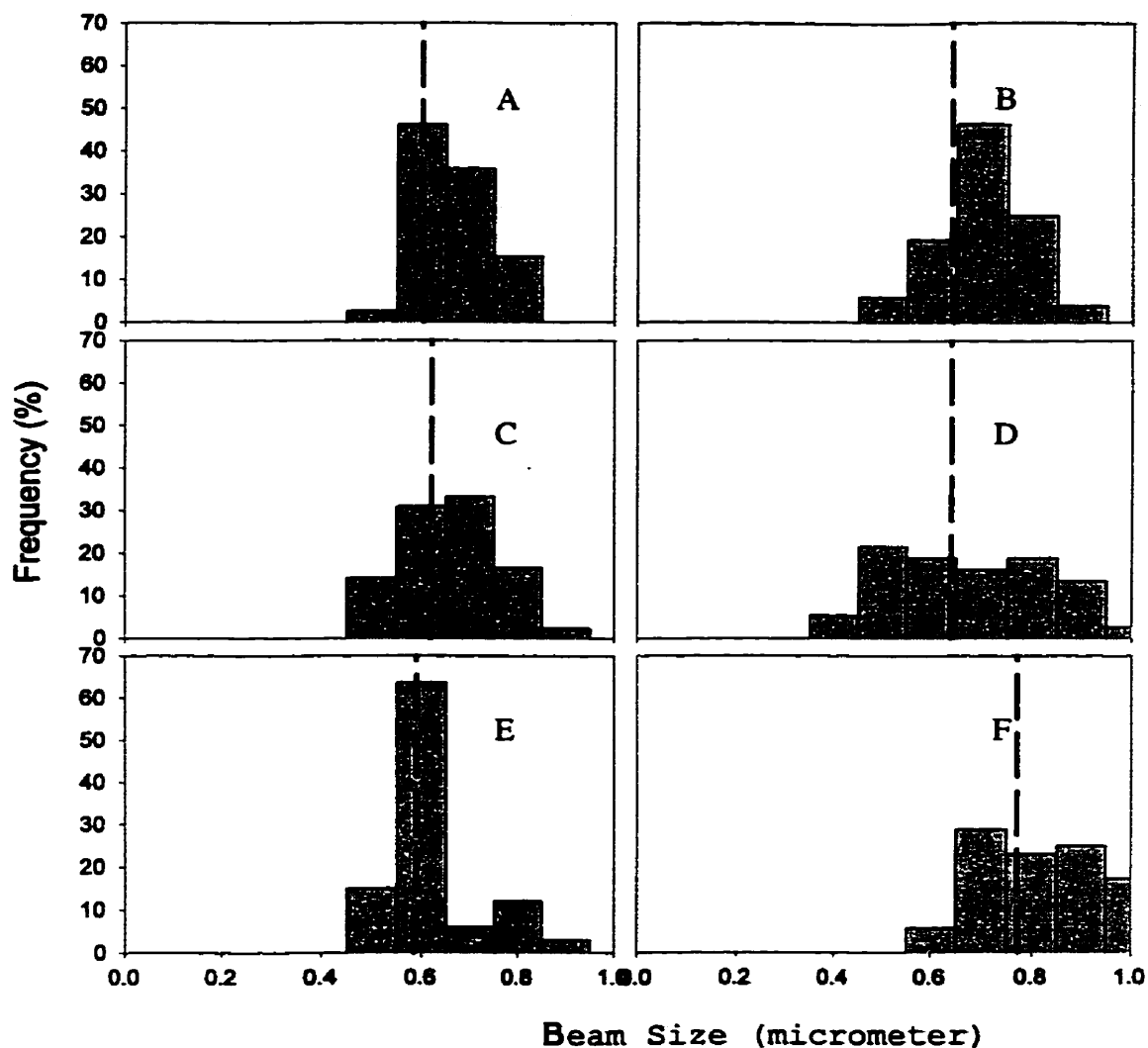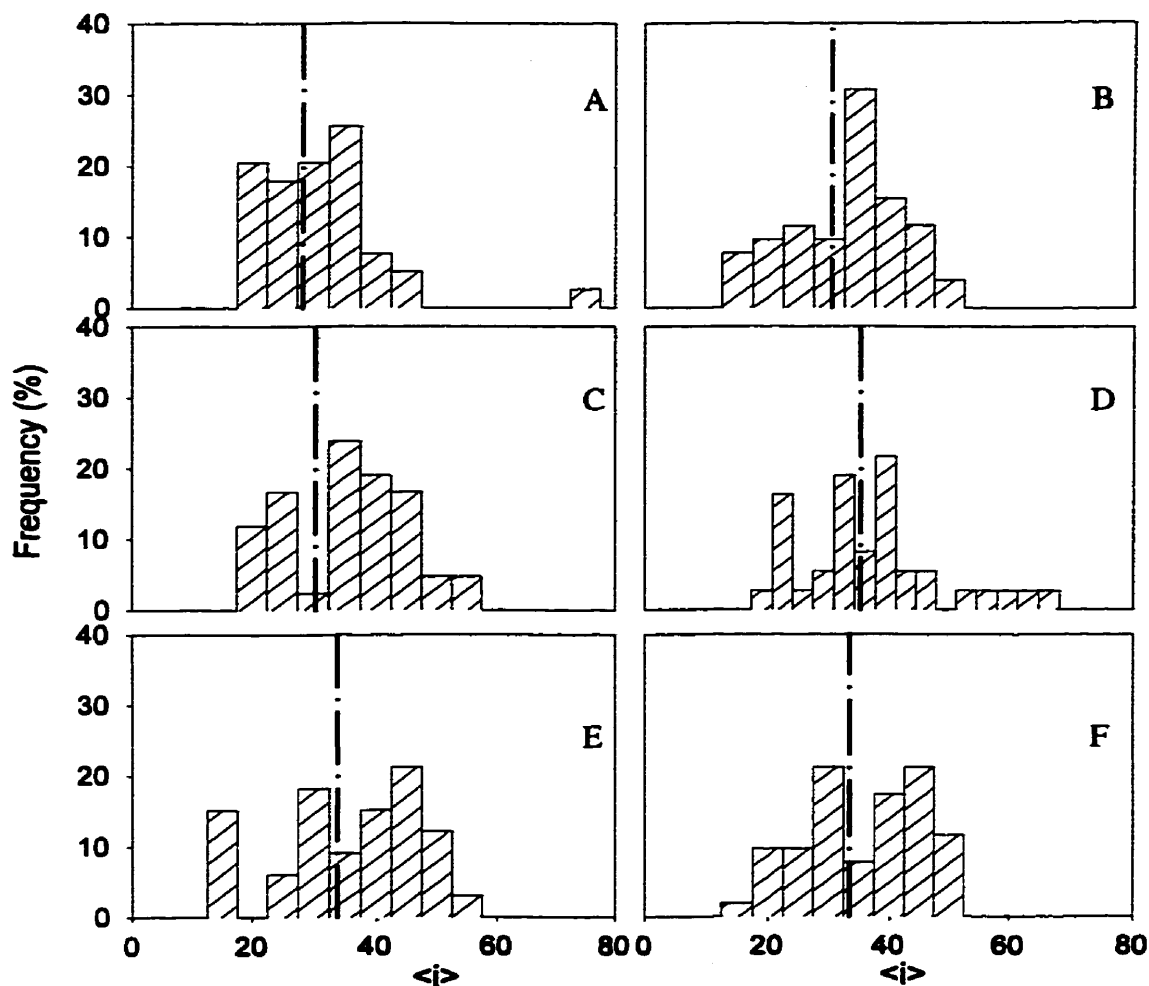
Figure 5.5: Percentage frequency distribution of the <i> values (average intensity) for fluorescent His-tagged thioredoxin monomers (A) and oligomeric complexes, such as $N_2[NTA-Ni]_2[RP]_2$ (B), $N_3[NTA-Ni]_3[RP]_3$(C), $N_4[NTA-Ni]_4[RP]_4$ (D), $N_5[NTA-Ni]_5[RP]_5$ (E), $N_6[NTA-Ni]_6[RP]_6$ (F). These complexes correspond to the samples which were obtained using specific chelating agents 6a, 6b, 6c, 6d, 6e and proportional molar ratios of protein and nickel ion solutions, respectively. The vertical dotted lines represent the average <i> values for each sample. The percentage frequency was normalized to the number of data points included in the distribution.
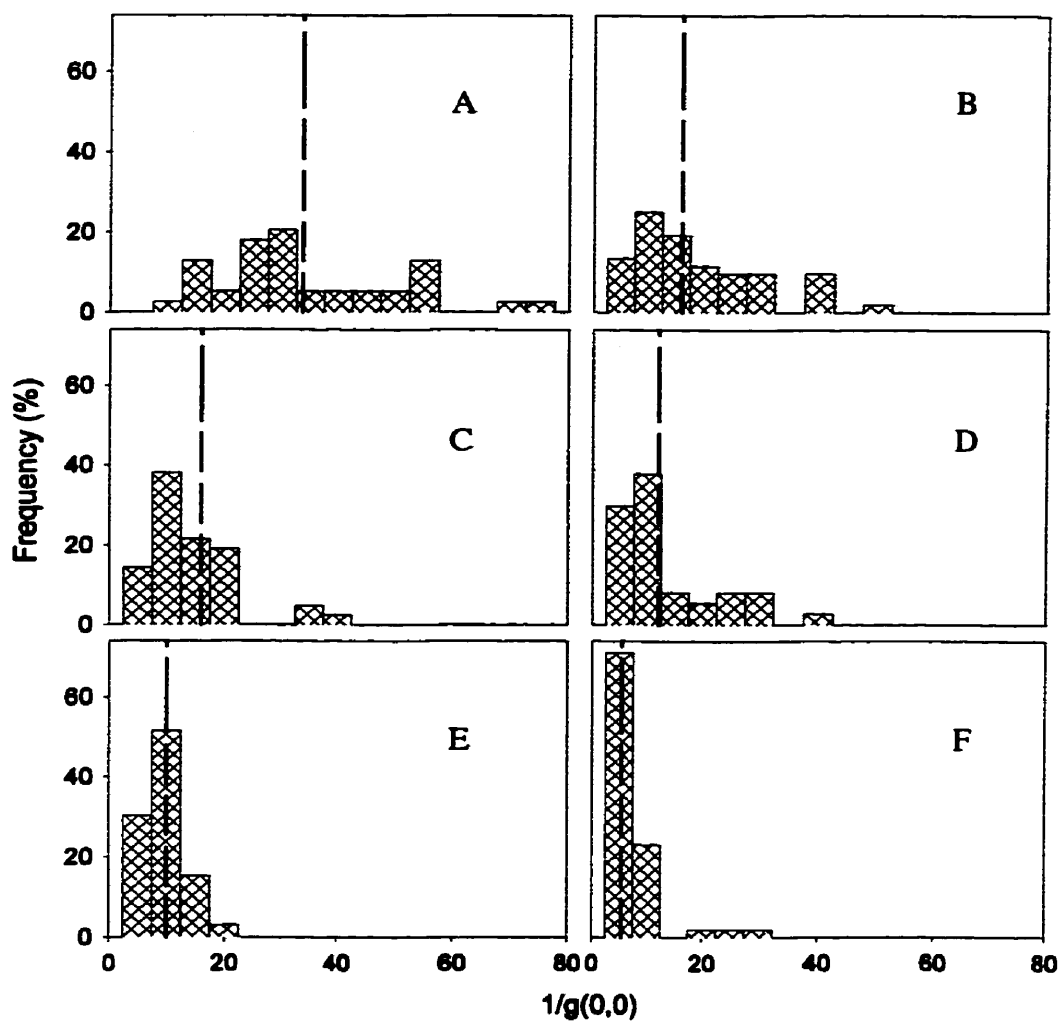
Figure 5.6: Percentage frequency distribution of the $1/g(0,0)$ values for fluorescent His-tagged thioredoxin monomers (A) and oligomeric complexes, such as $N_2[NTA-Ni]_2[RP]_2$ (B), $N_3[NTA-Ni]_3[RP]_3$ (C), $N_4[NTA-Ni]_4[RP]_4$ (D), $N_5[NTA-Ni]_5[RP]_5$ (E), $N_6[NTA-Ni]_6[RP]_6$ (F), respectively. These complexes correspond to the samples which were obtained using specific chelating agents 6a, 6b, 6c, 6d, 6e and proportional molar ratios of protein and nickel ion solutions, separately. The vertical dashed lines represent the average $1/g(0,0)$ values for each sample. The percentage frequency was normalized to the number of data points included in the distribution.

trend, which was just as expected by the ICS data interpretation. This phenomena means that the number of independent fluorescent particles in each observed image area is reduced as the size of cluster is going up. From the histograms of Figure 5.6, the disperse frequency distributions of these $1/g(0,0)$ values are observed for sample RP, $N_2[NTA-Ni]_2[RP]_2$. But, the frequency distributions for samples $N_3[NTA-Ni]_3[RP]_3$, $N_4[NTA-Ni]_4[RP]_4$, $N_5[NTA-Ni]_5[RP]_5$, $N_6[NTA-Ni]_6[RP]_6$ are reasonably narrow.

5.4.2.4 Variable values of cluster density (CD) and surface density (SD)

As indicated in Equation 5.4, the cluster density (CD), defined as the number of independent fluorescent clusters per $\mu m^2$ on the observed area, can be obtained from $g(0,0)$ and the beam area. The average CD values for each of the protein monomers and complexes are also given in Table 5.1 and the distribution of the CD values among the images is shown in Figure 5.7. The values of CD decrease as the number of NTA groups in the complexing agent increases. Thus the CD value for monomers of His-tagged thioredoxins is 31.5 ± 3.0 cluster/μm^2, and CD value of complexes with **6a, 6b, 6c, 6d, 6e** decreases in the order of 13.8 ± 1.3, 12.8 ± 1.1, 10.4 ± 1.8, 7.4 ± 0.8, 3.2 ± 0.5 clusters/μm^2. A "cluster" means an independent fluorescently labelled species, whether it contains one or more proteins, i.e. a number of fluorescent monomers or single monomer in one particle is one cluster, but a number of particles containing many protein aggregates or containing many monomers is also one cluster. So, the decrease in the CD values is consistent with an increase in the number of proteins per complex; that is, for a fixed number of proteins in solution or on the surface, a more clustered state would lead to fewer clusters - CD is smaller.

When observing fluorescent images at high magnification (at zoom factor of 10) (Figure 5.2A and Figure 5.3), it becomes apparent that there are a number of bright spots of variable intensity. It is reasonable to propose that these intense spots correspond to His-tagged thioredoxin aggregates containing a large number of monomers. We estimate the maximum numbers of protein monomers for each sample which was deposited on a surface area of about 3×10^8 μm^2, the surface densities (number of molecules per μm^2) and coefficients which were obtained by dividing the CD values. Table 5.2 gives these estimates.
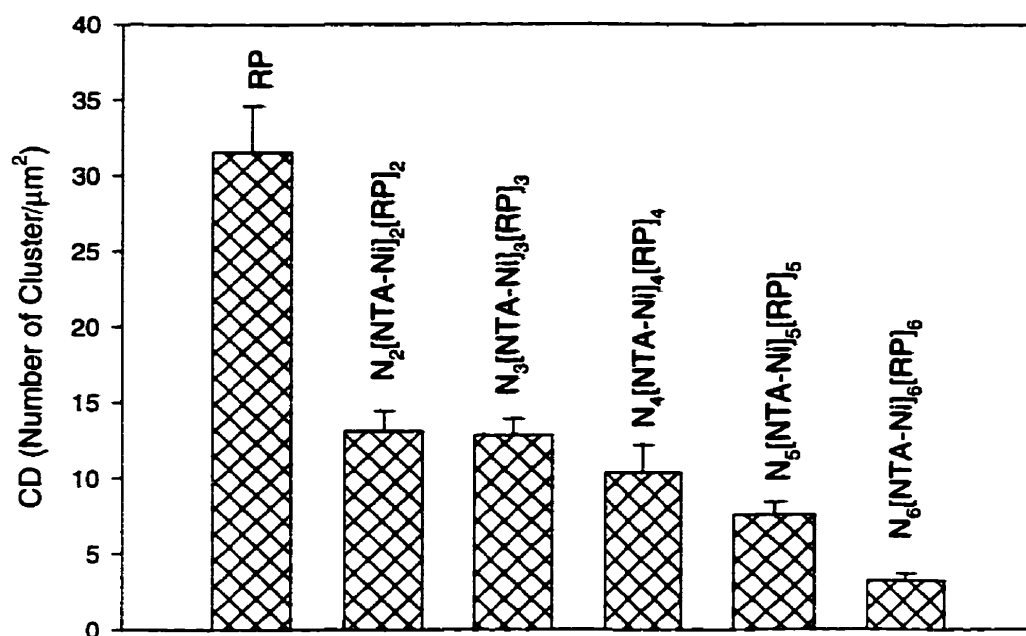
Figure 5.7: Simple bar plots of CD values in ICS measurements. The error bars stand for SEM. Bar RP stands for rhodamine labelled His-tagged thioredoxin monomers. Bar $N_2[NTA-Ni]_2[RP]_2$, $N_3[NTA-Ni]_3[RP]_3$, $N_4[NTA-Ni]_4[RP]_4$, $N_5[NTA-Ni]_5[RP]_5$, $N_6[NTA-Ni]_6[RP]_6$ stands for the dimeric, trimeric, tetrameric, pentameric, and hexameric rhodamine-labelled His-tagged thioredoxin complexes, which were fromed by using the dendritic chelating agent of **6a, 6b, 6c, 6d, 6e,** respectively.

Table 5.2: Correlation between the surface density and the cluster density

Sample	N_{max} ($\times 10^{11}$)	$A_{surface}$ (μm^2)	SD (# of molecule/μm^2)	N_c (# of molecule/cluster)	C
RP	6.02	3.14×10^8	1917	62	1
$N_2[NTA-Ni]_2[RP]_2$	6.62	3.14×10^8	2108	150	2.5
$N_3[NTA-Ni]_3[RP]_3$	7.22	3.14×10^8	2299	192	3.2
$N_4[NTA-Ni]_4[RP]_4$	7.221	3.14×10^8	2299	230	3.8
$N_5[NTA-Ni]_5[RP]_5$	7.46	3.14×10^8	2375	320	5.3
$N_6[NTA-Ni]_6[RP]_6$	7.46	3.14×10^8	2375	742	12.3

Where N_{max} = maximum number of molecules deposited on a surface area of 3.14×10^8 μm^2, $A_{surface}$ = surface area in a unit of μm^2, SD = surface density, represents a number of molecules per μm^2, N_c = number of molecules per cluster, C = normalized number of clusters per spot.

In Table 5.2, N_{max} is calculated as the total number of molecules of 20 μL of the corresponding solutions deposited on the coverslip with a surface area of 3.14×10^8 μm^2 ($A_{surface}$). The surface density (SD) is obtained by dividing N_{max} of each sample with $A_{surface}$ value, and N_c, the number of molecules per cluster, is obtained by dividing the SD of each sample with the corresponding CD values. Since the CD value represents the number of clusters per μm^2, N_c corresponds to the number of molecules per observed cluster, or the number of molecules per spot. C is a normalized coefficient which is obtained by dividing the N_c value with 60 (the number of protein monomers per cluster), thus it reflects the relative number of monomers per cluster in each spot. We therefore expect to have ~ 2108, 2299, 2299, 2375, 2375 protein monomers per square micrometer for each complex. The measured CD values of 31, 14, 13, 10, 7, 3 clusters per μm^2 for each sample suggest that there are as many as 60, 150, 192, 230, 320 monomers per cluster (or per surface aggregate).

Interestingly, since the CD values decrease as the larger complexing agents are employed, it must be true that the number of monomers per surface aggregate increases as we observed. Hence, it is more likely that each observed bright spot contains a certain

numbers of aggregates of complexes which were formed by the addition of chelating agents **6a-e**. The apparent difference of CD and SD values between protein monomers and complexes indicates the tendency of higher order His-tagged thioredoxin complexes are formed at the surface of glass as well as in solution.

5.4.2.5 Variable values of the degree of aggregation (DA)

The degree of aggregation (DA) is described in Equation 5.5. It can be obtained by the product of $g(0,0)$ and $<i>$ and is proportional to the number of particles per cluster. The DA value is thus proportional to $\bar{N}_m/\bar{N}_p$ with a proportionality constant, α, which depends on instrumental correction efficiencies, quantum yields and extinction coefficients. If we have simple distribution of molecules, then the product of these two parameters will give an estimate of the number of individual particles (monomers) in each cluster. The products of $g(0,0)$ and $<i>$ for His-tagged thioredoxin reacted with **6a-e** are also given in Table 5.1 and are illustrated in Figure 5.8. The degree of aggregation (DA) increases almost linearly as the chelating agents containing more NTA groups are used. This linear increase in the values of DA is caused by more and more individual monomers binding to ligand in each aggregate. We note that the values of DA vary from 1.1, 2.8, 3.6, 4.8, 5.2, 8.7 for each sample. In comparison to the C values (Table 5.2) from 1, 2.5, 3.2, 3.8, 5.3, 12.3, which represents the normalized number of particles per cluster, there is a coincidence between the estimate of C values and the calculation of DA values. This suggests that the values of C and DA are comparable with a proportionality coefficient (ratio of DA:C) from 1.10, 1.12, 1.12, 1.26, 0.98, 0.71 for each sample. These coefficients have a value of about 1, except for the largest complex formed by chelating agent **6e**. Nevertheless, the increase in DA values from monomers to the other complexes of the His-tagged thioredoxins supports the proposal made in Chapter 4 that there is a formation of larger and larger His-tagged thioredoxin aggregates in solution.
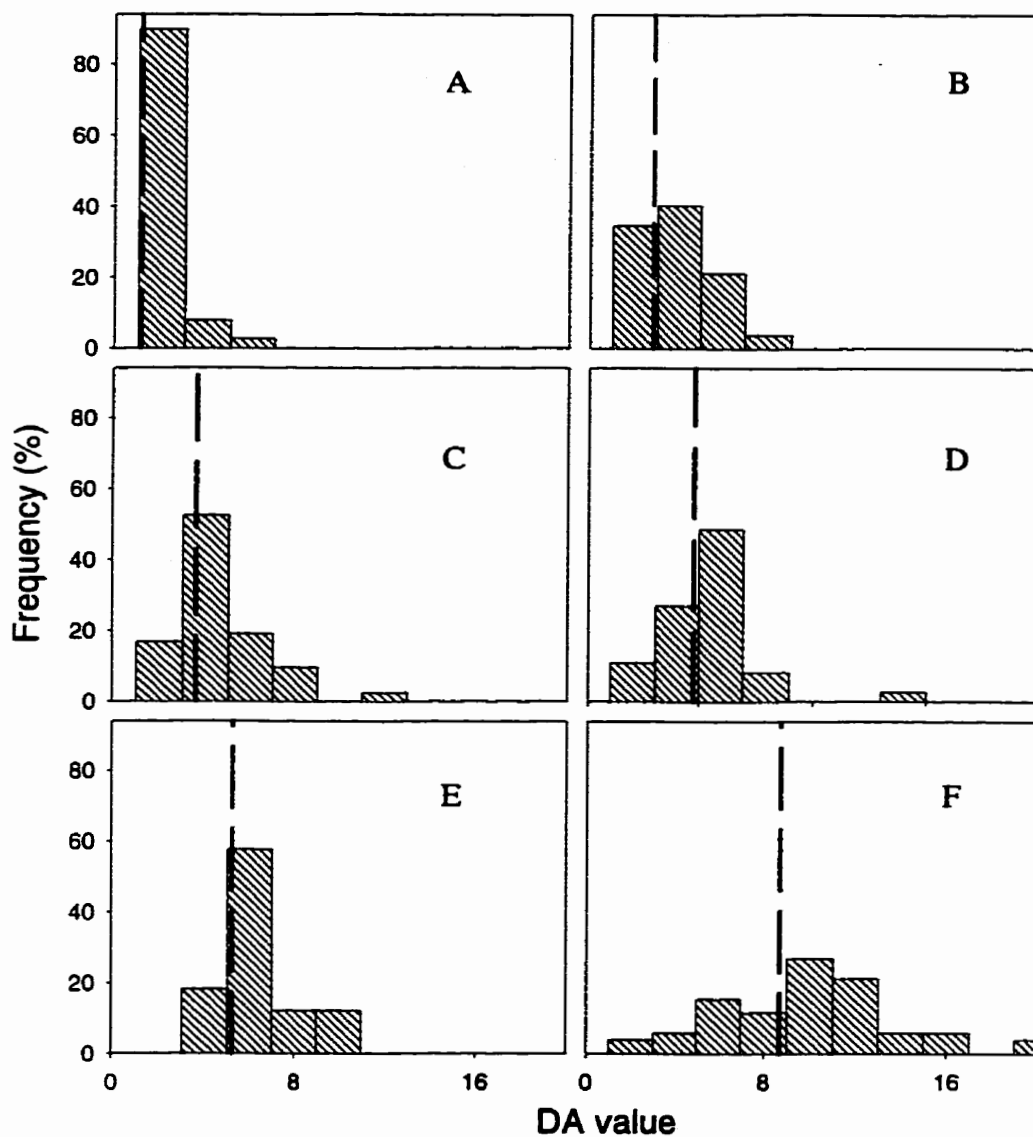
Figure 5.8: Frequency distribution of DA values for rhodamine labelled His-tagged *E. coli* thioredoxin complexes in ICS measurements. Rhodamine labelled His-tagged thioredoxin monomers (A) and complexes $N_2[NTA-Ni]_2[RP]_2$ (B), $N_3[NTA-Ni]_3[RP]_3$ (C), $N_4[NTA-Ni]_4[RP]_4$ (D), $N_5[NTA-Ni]_5[RP]_5$ (E), $N_6[NTA-Ni]_6[RP]_6$ (F), which were formed by using ligands **6a, 6b, 6c, 6d, 6e,** respectively.The vertical dash lines represent the average DA values for each sample. The percentage frequency was normalized to the number of data points included in the distribution.
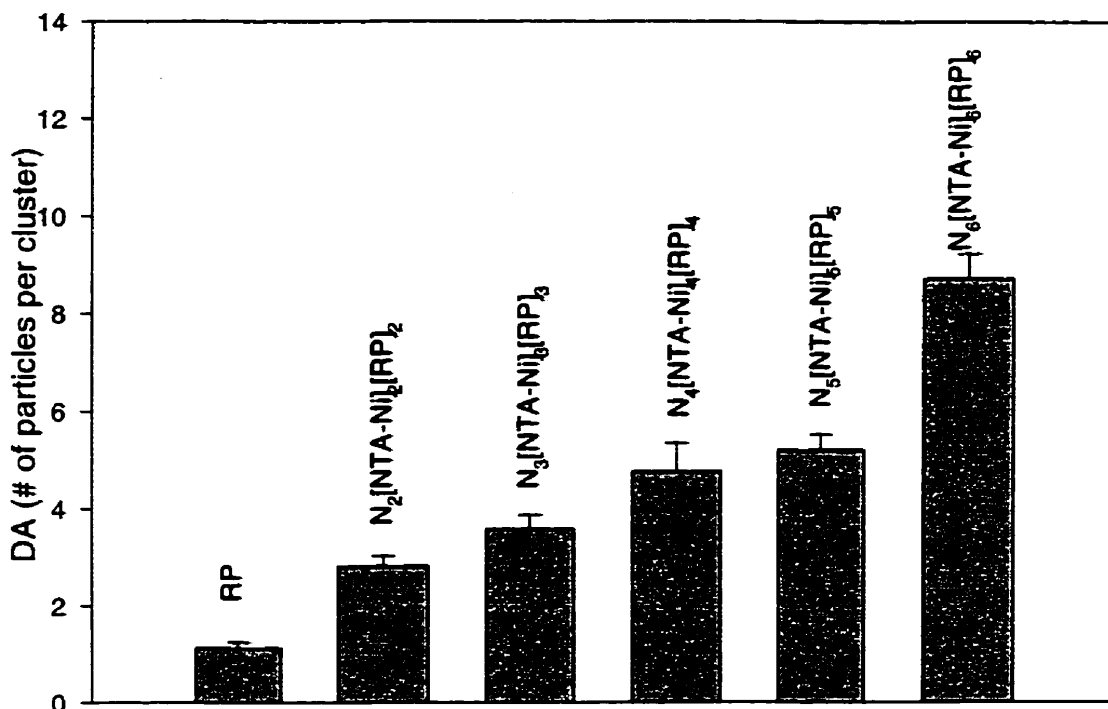
Figure 5.9: Vertical bar plots of DA values for rhodamine labelled His-tagged *E. coli* thioredoxin complexes in ICS measurements. The DA values were calculated from Equation 5.5, including standard error of the mean (SEM) for each independent complex. Each bar is the average DA value plus the SEM for all of six independent His-tagged thioredoxin samples. Bar RP stands for rhodamine labelled His-tagged thioredoxin monomers. Bar $N_2[NTA-Ni]_2[RP]_2$, $N_3[NTA-Ni]_3[RP]_3$, $N_4[NTA-Ni]_4[RP]_4$, $N_5[NTA-Ni]_5[RP]_5$, $N_6[NTA-Ni]_6[RP]_6$ stands for the dimeric, trimeric, tetrameric, pentameric, and hexameric rhodamine-labelled His-tagged thioredoxin complexes which were formed by using ligands **6a, 6b, 6c, 6d, 6e**, respectively.

Figure 5.8 depicts the frequency distribution and Figure 5.9 shows the increasing trend of the average values of DA from protein monomers to complexes. The percentage distributions of DA values from protein monomers to complexes are getting disperse. A disperse distribution is observed for the largest complex formed by chelating agent **6e**, this is consistent with the greatest variation of coefficient for this complex. The DA value is increased and varied with the number of NTA groups of each chelating agent for His-tagged thioredoxin monomers and aggregates. As we know that the labeling efficiency of proteins by RRX is 0.85, this value corresponds to almost one dye conjugated to one protein molecule. Therefore, the increasing trend of DA values reflects not only the number of monomers in each aggregate of the His-tagged thioredoxin clusters which were observed as fluorescent spots, but also the number of fluorophores in each cluster.

In Chapter 4, it was concluded that the stoichiometry of protein aggregates was defined by selective binding of ligands (**6a, 6b, 6c, 6d, 6e**) with His-tagged thioredoxin through the metal ion. In this Chapter, it is quantitatively confirmed that the number of NTA groups in dendritic chelating agent could control the size of each protein complex. Taken all together, the evidence described in this Chapter supports the assertion that independent fluorescent clusters can be visualized and different oligomeric aggregates were reliably detected by laser scanning confocal microscopy. Their individual corresponding images were collected and showed variable fluorescence intensity at the illumination conditions applied. The confocal fluorescent images were quantitatively analyzed by an autocorrelation function of intensity fluctuations. ICS measurements yield a decreasing trend of cluster density (CD), and an increasing trend of the degree of aggregation (DA), as the size of His-tagged thioredoxin aggregates becomes larger. These data provide indirect evidence for the formation of fluorescent His-tagged thioredoxin dimers, trimers, tetramers, pentamers and hexamers carrying two, three, four, five and six fluorescence labels, respectively.

5.5 Discussion

In this Chapter we have shown that ICS is sensitive enough to detect rhodamine labelled His-tagged thioredoxin monomers and oligomers. We observed constant levels of ω (which is the observed beam size) and $<i>$ values (which correspond to constant total concentration of fluorescent protein monomers). We also observed two decreasing trends of $1/g(0,0)$ values (equal to $\tilde{N}_p$) and corresponding CD values (average number of independent fluorescent particles per μm^2), and finally an increasing set of DA values (average number of monomers per aggregate). These trends in the ICS data are indicative of the various distributions of His-tagged thioredoxin monomers in its molecular aggregates as the protein complexes become larger.

Examination of the trends in the average DA values in Figure 5.10 provides further information. Here the $<i>$ value is plotted as a function of the $1/g(0,0)$ values for each image in each sample (monomers (A), dimers (B), trimers (C), tetramers (D), pentamers (E), hexamers (F)). According to Equation 5.5, the slopes of these plots should result in the DA values for each case. The data in (A), (B), (C), (D), (E), (F) yields slope values of 0.66, 1.42, 2.81, 3.69, 4.51, 6.53 (least square fitting at 95% confidence). The trend of slopes is similar to the average DA values outlined in Table 5.1. However, there were small differences for each corresponding sample, this could be interpreted because of different averaging methods when calculating the slope.

From the concentration of proteins in each sample and the area of the glass surface ($\sim 3.4 \times 10^8 \mu m^2$), we estimated the maximum number of protein molecules deposited on the surfaces and the surface density (SD) values as well as shown in Table 5.2. The parameter of SD was introduced to characterize the total number of protein molecules per μm^2, this set of SD values is proportional to the corresponding concentration for each sample. The CD values characterize the average number of independent clusters per μm^2, we calculated the total number of molecules per cluster (N_c) by dividing SD with the corresponding CD for each sample. Thus we normalized N_c values to give a set of coefficients C which represented the number of monomers per cluster. Each C value is comparable with the relative DA value of each sample. The ICS calculation gives the degree of aggregation (DA), which represents
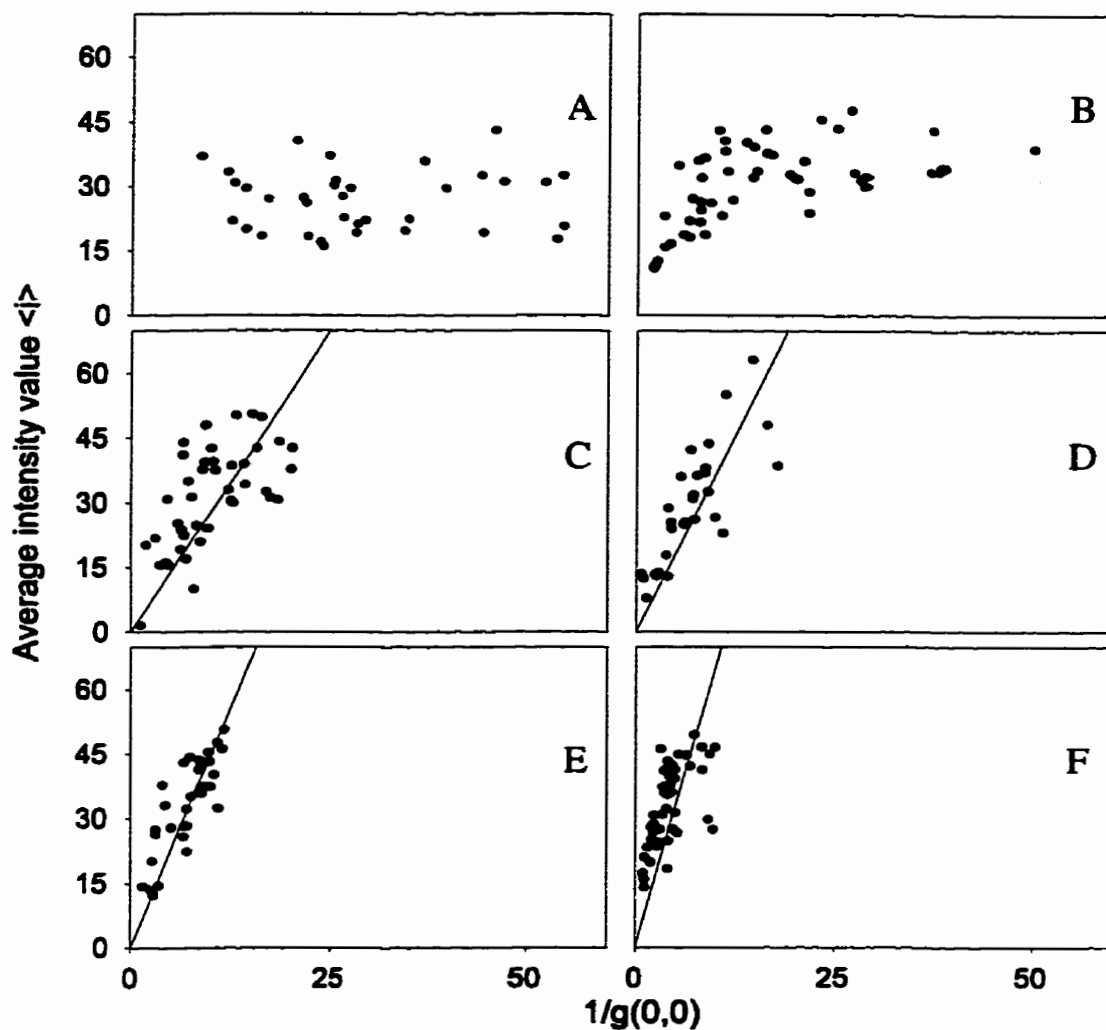
Figure 5.10: Scatter plots of the <i> values versus 1/g(0,0) values for all of ICS data. (A) is the plot of rhodamine-labelled His-tagged thioredoxin monomers, (B), (C), (D), (E), (F) corresponds to the samples of $N_2[NTA-Ni]_2[RP]_2$, $N_3[NTA-Ni]_3[RP]_3$, $N_4[NTA-Ni]_4[RP]_4$, $N_5[NTA-Ni]_5[RP]_5$, $N_6[NTA-Ni]_6[RP]_6$, which were produced by ligand **6a**, **6b**, **6c**, **6d**, **6e**, respectively. These plots are fitted by the first-order linear regression and the fittings yield a slope of plot (C), (D), (E), (F) equals to 2.81, 3.69, 4.51. 6.53 within the confidence of 95%, respectively.

the number of monomers in each cluster. The particle could be the independent monomeric, dimeric, trimeric, tetrameric, pentameric and hexameric aggregates in each sample. Thus the DA values should reflect the formation of His-tagged thioredoxin complexes which are specifically stoichiometric. It is possible that individual protein monomers or complexes are accumulated or crystallized on the glass surfaces to give clusters containing many aggregates. Therefore the fluorescent spots are observed as the accumulations of the various numbers of molecules, as represented in the estimated N_c values which are indicated in Table 5.2.

We immobilized the His-tagged thioredoxin monomers and complexes on glass surfaces without Brownian motion, thus the deposition of samples on surfaces has advantages in reducing possible photobleaching and fluorescence quenching of fluorescent molecules, which can be induced by solvent or dissolved material in the solvent used. We selected Rhodamine Red^{TM}-X (RRX) for the labeling of His-tagged thioredoxin molecules, since it is a dye molecule extensively studied in many aspects and has higher intensity than other dyes. Here, laser scanning confocal microscopy allows the characterization of fluorescence labelled His-tagged thioredoxin monomers and oligomers.

In summary, the fluorescent confocal images of protein monomers and complexes were collected using photon counting detection. The quantities of independent rhodamine labelled His-tagged thioredoxin particles such as monomers and complexes in isolated fluorescent spots were determined. It is imperative to adopt image correlation spectroscopy (ICS) measurements for the determination of stoichiometric bindings of these aggregates. ICS was originally developed and applied to detect the distribution of receptors on cell surfaces. This is the first attempt to adopt ICS in a model aggregation system. The ICS data provide evidence that the specific aggregation of His-tagged thioredoxin can be induced using dendritic chelating agent containing multiple NTA groups and monitored by ICS. The results of native PAGE provided direct evidence that dimers, trimers, tetramers, pentamers, and hexamers of His-tagged thioredoxin can be formed with the addition of dendritic multiple NTA ligands 6a-e in solution. High-resolution laser scanning confocal microscopy measurements have confirmed this observation. ICS results have shown this type of fluorescent images can be collected and analyzed successfully. This is important because it

demonstrates that analysis of cluster densities on surfaces is feasible with ICS and that the probes prepared in Chapter 3 may prove useful for inducing or exploring protein aggregates on cell surfaces.

5.6 References

1. Schmidt, T., Schütz, G.J., Baumgartner, W., Gruber, H.J., and Schindler, H. Imaging of single molecule diffusion. *Proc. Natl. Acad. Sci. USA* **1996**, 93, 2926-2929.

2. Eggeling, C., Fries, J.R., Brand, L., Günther, R., and Seidel, C.A.M. Monitoring conformational dynamics of a single molecule by selective fluorescence spectroscopy. *Proc. Natl. Acad. Sci. USA* **1998**, 95, 1556-1561.

3. Ishikawa, M., Yogi O., Ye, J.Y., Yasuda, T., and Maruyama, Y. Grouping of independent single molecules on silicon surfaces. *Anal. Chem.* **1998**, 70, 5198-5208.

4. Schütz, G.J., Trabesinger, W. and Schmidt, T. Direct observation of ligand colocalization on individual receptor molecules. *Biophys. J.* **1998**, 74, 2223-2226.

5. Schmidt, T, Hinterdorfer, P. and Schindler, H. Microscopy for recognition of individual biomolecules. *Microscopy Research and Technique.* **1999**, 44, 339-346.

6. Nie, S., Chiu, D.T., and Zare, R.N. Real-time detection of single molecules in solution by confocal fluorescence microscopy. *Anal. Chem.* **1995**, 67, 2849-2857.

7. Xu, X.-H and Yeung, E.S. Direct measurement of single-molecule diffusion and photodecomposition in free solution. *Science*, **1997**, 275, 1106-1109.

8. Moerner, W.E. and Orrit, M. Illuminating single molecules in condensed matter. *Science.* **1999**, 283, 1670-1676.

9. Vámosi, G., Gohlke, C. and Clegg, R.M. Fluorescence characterizations of 5-carboxytetramethylrhodamine linked covalently to the 5'-end of oligonucleotides: Multiple conformations of single-stranded and double-stranded dye-DNA complex. *Biophys. J.* **1996**, 71, 972-994.

10. Yanagida, T., Nakase, M., Nishiyama, K., and Oosawa, F. Direct observation of motion of single F-actin filaments in the presence of myosin. *Nature*, **1984**, 307, 58-60.

11. Kishino, A., and Yanagida, T. Force measurements by micromanipulation of a single actin filament by glass needles. *Nature*, **1988**, 334, 74-76.

12. Edman, L., Mets, Ü. And Rigler, R. Conformational transitions monitored for single molecules in solution. *Proc. Natl. Acad. Sci. USA* **1996**, 93, 6710-6715.

13. Simson, R., Sheets, E.D., and Jacobson, K. Detection of temporary lateral confinement of membrane proteins using single-particle tracking analysis. *Biophys. J.* **1995**, 69, 989-993.

14. Feder, T.J., Brust-Mascher, I., Slattery, J.P., Baird, B., Webb, W.W. Constrained diffusion or immobile fraction on cell surfaces: A new interpretation. *Biophys. J.* **1996**, 70, 2767-2773.

15. Sako, Y. and Kusumi, A. Barriers for lateral diffusion of transferrin receptor in the plasma membrane as characterized by receptor dragging by laser treezers: Fence versus tether. *J. Cell Biol.* **1995**, 129, 1559-1574.

16. Kapitza, H.G., Jacobson, K.A., in: Ragan, C.J., Cherry, R.J. (Eds), Techniques for the analysis of membrane proteins, Chapman and Hall, London, **1986**, pp. 345-375.

17. Schlessinger, J., Shechter, Y., Willingham, M.C., and Pastan, I. Direct visualization of binding, aggregation, and internalization of insulin and epidermal growth factor on living fibroblastic cells. *Proc. Natl. Acad. Sci. USA.* **1978**, 75, 2659-2663.

18. Haigler, H., Ash, J.F., Singer, S.J., and Cohen, S. Visualization by fluorescence of the binding and internalization of epidermal growth factor in human carcinoma cells A-431. *Proc. Acad. Sci. USA.* **1978**, 75, 3317-3321.

19. Gadella, T.W. Jr., and Jovin, T.M. Oligomerization of epidermal growth factor receptors on A431 cells studied by time-resolved fluorescence imaging microscopy. A stereochemical model for tyrosine kinase receptor activation. *J. Cell Biol.* **1995**, 129, 1543-1558.

20. Young, R.M., Arnette, J.F., Roess, D.A., and Barisas, B.G. Quantitation of fluorescence energy transfer between cell surface proteins via fluorescence donor photobleaching kinetics. *Biophys. J.* **1994**, 67, 881-888.

21. Morrison, I.E.G., Anderson, C.M., Gerorgiou, G.N., Stevenson, G.V.W. and Cherry, R.J. Analysis of receptor clustering on cell surface by imaging fluorescent particles. *Biophys. J.* **1994**, 67, 1280-1290.

22. Thompson, N.L. Fluorescence correlation spectroscopy. In Topics in Fluorescence Spectroscopy, Vol. 1. Lakowicz, J.R., editor. Plenum Press, New York. **1991**.

23. Petersen, N.O. Scanning fluorescence correlation spectroscopy, I: Theory and simulation of aggregation measurements. *Biophys. J.* **1986**, 49, 809-815.

24. Widengren, J. and Rigler, R. Fluorescence correlation spectroscopy as a tool to investigate chemical reactions in solutions and on cell surfaces. *Cell. Mol. Biol.* **1998**, 44, 857-879.

25. Wiseman, P.W. and Petersen, N.O. Image correlation spectroscopy.II. Optimization for Ultrasensitive detection of preexisting Platelet-Derived Growth Factor-β receptor oligomers on intact cells. *Biophys. J.* **1999**, 76, 963-977.

26. Petersen, N.O., Höddelius, P.L., Wiseman, P.W., Seger, O., and Magnusson, K.-E. Quantitation of membrane receptor distribution by Image Correlation Spectroscopy: Concept and application. *Biophys. J.* **1993**, 65, 1135-1146.

27. Srivastava, M. and Petersen, N.O. Diffusion of transferrin receptor clusters. *Biophys. Chem.* **1998**, 75, 201-211.

28. Srivastava, M. and Petersen, N.O. Image cross-correlation spectroscopy: A new experimental biophysical approach to measurement of slow diffusion of fluorescent molecules. *Methods in Cell Science.* **1996**, 18, 47-54.

29. Brown, C.M. and Petersen, N.O. An image correlation analysis of the distribution of clathrin associated adaptor protein (AP-2) at the plasma membrane. *J. Cell Sci.* **1998**, 111, 271-281.

30. Fire, E., Brown, C.M., Roth, M.G., Henis, Y.I., and Petersen, N.O. Partitioning of proteins into plasma membrane microdomains. *J. Biol. Chem.* **1997**, 272, 29538-29545.

31. Molecular Probes, Product Information Sheet. FluoroReporter Rhodamine Red™-X Protein Labeling kit (F-6161), *MP 06161*, **01/06/1998**.

32. Davidson, N. Statistical mechanics. McGraw-Hill Book Company, Inc. New York, **1962**.

33. Wiseman, P.W. Image correlation spectroscopy: Development and application to studies of PDGF receptor distributions. The University of Western Ontario, Ph. D. thesis, **1995**.

CHAPTER 6 CONCLUSIONS

6.1 Strategy of my thesis work

There are several ways to study membranes. For example, one can study monolayers as models for one plane of a bilayer, or probe membrane components in model bilayer membranes. In either case, labeling membrane components (proteins and lipids) with fluorescent probes allow studies of the dynamics and hence membrane fluidity. In this research program, we aim to understand the effect of structure of molecules on their diffusion rate and we seek ways in which to selectively and specifically control molecular associations in solution, in model membranes and eventually on cell surfaces.

The purpose of this chapter is to tie together all of results which were presented in this thesis. The overall goal of this work is to obtain information about dynamic properties of biological membranes by systematic approaches which allow control of molecular shapes and interactions. To address this purpose, we combine organic chemistry and biophysical chemistry with biochemistry. In total, three sets of dendritic molecules (twelve compounds) (1, 2, 3, 4, 5, 6a, 6b, 6c, 6d, 6e, and 12a, 12b) have been designed, synthesized and applied to biochemical problems. The first set of molecules (1, 2, 3, 4, 5, or abbreviated as $N_2L[NBD]$, $N_3L_2[NBD]$, $N_4L_3[NBD]$, $N_5L_4[NBD]$, $N_6L_5[NBD]$, respectively) were synthesized by Alison Paprica and used in this work (Figure 2.3). These compounds have a central hydrophilic polyamine ring of varing size, which contained one fluorescent group and either one, two, three, four, or five lauroyl groups. These molecules were used to carry out the diffusion work in the first project. The successful application of these compounds led to the other type of molecules, which are also derived from these macrocyclic polyamines. We felt it should be possible to make dendritic chelating agents, such as 6a, 6b, 6c, 6d, 6e, and 12a, 12b as shown in Figure 3.1 to use as reagents to complex multiple proteins at once. By sequential and convergent pathways, the desired dendritic chelating agents were successfully prepared. Testing of the usefulness of these new reagents as chelating agents was conducted in two ways: by electrophoresis and by correlation spectroscopy. A model protein, His-tagged *E. coli* thioredoxin was selected for testing, whether it is possible to prepare

stoichiometric complexes. The resulting investigation of oligomeric His-tagged thioredoxin complexes indicated that these approaches are reliable. The conclusion that protein aggregation can be controlled suggests that these reagents may be applied to biological systems where clustering is important.

6.2 Lateral diffusion studies

Recent reviews have proposed that it is necessary to modify the fluid mosaic model of membranes, including structural elements and heterogeneity of membranes (1, 2, 3). These proposals were mainly based on studies of lateral diffusion in cell membranes and model membranes. As discussed in Chapter 1 and Chapter 2, the lateral diffusion of membrane components is essential to a variety of physiological processes in cells. It has been increasingly considered that membrane skeleton and its interactions with cytoskeletal proteins are characterized as many subdomains. Within the domains, the diffusion of membrane components is rapid and comparable to that measured in model membranes. There is therefore a renewed relevance to establish what factors control the rate of diffusion of any molecule in a model membrane.

We have performed systematic diffusion measurements and have shown that the diffusion coefficients of a series of structurally similar NBD-labelled molecules, e.g. 1, 2, 3, 4, and 5, are size dependent at several temperatures. The size of NBD-labelled amphiphiles e.g. 1, 2, 3, 4, 5, was designed such that their surface areas were ranging from 0.3 nm^2 to 2.4 nm^2. The diffusion of lipids such as NBD-PE and lipid-like molecules such as 1, 2, can best be explained by a viscosity modified free area theory of diffusion (4). The cross-sectional area of about 0.6 nm^2 of the phospholipid head-group within a molecule is the controlling factor. The size dependence of those molecules with cross-sectional area 0.5-0.8 nm^2 was comparable to the diffusion of lipids. In contrast, the movement of large diffusants e.g. 3, 4, 5 with cross-sectional areas from 1 nm^2 to 2.5 nm^2 was much slower. The weak dependence of NBD-labelled amphiphiles can be predicted by an adaption of the Evans-Sackmann hydrodynamic theory (5). Balcom's earlier work showed that diffusion of lipid-like probes was unaffected by increasing the hydrophobic core of the molecule from 10 to well over 100

carbons (6). Accordingly, we have predicted and confirmed that the head group region at the interface is critical for controlling the diffusion rate, but the interior is not important if the molecule is amphiphilic. If the shape of molecule is close to a sphere, and hydrophobic, then the rate of diffusion would exhibit an Einstein-Stoke size dependence (7) (The diffusion coefficient is inversely proportional to the radius of molecule). This led to the proposal that the membrane should be viewed as a triple layer - two viscous regions at the surfaces with a less viscous region in the middle.

6.3 Summary of dendritic ligands' synthesis

We wanted to achieve defined sizes of protein aggregates selectively and specifically, e.g. dimers, trimers, tetramers, etc. These could be used to study ligand-protein, protein-protein and ligand-ligand interactions. If the binding of ligands with proteins is strong enough, the ligand-protein complex would be reproducible and reliable. We chose to use nitrilotriacetic acid (NTA) derivatives since they are well known to bind histidines in proteins. One derivative, lysine-NTA **17**, was originally developed for purification of proteins which were tagged with oligomeric histidines by genetic means (8). It has been widely used in immobilized metal affinity chromatography (IMAC) due to this specific binding of NTA to adjacent histidine residues of the tagged protein. To obtain protein aggregates we needed to have multiple NTA groups in the same molecule. Our approach was to attach NTA groups to the macrocyclic polyamine rings used successfully in the previous work. These compounds have a set of arms, which can chelate to a His-tagged protein through the affinity binding of nickel ion. Changing the size of the central polyamine ring will give a corresponding variation in the number of dendritic arms. Therefore, the protein aggregates such as dimers, trimers, tetramers, pentamers, hexamers, could be controlled by the number of NTA groups.

The two series of macrocyclic polyamide derivatives with different length of linkers were synthesized as dendritic ligands (Figure 3.2). The ligands contain two, three, four, five or six nitrilotriacetic acid (NTA) terminal groups, as outlined in Scheme 3.2 and Scheme 3.5, separately. The synthetic strategy adopted here by two different pathways is very versatile.

The cyclic polyamines acted as one of the starting materials for the first step in each pathway.

In the process of divergent strategy, the key step is the formation of amide bonds between the cyclic polyamine and pendant arms by using the coupling reagent, 2-(3,4-dihydro-4-oxo-1,2,3-benzotriazin-3-yl)-1,1,3,3-tetramethyluronium tetrafluoroborate (TBTU) (9). The desired polyamide intermediates were isolated in the first step, and were followed by hydrogenolysis to give polyamino acid derivatives, and finally the polyamino acid compounds were alkylated to produce the first set of chelating agents **6a-e**. During the convergent pathway, we prepared lysine-NTA **17** and activated tetrafluorophenyl esters separately. In the final step, lysine-NTA and cyclic polyamide activated esters were coupled to generate the second set of chelating agents **12a-b**.

The synthesis of these ligands is very important step for the longer term objectives. The target molecules were designed as polyamide derivatives instead of polyamine derivatives, since the conformation of polyamide ring is rigid and planar, thus the shape of ligands, or the shape of protein aggregates can be controlled in principle.

6.4 Testing of dendritic ligands

We have successfully implemented the synthesis of two sets of dendritic ligands. The next question is: can these chelating agents generate protein aggregates with defined size specificity? To address this question, His-tagged *E. coli* thioredoxin was selected as a model protein. We then relied on the simple technique of native polyacrylamide gel electrophoresis (native PAGE) to demonstrate the formation of large His-tagged thioredoxin complexes in solution. Also image correlation spectroscopy (ICS) was applied to confirm the protein aggregation on model surfaces.

6.4.1 Demonstration of protein aggregates by native PAGE in solution

His-tagged thioredoxin is an excellent model protein for our purpose since it is small, heat-stable, readily purified and available with the polyhistidine tag (obtained in collaboration with Dr. Ball from Department of Biochemistry). We used native (nondenaturing) PAGE to show that His-tagged thioredoxin oligomers such as dimers,

trimers, tetramers, pentamers, and hexamers could be produced. The formation of these oligomers was revealed in Figure 4.3. It is very clear that the stoichiometry of these protein complexes can be controlled by using the dimeric, trimeric, tetrameric, pentameric, and hexameric NTA ligands, corresponding to compounds **6a**, **6b**, **6c**, **6d**, **6e**, respectively. Also the protein aggregation can be dissociated into the monomers with the addition of EDTA (Figure 4.3 and Figure 4.9), which has much stronger binding to nickel ion. The concentration of polyacrylamides was varied and thus the molecular weight of these His-tagged protein aggregates was estimated.

6.4.2 Confirmation with image correlation spectroscopy

Chapter 5 presented the confirmation of stoichiometric protein complexes using confocal laser scanning microscopy (CLSM). His-tagged thioredoxin was fluorescently labelled by rhodamine red™-X (RRX). The fluorescent His-tagged thioredoxin was then used with the chelating agents **6a-e** to generate protein aggregates. The fluorescent protein oligomers such as dimers, trimers, trimers, tetramers, pentamers, and hexamers, were expected to contain two, three, four, five, and six dyes in each complex. The resulting fluorescent His-tagged thioredoxin aggregates were placed and immobilized on glass surface. These samples were directly used for confocal measurements.

Recent years have been made significant advances in both visualization and characterization of individual molecules. Fluorescence microscopy of single molecules is now possible although the observation of single molecules is challenging. A technique referred to as image correlation spectroscopy (ICS) was employed to confirm the presence of protein aggregates. ICS was originally developed and used for quantitative analysis of surface receptor interactions on cell membranes. Laser scanning confocal microscopy (LSCM) was exploited to collect fluorescent images. The ICS experiments confirmed the stoichiometric formation of His-tagged thioredoxin dimers, trimers, tetramers, pentamers, and hexamers. The two parameters, cluster density (CD) and the degree of aggregation (DA), were used to quantify the extent of protein aggregation. The changes in CD and DA values confirmed the presence of protein aggregates. This provided an additional evidence that the

protein aggregation can be controlled specifically and selectively.

6.5 A model for dendritic large protein complexes

Taken the testings of Chapter 4 and Chapter 5 together, we believe that the design of the dendritic ligands (**6a-e**, and **12a-b**) for investigation of large protein aggregations was successful. The formation of defined size of protein aggregation is selective and specific. We can propose a model for the dendritic multiprotein complexes as depicted in Figure 6.1. In this model, the central core comprises of macrocyclic polyamide ring, this ring is coplanar and rigid. The bond rotations are restricted due to the amide bond properties. Because of the high binding constant of NTA to His-tagged protein, the resulting protein complex formed by the NTA group is tight. Nevertheless, the complex is reversible due to the competition of EDTA to metal ion. Since the multiple binding sites, which are carried out by NTA groups, are independent and equivalent, each dendritic ligand molecule is saturated by surrounding protein molecules. Therefore, the formation of large protein complexes is stoichiometric and dependent only on the number of NTA binding sites. For example, ligand **6c** contains four nitrogen atoms in the ring, which is attached to four NTA groups, so the stoichiometry of the protein complexes is tetrametric. Whether the linkers of dendritic ligands between rings and arms are shorter like compounds **6a-e**, or relatively longer like **12a-b**, it is not important. The multiprotein complexes can be formed from either set of ligands.

The protein used was His-tagged *E. coli* thioredoxin, which functioned as an excellent model protein for the entire investigation of the aggregation of proteins in solution. The model proposed here could be expected to work for any His-tagged protein. Hence it should be possible to create cell surface receptor aggregations using dendritic ligands. It has been recognized that receptor aggregation on cell surface can induce signal transduction in cells. It may be possible to mimic this process by assembly of complexes of proteins. This may collectively enhance reactions by improved proximity. These molecules can then be used to initiate the earliest step of signal transduction.
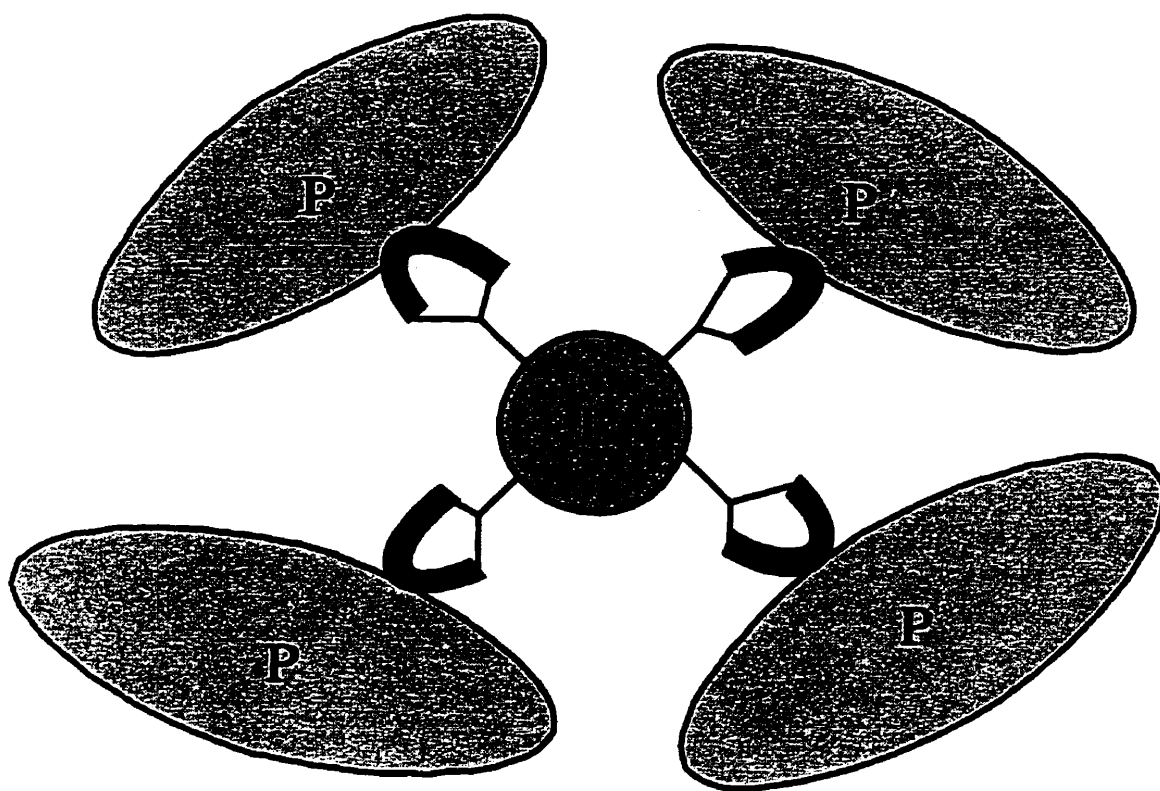
Figure 6.1: The schematic representation of protein aggregates induced by dendritic ligand, i.e. protein tetramer was formed by chelating agent **6c**. The dark circle represent the central ring structure of the dendritic ligand. The black line is the linker between ring and NTA terminal group. The half dark circle stands for the binding of NTA with two histidine residues in a octahedral coordination complex. The ellipse is the His-tagged protein. In this model, each binding site (each NTA group) can be treated to be equivalent and independent, and the fraction of binding sites occupied can be estimated as shown in Scatchard equation. NTA is a very strong chelator to His-tagged protein with association constant ~ 10^{13}, but it can be reversed by the competitive chelator EDTA. This model which is summarized here, should meet the goal of my thesis, which is aimed to create the protein aggregate with defined size and shape selectively and specifically. The figure was not drawn in scale.

6.6 Remarks on future work

Based on the design of one set of NBD-labelled macrocyclic polyamide amphiphiles **1-5**, and two sets of dendritic molecules such as **6a-e**, and **12a-b**, we have systematically begun to study the effects of molecular size and shape on their diffusion rate in model membranes. As depicted in Figure 2.11, biological membranes can be viewed as a three-layer model, which contains a less viscous (oil-like) intermediate layer with thickness of approximately 1-4 nm and two more viscous (pariffin-like) sheets with thickness of 1 nm in each layer. By using NBD-labelled macrocyclic amphiphiles **1-5**, we have conclusively reduced the transition gap, which was questioned by Vaz and his co-workers in 1985 (10), to the cross-sectional area at about 1nm^2 by FPR data presented in Chapter 2. Also we have fitted the diffusion coefficients with two various theoretical models, and indicated the two types of theories, such as modified free-area theory and Evans-Sackmann hydrodynamic theory, can be explained sufficiently. However, all of these investigations are only restricted to relatively small molecules compared to membrane proteins and membrane clusters. Therefore, the future works would be focused on studies on molecules which fully span the membrane and defined analogous transmembrane clusters. To carry out this work, Clarence Lee is continuing to work on the effect of aggregation on the lateral diffusion of peptides in model membranes. Clarence's approach is to make polypeptide aggregates by using our dendritic ligands and transmembrane His-tagged polypeptide from the b-subunit of the F_1F_0-ATP synthease. Hopefully this work will be productive in the near future. He is also continually synthesizing the rest analogues of dendritic ligands **6a-b**, and chemically putting fluorescent labels at these ligands to probe ligand-protein interactions.

In addition, another interest of Petersen's research group is concentrating on surface receptor interactions in cell membranes. To contribute to this aspect, it should be interesting to apply our dendritic ligands to stimulate cell growth. It would be interesting, but challenging to see receptor activation in signal transduction with the addition of these dendritic ligands. This work could be imagined as schematically represented in Figure 6.2. If any His-tagged receptor (R) is expressed on the surface of cells, these receptors would be
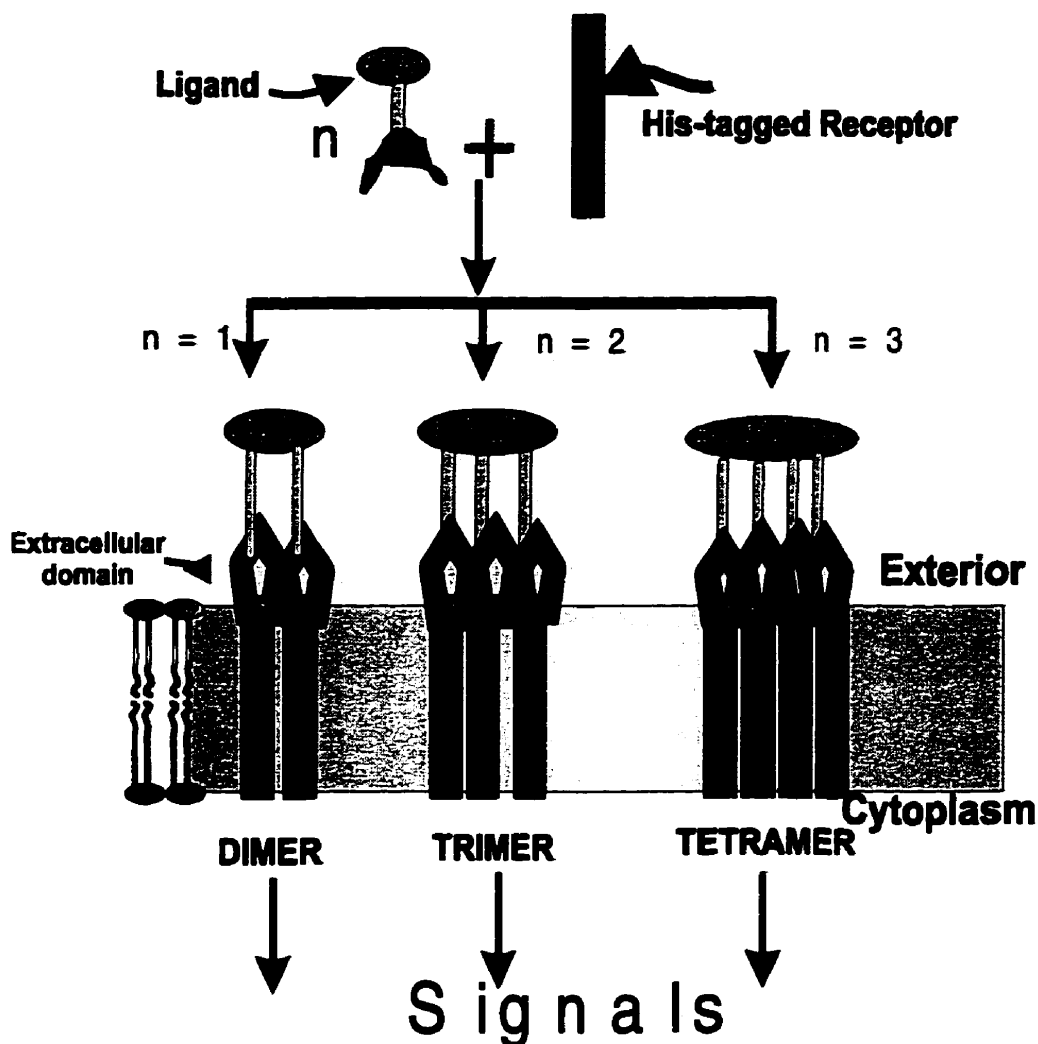
Figure 6.2: Schematic possibilities of receptor activation in biological membranes potentially induced by dendritic ligands. Assuming cell surface receptors are genetically expressed by polyhistidine tag (His-tagged), when the mixture solutions of dendritic ligands (only one unit is shown in this figure) such as compounds 6a-e, and 12a-b, with nickel chloride or nickel sulfate, is added separately, then the His-tagged receptors would bind to dendritic ligands consequently. The binding of receptor-ligand leads to the production of receptor-ligand complexes within the plane of membrane by the interaction of NTA-metal-protein. The generation of receptor-ligand aggregates, such as dimers, trimers, tetramers, may lead to conformational changes within the membrane, and thus may be involved in transmembrane signaling. The aggregation of transmembrane receptors may be reversed by an insertion of EDTA, which has been recognized to have higher binding to nickel ion. All of drawings are not in scale.

expected to bind the multiple sites of dendritic ligands, such as **6a-b** or **12a-b**, equivalently and independently. The resulting bindings could induce the aggregation of receptors. Subsequently, the signal transduction could be initiated.

In conclusion, the result of the diffusion project has demonstrated the effect of molecular sizes and shapes on their diffusion rate in model membranes. The results of protein aggregation have provided a possible model for study in the early step of signal transduction. The combination of strategic synthetic design and application to biochemical problems may prove very powerful.

6.7 References

1. Jacobson, K., Sheets, E.D., and Simson, R. Revisiting the fluid mosaic model of membranes. *Science (Washington, D.C.)*, **1995**, 268, 1441-1442.

2. Simons, K. and Ikonen, E. Functional rafts in cell membranes. *Nature*, **1997**, 387, 569-572.

3. Brown, R.E. Sphingolipid organization in biomembranes: what physical studies of model membranes reveal. *J. Cell Sci.* **1998**, 111, 1-9.

4. Vaz, W. L. C., Clegg, R. M. and Hallmann, D. Translational diffusion of lipids in liquid crystalline phase phosphatidylcholine multibilayers. A comparision of experiment with theory. *Biochemistry*. **1985**, 24, 781-786.

5. Evans, R., and Sackmann, E. Translational and rotational drag coefficients for a disk moving in a liquid membrane associated with a rigid substrate. *J. Fluid Mech.* **1988**, 194, 553- 561.

6. Balcom, B. J., and Petersen, N.O. Lateral diffusion in model membranes is independent of the size of the hydrophobic region of molecules. *Biophys. J.* **1993**, 65, 630-637.

7. Edward, J. T. Molecular volumes and the Stokes-Einstein equation. *J. Chem. Edu.* **1970**, 4, 261- 269.

8. Hochuli, E. Purification of recombinant proteins with metal chelate adsorbent. *Gen. Eng.* **1990**, 12, 87-98.

9. Knorr, R., Trzeciak, A., Bannwarth, W. and Gillessen, D. New coupling reagents in peptide chemistry. *Tetrahedron Lett.* **1989**, 30, 1927-1930.

10. Vaz, W. L. C., Goodsaid-Zalduondo, F. and Jacobson, K. Lateral diffusion of lipids and proteins in bilayer membranes. *FEBS Letters*. **1984**, 174, 199-207.